Atomic Polarisation in Molecular Photodissociation

A thesis submitted for the degree of Doctor of Philosophy

by

Ewen K. Campbell

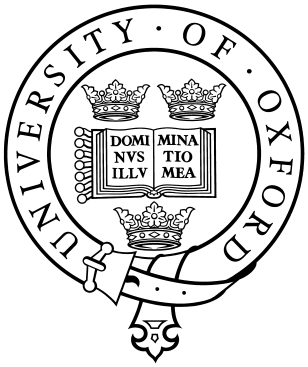

Merton College, University of Oxford

Trinity Term, 2011

Atomic Polarisation in Molecular Photodissociation

Ewen K. Campbell, Merton College

A thesis submitted for the degree of Doctor of Philosophy

Trinity Term, 2011

Abstract

Velocity mapped ion imaging has been used to experimentally investigate the photodissociation of the diatomic and triatomic molecules, Cl_2 and CS_2, respectively. For Cl_2, sets of results are presented following excitation from both the $v = 0$ and $v = 1$ vibrational levels of the electronic ground state. Dissociation of Cl_2 into both the $Cl(^2P_{3/2}) + Cl(^2P_{3/2})$ and $Cl(^2P_{3/2}) + Cl^*(^2P_{1/2})$ product channels was observed experimentally, with the photodissociation of vibrationally excited chlorine also investigated theoretically using a time-dependent wavepacket formalism. Results for CS_2 are presented following dissociation into both the singlet channel, $CS(X\,^1\Sigma^+) + S(^1D_2)$, and the spin-forbidden triplet channel, $CS(X\,^1\Sigma^+) + S(^3P_J)$.

Experimental results on the photodissociation of Cl_2 ($v = 0$) have been compared to recent time dependent wavepacket calculations performed on a set of *ab initio* potential energy curves. The experimental results include the first determination of high order electronic polarisation of $Cl(^2P_{3/2})$ atoms and, in general, good agreement was found between experiment and theory. Negligible cooling of the vibrational degree of freedom in the molecular beam allowed experimental investigation of the photodissociation of vibrationally excited Cl_2 ($v = 1$). These results are supplemented with theoretical time dependent wavepacket calculations. Although the same electronic states were found to be important as for the photodissociation of Cl_2 ($v = 0$), significant differences were found regarding many of the observables.

The indirect photodissociation of CS_2 giving rise to the singlet product channel has been investigated following excitation above and below the barrier to linearity in the $^1\Sigma_u^+(^1B_2)$ state. Above the barrier the vibrational populations of the $CS(X\,^1\Sigma^+)$ products appear inverted, while below the barrier the diatomic product state distributions point to a statistical partitioning of energy. Below the barrier, modelling of the spatial anisotropy parameter, based on angular momentum conservation, indicates the importance of non-axial recoil effects. In this region PHOFEX spectra point to an enhancement of the singlet channel for $K = 1$, relative to $K = 0$, in agreement with previous work. Surprisingly, in both regions the $S(^1D_2)$ atomic products were found to be unpolarised.

For the dissociation of CS_2 into the spin forbidden triplet channel, following excitation below the barrier to linearity in the $^1\Sigma_u^+(^1B_2)$ state, both the polarisation of triplet S-atoms and the populations of the fine-structure levels are found to depend on the vibronic band accessed. Following excitation of $K = 1$ levels, and like the singlet S-atoms, all $S(^3P_J)$ products were found to be unpolarised. For $K = 0$, however, the $S(^3P_2)$ species dominate, and are characterised by equal M_J populations, while the $S(^3P_1)$ species show a preference for the $M_J = \pm 1$ sub-levels. For these bands the electronic alignment is very similar to that observed in the dissociation of OCS, indicating a similar mechanism, at least in the exit channel, is responsible for the polarisation in both systems.

Acknowledgements

First and foremost, I would like to thank my supervisor, Professor Mark Brouard, who has been a constant source of help, guidance and encouragement during the last four years. I have thoroughly enjoyed my time in the group and it is difficult to imagine having had a better supervisor than Mark.

I would also like to thank Professor Gabriel Balint-Kurti, Dr Alex Brown and Dr Alex Johnsen for providing the dynamics code used in this thesis.

I am grateful to several members of the Brouard group for their contributions and assistance both in the office and the lab over the past few years. A big thank you goes to Dr Alex Johnsen who took the time to make sure I got up to speed with things both experimentally and theoretically. I wish to thank Dr Raluca Cireasa for her help and expertise, particularly with troublesome molecular beams. I also wish to thank both Benjamin Winter and Stephen Lucas for all their help during my final year, and both Wei-Hao Yuen and Craig Slater with whom it has been a pleasure to work.

I would like to extend my thanks to all members of the Brouard group, past and present, for making the last few years so much fun.

Finally, a big thank you goes to all my friends and family whose support is very much appreciated.

Contents

Chapter 1

Introduction

1.1 Motivation and context

When sunlight in the ultraviolet/visible region of the spectrum comes into contact with small molecules in the Earth's atmosphere one of the fundamental processes that occurs is the cleavage of a chemical bond, that is to say photodissociation takes place. The work contained in this thesis, which falls into the category of molecular reaction dynamics, seeks to understand how this bond breaking process takes place at a fundamental level. To do this, consideration needs to be given to the forces acting on the atoms during the dissociation. Information regarding these forces is encoded in the potential energy surface, one of the key concepts in reaction dynamics (see, for example, Refs [1–7]). The photodissociation process for a molecule AB may be represented by Equation (1.1). Here the species AB^* denotes the excited molecule following absorption of the photon at energy $h\nu$, and A and B are the resulting photofragments

$$AB + h\nu \rightarrow AB^* \rightarrow A + B\,. \tag{1.1}$$

One of the primary interests here is to understand how the electrons, which may be thought of as the glue holding two positive nuclei together in a chemical bond, rearrange as the two fragments separate. This information can be obtained by in-

terrogating the electronic angular momentum distribution associated with atomic photofragments. Additionally of interest here is how the photodissociation process changes when the parent molecule, AB, is vibrationally excited prior to the absorption of light.

The remainder of this chapter briefly introduces the concept of the potential energy surface, provides a general description of the different *types* of photodissociation and a discussion on the experimental techniques that can be used to probe the observables.

1.2 Photodissociation dynamics

1.2.1 The Born-Oppenheimer approximation

Exact solutions to the molecular Schrödinger equation, Equation (1.2), are difficult to find

$$\hat{H}|\Psi_i^T\rangle = E_i^T|\Psi_i^T\rangle\,. \tag{1.2}$$

The operator $\hat{H}$ corresponds to the total molecular Hamiltonian and E_i^T the exact energy levels, eigenvalues, that would be measured in an experiment. In order to solve Equation (1.2) an approximation, commonly referred to as the Born-Oppenheimer approximation [8], must be introduced, which leads to the concept of the potential energy surface. Briefly, the total wavefunction, $|\Psi_i^T\rangle$, is approximated as a product of electronic, $|\psi_{el,i}(\mathbf{r};\mathbf{R})\rangle$, and nuclear, $|\chi_i(\mathbf{R})\rangle$, parts,

$$|\Psi_i(\mathbf{r},\mathbf{R})\rangle = |\psi_{el,i}(\mathbf{r};\mathbf{R})\rangle|\chi_i(\mathbf{R})\rangle\,, \tag{1.3}$$

where the co-ordinates of the electrons and nuclei are collectively represented by $\mathbf{r}$ and $\mathbf{R}$, respectively, and the electronic part, $|\psi_{el,i}(\mathbf{r};\mathbf{R})\rangle$, is seen to depend parametrically on the nuclear co-ordinates. The approximate solutions, Equation (1.3), assume there is no coupling between the electronic and nuclear motions. The molec-

ular Hamiltonian[1] operator, $\hat{H}$, contains the nuclear kinetic energy, $\hat{T}_N$, the electron kinetic energy, $\hat{T}_e$, the Coulombic attraction between electrons and nuclei, $\hat{H}_{eN}$, nuclear-nuclear repulsion, $\hat{H}_{NN}$, and electron-electron repulsion operators, $\hat{H}_{ee}$

$$\hat{H} = \hat{T}_N + \hat{T}_e + \hat{H}_{eN} + \hat{H}_{NN} + \hat{H}_{ee}\,. \tag{1.4}$$

In general the nuclear kinetic energy term, $\hat{T}_N$, is much smaller than the other terms in the molecular Hamiltonian, $\hat{H}$, and can be ignored. The physical reason is that because the nuclei are so much more massive than the electrons, the electrons can move much faster than the nuclei for the same force. The electrons are therefore able to react quickly to changes in nuclear geometry, whereas on the timescale of electronic motion the nuclei can be regarded as stationary. Ignoring the nuclear kinetic energy term allows solutions of the electronic Hamiltonian ($\hat{H}_{el}$ = $\hat{H}$ - $\hat{T}_N$) to be found for each (fixed) nuclear co-ordinate $\mathbf{R}$

$$\hat{H}_{el}|\psi_{el,i}(\mathbf{r};\mathbf{R})\rangle = E_{el,i}(\mathbf{R})|\psi_{el,i}(\mathbf{r};\mathbf{R})\rangle \qquad i = 1, 2, 3, ..., n\,. \tag{1.5}$$

The electronic eigenfunctions in Equation (1.5) describe the potential energy experienced by the nuclei at a given value of $\mathbf{R}$, *i.e.* $E_{el,i}(\mathbf{R}) = V_i(\mathbf{R})$, and can be thought of as the potential energy surface on which the nuclei move. The Born-Oppenhiemer approximation allows the Schrödinger equation for nuclear motion on the i^{th} potential energy surface, $V_i(\mathbf{R})$, to be written as

$$\hat{H}_N|\chi_i(\mathbf{R})\rangle = \left[\hat{T}_N + V_i(\mathbf{R})\right]|\chi_i(\mathbf{R})\rangle = E_{N,i}|\chi_i(\mathbf{R})\rangle\,. \tag{1.6}$$

The eigenvalues, $E_{N,i}$, represent, in the case of bound state potentials, the set of vibrational and rotational levels for each adiabatic state, i. The slope of the potential energy surface, $V_i(\mathbf{R})$, determines the forces acting upon nuclei which in turn govern

[1] In fact, this is the non-relativistic Hamiltonian. To account for relativistic effects, usually dominated by spin-orbit coupling, a correction to the energy is given by including an extra term, $\hat{H}_{\text{SO}}$, in Equation (1.2).

their motion. For a diatomic molecule, the potential is a function of one parameter - the internuclear axis, however, for polyatomics the surface will in general be a function of $3N-5$ co-ordinates ($3N-6$ for a linear system), where N represents the number of atoms.

Neglected terms

Although in many cases the Born-Oppenheimer separation of the nuclear and electronic motions serves as a perfectly valid approximation, during photodissociation processes, of particular relevance here, it frequently breaks down [5]. In fact the derivation of Equation (1.6) assumes that the nuclear kinetic energy operator, $\hat{T}_N$, does not operate on the electronic wavefunction, $|\psi_{el,i}(\mathbf{r};\mathbf{R})\rangle$. If this assumption is no longer valid then Equation (1.6) can be represented by [9]

$$\left[\hat{T}_N + V_k(\mathbf{R})\right]\chi_k(\mathbf{R}) - \sum_i \Lambda_{ki}\chi_i(\mathbf{R}) = E_k\chi_k(\mathbf{R})\,, \tag{1.7}$$

where the matrix Λ_{ki}, given by [9]

$$\Lambda_{k,i} = \delta_{ki}\hat{T}_N - \langle\psi_{el,k}(\mathbf{r};\mathbf{R})|\hat{T}_N|\psi_{el,i}(\mathbf{r};\mathbf{R})\rangle\,, \tag{1.8}$$

involves operation on the electronic wavefunctions, $|\psi_{el,n}(\mathbf{r};\mathbf{R})\rangle$, with the nuclear kinetic energy operator, $\hat{T}_N$. This leads to the interpretation that the motions of the electrons and the nuclei are coupled. This non-adiabatic coupling effect becomes important when the adiabatic potentials are close in energy and/or when the nuclear kinetic energy is large. Both of these possibilities can arise in the case of photodissociation where the Born-Oppenheimer approximation is insufficient to describe fully the dynamics of the nuclear motion.

1.2.2 Photodissociation - general description

In a general description of photodissociation the absorption of a photon by a molecule results in an electronic transition from the ground to an electronically

excited state. This electronic state may be repulsive, or unbound, in nature such that the chemical bond holding the two fragments together breaks apart. In this way the interaction of light with the molecule has resulted in the breaking, or dissociation, of a chemical bond. The above description is consistent with a simple *direct* photodissociation occurring on a single *adiabatic* potential energy curve or surface. In reality many photodissociation processes are considerably more complicated, with many distinct potential energy surfaces involved. In fact the photoexcited state need not even be repulsive if it is crossed by or lies close in energy to another unbound state. Coupling of the two may allow a non-radiative transition to take place to the repulsive state allowing the bond to break. Direct photodissociation processes, characterised by the short timescales associated with the complete separation of the fragments, typically less than a vibrational period, where the photoexcitation takes place into the continuum, give rise to unstructured absorption (photodissociation) cross sections, $\sigma(E)$, as shown in the left hand panel of Figure 1.1. In this fast dissociation process, the energy dependence of the cross section, $\sigma(E)$, is directly related to the square of the initial nuclear wavefunction in the electronic ground state and the gradient of the excited state potential curve, often termed as the *reflection principle* [5].

On the other hand, if the molecule is promoted to a *quasi*-stable state, with lifetimes greater than a typical vibrational period, of the order of tens of femtoseconds, prior to bond breaking then the general process is referred to as *predissociation*. This general process has been classified by Herzberg [10] according to the mechanism giving rise to the fragmentation from the metastable state, now termed Herzberg type I (*electronic*), Herzberg type II (*vibrational*) and Herzberg type III (*rotational*) predissociations. Due to the presence of *quasi*-stable states, predissociation processes give rise to structures, termed resonances, in the absorption cross-section, similar to the features observed in bound state spectroscopy. In type I (*electronic*) predissociation the excitation takes place to a state belonging to a different electronic configuration than the state in which the fragmentation occurs. This process is

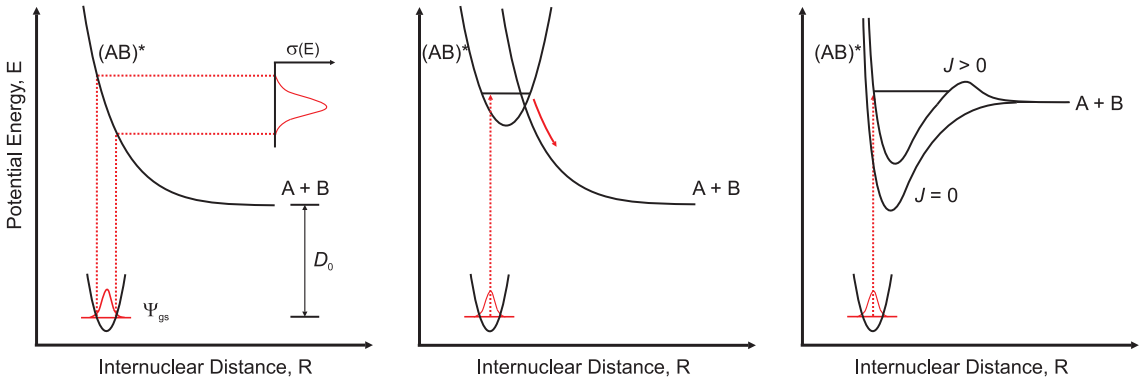

Figure 1.1: Schematic representation of direct (left) and indirect (middle and right) photodissociation processes of a diatomic molecule, AB. The middle panel represents a Herzberg type I *electronic* predissociation whereas the right panel corresponds to *predissociation by rotation*, or Herzberg type III.

shown schematically in the middle panel of Figure 1.1. The coupling between the bound and repulsive curves may be due to, for example, non-adiabatic, Coriolis or spin-orbit interactions. Herzberg type II predissociations differ in that the excited and final states correspond to the same *electronic* configurations of the molecule and arise in the case of tri- and polyatomic molecules. Herzberg type III, also called *predissociation by rotation*, can arise in the case of rotating parent molecules. For non-rotating diatomic species, the molecule may only dissociate if it is excited above the highest bound vibrational state. However, if the molecule is rotating an extra centrifugal term $\sim \hbar^2 J(J+1)/2\mu R^2$ should be added to the *electrostatic* potential. In effect this term gives rise to a barrier to dissociation, supporting *quasi*-bound levels higher in energy than the dissociation limit, as shown in the right hand panel of Figure 1.1. Tunnelling through this centrifugal barrier then allows type III predissociation to take place.

Mode Specific Photodissociation

The vibrational excitation of molecules in their electronic ground state can modify the pathway of a photodissociation process relative to those in their vibrational

ground state. The Franck-Condon factors, the overlap of ground and excited state vibrational wavefunctions, will be different for vibrationally excited reagents. As a result the molecule may be able to access different parts of the excited state potential which can influence, for example, the branching into distinct product channels [11]. A particularly noteworthy example of this *mode specificity* is given by Crim and Schinke on the photodissociation of HOD in the $\tilde{A}$ state [12]. In their experimental and theoretical study the authors found that the relative production of OH compared to OD fragments was dependent on the initial vibrational state of the parent molecule *and* the wavelength used for the photodissociation. They reported that excitation of four quanta in the O-H stretching mode ($4\nu_{\mathrm{OH}}$) led to a selective breaking of the O-H versus the O-D bond. At two of the photolysis wavelengths studied, 239.5 nm and 266 nm, the excess production of OD over OH was as high as 15. However, at higher energy, 218.5 nm, the OD and OH products were found to be formed in equal quantities. Wavepacket calculations on the *ab initio* potential surface showed that promotion of the molecule from high, $4\nu_{\mathrm{OH}}$, O-H stretching levels below the barrier separating the OD and OH product channels gave rise to a large Franck-Condon overlap between the OD + H channel continuum wavefunction and the HOD vibrational wavefunction, ultimately resulting in a large excess of OD products. On the other hand, excitation at the higher energy, 218.5 nm, was shown to reach the $\tilde{A}$ state potential above the energetic barrier separating the OD + H and OH + D product channels. In this region the continuum wavefunctions for both channels were shown to be significant, allowing for comparable Franck-Condon overlap of the initial vibrational wavefunction with the continuum wavefunctions for dissociation into OD + H and OH + D [12].

Electronic angular momentum polarisation

Of particular interest for the work in this thesis is the distribution of electronic angular momenta, J, of atomic products following a photodissociation process. The concept of anisotropy in the distribtion of J following diatomic dissociation was

first discussed by Van Brunt and Zare in 1968 [13]. They described the *adiabatic* photodissociation of a molecule, AB, in a well defined molecular Ω level, where Ω describes the projection of the electronic angular momentum onto the internuclear axis. If this projection quantum number is conserved throughout the dissociation process then the population of magnetic sublevels, M_{J_A}, for a given fragment will depend on the value of Ω and the projection quantum number of the cofragment, M_{J_B}, that gives rise to the specific electronic state, since

$$\Omega = |M_{J_A} + M_{J_B}| \,. \tag{1.9}$$

It turns out that the asymptotic electronic polarisation of an atomic fragment is highly sensitive to many features of the photodissociation process including the nature of the excitation and character of the electronic states populated in the Franck-Condon region and any non-adiabatic transitions that take place both in the short and long range regions of the potential energy surface(s). In fact, measurements of atomic polarisation are sensitive not only to the populations of the various M_J states but also to the coherences describing the correlation between photofragments in different M_J levels. Following the simultaneous excitation of different electronic states with a well-defined phase, coherent terms in the electronic angular momentum distribution can result from interference between different dissociation pathways. Additionally, coherent terms may arise as a result of a non-adiabatic transition between states along the dissociation co-ordinate, leading to interference between the two pathways. In essence, the photofragments' angular momentum polarisation provides an insight into the electronic motions taking place as the fragments separate.

1.3 Experimental probes

Laser induced fluorescence (LIF) based detection allows for the fully quantum state selection of the products of a photodissociation reaction. In LIF the photofragments, in a well defined quantum state, are promoted *via* absorption of a photon

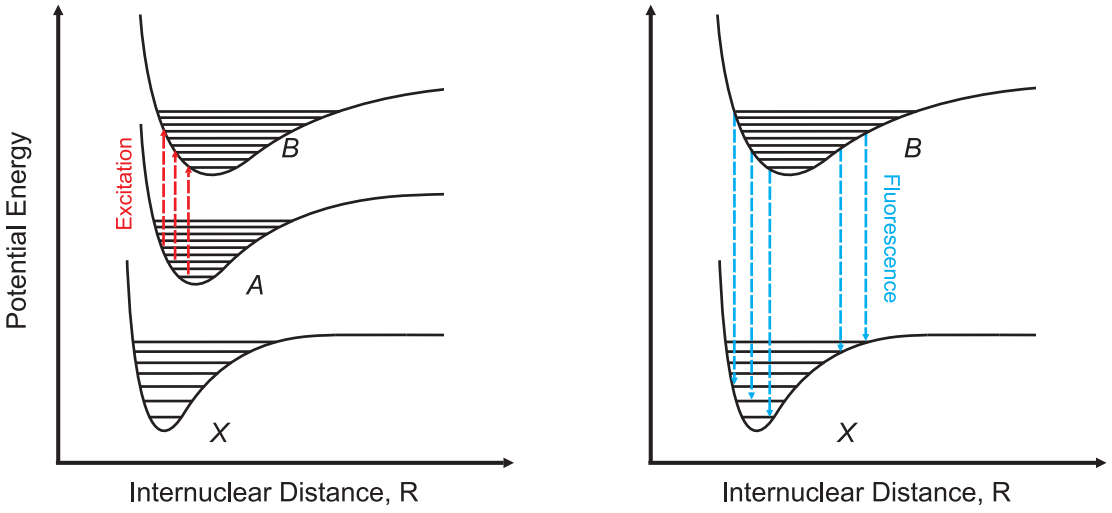

Figure 1.2: Schematic representation of the laser induced fluorescence technique. The diatomic products from a photodissociation process are born in various rovibrational levels of the A electronic state. Using a laser these fragments are electronically excited to the B state (left). The populated B state levels radiatively decay to the ground electronic state, X, by fluorescence which is detected experimentally (right).

to a state which is known to radiatively decay by fluorescence. The induced fluorescence at a particular wavelength is detected by, for example, use of a photomultiplier tube and monochromator setup. The laser induced fluorescence technique is schematically represented in Figure 1.2. Provided that the spectroscopy of the states involved in the LIF process is well known, the probe laser used to induce the fluorescence can be scanned over energetically accessible rovibrational states of the (diatomic) photofragment allowing one to effectively probe the characteristic energy disposal amongst the product degrees of freedom. LIF measurements on the products of photodissociation have been reported for a huge number of diatomic species including, for example, CN, NO, CS, and OH from ICN [14, 15], NO_2 [16–22], CS_2 [23], H_2O [24–30] and H_2O_2 [31, 32], respectively. Furthermore, use of a narrow-bandwidth laser allows sensitivity to the velocity (and therefore angular) distribution of the fragments since a sufficiently narrow bandwidth laser allows one to scan across (determine) the Doppler line shape of a *single* rovibrational transition. The Doppler-resolved line shape is characteristic of the velocity components of the

photofragments along the direction of laser propagation. Measurements of this kind are highly sensitive to the details of a photodissociation process since they can provide information on both the population of photofragment quantum states as well as the associated vector properties. The dependence of Doppler lineshapes on the spatial distribution of fragments and their rotational angular momenta, see later, has been provided by Dixon [33]. One drawback of LIF based detection techniques compared to, for example, mass spectroscopic techniques is that it is much harder to detect photons than charged species.

In photofragment translational spectroscopy [34] a molecular beam containing the species under investigation, typically seeded in an inert carrier gas (*e.g.*, He, Ar, Ne) to enhance cooling of the rotational degrees of freedom, is intersected by a pulsed laser beam, which dissociates the molecules. The neutral fragments, which possess a velocity distribution intrinsic to the photodissociation process, are allowed to travel under collision free conditions for some time prior to ionisation and detection. The ionisation process is typically achieved using an electron gun, and the resulting ions detected according to their time of flight (TOF). In this way the experiment can be sensitive to the energy disposal amongst the degrees of freedom of the photofragments. Rotating either the molecular beam propagation direction, detector or the polarisation vector of the photodissociation laser, allows further information to be obtained on the photofragment *angular* distributions. This experimental methodology was first introduced by Busch and Wilson in the 1960s [34], who investigated the photodissociation of the molecules Cl_2, I_2, IBr, NOCl and NO_2 [34–39].

The resonance enhanced multiphoton ionisation (REMPI) technique allows a fully quantum state selectivity in the detection of atoms and small photofragments. The principles and applications of this technique have been discussed by Ashfold *et al.* [40]. Briefly, population in the quantum state under study is transferred into an electronically excited state by the absorption of one or more photons. Absorption of a further one or more photons then allows ionisation to take place from this excited state. The number of photons involved in the initial excitation and ionisation steps

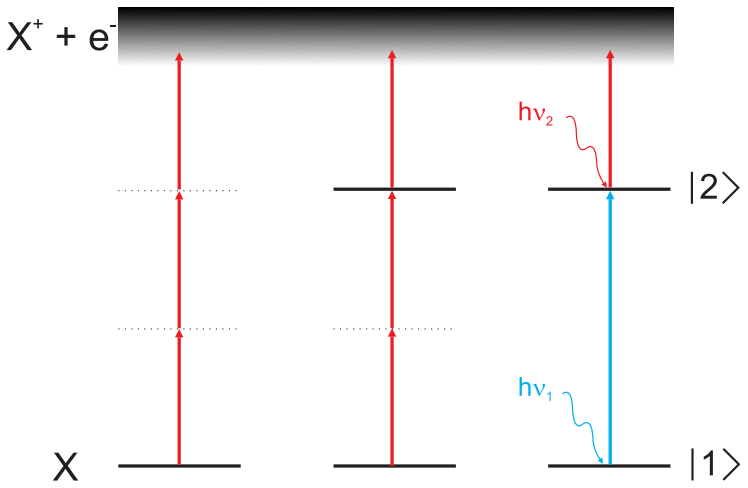

Figure 1.3: Illustration of conventional multiphoton ionisation (left) and REMPI (middle and right) processes for the neutral species, X. In conventional multiphoton ionisation no intermediate states are involved in the ionisation process, only *virtual* states (dotted lines) associated with the electric field. A (2+1) REMPI scheme *via* intermediate state $|2\rangle$ is illustrated in the middle, with a two colour (1+1′) REMPI scheme depicted on the right. Adapted from Ref [40].

are generally given in parenthesis (*e.g.*, (1+1), (2+1), (3+2) REMPI). The energy used for this multiphoton process may differ for the two steps involved, in which case a prime is used in the description (*e.g.*, (1+1′) REMPI). A diagram illustrating some commonly used REMPI schemes is provided in Figure 1.3. By utilising a *resonant* intermediate state the probability of absorption and subsequent ionisation are greatly enhanced, by several orders of magnitude, over a conventional multiphoton ionisation scheme, giving this procedure a significant advantage. The combination of REMPI state selectivity with time of flight (TOF) detection allows information regarding the kinetic energy and spatial distribution(s) of neutral fragments to be obtained at the quantum state-selected level.

The ion imaging technique, a combination of REMPI-TOF with 2 dimensional detection, was pioneered by Chandler and Houston [41]. The ion imaging technique allows for the extraction of the full three dimensional scattering distribution of fragments from a photodissociation process. In cases where the laser polarisation(s) are parallel to the detection plane and the angular momentum distribution is

isotropic a cylindrical symmetry exists and one can reconstruct the 3D distribution from the 2D image (projection) using an Abel inversion procedure [42, 43]. The first demonstrations of ion imaging by Chandler and Houston were limited by the velocity resolution that could be obtained using the Wiley-McLaren [44] electrode system. Eppink and Parker [45] showed that a greatly improved velocity resolution could be obtained by removal of the grid used in the Wiley-McLaren set up, and tuning the voltages applied to a system consisting of three open electrodes. Eppink and Parker were able to show that fine adjustment of their ion lens allowed each ion with the same mass and velocity to strike the detector at the same position regardless of its point of formation within the laser interaction region [45]. The use of event counting [46] algorithms during image acquisition allowed further improvement to the velocity resolution. More recently, a series of imaging techniques have been developed in which only the central portion or 'slice' of the 3D scattering distribution is actually recorded. Generally referred to as 'slice imaging', this technique allows for an improvement to the velocity resolution. Furthermore, at least in principle[1], the analysis of ion images recorded using a slicing technique should be simpler, removing the need for a procedure to recover the 3D distribution from a 2D projection. A detailed description of the types of slicing can be found in the recent review article by Ashfold *et al.* [48].

Probing angular momentum polarisation

The experimental techniques described above are sensitive to both the scalar and vector properties that characterise photodissociation processes. As such they can, in principle, probe the distribution of angular momenta, J, of the photofragments. The principles and methodolgy used to probe anisotropic distributions of J are entirely general and can be used to probe both rotational and electronic polarisations.

Experimental sensitivity to the distribution of **J** following a photodissociation

[1]Where the angular momenta of the photofragments is polarised the unambiguous extraction of the angular momentum distribution is very sensitive to the degree of slicing achieved, as discussed in Ref [47].

process can be intuitively understood since the 'direction' of J is inherently linked to the direction of $\boldsymbol{\mu}^{el}$, the electronic transition dipole moment associated with the optical transition involved in the detection process. Typically, in order to extract data regarding the angular momentum distribution of photofragments, experimental measurements are performed employing several different probe laser polarisation directions, with respect to some laboratory reference frame, see Section 2.1. Through the $|\boldsymbol{\mu}^{el} \cdot \boldsymbol{\epsilon}|^2$ transition probability for absorption, where $\boldsymbol{\epsilon}$ is the electric vector of the light, the relationship between $\mathbf{J}$ and $\boldsymbol{\mu}^{el}$ dictates that altering the direction of $\boldsymbol{\epsilon}$ will change the sensitivity to a particular part (moment) of the $\mathbf{J}$ distribution. Furthermore, by collecting data using a *different* optical transition *e.g.*, a different intermediate state in a REMPI process, one becomes sensitive to a different set of transition dipoles and therefore moments of the angular momentum distribution. Measurements using a comprehensive set of probe polarisation directions and/or optical transitions allows for the complete characterisation of the distribution of J in the laboratory frame.

The relationship between the transition dipole moment, $\boldsymbol{\mu}^{el}$, and the direction of J can be easily understood by taking the case of parallel and perpendicular electronic transitions of a diatomic molecule, for example $\Sigma - \Sigma$ or $\Sigma - \Pi$, respectively. For a diatomic molecule ($C_{\infty v}$ or $D_{\infty h}$ symmetry) the electronic transition dipole matrix elements may be written as

$$\langle \psi_f^{el}(\mathbf{r};\mathbf{R}) | \boldsymbol{\mu}^{el}(\mathbf{r}) | \psi_i^{el}(\mathbf{r};\mathbf{R}) \rangle \,, \tag{1.10}$$

where $|\psi_i^{el}(\mathbf{r};\mathbf{R})\rangle$ and $|\psi_f^{el}(\mathbf{r};\mathbf{R})\rangle$ represent the initial and final states. A parallel type transition is only allowed if the direct product[2]

$$\Gamma_f \otimes \Gamma_\mu \otimes \Gamma_i \,, \tag{1.11}$$

contains the totally symmetric species Σ. For this electronic transition the symmetry

[2]Here Γ_i is used to denote the symmetry of species i.

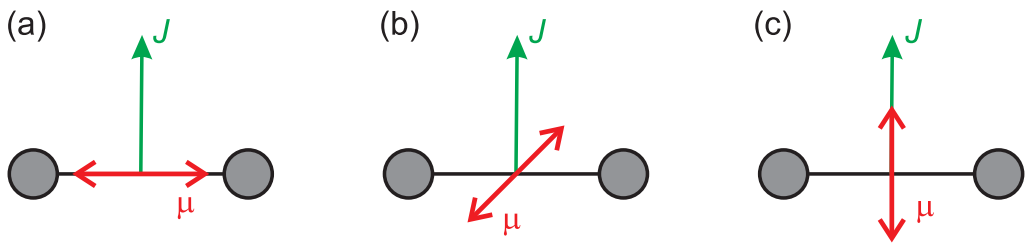

Figure 1.4: Relationship between the electronic transition dipole moment, $\boldsymbol{\mu}$, and the rotational angular momentum, J, in the high J limit where J lies perpendicular to the bond axis. (a) corresponds to the case of a parallel transition (P or R-branch), while (b) and (c) are following a perpendicular electronic transitions for P (and R)-branch and Q-branch excitation, respectively. Adapted from Ref [49].

species of the transition dipole moment, $\boldsymbol{\mu}^{el}$, transforms as Σ and therefore the relation

$$\Gamma_f \otimes \Gamma_i \supset \Sigma\,, \tag{1.12}$$

must hold, such that $\Gamma_f = \Gamma_i$ and $\Delta\Lambda = 0$. The symmetry species Σ dictates that the electronic transition dipole moment, $\boldsymbol{\mu}^{el}$, lies parallel to the bond axis, R. In the high J limit, where the rotational angular momentum becomes perpendicular to R, an orthogonal relationship therefore exists between $\boldsymbol{\mu}^{el}$ and J. Examination of the rotational selection rules shows that only P ($\Delta J = -1$) and R-branch ($\Delta J = +1$) transitions exist for this case.

For a perpendicular transition, $\Delta\Lambda = \pm 1$ and $\Gamma_f \neq \Gamma_i$, examination of Equation (1.11) shows that the transition dipole moment, $\boldsymbol{\mu}^{el}$, must transform as Π, *i.e.* perpendicular to the bond axis, R. This symmetry species means that in the high J limit the transition dipole moment may be either parallel or perpendicular to the rotational angular momentum, J. Similar group theoretical arguments for the matrix elements of $\boldsymbol{\mu}^{el}$ in the $|JM\rangle$ basis show that for Q-branch ($\Delta J = 0$) excitation the electronic transition dipole moment is parallel to J, whereas for P and R-branch excitations ($\Delta J = \pm 1$) $\boldsymbol{\mu}^{el}$ is perpendicular to J. These three simple cases are illustrated in Figure 1.4.

1.4 Outline of thesis

The work contained herein concerns the photodissociation of the diatomic and triatomic molecules, Cl_2 and CS_2, respectively. For Cl_2 ion images were recorded for both the ground and excited state photofragments, $Cl(^2P_{3/2})$ and $Cl^*(^2P_{1/2})$, at several photodissociation wavelengths across the first absorption band. The results of the experimental work, which includes the determination of the fragments electronic angular momentum polarisation are compared to recent state-of-the-art time dependent wavepacket calculations [50] performed on a set of high level *ab initio* potential energy curves [51]. In this work these calculations were extended to encompass the photodissociation of vibrationally excited chlorine molecules. For the triatomic molecule CS_2, two sets of experiments are reported here, with both the $S(^1D_2)$ and $S(^3P_J)$ fragments observed. The first study at 193.3 nm concerns the indirect photodissociation following excitation *above* the barrier to linearity in the $^1\Sigma_u^+(^1B_2)$ state. For the latter study, in which several photodissociation wavelengths are reported, the excitation takes place *below* the barrier, close to the energetic threshold for production of $S(^1D_2)$.

Chapter 2 describes the underlying photodissociation theory used to rationalise the experimental results. Chapter 3 provides a detailed description of the experimental methodology and the analysis used to extract results from raw measurements. Chapter 4 is concerned with the photodissociation of Cl_2, while Chapters 5 and 6 present results on the photodissociation of CS_2.

Chapter 2

Theory

A wealth of information can be gained from experimental studies on the photodissociation of simple gas phase molecules, including, for example, scalar properties such as the distribution of available energy amongst the various degrees of freedom of the fragments and branching ratios between different product channels. Additional information on the characteristic directional properties associated with photodissociation processes, for example the angular distribution of the photofragments and the alignment/orientation of their angular momenta, may also be observed, allowing the detailed dynamics of the bond breaking process to be unravelled. This chapter seeks to link the observables available from such studies with the dynamical and mechanistic information that can be inferred.

The underlying treatment used to describe the light-matter interaction, from which all theoretical equations described herein are based, gives an expression for the photodissociation cross-sections $\sigma(\omega)$ as [5, 52–54]

$$\sigma(\omega) \propto \omega |\langle \Psi_f | \boldsymbol{\epsilon} \cdot \hat{\boldsymbol{\mu}} | \Psi_i \rangle|^2 \,. \tag{2.1}$$

In Equation (2.1), which may be derived using time-dependent or time-independent perturbation theory (see, for example, Refs [55–57]), $|\Psi_i\rangle$ and $|\Psi_f\rangle$ describe the initial and final states, ω is the transition frequency, $\hat{\boldsymbol{\mu}}$ is the electric dipole operator and $\boldsymbol{\epsilon}$ is a unit vector describing the light polarisation. Equation (2.1) is derived by

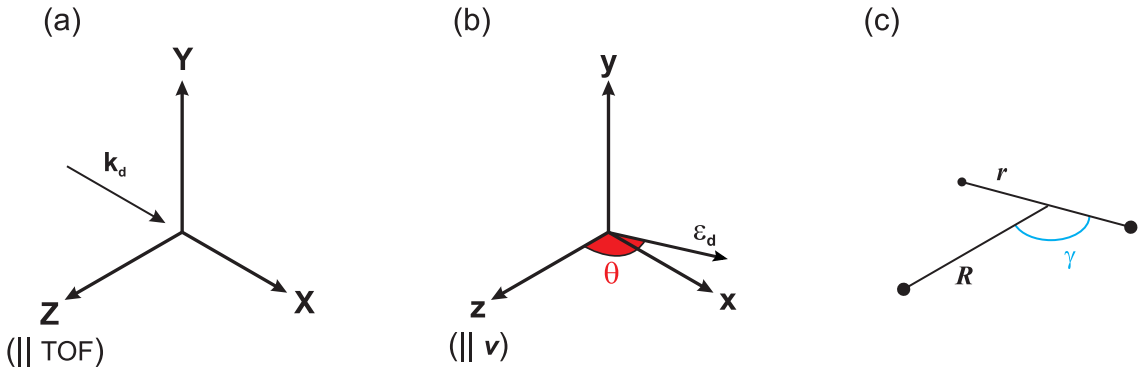

Figure 2.1: Laboratory (time of flight) (**a**), molecular (**b**) and Jacobi (**c**) frames of reference. See the text for a definition of the symbols used.

treating the light as a classical electromagnetic field interacting with the molecule which is described quantum mechanically. It is based on the assumption that the interaction between the light and the molecule is weak, treated as a first order perturbation, and long in duration, so that the molecule sees the electric field as a periodic perturbation [5].

2.1 Frames of reference

Three frames of reference are commonly used throughout this thesis, referred to as the laboratory, molecular and Jacobi frames, as shown in Figure 2.1. Experimental measurements can only be directly sensitive to *laboratory* frame properties, however, in order to elucidate the origins of certain dynamical quantities, it becomes necessary to transform to a *molecular* reference frame, with the two related *via* a simple set of rotations [52]. The laboratory frame used in this thesis, also referred to as the time of flight (TOF) frame, defines the **Z** axis as the TOF direction with the **X** axis parallel to the direction of propagation of the photolysis laser, $\mathbf{k_d}$ [58–61]. In the molecular frame the **z** axis is defined as the recoil direction of the photofragment, $\boldsymbol{v}$, with the electric polarisation vector of the linearly polarised photolysis light contained within the **xz**-plane [62–66]. For circularly polarised photolysis light, the propagation direction, $\mathbf{k_d}$, rather than the electric vector, $\boldsymbol{\epsilon_d}$, is used. The Jacobi

frame, frequently used to treat three atom systems [5], is defined in terms of the **R** co-ordinate which lies parallel to the recoil direction, the diatomic fragment bond direction, **r**, and γ which refers to the angle between the two. Note this definition has no dependence on any laboratory frame axis. Furthermore, assuming that axial recoil of the fragments takes place, the **R** axis can be considered to become parallel to the *molecular* frame **z** axis in the limit of large **R**.

2.2 Scalar properties

2.2.1 Internal energy distributions

Following the absorption of a photon the excess energy, E_{avl}, given as the difference between the photon energy, $h\nu$, and the bond energy, D_0, plus any energy contained within the internal degrees of freedom of the parent molecule, E_{int}, can be partitioned into the kinetic energy of the dissociating fragments and/or their internal degrees of freedom, *e.g.*, rotation and vibration for polyatomic fragments,

$$E_{\text{avl}} = h\nu - D_0 + E_{\text{int}} \,. \tag{2.2}$$

In the case of a diatomic system, where no rotation or vibration of the fragment is possible, this excess energy necessarily goes into the translational motion of the fragments. The atomic fragments can, of course, be electronically excited and therefore several distinct product channels may exist, each associated with different dissociation energies, D_0, giving rise to a distinct recoil velocity for each atomic state.

As an example an ion image of the the $\text{Cl}(^2\text{P}_{3/2})$ fragments following the photodissociation of Cl_2 at 398 nm, taken from Chapter 4, is shown in Figure 2.2. The three intense features in the ion image correspond to the three peaks in the speed distribution, $P(v_P)$, shown on the right hand side of Figure 2.2. Specifically, these

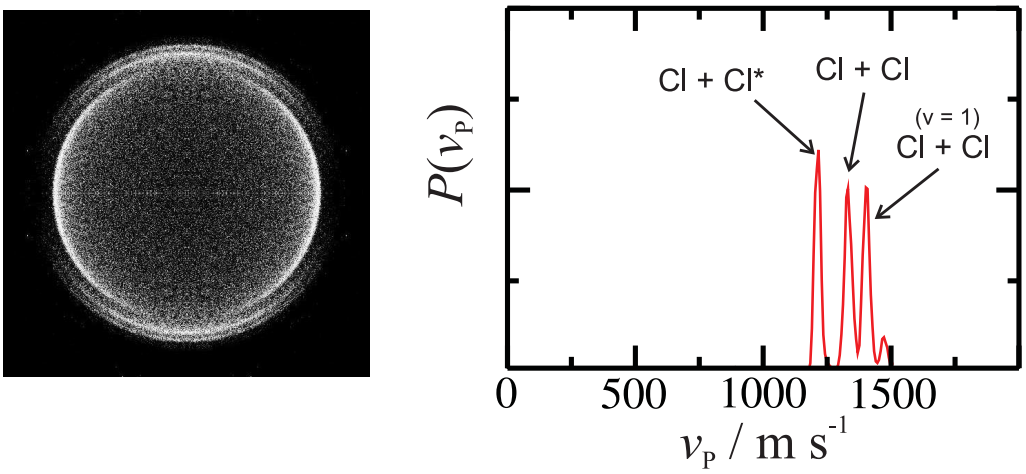

Figure 2.2: Velocity map ion image (left) and speed distribution (right) for the $Cl(^2P_{3/2})$ fragments following the photodissociation of Cl_2 at 398 nm.

features are due to the processes

$$Cl_2 + h\nu \longrightarrow Cl(^2P_{3/2}) + Cl^*(^2P_{1/2}) \tag{2.3}$$

$$Cl_2 + h\nu \longrightarrow Cl(^2P_{3/2}) + Cl(^2P_{3/2}) \tag{2.4}$$

$$Cl_2(v = 1) + h\nu \longrightarrow Cl(^2P_{3/2}) + Cl(^2P_{3/2}) \ . \tag{2.5}$$

Given the dissociation energy, D_0, for the process detailed in Equation (2.4) of $\sim 2 \times 10^4\,cm^{-1}$, the spin-orbit energy $E_{SO} \sim 882\,cm^{-1}$ [67] and the vibrational energy $\bar{\nu} \sim 600\,cm^{-1}$, the velocities of the fragments associated with each of the above processes can be calculated as 1204, 1323 and $1400\,m\,s^{-1}$.

The distributions can be considerably more complicated in the case of systems with greater than 2 atoms. In such cases the excess energy can also be distributed amongst the vibrational and rotational degrees of freedom of the photofragments. Important dynamical information regarding, for example, the forces acting on the nuclei in the exit channel [5] can be made by measurements of the internal energy distributions of such fragments.

2.2.2 Atomic spin-orbit state populations

In the case of atomic fragments formed in states with non-unity spin multiplicity (*e.g.*, $^2\mathrm{P}_J$ and $^3\mathrm{P}_J$), the relative populations of each spin-orbit (fine structure) level (*e.g.*, $^2\mathrm{P}_{1/2}$ and $^2\mathrm{P}_{3/2}$) can be used, in some cases, to describe the character of the dissociation process. In particular, measurements of the relative population of each spin-orbit level, $\mathrm{P}(J)$, have been frequently used to determine the degree to which non-adiabatic transitions play a role in the dissociation process. Of course, these populations will be highly sensitive to the exact nature of the excitation process itself in addition to the couplings between potential energy curves anywhere from the Franck-Condon region to the long range, asymptotic region.

In several diatomic photodissociation systems attempts have been made to interpret the relative populations of spin-orbit states in terms of the criteria set out by Massey [68]. The parameter ξ_t, sometimes referred to as the translational adiabaticity parameter [69], is (qualitatively) used to give the probability that transitions will take place between *adiabatic* molecular states as the dissociation proceeds through the region of $\mathbf{R}$ where the separation between molecular states becomes comparable in energy to the spin-orbit splitting of the atomic fragments. ξ_t depends on the time spent in this region, termed the 'recoupling zone', and can be written as [68, 69]

$$\xi_t = \frac{\Gamma \Delta_{\mathrm{SO}}}{\hbar v}\,, \tag{2.6}$$

where Γ is the width (length) of the recoupling zone, v the velocity of the fragments and Δ_{SO} the spin-orbit splitting. When the separation of the fragments is slow and/or the atomic spin-orbit splitting is very large, $\xi_t \gg 1$, and the dissociation may be regarded as occurring on a single *adiabatic* curve, with the spin-orbit populations, $\mathrm{P}(J)$, determined by the *adiabatic* correlation diagram linking the atomic and molecular states. On the other hand, when the separation between fragments is very fast and/or the spin-orbit splitting is small, $\xi_t \ll 1$, the *diabatic* limit is reached. Since the diabatic limit arises when the separation of fragments is very fast the spin-

orbit populations are determined by projecting the molecular wavefunction in the recoupling zone onto the spin-orbit states of the separated fragments. The above categorisation has been used to interpret atomic spin-orbit population data in the photodissociation of numerous small molecules, for example O_2 [70–72], Cl_2 [61], SH [73–75] and SO_2 [59, 76, 77]. As a note of caution, however, the trends in the adiabatic nature of the photodissociation expected solely by consideration of ξ_t with respect to, for example, the recoil velocity, have been proved entirely wrong in some cases, with the photodissociation of Cl_2 into two ground state $Cl(^2P_{3/2})$ fragments a good example [50, 61, 62, 78, 79].

2.3 Vector properties

In addition to the picture of a dissociation that can be built up from consideration of the scalar properties mentioned above, significant, additional insight into the dynamics can come from investigation of the vectors associated with the process, see, for example, Refs [33, 66, 80–86]. The important vectors used to characterise a photodissociation event include the transition dipole moment of the parent molecule, $\boldsymbol{\mu}$, the electric vector of the dissociation light, $\boldsymbol{\epsilon}_\mathbf{d}$, the recoil direction of the fragments, $\boldsymbol{v}$, and their associated angular momenta, $\mathbf{J}$. The investigation of the relationships between important vectors in photodissociation dates back to the early 1960's [87].

2.3.1 Spatial anisotropy parameter

Excitation of a randomly oriented (isotropic) gas sample with a source of laser radiation gives rise to an anisotropic distribution of excited molecules in the laboratory frame. This result comes about since, as discussed in Section 1.3, the excitation probability, $|\boldsymbol{\mu} \cdot \boldsymbol{\epsilon}_\mathbf{d}|^2$, dictates that an anisotropic distribution of transition dipole moments will follow the absorption. Coupling this with the relationship between the vectors $\boldsymbol{\mu}$ and the recoil direction, $\boldsymbol{v}$, which for the simplest diatomic case[1] are

[1]Under the axial recoil approximation.

either parallel or perpendicular[2], leads to an easily understood anisotropic distribution of photofragment velocities in the laboratory frame. In fact this correlation between $\boldsymbol{\epsilon_d}$ and $\boldsymbol{v}$, mediated by the transition dipole moment $\boldsymbol{\mu}$ is the most studied of all vector correlations and provides information on the symmetry and lifetime of the excited state. The first theoretical treatment by Zare [87] led to the now widely known result for the scattering (angular) distribution of photofragments,

$$\mathcal{I}(\theta, \phi) = \frac{1}{4\pi}[1 + \beta P_2(\cos\theta)]\,, \tag{2.7}$$

where θ and ϕ are the polar angles describing the relationship between the vectors $\boldsymbol{\epsilon_d}$ and $\boldsymbol{v}$, and $P_2(x)$ is the second order Legendre polynomial. The spatial anisotropy parameter, β, is defined as

$$\beta = 2\langle P_2(\cos\theta')\rangle\,, \tag{2.8}$$

where θ' is the angle between $\boldsymbol{\mu}$ and $\boldsymbol{v}$. Since the products recoil over a range of possible dissociation angles, the β parameter is usually expressed as a weighted average $\langle \cdots \rangle$ over this distribution. Consideration of Equations (2.7) and (2.8) show that the spatial anisotropy parameter takes the limiting value of $+2$ when $\mathcal{I}(\theta, \phi) \propto \cos^2(\theta)$ and -1 for the case where $\mathcal{I}(\theta, \phi) \propto \sin^2(\theta)$. These two limiting values for the photofragment anisotropy parameter are obtained for the instantaneous, axial recoil, dissociation of molecules following parallel ($\Delta\Omega = 0$) and perpendicular ($\Delta\Omega = \pm 1$) transitions, respectively. The photofragment angular distributions for the limiting cases of β are shown in Figure 2.3. Of course, if the excitation process involves a mixture of parallel and perpendicular transitions, then the β parameter can be regarded as a weighted sum for the relative transition probabilities. Several factors can result in a reduction in β from its limiting values and are discussed below.

If the excited parent molecule has time to rotate prior to fragmentation, as can

[2]Following $\Delta\Omega = 0$ and $\Delta\Omega = \pm 1$ transitions, respectively.

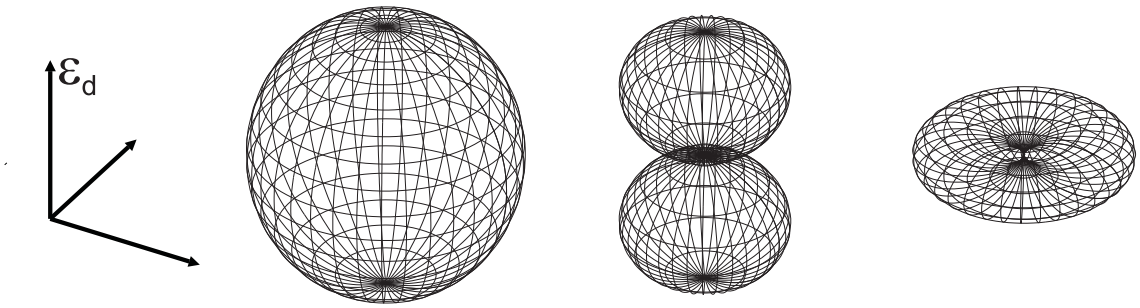

Figure 2.3: Photofragment angular distributions, $\mathcal{I}(\theta, \phi)$, for the limiting cases of $\beta = 0$ (left), $+2$ (middle) and -1 (right). The spherical angles θ and ϕ describe the relationship between the vectors $\boldsymbol{\epsilon_d}$ and $\boldsymbol{v}$.

be the case in predissociation processes in which the lifetime of the predissociative state may be comparable to the rotational period of the molecule, typically a few picoseconds, then the correlation between the electric vector of the light, $\boldsymbol{\epsilon_d}$, and the transition dipole moment, $\boldsymbol{\mu}$, will become degraded. The overall result of this is a reduction in the β parameter. In the limit of infinite parent lifetime, Busch and Wilson [37], and Jonah [88] have shown that β will be reduced by a factor of 4 for a diatomic molecule. Bersohn and Yang [89] and Zare and co-workers [90] have investigated the more complex problem of the dissociation of triatomic molecules. For the specific case of a prolate symmetric top molecule, β can be reduced by a factor of 5 in the long lifetime limit [89].

In the case of polyatomic species, the transition dipole moment, $\boldsymbol{\mu}$, is no longer constrained by symmetry to lie either parallel or perpendicular to the breaking bond. Therefore, non-limiting values of β should be expected even in the case of a prompt, direct dissociation process. As an example, consider the case of the dissociation of a bent symmetric triatomic molecule, AB_2, into the fragments AB and B. If, for example, the ground and excited electronic states are of A_1 and B_2 symmetry, taking the system in the C_{2v} point group, then group theory dictates that the transition dipole moment, $\boldsymbol{\mu}$, must have B_2 symmetry, since the direct product,

$$\Gamma^i \otimes \Gamma^{\boldsymbol{\mu}} \otimes \Gamma^f \,, \tag{2.9}$$

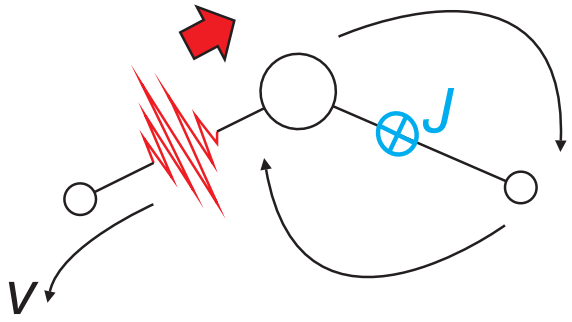

Figure 2.4: Cartoon showing non-axial recoil following photodissociation of a triatomic species. The breaking of the bond results in significant rotational angular momentum, J, in the diatomic fragment. The velocity of the atomic fragment, $\boldsymbol{v}$, must therefore deviate from the direction of the initial bond orientation to ensure angular momentum conservation.

has to contain the totally symmetric species, A_1. Here the symbol Γ is taken to represent the symmetry of the species given in superscript, with $\Gamma^i = A_1$ and $\Gamma^f = B_2$. In the C_{2v} point group the vector B_2 lies in the molecular plane, perpendicular to the C_2 axis. For instantaneous dissociation from a bent molecular configuration the transition dipole moment will necessarily contain both parallel and perpendicular components with respect to the fragmenting bond, and reductions in β from the limiting cases outlined above therefore come as no surprise. As in the case of diatomics, rotation of the molecular framework prior to bond breaking can further complicate the relationship between $\boldsymbol{\epsilon_d}$ and $\boldsymbol{\mu}$.

A final point is that non-axial (or transverse) recoil effects may be important in polyatomics even in the absence of molecular rotation. Taking the above example of the dissociation of a bent triatomic molecule leads to an intuitive picture of the origin of such effects. Here, if the dissociation gives rise to a rotationally excited diatomic fragment then transverse components to the recoil direction, $\boldsymbol{v}$, must arise due to the conservation of the total angular momentum, as illustrated in Figure 2.4. Demanyenko *et al.* have provided a model for triatomic cases leading to large (classical) rotational angular momentum, with the transverse components to the recoil simply determined by angular momentum conservation arguments [91]. Non-axial effects were shown to be important for dissociation processes where the kinetic en-

ergy release is small and the rotational excitation of the diatomic is large. Note that in this case the torque and therefore the degree of rotational excitation of the co-fragment is determined by the angular anisotropy of the potential energy surface involved. As discussed by Schinke, simple impulsive models, in which this angular anisotropy of the potential is neglected, are unlikely in many cases to be able to determine the rotational excitation of the diatomic [5].

2.3.2 Atomic angular momentum polarisation

Similar to the distribution of velocities following a photodissociation process, the angular momenta of the fragments may have an anisotropic distribution in space. In other words, the fragments angular momenta may be polarised. Like the spatial anisotropy, measurements of electronic angular momentum polarisation provides information on the nature of the excitation process, symmetries of the excited state(s) and their lifetimes. However, unlike the β parameter, measurements of the electronic angular momentum polarisation of the fragments are also sensitive to features of the potential energy surface(s) *far* from the Franck-Condon window, in the long range asymptotic region, and can therefore lead to a much more complete description of the dissociation.

Laboratory frame polarisation

The fully quantum mechanical description of atomic angular momentum polarisation following the dissociation of diatomic molecules presented by Siebbeles *et al.* [92] and Vasyutinskii [93] forms the theoretical basis for interpretation of experimental work presented in this thesis. In this treatment the laboratory frame distribution, see also Section 3.5, of fragments with angular momentum J is described using the

state multipoles, $\rho^{\rm lab}_{KQ}(\theta,\phi)$, where

$$\rho^{\rm lab}_{KQ}(\theta,\phi) = \sum_{M',M} (-1)^{J-M'} \times \begin{pmatrix} J & J & K \\ M_J & -M'_J & -Q \end{pmatrix} \langle JM_J|\rho^{\rm lab}|JM'_J\rangle \,. \tag{2.10}$$

The elements of the photofragment density matrix, $\langle JM_J|\rho^{\rm lab}|JM'_J\rangle$, can be generated by taking a linear combination of the state multipoles, $\rho^{\rm lab}_{KQ}(\theta,\phi)$, giving rise to a complete description of the system [52, 94]. As can be seen from the $3J$ symbol, the rank K is restricted to taking values of between $K = 0$ and $K = 2J$. The elegance of the treatment by Siebbeles *et al.* is that the expansion can be separated into a geometrical part, depending on K, Q, and the experimental geometry and a dynamical part described by the functions $f_K(q,q')$ which provide a complete dynamical description of the photodissociation process [92]. The theoretical treatment by Siebbeles *et al.*, initially for atomic products accompanied by closed-shell fragments, was extended to the case of two open-shell fragments [62, 95], with angular momenta J_A and J_B[3]. Explicitly, it was found that the dynamical functions could be expressed by [95]

$$\begin{aligned} f_K(q,q') = \sum_{n,\Omega,\Omega_A,n',\Omega',\Omega'_A} & (-1)^{K+J_A+\Omega'_A} \begin{pmatrix} J_A & J_A & K \\ -\Omega_A & \Omega'_A & q-q' \end{pmatrix} \\ & \times \mathcal{T}^{n\Omega}_{J_A\Omega_A J_B\Omega_B} (\mathcal{T}^{n'\Omega'}_{J_A\Omega'_A J_B\Omega_B})^* \\ & \times \langle \Psi^-_{n,\Omega}|\hat{d}_q|\Psi_{\Omega_i}\rangle^* \langle \Psi^-_{n',\Omega'}|\hat{d}_q|\Psi_{\Omega_i}\rangle \,, \end{aligned} \tag{2.11}$$

[3]Current theory only treats the case in which one of the fragments is observed experimentally. By using coincidence techniques, it may be possible to simultaneously detect the polarisation of both photofragments.

where

$$\begin{aligned}
\Omega_i, \Omega &- \text{spin-orbit level of ground and excited state(s), with } \Omega = \Omega_A + \Omega_B \\
q, q' &- \text{cyclic component of electronic transition dipole moment} \\
\Psi^-_{n,\Omega} &- \text{scattering wavefunction} \\
\Psi^{J_i}_{v_i,\Omega_i} &- \text{ground state wavefunction} \\
\hat{d}_q &- \text{electronic transition dipole moment operator in the spherical basis} \\
\mathcal{T}^{n\Omega}_{j_A\Omega_A j_B\Omega_B} &- \text{expansion coefficients of the molecular states in the atomic basis} \\
\langle\Psi^-_{n,\Omega}|\hat{d}_q|\Psi_{\Omega_i}\rangle &- \text{photofragment } T \text{ matrix element} \\
n &- \text{describes the asymptotic product channel.}
\end{aligned} \tag{2.12}$$

The cyclic components, q, for each distinct product channel take values of 0 or ± 1 following parallel and perpendicular electronic transitions, respectively. The specific case in which $q \neq q'$ describes the coherent excitation of different transitions [92]. Balint-Kurti *et al.* have shown that the photofragment T matrix elements can be expressed in terms of the amplitude, $r_{n\Omega}$, and phase, $\varphi_{n,\Omega}$, for each dissociation channel [95],

$$\langle\Psi^-_{n,\Omega}|\hat{d}_q|\Psi^{J_i}_{v_i,\Omega_i}\rangle = r_{n,\Omega}\mathrm{e}^{\mathrm{i}\varphi_{\mathrm{n},\Omega}}\,. \tag{2.13}$$

The amplitudes, $r_{n,\Omega}$, can provide information, for example, on the probability for non-adiabatic transitions to take place during the dissociation [84]. Furthermore, in the case of coherent excitation, phase differences between dissociation channels, $\varphi_{n,\Omega} - \varphi_{n',\Omega'}$, may also appear in Equation (2.11) giving rise to experimentally measurable signals [84]. The photofragment T matrix elements can be computed using a time-dependent wavepacket formulism [95–100], as shown by Balint-Kurti and co-workers for theoretical treatments of the photodissociation of the hydrogen halides [95, 101, 102].

Picheyev *et al.* introduced a set of *polarisation parameters* composed of lin-

ear combinations of various normalised dynamical functions, $f_K(q, q')$, which have implicit physical meanings with regards to the dynamics of the dissociation of diatomic molecules [103]. These parameters also serve the purpose of providing a complete description of the angular momentum polarisation in the laboratory frame. This treatment was extended in several later publications for the parameters of up to photofragment rank $K = 4$ [65, 104]. Specifically, for even K, the alignment anisotropy parameters are defined as [103]

$$s_K = \frac{1}{V_K(J)} \frac{f_K(0,0) + 2f_K(1,1)}{f_0(0,0) + 2f_0(1,1)} \tag{2.14}$$

$$\alpha_K = \frac{1}{V_K(J)} \frac{f_K(1,1) - f_K(0,0)}{f_0(0,0) + 2f_0(1,1)} \tag{2.15}$$

$$\gamma_K = \frac{\sqrt{3}}{V_K(J)} \frac{2\mathrm{Re}[f_K(1,0)]}{f_0(0,0) + 2f_0(1,1)} \tag{2.16}$$

$$\eta_K = \frac{\sqrt{6}}{V_K(J)} \frac{f_K(1,-1)}{f_0(0,0) + 2f_0(1,1)} \,. \tag{2.17}$$

The parameters s_K and α_K describe the incoherent alignment that results following excitation *via* parallel ($\Delta\Omega = 0$, $q = q'$, $\Omega = \Omega'$) and/or perpendicular ($\Delta\Omega = \pm 1$, $q = q'$, $\Omega = \Omega'$) transitions. For the limiting case of a pure parallel transition, inspection of Equations (2.14) and (2.15) shows that the two parameters will have the relationship $s_K = -\alpha_K$. On the other hand, for a pure perpendicular transition the relation $s_K = 2\alpha_K$ holds. The parameter γ_K describes the coherent ($q \neq q'$) alignment that results following excitation of parallel and perpendicular transitions, whereas η_K describes the coherent alignment due the the excitation of perpendicular transitions.

For odd K the orientation anisotropy parameters are given by [65, 103, 104]

$$\alpha_K = \frac{1}{V_K(J)} \frac{f_K(1,1)}{f_0(0,0) + 2f_0(1,1)} \tag{2.18}$$

$$\gamma_K = \frac{1}{V_K(J)} \frac{2\mathrm{Re}[f_K(1,0)]}{f_0(0,0) + 2f_0(1,1)} \tag{2.19}$$

$$\gamma'_K = \frac{1}{V_K(J)} \frac{2\mathrm{Im}[f_K(1,0)]}{f_0(0,0) + 2f_0(1,1)} \,. \tag{2.20}$$

In this case the parameter α_K represents the incoherent orientation following excitation *via* a perpendicular transition. The parameters γ_K and γ'_K describe the photofragment orientation as a result of the coherent excitation of parallel and perpendicular transitions. γ_K is related to the helicity of the circularly polarised dissociation photon, whereas γ'_K can arise following photolysis using linearly polarised light and is related to the alignment of the dissociation photon [66, 84]. In the absence of the Coriolis interaction, no orientation arises through a pure parallel transition [105]. The $V_K(J)$ are normalisation factors, given by [65, 103, 104]

$$\begin{aligned} V_1(J) &= 1 \\ V_2(J) &= \frac{5J(J+1)^{1/2}}{[(2J+3)(2J-1)]^{1/2}} \\ V_3(J) &= \frac{J(J+1)}{[(J-1)(J+2)(2J-1)(2J+3)]^{1/2}} \\ V_4(J) &= \frac{9[J(J+1)]^{3/2}}{[(J-1)(J+2)(2J-3)(2J-1)(2J+3)(2J+5)]^{1/2}} \,. \end{aligned} \tag{2.21}$$

The higher order $K = 3-4$ parameters all vanish after averaging over recoil angles, however, the parameters α_1, γ_1, α_2, γ_2 and η_2 contribute to the total (average over recoil angles) orientation and alignment in the laboratory frame. The **Z** component of the total orientation and alignment in the laboratory frame may be expressed in terms of these parameters as [106]

$$\begin{aligned} \langle A^1 \rangle &= \sqrt{\frac{2}{5}} V_1(J)(\alpha_1 + \gamma_1) \\ \langle A^2 \rangle &= \sqrt{\frac{2}{5}} V_2(J)(\alpha_2 + \gamma_2 + \eta_2) \,. \end{aligned} \tag{2.22}$$

Finally, the spatial anisotropy parameter, β, expressed in terms of the zeroth order dynamical functions, $f_0(q, q')$, is given by [92]

$$\beta = \frac{2[f_0(0,0) - f_0(1,1)]}{f_0(0,0) + 2f_0(1,1)} \,. \tag{2.23}$$

The molecular frame polarisation

The polarisation parameters defined in the previous section describe the *laboratory* frame polarisation following the photodissociation of diatomic molecules. In some cases, including the dissociation of triatomic molecules where the physical meaning of the polarisation parameters is lost, it is more useful to examine the polarisation in the *molecular* frame, where the **z** axis is taken as the recoil direction, $\boldsymbol{v}$. As described in Section 2.1 the two reference frames can be related by a set of simple rotations [52], allowing the photofragment state multipoles in the molecular frame to be written as [106, 107]

$$\rho_{KQ}^{\mathrm{mol}}(\theta,\phi) = \frac{3}{4\pi}\left(\frac{2K+1}{2J+1}\right)^{1/2}\frac{1}{\rho_{00}^{\mathrm{mol}}(\theta,\phi)}\sum_{k_d}\sum_{q,q'}(-1)^{K+q+s}(2k_d+1) \times f'_K(q,q')\begin{pmatrix} 1 & 1 & k_d \\ s & -s & 0 \end{pmatrix}\begin{pmatrix} 1 & 1 & k_d \\ q' & -q & Q \end{pmatrix} C_{k_dQ}(\theta,0)\,, \quad (2.24)$$

where $C_{k_dQ}(\theta,0)$ is a modified spherical harmonic [52], and s takes values of 0 for linearly and ± 1 for circularly polarised photolysis light, with

$$\rho_{00}^{\mathrm{mol}}(\theta,\phi) = \frac{[1+\beta P_2(\cos\theta)]}{4\pi(2j+1)^{1/2}}\,, \quad (2.25)$$

and

$$f'_K(q,q') = \frac{f_K(q,q')}{f_0(0,0)+2f_0(1,1)}\,. \quad (2.26)$$

In addition to the laboratory frame polarisation parameters described above, a set of *molecular* frame polarisation parameters, $a_Q^{(K)}(p)$, has been introduced by Rakitzis and Zare [108, 109]. Here the symbol (p) is used to define the symmetry of the transition process and can be defined as $(\parallel)$ or $(\perp)$ as well as $(\parallel,\perp)$ and $(\perp,\perp)$ for coherent processes. These parameters, which are defined in terms of the dynamical functions $f_K(q,q')$, contain equivalent information regarding the internal dynamics as the parameters of Picheyev *et al.* [103], with the relationship between the two

formulations, for the low rank $K = 1 - 2$ cases, summarised in Table 2.1.

Molecular Frame	Dynamical Function	Laboratory Frame
$a_0^{(1)}(\perp)$	$\frac{f_1(1,1)}{f_0(1,1)}$	$\frac{6}{2-\beta}\alpha_1$
$\mathrm{Re}[a_1^{(1)}(\parallel,\perp)]$	$\frac{\mathrm{Re}[f_1(1,0)]}{[2f_0(1,1)f_0(0,0)]^{1/2}}$	$\frac{3}{2[(2-\beta)(1+\beta)]^{1/2}}\gamma_1$
$\mathrm{Im}[a_1^{(1)}(\parallel,\perp)]$	$\frac{\mathrm{Im}[f_1(1,0)]}{[2f_0(1,1)f_0(0,0)]^{1/2}}$	$\frac{-3}{2[(2-\beta)(1+\beta)]^{1/2}}\gamma_1'$
$a_0^{(2)}(\perp)$	$\frac{5}{V_2}\frac{f_2(1,1)}{f_0(1,1)}$	$\frac{10}{2-\beta}(\alpha_2 + s_2)$
$a_0^{(2)}(\parallel)$	$\frac{5}{V_2}\frac{f_2(0,0)}{f_0(0,0)}$	$\frac{5}{1+\beta}(s_2 - 2\alpha_2)$
$\mathrm{Re}[a_1^{(2)}(\parallel,\perp)]$	$\frac{-5}{V_2}\frac{\mathrm{Re}[f_2(1,0)]}{[2f_0(1,1)f_0(0,0)]^{1/2}}$	$\frac{-5\sqrt{3}}{2[(2-\beta)(1+\beta)]^{1/2}}\gamma_2$
$\mathrm{Im}[a_1^{(2)}(\parallel,\perp)]$	$\frac{-5}{V_2}\frac{\mathrm{Im}[f_2(1,0)]}{[2f_0(1,1)f_0(0,0)]^{1/2}}$	$\frac{-5\sqrt{3}}{2[(2-\beta)(1+\beta)]^{1/2}}\gamma_2'$
$a_2^{(2)}(\perp)$	$\frac{-5}{2V_2}\frac{f_2(1,-1)}{f_0(1,1)}$	$\frac{-5}{\sqrt{6}}\frac{3}{2-\beta}\eta_2$

Table 2.1: Definitions of the molecular frame polarisation parameters [108, 109] in terms of expressions for the dynamical functions, $f_K(q, q')$ [92], and expressions for the laboratory frame polarisation parameters of Picheyev *et al.* [103]. Adapted from Ref [84].

Adiabatic Dissociation Example

For the specific case of dissociation from a single adiabatic state, the atomic polarisation can be calculated in a simple manner without the need to determine the photofragment T matix. The coefficients $\mathcal{T}^{n\Omega}_{J_A\Omega_A J_B\Omega_B}$ in Equation (2.11) are expansion coefficients of the molecular *adiabatic* states in the atomic $|JM_J\rangle$ basis at large values of internuclear separation, $\mathbf{R}$ [93, 105, 110]

$$\Psi^{el}_{n,\Omega}(\mathbf{r},\mathbf{R}) \xrightarrow{R\to\infty} \sum_{M_{J_A},M_{J_B}} \mathcal{T}^{n,\Omega}_{J_A,M_{J_A},J_B,M_{J_B}} |J_A, M_{J_A}\rangle |J_B, M_{J_B}\rangle \,. \tag{2.27}$$

The square moduli of the expansion coefficients, $|\mathcal{T}^{n,\Omega}_{J_A,M_{J_A},J_B,M_{J_B}}|^2$, can be used to determine the $|JM_J\rangle$ populations in the molecular frame. These coefficients can be calculated by diagonalization of the Hamiltonian matrix at large values of internuclear separation, $\mathbf{R}$. Specific cases have been calculated by Vasyutinskii and co-workers [110–112] and a comprehensive set encompassing many atomic levels for the case of the quadrupole-quadrupole interaction has also been provided by Alexander [113].

As an example take the *adiabatic* dissociation of a molecule in a $\Omega = 1_u$ state correlating with two $J = 1$ atoms. Based on the quadrupole-quadrupole interaction only one such state exists, and it can be written as [113]

$$\begin{aligned} |1_u\rangle &\xrightarrow{R\to\infty} \frac{1}{\sqrt{2}}\{|J_AM_{J_A}, J_BM_{J_B}\rangle - |J_BM_{J_B}, J_AM_{J_B}\rangle\} \\ |1_u\rangle &\xrightarrow{R\to\infty} \frac{1}{\sqrt{2}}\{|10, 11\rangle - |11, 10\rangle\}\,. \end{aligned} \tag{2.28}$$

The long range coefficients are given by $\mathcal{T}^{1_u}_{10,11} = \frac{1}{\sqrt{2}}$ and $\mathcal{T}^{1_u}_{11,10} = -\frac{1}{\sqrt{2}}$. The quadrupole alignment tensor, $A^{(2)}_0$, for a specific $|JM_J\rangle$ state is given by [52]

$$A^{(2)}_0 = \frac{\sqrt{6}}{J(J+1)} Re\langle(J|J^{(2)}_0|J)\rangle\,, \tag{2.29}$$

where $\langle(J|J^{(2)}_0|J)\rangle$, or equivalently $\langle J^{(2)}_0\rangle$, is the matrix element of the spherical tensor operator $J^{(2)}_0$ [52]. This matrix element may be written as

$$\langle J^{(2)}_0\rangle = \sum_M \rho_{MM}(-1)^{J-M} \begin{pmatrix} J & 2 & J \\ -M & 0 & M \end{pmatrix} \langle J\|J^{(2)}\|J\rangle\,, \tag{2.30}$$

where the reduced matrix element $\langle j\|J^{(2)}\|j\rangle = \left[\frac{j(j+1)(2j-1)(2j+1)(2j+3)}{6}\right]^{1/2}$ [52]. The square moduli of the expansion coefficients give the population of the $|JM_J\rangle$ state, and so yield the diagonal elements of the density matrix, ρ_{MM}, in Equation (2.30). In this case ρ_{00} and $\rho_{11} = 1/2$, which results in a molecular frame alignment, Equation (2.29), of $-1/4$ under the axial recoil approximation.

2.4 Theoretical calculations

Where high level *ab initio* potential energy curves are available, sophisticated quantum mechanical calculations can be performed allowing detailed theoretical information to be gained on the photodissociation of diatomic molecules. Time-dependent treatments, of particular relevance here, can often be advantageous in that they allow the simultaneous determination of observables over a wide range of energies. In Chapter 4 the results of time dependent wavepacket calculations performed on a set of *ab initio* potentials relevant to the photodissociation of Cl_2 ($v = 1$) are presented. Section 2.4.1 sets out the principles behind these calculations.

For the photodissociation of polyatomic molecules more approximate methods are commonly used to rationalise experimental measurements. In particular, for the interpretation of electronic polarisation effects in such systems several approximate models have been developed. One of these models, termed the long range model, has been used in Chapter 5 in relation to the photodissociation of CS_2, and is described in Section 2.4.2.

2.4.1 Time-dependent wavepacket treatment

The theoretical procedure used here to investigate the photodissociation of vibrationally excited Cl_2 is identical to the method set out by Balint-Kurti and co-workers for the photodissociation of the hydrogen halides [95, 101, 102, 114, 115] and Johnsen *et al.* for the photodissociation of Cl_2 ($v = 0$) [50], and only the principles and key equations are described here. The fully quantum mechanical method seeks to solve the time-dependent Schrödinger equation,

$$i\hbar\frac{\partial}{\partial t}\Theta(R,t) = \hat{H}(R)\Theta(R,t)\,, \tag{2.31}$$

where the Hamiltonian $\hat{H}(R)$ is time independent and includes the radial nuclear kinetic energy operator, the electrostatic potential, $V(R)$, and the spin-orbit oper-

ator [114, 115]

$$\hat{H} = -\frac{\hbar^2}{2\mu}\frac{d^2}{dR^2} + \frac{\hbar^2}{2\mu R^2}\hat{l}^2 + V(R) + \hat{H}_{\mathrm{SO}}(R)\,. \tag{2.32}$$

Nuclear rotational motion is neglected in the current treatment, with the term $\frac{\hbar^2}{2\mu R^2}\hat{l}^2$ set to zero. Note that this is equivalent to neglecting the effect of Coriolis coupling, which couples states that differ in Ω by ± 1. The total Hamiltonian can therefore be represented by the total potential, $V^{\mathrm{tot}} = V(R) + \hat{H}_{\mathrm{SO}}(R)$, and nuclear kinetic energy terms, $-\frac{\hbar^2}{2\mu}\frac{d^2}{dR^2}$ [114, 115].

An initial wavepacket at time zero, $\Theta(R, t = 0)$, is generated on the excited state potential *via* the product of the ground electronic state nuclear wavefunction, $\Psi_{\Omega_i}(R)$, with the electronic transition dipole moment function, $d_{q'}(R)$ [114, 115]

$$\Theta(R, t = 0) = d_{q'}(R)\Psi_{\Omega_i}(R)\,. \tag{2.33}$$

When more than one state is involved, $\Theta(R, t)$ can be written as [114, 115]

$$\begin{pmatrix} \chi_1(R, t = 0) \\ \chi_2(R, t = 0) \\ \vdots \\ \chi_n(R, t = 0) \end{pmatrix} = \begin{pmatrix} d_q^1(R)\Psi_{\Omega_i}(R) \\ d_q^2(R)\Psi_{\Omega_i}(R) \\ \vdots \\ d_q^n(R)\Psi_{\Omega_i}(R) \end{pmatrix}, \tag{2.34}$$

where $\chi_n(R, t)$ and $d_q^n(R)$ represent the wavepacket and transition dipole moment associated with the excited state n. The resulting wavepacket(s) are then propagated according to the formal solution of the time-dependent Schrödinger equation

$$\Theta(R, t) = \exp^{-i\hat{H}t/\hbar}\Theta(R, t = 0)\,. \tag{2.35}$$

The ground electronic state nuclear wavefunction is calculated using the Fourier grid Hamiltonian technique [116]. In this method numerical calculation of bound state eigenvalues and eigenfunctions can be made at a series of discrete grid

points [116]. Following their creation, the wavepackets are propagated using the Chebychev method for the time evolution operator $\exp^{-i\hat{H}t/\hbar}$ [117]. The wavepackets see the edge of the grid as an infinite potential wall and must therefore be damped to avoid reflection back to lower values of R, with the damping provided by a complex cubic absorbing potential [118].

Incorporation of non-adiabatic effects

In order to take into account non-adiabatic effects the calculation is performed using two different electronic bases. In the first electronic basis, which is referred to as the fully adiabatic basis, the spin orbit operator, $\hat{H}_{\mathrm{SO}}$, is diagonal and off diagonal matrix elements arise due to the nuclear kinetic energy term, $-\frac{\hbar^2}{2\mu}\frac{d^2}{dR^2}$, which couples different electronic states of the same Ω. On the other hand, in the diabatic basis the good quantum numbers are Λ and Σ, $-\frac{\hbar^2}{2\mu}\frac{d^2}{dR^2}$ and $V(R)$ are diagonal, with off diagonal terms in the spin-orbit operator, $\hat{H}_{\mathrm{SO}}$. The two bases are related by a unitary transformation [114, 115].

Propagation of the excited wavepackets, using the Chebychev method [117], is performed in a series of short time steps. As discussed by Balint-Kurti and coworkers [114, 115], initially a fast Fourier transform is used to convert the diabatic wavepackets from the position to momentum representation. The reason for performing a transformation to the momentum representation is to simplify the computation of the effect of the nuclear kinetic energy operator, which becomes a multiplication as opposed to a derivative [114, 115, 119, 120]. The wavepackets are then transformed back to the position representation using an inverse fast Fourier transform and converted to the adiabatic representation. The effect of the total potential energy term, V^{tot}, is then calculated. Finally, a new set of diabatic wavepackets is generated in the position representation, completing the calculation for the time step [114, 115].

Absorption cross section and photofragment T matrix elements

Analysis of the wavepackets can yield the absorption cross section and photofragment T matrix elements, as defined in Equation (2.13), over a wide range of excitation energies.

The autocorrelation function, $A(t)$, gives the overlap of the initial wavepacket with that observed at time t, and can be calculated after each time step [114, 115]

$$A(t) = \sum_n \int_0^\infty \chi_n^*(R, t=0)\chi_n(R,t)\mathrm{d}R\,, \tag{2.36}$$

where the summation is over all states n. Taking the Fourier transform of the autocorrelation function, $A(t)$, over time yields the absorption cross-section, $\sigma^{\mathrm{abs}}(\nu)$ [114, 115, 121–123],

$$\sigma^{\mathrm{abs}}(\nu) = \frac{\pi\nu}{3c\epsilon_0\hbar}\int_{-\infty}^{+\infty} \exp[i(E_{\mathrm{int}} + h\nu)t/\hbar]A(t)\mathrm{d}t\,, \tag{2.37}$$

where E_{int} is the energy of the initial state.

The partial cross sections and photofragment T matrix elements are computed by inspection of the wavepackets at large values of internuclear distance, $R = R_\infty$. As shown by Balint-Kurti and co-workers, for dissociation into a particular channel, n, the photofragment T matrix element may be expressed as [95, 101]

$$\langle \Psi^-_{n,\Omega}(R,E)|\hat{d}_q|\Psi_{\Omega_i}\rangle = i\left(\frac{h^2k}{2\pi\mu}\right)^{1/2}\exp(-ikR_\infty)A_n(R_\infty,E)\,, \tag{2.38}$$

where $A_n(R_\infty, E)$ is given by [95, 101]

$$A_n(R_\infty,E) = \frac{1}{2\pi}\int_0^\infty \chi_n(R_\infty,t)\exp[i(E_{\mathrm{int}}+h\nu)t/\hbar]\mathrm{d}t\,, \tag{2.39}$$

where k represents the asymptotic wavevector and μ the reduced mass of the photofragments [95, 101]. The value of R_∞ is chosen to be sufficiently large such that the potentials have, within some small error margin, reached their asymptotic

values. The analysis, performed by taking cuts through the wavepackets at R_∞, takes place in the adiabatic representation.

2.4.2 Approximate theoretical treatments

For dissociation of non-linear polyatomic species the physical meaning of the polarisation parameters described in Section 2.3.2 is lost. Although the parameters can no longer be used to unravel the mechanism of the dissociation directly, they can still be used to completely characterise the angular momentum distribution in the laboratory and molecular frames. In order to further understand the origins of polarisation effects following the photodissociation of polyatomic species a series of approximate models have been developed. A detailed description of these models can be found in the recent review article by Brouard and co-workers [86]. For the present work only the long-range interaction model has been used, in Chapter 5, the underlying principles of which are set out below.

The long-range model

The long-range interaction model is an approximate theoretical treatment used to rationalise the electronic polarisation of atomic fragments following the photodissociation of triatomic molecules. The principle of this approximate treatment is that the atomic polarisation is solely determined in the long range, asymptotic, region of the dissociation co-ordinate where the potentials involved are close in energy. This model was first introduced by Teule *et al.* [124] to rationalise experimental measurements of $O(^1D_2)$ polarisation resulting from the the photodissociation of N_2O. It has since been applied to the $O(^3P_J)$ fragments from N_2O [125] and SO_2 [59] dissociations, and to the $O(^1D_2)$ fragments from the photodissociation of O_3 [126] and NO_2 [127]. A thorough description of this model and its application to the systems mentioned above can be found in the recent review article by Brouard and co-workers [86], with only a brief description of the approximations and important equations contained here.

The long-range interaction model assumes that the triatomic molecular system evolves to the asymptotic region on a *single* adiabatic potential. The Jacobi coordinate system, as defined in Section 2.1, is used to describe the molecular geometry. At some critical distance, R_c, the model assumes that the dominant interaction between the diatomic and atomic species is electrostatic in origin. At R_c, the character of the dissociation wavefunction, which determines the electronic polarisation, is given solely by consideration of this electrostatic interaction. For $R > R_c$ the diatomic and atomic species are assumed to lose all contact, with the result that the interactions at R_c determine the electronic polarisation of the atomic photofragment. The starting point is therefore the determination of the electrostatic interaction between the atomic, C, and diatomic, AB, fragments at the critical distance, R_c. In the Jacobi frame this interaction can be expressed by the matrix [59, 128]

$$\begin{aligned} V_{M_L M_L'}(R_c,\gamma) &= \langle \chi L M_L | \widehat{V}(R_c,\gamma) | \chi L M_L' \rangle \\ &= \sum_{l_{\rm AB}} \sum_{l_{\rm C}} \frac{\langle \chi | \widehat{Q}_{l_{\rm AB},0} | \chi \rangle \langle L \| \widehat{Q}^{(l_{\rm C})} \| L \rangle}{R_c^{l_{\rm AB}+l_{\rm C}+1}} (-1)^{l_{\rm AB}+L-M_L} \\ &\times \left[\frac{(2l_{\rm AB}+2l_{\rm C}+1)!}{(2l_{\rm AB})!(2l_{\rm C})!} \right]^{1/2} \sum_{m_{\rm AB},m_{\rm C}} \begin{pmatrix} l_{\rm AB} & l_{\rm C} & l_{\rm AB}+l_{\rm C} \\ m_{\rm AB} & m_{\rm C} & 0 \end{pmatrix} \\ &\times \begin{pmatrix} L & l_{\rm C} & L \\ -M_L & m_{\rm C} & M_L' \end{pmatrix} C_{l_{\rm AB},m_{\rm AB}}(\gamma,0)\,, \end{aligned} \tag{2.40}$$

where $\widehat{Q}_{l_{\rm Z},m_Z}$ are the multipole operators. The arguments $l_{\rm Z}$ define the order of the multipole with $l_{\rm Z} = 1$ for dipole and $l_{\rm Z} = 2$ for quadrupole, and $-l_{\rm Z} \leq m_Z \leq +l_{\rm Z}$. $|\chi\rangle$ and $|LM_L\rangle$ represent the wavefunctions of the diatomic and atomic species, respectively, and $\langle L \| \widehat{Q}^{(l_{\rm C})} \| L \rangle$ denotes a reduced matrix element [52]. For the case in which the diatomic fragment is born in a Σ electronic state, diagonalization of Equation (2.40) gives a set of three potential energy surfaces if $L = 1$, where L refers to the orbital angular momentum of the atomic state, and five when $L = 2$ for both the quadrupole-quadrupole and dipole-quadrupole interactions between the diatomic and atomic fragments.

The potentials, as a function of Jacobi angle γ, are given by the eigenvalues returned from the diagonalization procedure with the eigenfunctions simply linear combinations of $|\chi\rangle|LM_L\rangle$ states. The expansion coefficients of these linear combinations of $|\chi\rangle|LM_L\rangle$ states, $c_{M'_L}c_{M_L}$, determine the diagonal elements of the density matrix, $\rho_{M_L,M_L}(L)$, giving the photofragment M_L populations. The polarisation predicted from this model may also be expressed in terms of the state multipole moments in the Jacobi frame, since [59]

$$\rho_{KQ}(L) = \sum_{M_L,M'_L} (-1)^{L-M_L}(2K+1)^{1/2} \begin{pmatrix} L & L & K \\ M_L & -M'_L & -Q \end{pmatrix} \rho_{M_L M'_L}(L) \,. \quad (2.41)$$

The long range interaction model itself does not determine the critical distance, R_c, and in the case of a heteronuclear diatomic fragment with a dipole moment knowledge of this distance is required to predict which of the electrostatic interactions, for example quadrupole-quadrupole or quadrupole-dipole, determines the character of the dissociation wavefunction and therefore atomic polarisation. Furthermore, the sign of the electrostatic interaction is also required in order to determine the energy ordering of the potentials calculated in the model. When the photofragment is formed in a state with non-unity spin multiplicity, further assumptions are required regarding the role of electron spin with respect to the asymptotic polarisation of the total angular momentum, J, see, for example, Ref [86]. In order to compare the predicted polarisation moments, Equation (2.41), with experimental measurements it is assumed that the Jacobi distance R is sufficiently large such that the **z** axis in both the Jacobi and molecular frames are coincident. In this case a frame transformation between the two reference frames is not necessary.

2.5 Summary

In this Chapter a summary of the dynamical information that can be inferred from experimental measurements of different properties, both scalar and vector, of gen-

eral photodissociation processes has been given. In addition, the fully quantum mechanical treatment of electronic polarisation in photodissociation was described, with this parameterisation used extensively in Chapter 4 to interpret experimental results on the photodissociation of the diatomic molecule Cl_2. Furthermore, the principles behind the quantum mechanical time-dependent wavepacket method, used to theoretically treat the dissociation of Cl_2 ($v = 1$) in Chapter 4, have been set out. For more complicated polyatomic species approximate models must be used to rationalise electronic polarisation effects, and an account of one such model, termed the long range interaction model, has been given. This treatment is used in Chapter 5 to discuss the $S(^1D_2)$ electronic polarisation effects from the photodissociation CS_2.

Chapter 3

Experimental technique and data analysis

Experimental results presented in this thesis were obtained using a standard velocity map [45] ion imaging [41] apparatus. This chapter contains a description of the experimental technique employed in addition to the procedure used for analysing and extracting valuable information from the experimentally acquired data. The chapter will begin by briefly describing the underlying principles of the ion imaging experiment.

3.1 Experimental principles

A cartoon of the experimental apparatus is shown in Figure 3.1 to illustrate the principles behind the experiment. A pulsed molecular beam containing the sample of interest is expanded (supersonically) into high vacuum apparatus and is collimated $\sim 4\,\text{cm}$ downstream by a skimmer. The skimmed molecular beam enters the ion optic assembly and is intersected at 90° by counter propagating pump and probe lasers in the region between the repeller and extractor plates. A pulse of pump laser radiation excites the molecules in the beam, allowing photodissociation to take place, and after a short delay of $\leq 25\,\text{ns}$ the probe laser pulse ionises the atomic fragments formed in the photolysis step in a $(2+1)$ resonance enhanced multiphoton ionisation (REMPI) process. The resulting ions are then repelled and extracted along the time of flight tube eventually reaching a two-dimensional detector. The voltages supplied

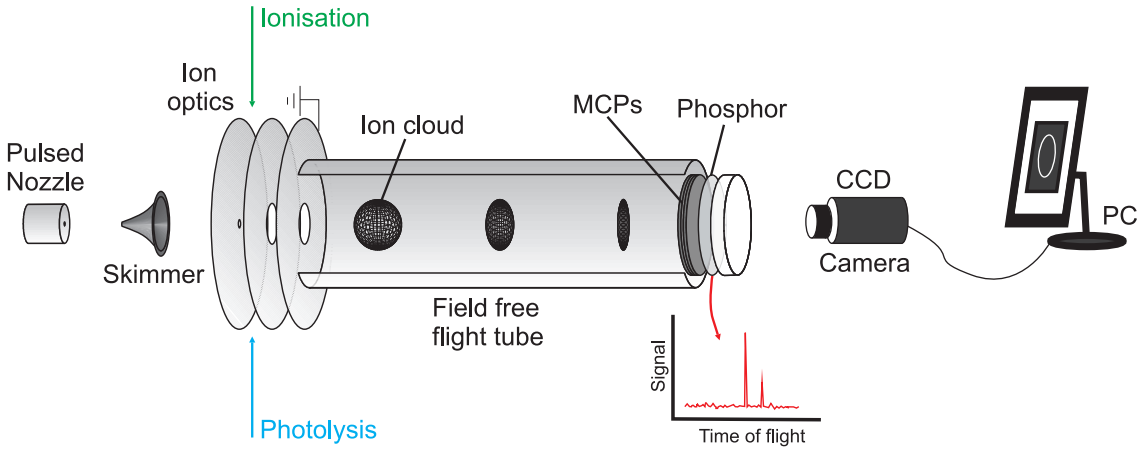

Figure 3.1: Illustration of the velocity map ion imaging experiment. The molecular beam is introduced to the experiment using a pulsed nozzle and collimated by a skimmer. Between the repeller and extractor plates counterpropagating lasers dissociate the molecules and ionise the resulting photofragments. The ions are accelerated and crushed onto a 2D detector under velocity mapping [45] conditions. The ions striking the detector cause flashes of light which are captured with a CCD camera.

to the ion optic assembly are such that velocity mapping [45] of the ions takes place. As discussed in Section 1.3, this means that every ion possessing the same mass and velocity will impact upon the detector at the same position, irrespective of its point of formation within the laser interaction region. The distance from the centre of the detector, *i.e.* the radial position of the ion, is proportional to its velocity component in the plane of the detector at the point of formation. The two dimensional detector consists of a pair of micro-channel plates (MCPs) which are coupled with a phosphor screen. The ions arrive at the MCPs causing them to produce bundles of electrons which are accelerated across the the plates towards the phosphor screen. The high kinetic energy electrons then excite the phosphor in the screen, which decays by fluorescence. The flashes of light produced by the screen are captured by an intensified charge coupled device (CCD) camera. The camera is electronically gated and only accumulates data over the peak in the time of flight spectrum of interest.

3.2 The imaging apparatus

3.2.1 Vacuum systems

Experiments were performed on a typical ion imaging rig shown schematically in Figure 3.2. The rig consists of three components, the source chamber where the molecular beam is introduced, the reaction chamber containing the ion optic assembly, and the time of flight detector. The source and reaction chambers are separated by a skimmer (Beamdynamics Inc.) which has a 0.98 mm orifice. The source chamber is differentially pumped using a $3700\,\mathrm{l\,s^{-1}}$ water cooled diffusion pump (Varian VHS-250). A water cooled baffle is inserted between the pump and the chamber in order to minimise the effect of oil backstreaming and contaminating surfaces in the chamber. Backing pumping is provided by a Leybold Trivac type D40V rotary pump. The diffusion pump allows base pressures in the source chamber of $\sim 9 \times 10^{-8}$ Torr to be reached.

The reaction chamber contains the ion-optic assembly and is pumped using a turbomolecular pump (Pfeiffer Vacuum TMH-521P ($510\,\mathrm{l\,s^{-1}}$)) backed by a rotary pump (Leybold Trivac D40V). Background pressures in the reaction chamber were around 3×10^{-8} Torr. The time of flight detector is pumped by a smaller turbomolecular pump (Pfeiffer Vacuum TMU 071P ($60\,\mathrm{l\,s^{-1}}$)), also backed by a rotary pump (Leybold Trivac D40V). The TOF detector is separated from the reaction chamber by a gate valve allowing the reaction/source chambers to be brought up to atmospheric pressure while isolating the vacuum at the detector.

3.2.2 Molecular beam source

Two pulsed nozzles have been used for experiments described herein, General valve (Series 9) for the 193.3 nm experiments on CS_2, and Jordan valve (Jordan TOF) for all other measurements. The samples were introduced into the apparatus using these valves at backing pressures of $1 - 2$ bar. The valves were mounted in such a way to allow complete **XYZ** translation of the valve orifice relative to the (fixed)

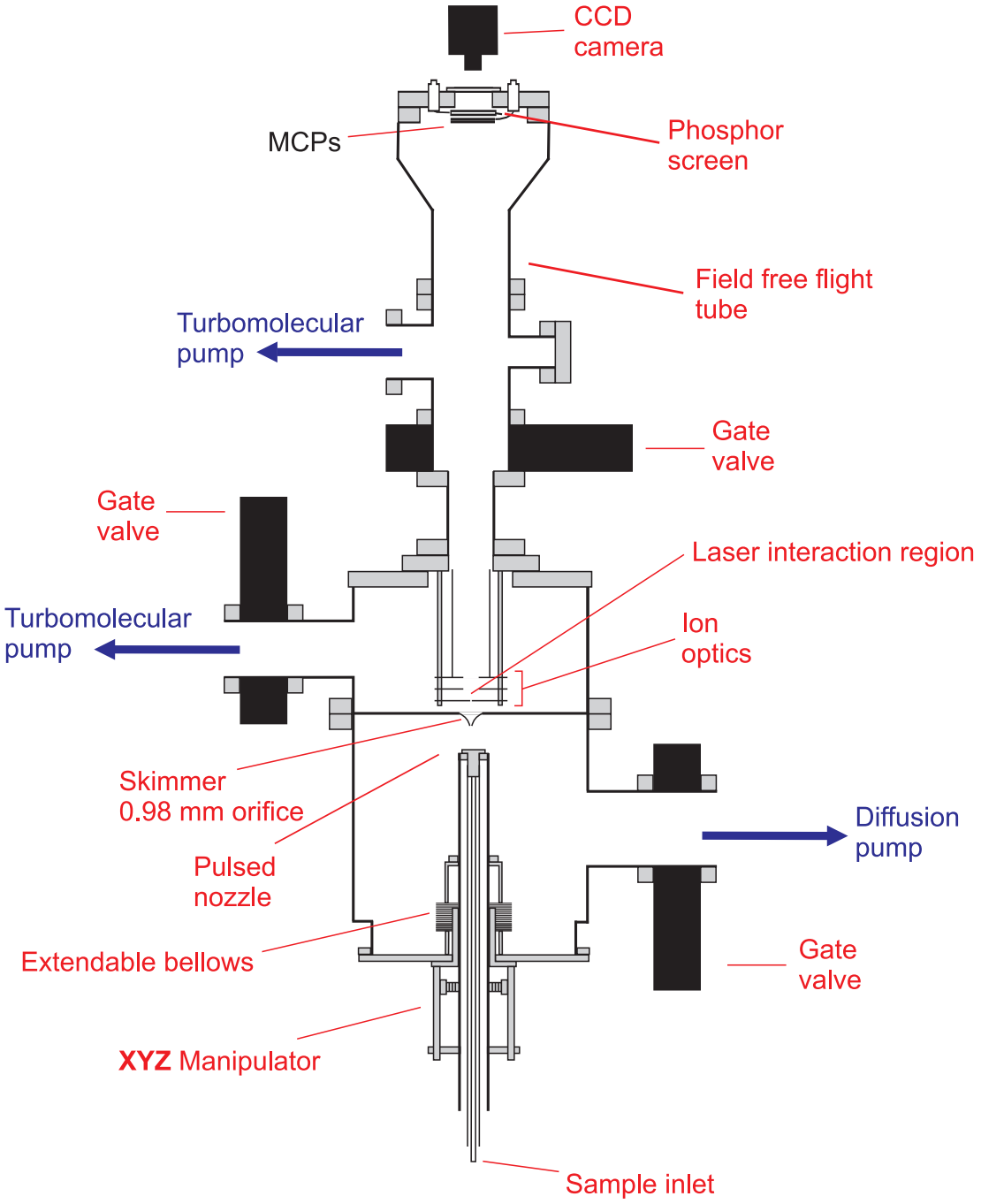

Figure 3.2: Schematic representation of the experimental apparatus. Adapted from Ref [47].

skimmer position, in order to optimise experimental signals. While the molecular beam was operational the pressures in the source and reaction chambers rose to $\sim 1 \times 10^{-6}$ Torr and $\sim 1 \times 10^{-7}$ Torr, respectively.

3.2.3 Ion optics

The ion optics, shown in Figure 3.2, are mounted on four rods with the total assembly consisting of three stainless steel discs of 1 mm thickness and 93 mm diameter. The plates are separated from those adjacent by 15 mm MACOR ceramic spacers. The repeller plate is closest to the skimmer, followed by the extractor plate. The third plate was not used in the present work, and grounded during experimental measurements. To allow the skimmed molecular beam to enter the laser interaction region, which is located between the repeller and extractor plates, the repeller plate has a central hole of 2 mm diameter. The extractor and third plates have larger, 20 mm central apertures. During experimental measurements the repeller and extractor plates are held at constant voltages in order to achieve velocity mapping conditions [45]. Part of the field free time of flight tube is mounted on the third plate. The laser beams enter the reaction chamber through fused silica windows adjacent to the interaction region.

3.2.4 Detector

The detector used for experiments described in this thesis consisted of a pair of 78 mm diameter microchannel plates (MCPs, Burle Technologies Inc.) mounted in a Chevron configuration, and coupled to a P47 phosphor screen. The light from the P47 phosphor was recorded using an electronically gated intensified charge-coupled device (CCD) camera (576×768 pixels, Photonic Science). Prior to any experimental run the focussing of the CCD camera onto the back of the phosphor was checked by the imaging of a card depicting a fine grid. The recorded frames were transferred to a PC using a frame grabber card (Euresys Picolo Pro 2), allowing summation, thresholding and ion-counting [129] to be performed.

3.2.5 Laser systems

Pump lasers

Two different pump lasers have been employed for the experiments described in this thesis. The 193.3 nm pump laser radiation was provided by a Lambda Physik EMG 103 MSC laser operating with an Argon Fluoride gas mixture. Operated at 10 Hz, this excimer laser gives a pulse duration of 25 ns. Maximum energies obtained using this laser were around 200 mJ/pulse, however, for measurements performed here this energy was attenuated significantly.

The pump laser radiation for all other wavelengths was given by a Lambda Physik LPD 3000 dye laser system pumped using the third harmonic of a Continumm Powerlite Precision II Scientific Nd:YAG laser. The energy output of the Nd:YAG at 355 nm was 420 mJ, although for experiments this was attenuated to between 80 mJ and 150 mJ by increasing the time delay between the flashlamps and Q-switch. Dye solutions were prepared for the appropriate wavelengths required in the experiments. When frequency doubling of the dye fundamental was required this was performed with a BBO type I or BBO type II Lambda Physik crystal, and separated from the fundamental using an array of four Pelin-Broca prisms. Details of the dye solutions used in this thesis are given in Table 3.1.

For both types of pump laser, the beam was linearly polarised using a quartz Rochon polariser and focussed using a 30 cm lens before entering the reaction chamber. Where circular polarisation of the pump beam was necessary the beam was passed through a Frensel rhomb with the linear polarisation axis at 45° to the principle axis of the rhomb.

Probe laser

The probe laser radiation was provided by a Sirah Cobra Stretch dye laser pumped using the second or third harmonic of a Continumm Powerlite Precision II Scientific Nd:YAG laser. Maximum energy output of the second and third harmonics of the Nd:YAG laser are $\sim$ 600 mJ and $\sim$ 380 mJ, respectively. Dye solutions and

Parent Molecule	Wavelength	Dye	Solvent
CS_2	207-215nm	Stilbene 420	MeOH
Cl_2	470 nm	Coumarin 480	MeOH
Cl_2	450 nm	Coumarin 450	MeOH
Cl_2	420 nm	Stilbene 420	MeOH
Cl_2	398 nm	Exalite 398	Dioxane
Cl_2	389 nm	Exalite 389	Dioxane
Cl_2	384 nm	Exalite 384	Dioxane
Cl_2	376 nm	Exalite 376	Dioxane

Table 3.1: Details of the dye solutions used to create the pump laser radiation.

frequency conversion crystals were chosen to produce the required (2+1) REMPI wavelengths for the S and Cl photofragments investigated in this thesis. All REMPI wavelengths required frequency doubling of the dye fundamental with details of the wavelengths, (2+1) REMPI assignments, and non-linear crystals used provided in Table 3.2. As with the pump dye laser, the frequency doubled radiation was isolated from the fundamental using an array of four Pelin-Broca prisms. The linearly polarised probe radiation was passed through a photoelastic modulator (Hinds Instruments PEM-90). This allowed the laser polarisation to switch between parallel and perpendicular linear polarisations with respect to the TOF **Z** axis on alternate laser shots. Furthermore, the PEM was also used to generate circularly polarised probe radiation and was used to switch between two circular polarisations (L or R) on alternate laser shots. Use of the PEM allowed the collection of two experimental geometries on a single image aquisition.

Prior to entering the reaction chamber the probe laser radiation was focussed using a 30 cm focal length lens. The power was attenuated so as to avoid saturation of

Fragment	Transition[67]	Wavelength	Pumping	Dye	Solvent	Crystal
$S(^1D_2)$	$^3P_1 \leftarrow ^1D_2$	291.4 nm	532 nm	Pym 597	MeOH	KDP
$S(^1D_2)$	$^1F_3 \leftarrow ^1D_2$	288.1 nm	532 nm	Pym 597	MeOH	KDP
$S(^3P_0)$	$^3P_2 \leftarrow ^3P_0$	310.8 nm	532 nm	Rhm 101	MeOH	KDP
$S(^3P_1)$	$^3P_2 \leftarrow ^3P_1$	310.0 nm	532 nm	Rhm 101	MeOH	KDP
$S(^3P_2)$	$^3P_1 \leftarrow ^3P_2$	308.1 nm	532 nm	Rhm 101	MeOH	KDP
$Cl^*(^2P_{1/2})$	$^2P_{3/2} \leftarrow ^2P_{1/2}$	236.4 nm	355 nm	C 480	MeOH	BBOI
$Cl(^2P_{3/2})$	$^2P_{1/2} \leftarrow ^2P_{3/2}$	234.5 nm	355 nm	C 480	MeOH	BBOI
$Cl(^2P_{3/2})$	$^2D_{5/2} \leftarrow ^2P_{3/2}$	236.2 nm	355 nm	C 480	MeOH	BBOI

Table 3.2: Details of the YAG wavelengths, dyes and non-linear crystals used to generate the radiation for investigation of Cl and S atomic fragments. Details of the (2+1) REMPI transitions also provided. Pym = Pyromethane, Rhm = Rhodamine, and C = Coumarin.

the two photon step of the (2+1) REMPI process. While recording experimental ion images the probe laser wavelength was scanned over the Doppler profile of the (2+1) REMPI transition ensuring equal detection sensitivities for all product velocities.

3.3 Experimental characteristics

3.3.1 REMPI spectra

Spectra were recorded by monitoring the total ion signal generated at the detector following a REMPI process as a function of the wavelength of either the pump or probe laser. The total ion signal from the relevant peak in the time of flight spectrum was measured by observing the current drawn by the phosphor screen. Integration of the current intensity by a boxcar integrator (Stanford Research Systems SRS250) allowed the total ion signal to be monitored by electronically gating over the relevant

TOF peak. During acquisition of any given spectrum the data was transferred to a PC for averaging through an analogue-to-digital converter (Stanford Research Systems). The wavelength of the laser required to generate the spectrum was scanned with averaging over ~ 25 laser shots typical at each wavelength increment.

Two types of REMPI spectra are presented in this thesis. The first, termed REMPI excitation spectra, and relevent to Chapters 5 and 6, were generated by monitoring the S^+ signal from the photodissociation of CS_2 as the photolysis wavelength was scanned, the probe wavelength being fixed on the (2+1) REMPI transition of the $S(^1D_2)$ or $S(^3P_J)$ atomic fragments. Generating the second type of REMPI spectra involved fixing the photolysis wavelength and scanning the probe laser over the Doppler width of the REMPI transitions of the $S(^3P_J)$ spin-orbit states of the atomic photofragments. Spectra generated in this manner were used to estimate populations in different photofragment spin-orbit levels.

Rotational temperature of the molecular beam

REMPI spectra were also recorded in order to elucidate the rotational temperature associated with the molecular beam. For experiments performed with the Jordan valve this was achieved by monitoring the (1+1) REMPI signal from a beam of $< 1\%$ NO seeded in Helium with a 2 bar stagnation pressure. The molecular beam of neutral NO was ionised in a one-colour experiment using an unfocussed laser at wavelengths relevant to the NO $A(v = 0) - X(v = 0)$ rotational transitions located around 226 nm. Under velocity mapping conditions the ionisation of NO molecules results in NO^+ ions with effectively zero velocity components perpendicular to the TOF axis. The ions therefore appear as a single spot in the centre of the detector. Due to the extremely high absorption coefficients the intensities of the lines in the experimental spectrum may have been saturated making a quantitative assignment of the rotational temperature difficult. However, the lack of lines in the experimentally recorded spectra, shown in Figure 3.3, indicate that the molecular beam would have an associated rotational temperature of < 5 K. For experiments carried out

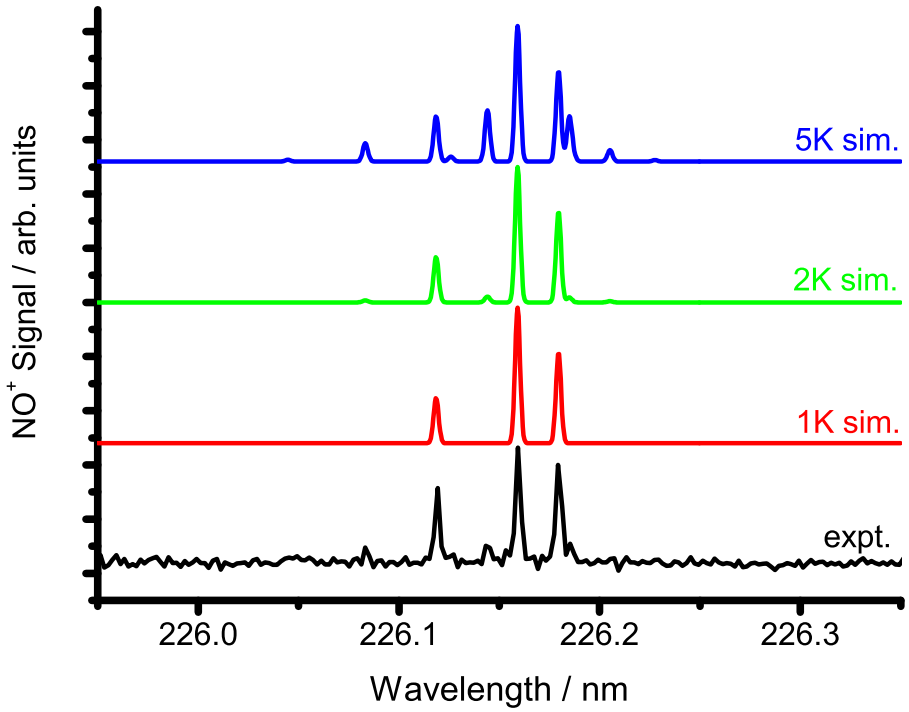

Figure 3.3: NO (1+1) REMPI spectrum. The lower trace shows the experimental spectrum while the top three traces show simulations of the spectrum based on rotational temperatures of 1, 2 and 5 K. The simulations were performed using LIFBASE [130].

using the General valve, previous measurements performed by the group indicate a rotational temperature on the order of 25 K [47, 50, 77].

3.3.2 Ion images

Ion images presented in this thesis have been averaged over $\geq$ 20,000 laser shots. As mentioned previously, the use of a photoelastic modulator to flip the polarisation of the probe beam allowed images to be recorded in two experimental geometries during a single image acquisition. In the case of the photodissociation of CS_2, however, a further complication arose in that the molecules absorbed and subsequently generated S^+ signals at the REMPI wavelengths used, *i.e.* without the pump laser on. This problem was minimised by reducing the power of the probe laser, however, the magnitude of the probe-only signal was sufficient to require a background subtrac-

tion procedure in order to isolate the pump-probe, one-photon photodissociation, signal of interest. The background subtraction was achieved by recording the ion images using a 4-channel acquisition. For each laser shot the probe polarisation was alternated by 90° relative to the previous shot, while the pump laser was triggered in an 'ON-ON-OFF-OFF' pattern, achieved by patterning the signal sent to either the excimer laser, for the 193.3 nm experiments, or to the Q-switch of the Nd:YAG laser used to pump the LPD 3000 dye laser. In this way the background probe-only signal, *e.g.*, channels three and four in the above, could be directly subtracted from the total (pump-probe + probe-only) signal, *e.g.*, channels one and two in the above, leaving the desired pump-probe signal.

3.4 Reagent sources

3.4.1 CS_2

A $< 1\%$ mixture of CS_2 (99.9% spectroscopic grade, Sigma Aldrich) in 1 bar Helium was prepared for experiments described herein. CS_2 (vapour pressure ~ 300 mmHg at 20° C) was expanded into a cylinder and diluted several times with He in order to prepare the $< 1\%$ mixture. This low seeding ratio was used to minimise the probability of cluster formation.

3.4.2 Cl_2

A 0.5% mixture of Cl_2 (99.9% purity, CK Gas) seeded in 2 bar He was used for the experiments carried out in this thesis. This low seeding ratio was used to prevent cluster formation and preserve the lifetime of the nozzle.

3.5 Data analysis

In the following section the procedure for extracting meaningful physical quantities from a set of velocity mapped ion images is described. The analysis of experi-

mental ion images follows the well-established Fourier moment scheme proposed by Brouard and co-workers [58] allowing the (analytic) determination of the observables of interest. In this framework, the angular dependence of an experimental ion image is expressed as a Fourier expansion. The quantities of interest, including a complete description of the angular momentum polarisation, are then found by fitting these experimental moments to a set of simulated moments. The equations describing the simulated moments are derived from the rigorous and fully quantum mechanical description of photodissociation processes provided by Vasyutinskii and co-workers [92], as discussed in Section 2.3.2. The Fourier moment analysis scheme has been described in detail previously [47, 77, 106], and only the principles and key equations are set out below.

3.5.1 Image processing

Subsequent to the recording of ion counted [129] data, images are processed to allow the extraction of the raw Fourier moments (described below). The processing procedure involves a manual centering of the ion images. Centering is achieved by superimposing a series of concentric circles on the image. Once the centre has been roughly determined, by lining up the circles on the image, the images are symmetrised, which involves reflecting the images along the horizontal and vertical axis of the 2D image. If the centering is incorrect, large distortions of the (circular) ion images become apparent in the symmetrised image. The manual centering process is repeated until no distortions are visible. For a single pump-probe geometry, several experimental acquisitions of between $5{,}000 - 20{,}000$ laser shots were recorded. Once correctly centred, these images could be summed together prior to extracting the Fourier moments (see below). Furthermore, at this stage any background images arising solely from the probe laser, *e.g.*, following a 4-channel acquisition as described in Section 3.3.2, could be subtracted, leaving the desired summed images.

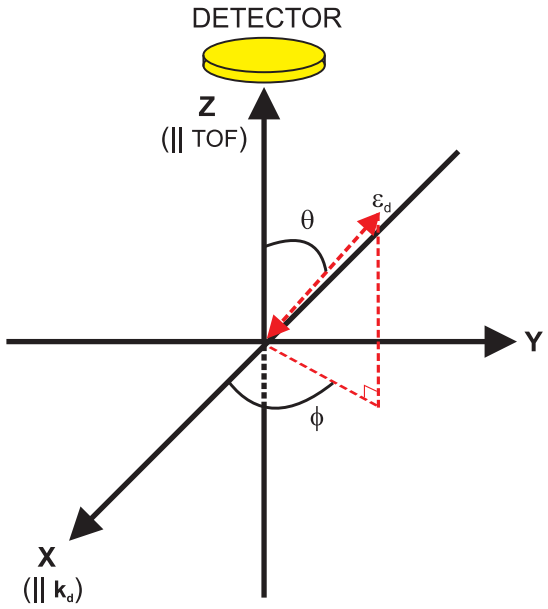

Figure 3.4: The TOF frame of reference used to define the laser polarisations employed in this work.

3.5.2 Experimental geometries

In general ion images were collected using several different pump-probe laser polarisations in order to allow the extraction of all moments of the electronic angular momentum distribution for a given photofragment, as discussed in Section 1.3. In order to define the experimental geometry two polar angles, θ and ϕ, are used to describe the electric vector of linearly polarised radiation in the time of flight reference frame. For circularly polarised radiation, the direction of laser propagation is used to define the experimental geometry. Recall that in the TOF reference frame the **Z** axis lies parallel to the time of flight direction with the pump and probe propagation directions lying along the $+\mathbf{X}$ and $-\mathbf{X}$ axis, respectively. For convenience, the labels used to define the experimental geometries used in this thesis, and their polar angles, illustrated in Figure 3.4, are tabulated in Table 3.3.

Throughout this thesis ion images are commonly referred to using two labels. The first label is used to define the pump laser polarisation in the time of flight frame while the second refers to the probe laser. Furthermore, as a convention,

θ/degrees	ϕ/degrees	Label	Laser
0	N/A	V	Pump and probe
90	90	H	Pump and probe
$\pm$45	90	$\pm$45	Pump
90	0	C	Pump
90	180	C	Probe

Table 3.3: Angles, θ and ϕ, used to define the polarisation vector of the linearly polarised or the propagation direction of the circularly polarised pump and probe lasers in the time of flight reference frame.

the ion images presented in this thesis are oriented in such a way that the H laser polarisation lies horizontally across the page.

3.5.3 Fourier moment analysis

As illustrated in Figure 3.5, an experimental ion image recorded in pump-probe geometry g is a function of the polar co-ordinates r and θ. Therefore, it may be expanded as a Fourier series in the angular co-ordinate θ

$$I^g(r,\theta) = C_0^g(r) + 2\sum_{n>0} C_n^g(r)\cos n\theta + C_n^g(r)'\sin n\theta\,, \tag{3.1}$$

where $C_n^g(r)$ and $C_n^g(r)'$ are the Fourier moments (coefficients) of the experimental image. Due to the symmetry of the experimental ion images, a consequence of the random orientation of molecules in the molecular beam prior to fragmentation, only the even moments need to be determined for the work carried out in this thesis.

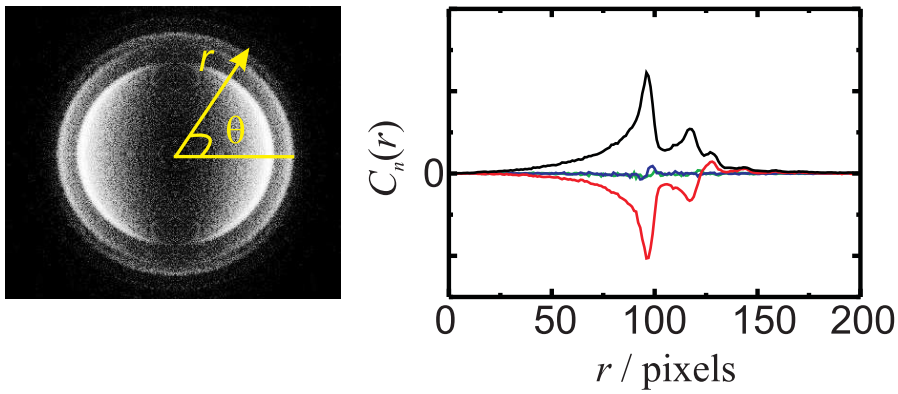

Figure 3.5: Ion image (left) and Fourier moments of ion image (right) of the $Cl(^2P_{3/2})$ fragments following photodissociation of Cl_2 at 450 nm, see Chapter 4. The Fourier moments are colour coded, C_0 (black), C_2 (red), C_4 (blue) and C_6 (green). Data shown was recorded in a HH geometry using the $^2P_{1/2} \leftarrow ^2P_{3/2}$ (2+1) REMPI transition at 234.54 nm.

Explicitly, the Fourier moments are described by

$$C_n^g(r) = \int_0^{2\pi} I^g(r,\theta) \cos n\theta \, r\mathrm{d}\theta \tag{3.2}$$

$$C_n^g(r)' = \int_0^{2\pi} I^g(r,\theta) \sin n\theta \, r\mathrm{d}\theta \,. \tag{3.3}$$

Numerical integration over the angular co-ordinate θ is carried out at each value of r in order to extract the Fourier moments of the images. These moments are initially normalised to the 0^{th} order moment, however, where angular momentum polarisation effects are important, a careful renormalisation is required at a later stage of the data analysis procedure, as described in Section 3.5.4.

Having defined the Fourier moments of the experimental images the next step is to define the simulated Fourier moments, by making a connection with the theoretical description of the photodissociation process. As detailed in Chapter 2, Vasyutinskii and co-workers have provided explicit expressions describing the electronic angular momentum distribution following a one-photon dissociation of a diatomic molecule within the axial recoil approximation [63]. The laboratory frame distribution of electronic angular momenta is described by the $\rho_{KQ}^{\text{lab}}(\theta,\phi)$ state mul-

tipole moments [63, 104], adapted for multiple recoil velocities to give [106]

$$\rho_{KQ}^{\mathrm{lab}}(\theta,\phi;v) = \frac{3}{4\pi}\left(\frac{[K]}{[J_{\mathrm{A}}]}\right)^{1/2} \sum_{k_{\mathrm{d}},q_{\mathrm{d}},Q'} \sum_{q,q'} (-1)^{K+q'} E_{k_{\mathrm{d}}q_{\mathrm{d}}}(\mathbf{e}) \times \frac{f_K(q,q';v)}{\langle f_0(0,0;v)\rangle + \langle 2f_0(1,1;v)\rangle} [k_{\mathrm{d}}]^{1/2} \begin{pmatrix} 1 & 1 & k_{\mathrm{d}} \\ q' & -q & -Q' \end{pmatrix} \times D^{K^*}_{QQ'}(\phi,\theta,0) D^{k_{\mathrm{d}}}_{q_{\mathrm{d}}Q'}(\phi,\theta,0)\,, \tag{3.4}$$

where the angles θ and ϕ are the polar angles defined in the time of flight (TOF) frame, v represents the velocity of the photofragment, and $[C] = (2C+1)$. The other terms in Equation (3.4) are defined as follows: $E_{k_{\mathrm{d}}q_{\mathrm{d}}}(\mathbf{e})$ are the matrix elements of the photodissociation light of rank k_{d}, $D^a_{b,c}$ are rotation matrices [52], $Q' = q' - q$ and $f_K(q,q';v)$ are the velocity-dependent dynamical functions [92]. Since the experimental measurements described herein were performed by recording a 2D projection of the 3D scattering distribution, *i.e.* traditional 'crushed' imaging, integration over the velocity component along the TOF **Z** direction allows one to define the state multipoles for the two dimensional projection of the full three dimensional scattering distribution. As detailed previously, the resulting expression is [106]

$$\rho_{KQ}^{\mathrm{lab}}(r,\phi) = \frac{3}{4\pi}\left(\frac{[K]}{[J_{\mathrm{A}}]}\right)^{1/2} \sum_{k_{\mathrm{d}}q_{\mathrm{d}}} \sum_{qq'} (-1)^{K+q'} E_{k_{\mathrm{d}}q_{\mathrm{d}}}(\mathbf{e}) [k_{\mathrm{d}}]^{1/2} \begin{pmatrix} 1 & 1 & k_{\mathrm{d}} \\ q' & -q & -Q' \end{pmatrix} \times (-1)^{Q-Q'} \sum_{K'} [K'] \begin{pmatrix} K & k_{\mathrm{d}} & K' \\ -Q & q_{\mathrm{d}} & n \end{pmatrix} \begin{pmatrix} K & k_{\mathrm{d}} & K' \\ -Q' & Q' & 0 \end{pmatrix} \mathrm{e}^{in\phi} \times [1 + (-1)^{K'+n}] \int C_{K'n}(\theta,0) f'_K(q,q';v) \mathrm{d}v_Z\,, \tag{3.5}$$

where $C_{K'n}(\theta,0)$ is a modified spherical harmonic [52] and the integral is performed over the time of flight **Z** axis. The dynamical functions in Equation (3.5) have been renormalised, with $f'_K(q,q';v) = f_K(q,q';v)/\left(\langle f_0(0,0;v)\rangle + \langle 2f_0(1,1;v)\rangle\right)$. In the Fourier moment analysis scheme [58], the speed dependence of these dynamical functions is expressed as a linear combination of equally spaced Gaussian functions,

with the expansion coefficients representing the (Gaussian specific) polarisation parameters [106]

$$f'_K(q,q';v) = \sum_i N a_K(q,q';i)\mathrm{e}^{-\sigma(v_i-v)^2}\,. \tag{3.6}$$

By inserting Equation (3.6) into Equation (3.5) and rearranging, the expression for the crushed state multipole moments may be shown to take the form of a Fourier series [106]

$$\begin{aligned}\rho^{\mathrm{lab}}_{KQ}(r,\phi) = \sum_i \sum_{qq'} a_K(q,q';i)\Big(&\rho_{KQ}(q,q',i,0,g;r)\\ &+ \sum_{n>0}\Big[\rho_{KQ}(q,q',i,n+,g;r)\cos n\phi\\ &+ \rho_{KQ}(q,q',i,n-,g;r)\Big] i\sin n\phi\Big)\,,\end{aligned} \tag{3.7}$$

with

$$\begin{aligned}\rho_{KQ}(q,q',i,n+,g;r) &= \rho_{KQ}(q,q',i,+n,g;r) + \rho_{KQ}(q,q',i,-n,g;r)\\ \rho_{KQ}(q,q',i,n-,g;r) &= \rho_{KQ}(q,q',i,+n,g;r) - \rho_{KQ}(q,q',i,-n,g;r)\,.\end{aligned} \tag{3.8}$$

The modified state multipoles, $\rho_{KQ}(q,q',i,n,g;r)$, are given by [106]

$$\begin{aligned}\rho_{KQ}(q,q',i,n,g;r) = \frac{3}{4\pi}&\left(\frac{[K]}{[J_{\mathrm{A}}]}\right)^{1/2}\sum_{k_{\mathrm{d}}q_{\mathrm{d}}}\sum_{qq'}(-1)^{K+q'}E_{k_{\mathrm{d}}q_{\mathrm{d}}}(\mathbf{e})[k_{\mathrm{d}}]^{1/2}\\ &\times\begin{pmatrix}1 & 1 & k_{\mathrm{d}}\\ q' & -q & -Q'\end{pmatrix}\sum_{K'}[K']\begin{pmatrix}K & k_{\mathrm{d}} & K'\\ -Q & q_{\mathrm{d}} & n\end{pmatrix}\\ &\times\begin{pmatrix}K & k_{\mathrm{d}} & K'\\ -Q' & Q' & 0\end{pmatrix}\Big[1+(-1)^{K'+n}\Big]\\ &\times\int W\mathrm{e}^{-\sigma(v_i-v)^2}C_{K'n}(\theta,0)\mathrm{d}v_Z\,,\end{aligned} \tag{3.9}$$

where W is a normalization constant.

Previous work by Kummel, Sitz and Zare [131, 132] has allowed the extraction of polarisation moments from experimental (2+1) REMPI signals. In the present case, the ion image intensity of a crushed velocity map image in geometry g may be written as [104, 106]

$$\mathcal{I}^g(r,\phi) = W \sum_{KQ} \tilde{P}_K \rho^g_{KQ}(r,\phi) C^*_{KQ}(\theta^g_{\rm pr}, \phi^g_{\rm pr}) \,, \tag{3.10}$$

where the $\tilde{P}_K$ are linestrength factors [133] which are defined below, and the angles $\theta^g_{\rm pr}$ and $\phi^g_{\rm pr}$ give the direction of the probe laser polarisation in the time of flight frame. By substituting in the expression for the crushed state multipoles, $\rho^{\rm lab}_{KQ}(r,\phi)$, from Equation (3.7), one can recast the ion image intensity as a Fourier series [106],

$$\mathcal{I}^g(r,\phi) = {\rm Re}[c_0(r)] + \sum_{n>0} {\rm Re}[c_{n+}(r)] \cos n\phi - {\rm Im}[c_{n-}(r)] \sin n\phi \,, \tag{3.11}$$

with the expansion coefficients depending on the $a_k(q,q';i)$ polarisation parameters, which were defined in Equation (3.6) [106],

$$c^g_{n\pm}(r) = \sum_{i=1}^{nGauss} \sum_{K,q,q'} a_K(q,q';i) G(K,q,q',i,n\pm,g;r) \,. \tag{3.12}$$

The $G(K,q,q',i,n,g;r)$ are geometry (g) dependent basis functions for the simulated moments, explicitly given by [106]

$$G(K,q,q',i,n\pm,g;r) = W' \sum_{Q} \tilde{P}_K \rho_{KQ}(q,q',i,n\pm,g;r) C^*_{KQ}(\theta^g_{\rm a}, \phi^g_{\rm a}) \,. \tag{3.13}$$

The Fourier moment analysis scheme is conceptually simple and involves fitting the simulated Fourier moments to the experimental moments by adjusting the values of the $a_k(q,q',i)$ parameters. Once the best agreement is found, these $a_k(q,q',i)$ parameters allow the speed, angular, and angular momentum distribution to be extracted from a set of velocity map ion images. The fitting procedure itself, described in Section 3.5.5, is usually performed globally with all experimental pump-probe ge-

ometries and (2+1) REMPI transitions included. When angular momentum polarisation is important, the intensity of an ion image depends on the total (integrated over velocity) alignment and/or orientation [106]. In such cases, a careful renormalisation procedure must be used, as discussed in Section 3.5.4.

Line strength factors, $\tilde{P}_K$

The sensitivities to particular ranks, K, of the electronic angular momentum distribution following a specific (2+1) REMPI transition can be described by the linestrength factors, $\tilde{P}_K$. They have been defined by Mo and Suzuki as [133]

$$\tilde{P}_K = 5\sqrt{2K+1}\sqrt{2J_\mathrm{i}+1}(-1)^{J_\mathrm{f}+J_\mathrm{i}} \begin{pmatrix} 2 & 2 & K \\ 2s & -2s & 0 \end{pmatrix} \begin{Bmatrix} J_\mathrm{i} & J_\mathrm{i} & K \\ 2 & 2 & J_\mathrm{f} \end{Bmatrix}, \quad (3.14)$$

where J_i and J_f are the initial and intermediate states involved in the REMPI process, and the parameter s can take values of 0 for linearly polarised and ± 1 for circularly polarised probe radiation. Equation (3.14) is general and can be used for all cases except where $J_i = J_f$. The calculated numerical results for all REMPI processes used in this thesis can be found in Tables 3.4 to 3.9.

For the case of $\mathrm{Cl}(^2\mathrm{P}_{3/2})$ and $\mathrm{Cl}^*(^2\mathrm{P}_{1/2})$ atoms, a complication exists in that coupling of the electronic angular momentum with the unpolarised nuclear spin reduces the polarisation intrinsic to the photodissociation process. This hyperfine depolarisation effect, however, can be quantified by the equation [52]

$$g^k = \sum_F \frac{(2F+1)^2}{(2I+1)} \begin{Bmatrix} F & F & k \\ J & J & I \end{Bmatrix}^2, \quad (3.15)$$

where k describes the photofragment rank, I is the nuclear spin, and F the total (electronic + spin) angular momentum. Specifically for $\mathrm{Cl}(^2\mathrm{P}_{3/2})$, Equation (3.15) gives $g^1 = 0.5$, $g^2 = 0.27$ and $g^3 = 0.2$, and for $\mathrm{Cl}^*(^2\mathrm{P}_{1/2})$ $g^1 = 0.375$. The reduction coefficients, g^k, are absorbed into the linestrength factors, $\tilde{P}_K$, to account for the hyperfine depolarisation in the data analysis.

	$^2P_{1/2} \leftarrow {}^2P_{3/2}$				
Geometry	$\tilde{P}_1$	$\tilde{P}_2$	$\tilde{P}_3$	b_1	b_2
HH/VV	0	1.0	0	0	1.41
HV/VH	0	1.0	0	0	-0.71
+45L	1.34	-1.0	0.45	0	-0.35
RR	-1.34	-1.0	-0.45	-1.64	0.71

Table 3.4: Linestrength factors, $\tilde{P}_K$, defined in Equation (3.14) and constants, b_K, defined in Equation (3.17) for REMPI transition and laser geometries used to probe Cl($^2P_{3/2}$) fragments. Note that left and right circular polarisation produce opposite sign $\tilde{P}_{1,3}$ and b_1 factors.

	$^2D_{5/2} \leftarrow {}^2P_{3/2}$				
Geometry	$\tilde{P}_1$	$\tilde{P}_2$	$\tilde{P}_3$	b_1	b_2
HH/VV	0	-0.71	0	0	-1.01
HV/VH	0	-0.71	0	0	0.51
+45L	0.15	0.71	0.19	0	0.25
RR	-0.15	0.71	-0.19	-0.18	-0.51

Table 3.5: Linestrength factors, $\tilde{P}_K$, defined in Equation (3.14) and constants, b_K, defined in Equation (3.17) for REMPI transition and laser geometries used to probe Cl($^2P_{3/2}$) fragments. Note that left and right circular polarisation produce opposite sign $\tilde{P}_{1,3}$ and b_1 factors.

	$^2P_{3/2} \leftarrow {}^2P_{1/2}$	
Geometry	$\tilde{P}_1$	b_1
HH/VV	0	0
HV/VH	0	0
+45L	1.0	0
RR	-1.0	-1.23

Table 3.6: Linestrength factors, $\tilde{P}_K$, defined in Equation (3.14) and constants, b_K, defined in Equation (3.17) for REMPI transition and laser geometries used to probe Cl*($^2P_{1/2}$) fragments. Note that left and right circular polarisation produce opposite sign $\tilde{P}_1$ and b_1 factors.

	$^3P_1 \leftarrow {}^1D_2, {}^3P_2$					
Geometry	$\tilde{P}_1$	$\tilde{P}_2$	$\tilde{P}_3$	$\tilde{P}_4$	b_1	b_2
HH/VV	0	-0.60	0	-1.07	0	0.84
HV/VH	0	-0.60	0	-1.07	0	-0.42
+45L	-1.18	0.60	0	-0.18	0	0.42
LL	-1.18	0.60	0	-0.18	-1.43	0.42

Table 3.7: Linestrength factors, $\tilde{P}_K$, defined in Equation (3.14) and constants, b_K, defined in Equation (3.17) for REMPI transitions and laser geometries used to probe S($^1D_2$) and S($^3P_2$) fragments. Note that left and right circular polarisation produce opposite sign $\tilde{P}_{1,3}$ and b_1 factors.

	$^1F_3 \leftarrow {}^1D_2$					
Geometry	$\tilde{P}_1$	$\tilde{P}_2$	$\tilde{P}_3$	$\tilde{P}_4$	b_1	b_2
HH/VV	0	0.68	0	-0.11	0	-0.96
HV/VH	0	0.68	0	-0.11	0	0.48
+45L	0	-0.68	-0.25	-0.02	0	-0.48
LL	0	-0.68	-0.25	-0.02	0	-0.48

Table 3.8: Linestrength factors, $\tilde{P}_K$, defined in Equation (3.14) and constants, b_K, defined in Equation (3.17) for REMPI transition and laser geometries used to probe S($^1D_2$) fragments. Note that left and right circular polarisation produce opposite sign $\tilde{P}_{1,3}$ and b_1 factors.

	$^3P_2 \leftarrow {}^3P_1$			
Geometry	$\tilde{P}_1$	$\tilde{P}_2$	b_1	b_2
HH/VV	0	0.71	0	-0.96
HV/VH	0	0.71	0	0.48
+45L	-0.41	-0.71	0	-0.48
LL	-0.41	-0.71	0.48	-0.48

Table 3.9: Linestrength factors, $\tilde{P}_K$, defined in Equation (3.14) and constants, b_K, defined in Equation (3.17) for REMPI transition and laser geometries used to probe S($^3P_1$) fragments. Note that left and right circular polarisation produce opposite sign $\tilde{P}_1$ and b_1 factors.

3.5.4 Total signal normalisation

As mentioned in Section 3.5, a careful renormalisation of the ion image intensity must be used in the data analysis. In particular, the ion image intensity must be normalised to take into account the total (integrated over velocity) orientation and alignment, $\langle A^1 \rangle$ and $\langle A^2 \rangle$, respectively, for each pump-probe geometry, g. Expressions for these parameters are given below, however, for a complete derivation see Ref [106]. The ion image intensity, given by the integrated zeroth order Fourier moment, can be expressed in terms of the total integrated orientation and alignment as [106]

$$\langle I^g \rangle = b_0 + b_1 \langle A^1 \rangle + b_2 \langle A^2 \rangle \,, \tag{3.16}$$

since higher order ($K > 2$) moments of the angular momentum distribution vanish upon averaging over recoil direction [84]. The constants, b_K, are defined as [106]

$$b_K = \tilde{P}_K \left(\frac{3[K]}{[J]} \right)^{1/2} (-1)^{K+1} \begin{pmatrix} 1 & 1 & K \\ s & -s & 0 \end{pmatrix} P_K(\cos\varphi) \,, \tag{3.17}$$

where φ describes the angle between the pump and probe lasers. Values of the constants, b_K, can be found in Tables 3.4 to 3.9 for all the (2+1) REMPI transitions used in this thesis. The total orientation and alignment, $\langle A^K \rangle$, may be expressed in terms of the dynamical functions [106],

$$\langle A^K \rangle = \sum_{qq'} (-1)^{q'+1} \sqrt{3} \begin{pmatrix} 1 & 1 & K \\ q' & -q & -Q' \end{pmatrix} \langle f'_K(q, q'; v) \rangle \,, \tag{3.18}$$

or in terms of the laboratory frame polarisation parameters, as detailed in Equation (2.22).

The total alignment and orientation can be calculated from the simulated Fourier coefficients, in this way allowing renormalisation of the experimental image intensities to take place at each iteration of the fitting process, 'on-the-fly'.

3.5.5 Data fitting

In order to determine the polarisation parameters of interest the experimental Fourier moments, C_n, are fitted to the simulated moments, c_n, *via* a χ^2 minimisation [106]

$$\chi^2 = \sum_g \sum_n \sum_i \left[C_n^g(r_i) - \mathrm{Re}[c_{n+}^g(r_i)]\right]^2 . \tag{3.19}$$

Note that the summation runs over all recorded geometries, g, and therefore Fourier moments for all geometries are fit simultaneously. The minimisation procedure itself is performed by a well-known genetic algorithm routine [134]. The genetic algorithm is used to vary the values taken by the polarisation parameters, themselves linear combinations of the $a_k(q, q', i)$ factors, between their physically allowed extrema [84]. In fact, the speed dependence of higher order ($n > 0$) $a_k(q, q', i)$ factors was expressed as a Legendre polynomial expansion, multiplied by the speed distribution $a_0(i)$ [106]

$$a_K(q, q'; i) = a_0(i) \sum_{l=0}^{nleg} a'_K(q, q'; l) P_l(x_i) , \tag{3.20}$$

where

$$x_i = 2\frac{i-1}{i_{\max}-1} - 1 , \tag{3.21}$$

is constrained between the physically allowed limits of $\pm$ 1. This allows one to reduce the number of fitting parameters when the speed dependence of the polarisation parameters takes on a relatively simple form. This is useful when the number of Gaussians required to reproduce the speed distribution is large, but the speed dependence of the angular distribution and polarisation are simple.

Error analysis

A Monte Carlo procedure was used to determine the errors associated with the experimental data [135]. In this method sets of $a_k(q, q', i)$ parameters were randomly chosen so as to generate a value of χ^2 below a certain cut-off. The selected value of χ^2 was chosen based on the noise associated with individual experimental Fourier moments, with the optimal value selected to fully encompass this experimental uncertainty. The errors in the experimental data were determined by the limits obtained from a large set of these $a_k(q, q', i)$ parameters, giving the errors in the speed, angular and angular momentum distributions.

Chapter 4

Cl_2 Photodissociation

The experimental results presented in this chapter were obtained following the photodissociation of Cl_2 at a range of dissociation energies from the long wavelength tail, 470 nm, to close to the peak in the absorption spectrum, 355 nm. Ion images were collected for both the $Cl(^2P_{3/2})$ and $Cl^*(^2P_{1/2})$ fragments in order to measure the electronic angular momentum alignment and orientation for dissociation into both product channels of significance to the first absorption band. These results are compared to recent high level time dependent wavepacket calculations [50] performed on a set of *ab initio* potentials [51]. In addition, theoretical results from time dependent wavepacket calculations are presented for the photodissociation of vibrationally excited parent molecules. The results of these calculations are compared to the first experimental measurements on the photodissociation of Cl_2 ($v = 1$).

4.1 Background

The ultraviolet absorption spectrum of molecular chlorine consists of a single broad distribution with a maximum around ~ 335 nm, as shown in Figure 4.1. The spectrum arises primarily as a result of excitation to the unbound, repulsive, $C\,^1\Pi_{1u}$ state. A weaker spin-forbidden transition to the $B\,^3\Pi_{0_u^+}$ state becomes prevalent in the long wavelength region giving the profile a slight asymmetry, as illustrated in Figure 4.1. Of significance to this absorption band are the two product channels,

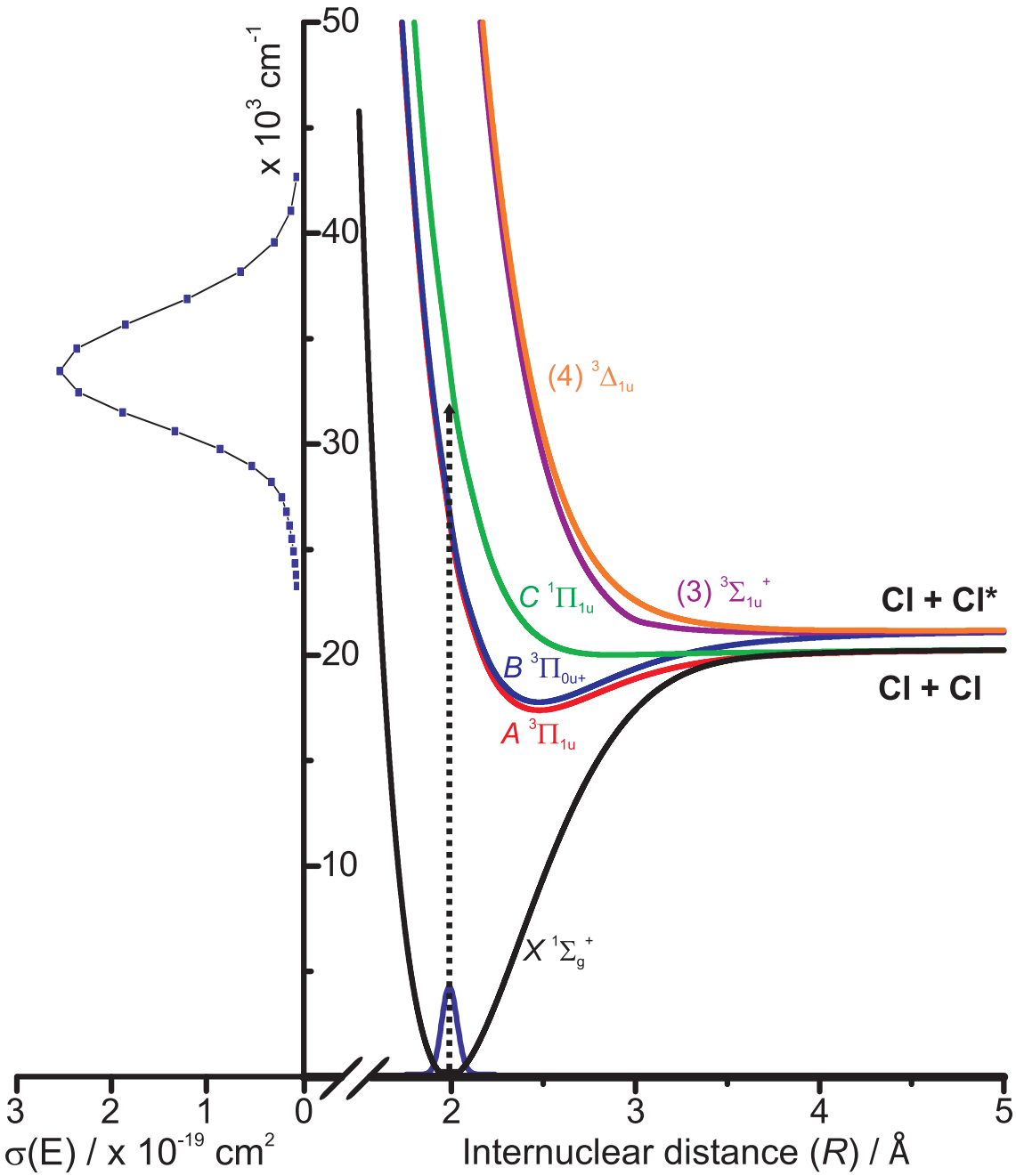

Figure 4.1: Adiabatic potential energy curves of Cl_2 (right) [136] important for dissociation in the first absorption band (left) [137]. At short wavelengths the $C\,^1\Pi_{1u}$ state (green) dominates with the $B\,^3\Pi_{0_u^+}$ state (blue) becoming more important as the wavelength increases.

$Cl(^2P_{3/2}) + Cl(^2P_{3/2})$, and $Cl(^2P_{3/2}) + Cl^*(^2P_{1/2})$. These are termed the ground and excited state product channels, respectively, in subsequent discussions.

The electronic states relevant to the present work are derived from a single electron promotion between two antibonding orbitals of π_g and σ_u symmetries, respectively. The electronic states derived from the molecular orbitals involved are detailed in the adiabatic correlation diagram shown in Figure 4.2. The correlation diagram connects the *molecular* states in both Hunds case (a) and (c) with the separated *atomic* states. The diagram, which follows the adiabatic correlation rules first described by Mulliken [138], can also been seen in Refs [139–142] and is included here for completeness. As shown in Figure 4.2 the $C\,^1\Pi_{1u}$ state correlates adiabatically with the ground state product channel, while the $B\,^3\Pi_{0_u^+}$ state, important in the enhanced long wavelength portion of the absorption, correlates with the excited state product channel. The adiabatic potential energy curves for the states believed to be important for photodissociation are shown in Figure 4.1.

The generally accepted mechanism for photodissociation giving rise to the ground state product channel involves photoexcitation to and dissociation on the $C\,^1\Pi_{1u}$ state surface, with an additional contribution from the $A\,^3\Pi_{1u}$ state following non-adiabatic coupling between the two in the long range region where the potentials are close in energy. The excited state product channel arises following the formally spin-forbidden excitation to the $B\,^3\Pi_{0_u^+}$ state, which becomes weakly allowed due to the spin-orbit interaction [51]. At long wavelengths the dissociation is believed to proceed adiabatically on the $B\,^3\Pi_{0_u^+}$ state. The character of this dissociation channel, as opposed to the ground state channel, is wavelength dependent, with the perpendicular component primarily arising through a non-adiabatic transition from the $C\,^1\Pi_{1u}$ to $(3)^3\Sigma_{1u}^+$ state. A further contribution is believed to arise from a non-adiabatic transition between the $(3)^3\Sigma_{1u}^+$ and $(4)^3\Delta_{1u}$ states. In the following section the experimental and theoretical work which has given rise to the above described mechanism is reviewed.

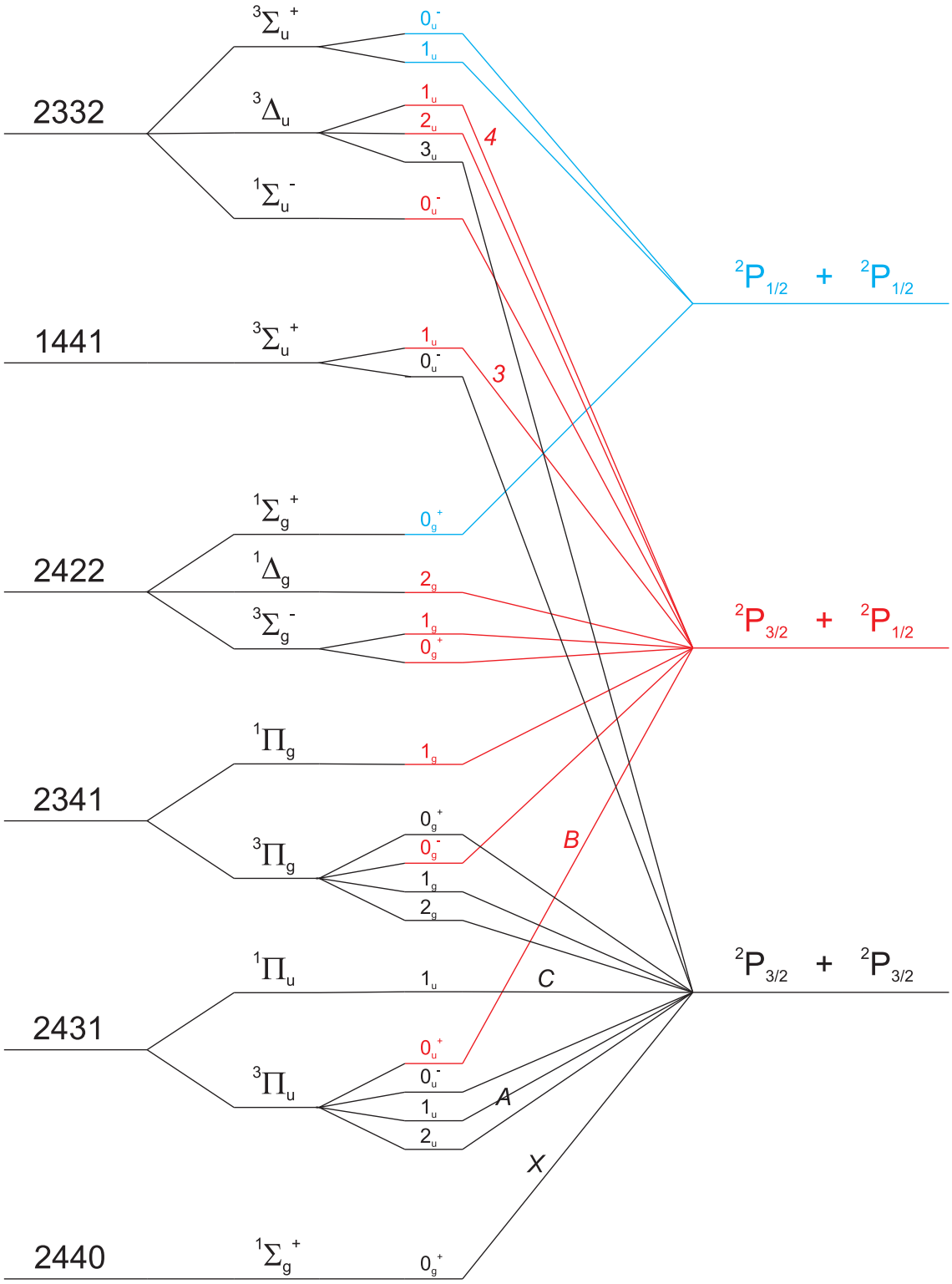

Figure 4.2: Adiabatic correlation diagram linking the *atomic* $Cl(^2P_J)$ states (right) with the *molecular* states in Hunds case (c) and (a) (middle) and molecular orbitals (left). The numbers give the occupancy of the $5\sigma_g 2\pi_u 2\pi_g^* 5\sigma_u^*$ molecular orbitals. The five states believed to be important in the photodissociation are also labelled. Adapted from Refs [139–142].

4.2 Previous work

4.2.1 Experimental studies

Studies of chlorine photodissociation date back to the early years in molecular reaction dynamics research. The first translational spectroscopy experiments were performed on Cl_2 by Busch [34] *et al.* and Diesen *et al.* [143] in the late 1960s. By probing translational energy and angular distributions following excitation using the second harmonic of a ruby laser, 347.1 nm, both studies showed that the atomic fragments were dissociating preferentially perpendicular to the electric vector of the linearly polarised dissociation light. Busch *et al.* were also able to assign the ground state product channel from their translational energy distribution, with both studies interpreting their results in terms of dissociation on the $C\,^1\Pi_{1u}$ state.

Significant advances in experimental methodologies allowed Li *et al.* to investigate the photolysis reaction near 325 nm at the fully quantum state specific level some 20 years later [140]. (3+1) REMPI spectra were recorded in this region and due to the absence of any signal intensity at the known $Cl^*(^2P_{1/2})$ resonances, the dissociation was understood to proceed in a purely *adiabatic* manner on the photoexcited $C\,^1\Pi_{1u}$ state, in agreement with the earlier studies [34, 143]. Matsumi *et al.*, in two publications in 1989 [144] and 1992 [139], recorded Doppler profiles following (2+1) REMPI in a comprehensive study of the photodissociation right across the absorption band, $266 - 485$ nm. From their experiments Matsumi *et al.* were able to extract wavelength dependent $Cl^*(^2P_{1/2})/Cl(^2P_{3/2})$ branching ratios and spatial anisotropy parameters, β. The $Cl^*(^2P_{1/2})/Cl(^2P_{3/2})$ branching ratio was shown to increase with wavelength from $\sim 1 \times 10^{-2}$ at 308 nm to ~ 0.5 at 475 nm. At short wavelengths, 355 nm, the authors measured a limiting β parameter of -1.0 for the $Cl(^2P_{3/2})$ fragments, assigning adiabatic dissociation on the $C\,^1\Pi_{1u}$ state. On the other hand the β parameter for the excited $Cl^*(^2P_{1/2})$ fragment was given as a limiting parallel 2.0 at 400 nm, decreasing to a predominantly perpendicular -0.7 at shorter wavelengths, 308 nm. The parallel component of this channel was assigned to

the $B\,^3\Pi_{0_u^+}$ state, with the perpendicular character at shorter wavelengths suggested to arise from non-adiabatic coupling of the $C\,^1\Pi_{1u}$ and $\Omega = 1$ states correlating with $Cl(^2P_{3/2}) + Cl^*(^2P_{1/2})$ at long internuclear distances.

More recently, the first ion imaging study was performed by Samartzis *et al.* [145] using (2+1) and (3+1) REMPI. At 355 nm the authors report β parameters of 1.78 and -0.87 for the $Cl^*(^2P_{1/2})$ and $Cl(^2P_{3/2})$ fragments, respectively, as well as a $Cl^*(^2P_{1/2})/Cl(^2P_{3/2})$ branching ratio ~ 5 times greater than previously given by Matsumi *et al.* [139, 144]. Combined, the non-limiting β parameter for the $Cl(^2P_{3/2})$ fragments and larger $Cl^*(^2P_{1/2})/Cl(^2P_{3/2})$ branching ratio suggested a greater influence of the $B\,^3\Pi_{0_u^+}$ state [145].

Atomic alignment measurements

In addition to the above mentioned studies, there have been several investigations into the electronic polarisation of both the $Cl(^2P_{3/2})$ and $Cl^*(^2P_{1/2})$ photofragments. The first measurements to probe the atomic alignment in the molecular frame were performed by Wang *et al.* [146]. REMPI-TOF profiles were recorded using different pump-probe laser polarisations to investigate electronic alignment effects at 355 nm. The authors interpreted their results, utilising the theoretical description provided by Band *et al.* [97, 147], as showing a preference for the $M_J = \pm 1/2$ sub-levels, consistent with adiabatic dissociation on the $C\,^1\Pi_{1u}$ state.

In 1997 Bracker *et al.* were able to directly link the fully quantum mechanical treatment of atomic polarisation effects in the recoil frame [92] with experimentally measurable signals [62]. For the first time a description of the underlying physics of the dissociation that result in atomic polarisation effects was provided [62]. Although pre-dating velocity mapping, their ion imaging study used a combination of different pump-probe laser polarisations and $Cl(^2P_{3/2})$ (2+1) REMPI transitions in order to extract the $K = 2$ alignment parameters, rigorously including coherent alignment effects at 355 nm [62, 63]. The authors showed that in addition to the incoherent alignment resulting from dissociation on the $C\,^1\Pi_{1u}$ state, a description including a

	Wavelength / nm					
Parameter	308[61]	320[78]	355[62]	355[79]	375 − 450[145]	470[78]
β	-0.88(3)	-1.0	-1.0	-1.0	~ 2	~ 2
s_2	-0.12(2)	-0.10(2)	-0.074(9)	-0.10(2)	-0.16	-0.14(4)
α_2	-0.06(1)	-0.05(1)	-0.032(3)	-0.05(1)	0.16	0.14(4)
γ_2	-0.05(1)	-	0.001(16)	-	-	-
η_2	0.16(4)	0.16(3)	0.075(20)	0.15(5)	-	-
$\langle A_{20} \rangle$	-0.10(6)	-0.10(7)	-0.09(8)	-0.08(10)	-0.32	-0.28(8)

Table 4.1: Laboratory frame alignment parameters reported from previous studies by Brouard and co-workers [61], Rakitzis *et al.* [78], Bracker *et al.* [62], and Rakitzis and Kitsopoulos [79] at 308, 320 and 355 nm, respectively, for the $Cl(^2P_{3/2})$ photofragments in the ground state product channel, and from Samartzis *et al.* [145] and Rakitzis *et al.* [78] for the excited state product channel. Errors (1σ) in the final digit(s) are given in parenthesis where appropriate.

non-adiabatic transition to the $A\,^3\Pi_{1u}$ state in the long range region of the potentials is required to understand the measured coherent effects.

In 1999 Zare and co-workers [78] performed core extraction TOF experiments to probe the $Cl(^2P_{3/2})$ alignment at two wavelengths, 320 nm and 470 nm. Close to the absorption maximum at 320 nm Zare and co-workers found the measured incoherent and coherent alignment to be in agreement with previous work at 355 nm. At the 470 nm tail of the absorption, only incoherent contributions to the alignment were found, with the $Cl(^2P_{3/2})$ fragments showing a strong (near limiting) preference for $M_J = \pm 1/2$ and a positive spatial ansiotropy, $\beta \sim 2.0$, consistent with adiabatic dissociation on the $B\,^3\Pi_{0_u^+}$ state curve. Around the same time Samartzis *et al.* performed a comprehensive ion imaging study, recording ion images of the $Cl(^2P_{3/2})$ and $Cl^*(^2P_{1/2})$ fragments at several dissociation wavelengths from 310 − 450 nm [148]. The ion images, all recorded in a HH geometry, see Section 3.5.2, were used to

	Wavelength / nm					
Parameter	308[61]	320[78]	355[62]	355[79]	375 – 450[148]	470[78]
β	-0.88(3)	-1.0	-1.0	-1.00(3)	$\sim$ 2.0	2.0
$a_0^{(2)}(\perp)$	-0.62(9)	-0.5(10)	-0.35(4)	-0.50(10)	-	-
$a_2^{(2)}(\perp)$	-0.26(7)	-0.32(6)	-0.15(4)	-0.30(10)	-	-
$a_0^{(2)}(\parallel)$	-	-	-	-	$\sim$ -0.8	-0.70(20)

Table 4.2: Molecular frame alignment parameters reported from previous studies by Brouard and co-workers [61], Rakitzis *et al.* [78], Bracker *et al.* [62], Rakitzis and Kitsopoulos *et al.* [79], and Samartzis *et al.* [148]. $a_0^{(2)}(\perp)$ and $a_2^{(2)}(\perp)$ data are shown for the $Cl(^2P_{3/2})$ fragments in the ground state product channel (top) while $a_0^{(2)}(\parallel)$ data are shown for the excited state product channel (bottom). Errors (1σ) in the final digit(s) are given in parenthesis where appropriate.

investigate the $Cl^*(^2P_{1/2})/Cl(^2P_{3/2})$ branching ratio and spatial anisotropy parameters for both fragments, in addition to probing the angular momentum alignment effects of the $Cl(^2P_{3/2})$ products. For the ground state product channel the angular distributions extracted from the ion images, analysed using the Abel inversion [43] method, were found to be characterised by a within experimental error wavelength independent β_2 component of -1 with zero contribution from higher order moments. Although the lack of higher order moments to the angular distribution indicates negligible alignment in the laboratory frame, the authors explain that for this particular pump-probe geometry, the same sign and similar magnitude incoherent and coherent alignment in the *molecular* frame can lead to this at first surprising result. The authors noted that this was consistent with the previously reported values of Bracker *et al.* [63]. The distributions for the $Cl(^2P_{3/2})$ fragments belonging to the the excited state product channel suggested a limiting spatial anisotropy parameter, $\beta = 2.0$, and maximum alignment in the molecular frame, $M_J = \pm 1/2$, for the region $375 - 450$ nm. For this channel the β parameter was shown to decrease

with decreasing wavelength below 375 nm, reaching a value of -0.64 at 310 nm. In agreement with the previous work near the absorption peak, a later slice imaging study by Rakitzis and Kitsopoulos [79], also at 355 nm, showed a preference for $M_J = \pm 1/2$ in the recoil frame for the ground state product channel.

The most recent ion imaging study of $Cl(^2P_{3/2})$ alignment was performed by Brouard and co-workers at 308 nm [61]. By recording ion images using several laser pump-probe geometries and (2+1) REMPI transitions, the authors were able to extract the spatial anisotropy parameter, β, and all $K = 2$ alignment terms from their experimental data. The analysis yielded a non-limiting β of -0.9. It was noted that the rotational temperature of the molecular beam had to be in the range $50 - 100$ K to account for the reduction in β on the basis of the electronic transition being purely perpendicular in character. The alignment parameters were found to be in good accord with previous studies at 355 nm [63], and illustrate the importance of coherence effects even at this short wavelength. Tables 4.1 and 4.2 provide a summary of the previous laboratory and molecular frame angular momentum alignment measurements.

Atomic orientation measurements

In addition to the electronic alignment of the $Cl(^2P_{3/2})$ photofragments, two studies have also probed the $K = 1$ orientation of both the $Cl(^2P_{3/2})$ and $Cl^*(^2P_{1/2})$ photofragments. The first such study by Kim *et al.* reported values of the coherent $\mathrm{Im}[a_1^{(1)}(\parallel, \perp)]$ parameter for the $Cl^*(^2P_{1/2})$ fragments following dissociation in the range $270 - 400$ nm using linearly polarised light [149]. The $\mathrm{Im}[a_1^{(1)}(\parallel, \perp)]$ parameter, which was believed to arise following interference between the parallel, $B\,^3\Pi_{0_u^+}$ state, and perpendicular, $C\,^1\Pi_{1u}$ state, pathways was shown to oscillate as a function of dissociation wavelength. The authors also reported measurements for the $^{37}Cl^*(^2P_{1/2})$ fragment, which show a phase shift in the $\mathrm{Im}[a_1^{(1)}(\parallel, \perp)]$ parameter due to a difference in the de Broglie wavelengths associated with the ^{35}Cl and ^{37}Cl isotopes [149]. The wavelength dependence of the experimental $\mathrm{Im}[a_1^{(1)}(\parallel, \perp)]$ pa-

	$Cl(^2P_{3/2})$		$Cl^*(^2P_{1/2})$	
Parameter	310[142]	330[142]	310[142, 149]	330[142, 149]
β	-1.0	-1.0	-0.64	0.24
α_1	0.07(1)	0.12(1)	-0.11	-0.08(5)
$\gamma_1^{'}$	-	-	-0.07	0.03

Table 4.3: Laboratory frame orientation parameters reported from previous studies by Kim *et al.* [149] and Alexander *et al.* [142]. Note that the authors used the values of the spatial anisotropy, β, from the work of Samartzis *et al.* [148] to calculate their orientation moments. Errors (1σ) in the final digit(s) are given in parenthesis where appropriate

rameters for the ^{35}Cl and ^{37}Cl isotopes were modelled theoretically, with qualitative agreement between experiment and theory observed.

In a separate study Alexander *et al.* used circularly polarised photolysis light to measure the incoherent orientation, $a_0^{(1)}(\perp)$, for the $Cl(^2P_{3/2})$ and $Cl^*(^2P_{1/2})$ fragments following dissociation at 310 and 330 nm [142]. The authors found that for the ground state product channel the measured $a_0^{(1)}(\perp)$ parameters were consistent with dissociation on the $C\,^1\Pi_{1u}$ state potential with a contribution arising from the $A\,^3\Pi_{1u}$ state due to a non-adiabatic transition between the two. A mechanism based on a small fraction of the excited $C\,^1\Pi_{1u}$ state molecules making a non-adiabatic transition to the $(3)^3\Sigma_{1u}^+$ state was necessary to explain the $Cl^*(^2P_{1/2})$ orientation. It was proposed that $\sim 67\,\%$ of $Cl^*(^2P_{1/2})$ atoms dissociate on the $(3)^3\Sigma_{1u}^+$ surface, while $\sim 21\,\%$ undergo a further non-adiabatic transition to the $(4)^3\Delta_{1u}$ state along the dissociation co-ordinate [142]. A summary of the previously measured laboratory and molecular frame $K = 1$ orientation moments is provided in Tables 4.3 and 4.4.

	$Cl(^2P_{3/2})$		$Cl^*(^2P_{1/2})$	
Parameter	310[142]	330[142]	310[142, 149]	330[142, 149]
β	-1.0	-1.0	-0.64	0.24
$a_0^{(1)}(\perp)$	0.13(2)	0.23(1)	-0.24	-0.26(17)
$\mathrm{Im}[a_1^{(1)}(\parallel, \perp)]$	-	-	0.1	0.03

Table 4.4: Molecular frame orientation parameters reported from previous studies by Kim *et al.* [149] and Alexander *et al.* [142]. Note that the authors used the values of the spatial anisotropy, β, from the work of Smaratzis *et al.* [148] to calculate their orientation moments. Errors (1σ) in the final digit(s) are given in parenthesis where appropriate

4.2.2 Theoretical studies

There have been several theoretical studies on the Cl_2 molecule over a period of around 30 years. In the following both the electronic structure theory and studies regarding the photodissociation dynamics are briefly reviewed.

In 1981 Peyerimhoff and Buenker computed the first *ab initio* curves for the Cl_2 molecule using a multi-reference configuration interaction method (MRD-CI) neglecting spin-orbit coupling [150]. Some 20 years later Asano and Yabushita performed the first of several studies including spin-orbit coupling [151], calculating all valence $\Omega = 0$ and 1 states. Also in 2001, Buenker *et al.* performed a multi-reference single and double excitation configuration study (MRD-CI) focussing on the low lying ion pair states [152]. More recently, Buenker *et al.* were able to calculate the valence states more accurately, including relativistic effects, allowing computation of the absorption spectrum and $Cl^*(^2P_{1/2})/Cl(^2P_{3/2})$ branching ratio, finding good agreement with the experimental data [51]. A relatively recent study by Macedo and Wong was able to compute all 23 adiabatic states correlating with the $Cl\,(^2P_J) + Cl\,(^2P_J)$ asymptote with spectroscopic properties in good agreement with experimental work [153].

Yabushita *et al.* used their $\Omega = 0$ and 1 potentials to perform a semi-classical calculation on the photodissociation with non-adiabatic interactions included *via* the Rosen-Zener-Demkov (RZD) model [151]. Their study was able to calculate the wavelength dependence of the spatial anisotropy parameter, β, as well as the $Cl^*(^2P_{1/2})/Cl(^2P_{3/2})$ branching ratio in good agreement with experimentally available data. Furthermore, using the Youngs double slits model [154, 155], Yabushita *et al.* calculated the coherent $Im[a_1^{(1)}(\parallel, \perp)]$ parameter for the $Cl^*(^2P_{1/2})$ photofragments. They were able to model the oscillatory nature of this parameter, both phase and magnitude, to be in good agreement with the experiments performed by Kim *et al.* [149]. The mechanistic origins of the $Im[a_1^{(1)}(\parallel, \perp)]$ parameter were described as due to an interference between the parallel $B\,^3\Pi_{0_u^+}$ and the perpendicular $(3)^3\Sigma_{1u}^+$ transitions with the latter state populated *via* a non-adiabatic transition from the $C\,^1\Pi_{1u}$ state, as calculated using the RZD model [151]. A more recent semi-classical study by Yabushita *et al.* in 2003 contrasted their Cl_2 results to the photodissociation of the heavier halogen molecule Br_2 [136]. In particular, it was found that non-adiabatic effects were much more important in Cl_2 than for the mostly adiabatic dissociation of the heavier Br_2.

The most recent, comprehensive study on Cl_2 photodissociation was performed by Johnsen *et al.* in 2010 [50]. The calculation, similar in spirit to those performed by Balint-Kurti *et al.* on the hydrogen halides [95, 101, 102], allowed the extraction of all dynamical information regarding the photodissociation, including angular momentum polarisation. The fully quantum mechanical time-dependent wavepacket treatment, the first undertaken on a system of this complexity, was performed on the set of *ab initio* potentials computed by Buenker *et al.* [51]. The calculation, in which non-adiabatic effects are implicitly included by transforming between diabatic and adiabatic bases, yielded an absorption cross section and wavelength dependent $Cl^*(^2P_{1/2})/Cl(^2P_{3/2})$ branching ratio in excellent agreement with experimental data. Generally good agreement was also found with the experimental β and angular momentum polarisation parameters, where available. Interestingly, the calculations

also predict higher order $K = 3$ orientation parameters to be important, particularly for the ground state product channel, however, no previous experimental data on these parameters was available.

Motivation

In spite of the extensive literature on Cl_2 photodissociation, the progressively increasing complexity of studies through the years, particularly those including atomic polarisation effects, mean that experiments continue to reveal surprising results on the dynamics of this *relatively* simple system. The experimental measurements of polarisation effects date over a period of several years, use a variety of different techniques and do not include any higher order $K = 3$ moments, therefore in order to stringently test the recent high level theory [50] a comprehensive set of experimental data has been collected over a range of dissociation wavelengths. The results of the current experimental study are compared with those from the dynamical calculation [50] in Section 4.3. Additionally, the recent theoretical work has been extended here to encompass the photodissociation of vibrationally excited chlorine molecules, with the results of these calculations presented along with the first experimental measurements on the photodissociation of Cl_2 ($v = 1$).

4.3 The $Cl(^2P_{3/2})$ fragment

4.3.1 Experimental results

Following photodissociation of Cl_2 at 355, 376, 384, 389, 398, 420, 450 and 470 nm, pump-probe images of the $Cl(^2P_{3/2})$ fragment were collected using two (2+1) REMPI transitions, $^2P_{1/2} \leftarrow {}^2P_{3/2}$ and $^2D_{5/2} \leftarrow {}^2P_{3/2}$ at 234.5 nm and 236.2 nm, respectively. The (2+1) REMPI transitions were chosen so as to be sensitive to all ranks, $K = 0 - 3$, of the electronic angular momentum distribution, as detailed in Tables 3.4 and 3.5. In general images were collected using a variety of pump-probe geometries using both linearly and circularly polarised pump and probe laser radiation, giving

a total of 16 ion images for each dissociation wavelength. For a particular photolysis wavelength, the Fourier moments extracted from all pump-probe geometries were fit globally allowing the extraction of the speed, angular and angular momentum distributions, as described in Section 3.5. The ion images, Fourier moments and fits to the data are shown in Figures 4.3 to 4.30. For the data collected at 450 nm the 45L and 45R geometries were of insufficient quality to be included in the global fit. For this wavelength the parameters γ_1', γ_3', and η_3 were not determined. At 420 nm the HH and HV geometries following ionisiation *via* the $^2D_{5/2}$ state were also not included. For 470 nm ion images were only recorded using linearly polarised pump and probe radiation, and at this wavelength only the even rank alignment parameters were determined. The data displayed over the following pages are shown in order of increasing photolysis wavelength. Speed distributions returned from the fits to the Cl($^2P_{3/2}$) Fourier moments are shown in Figure 4.31, and a complete list of β parameters and laboratory frame alignment and orientation parameters are provided in Tables 4.5 and 4.6.

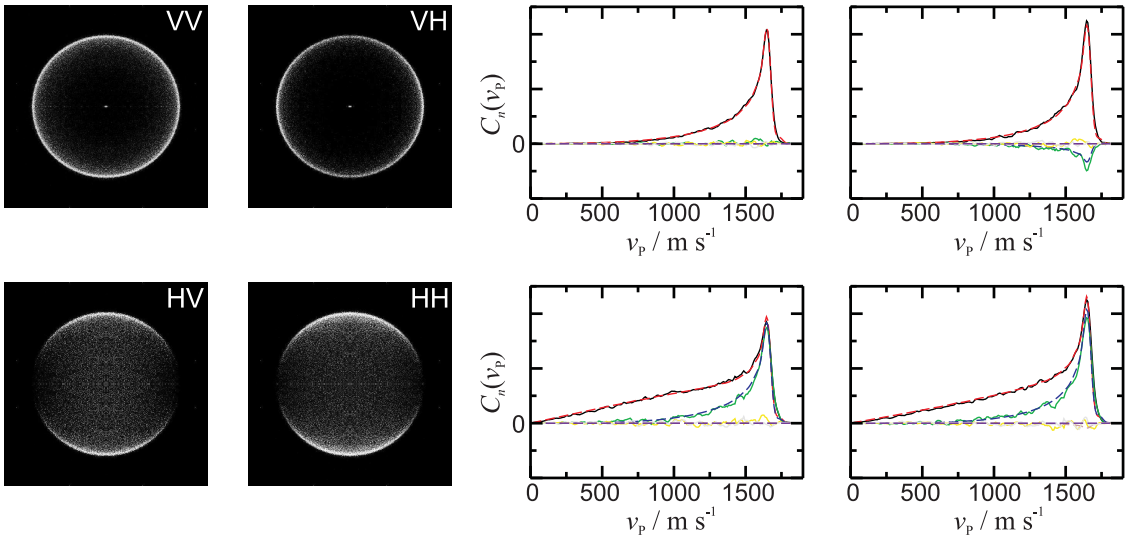

Figure 4.3: Cl($^2P_{3/2}$) ion images, Fourier moments (——) and fits (- - -) for linear geometries using the $^2P_{1/2}$ transition following photodissociation at 355 nm. The Fourier moments are colour coded, C_0 (black), C_2 (green), C_4 (yellow), C_6 (grey).

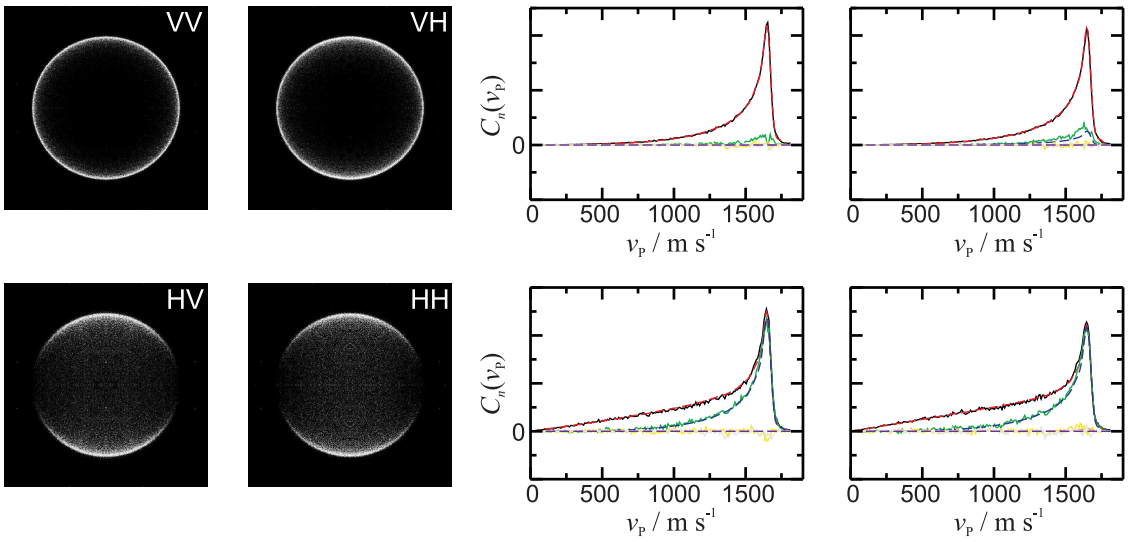

Figure 4.4: Cl($^2P_{3/2}$) ion images, Fourier moments (——) and fits (- - -) for linear geometries using the $^2D_{5/2}$ transition following photodissociation at 355 nm. The Fourier moments are colour coded, C_0 (black), C_2 (green), C_4 (yellow), C_6 (grey).

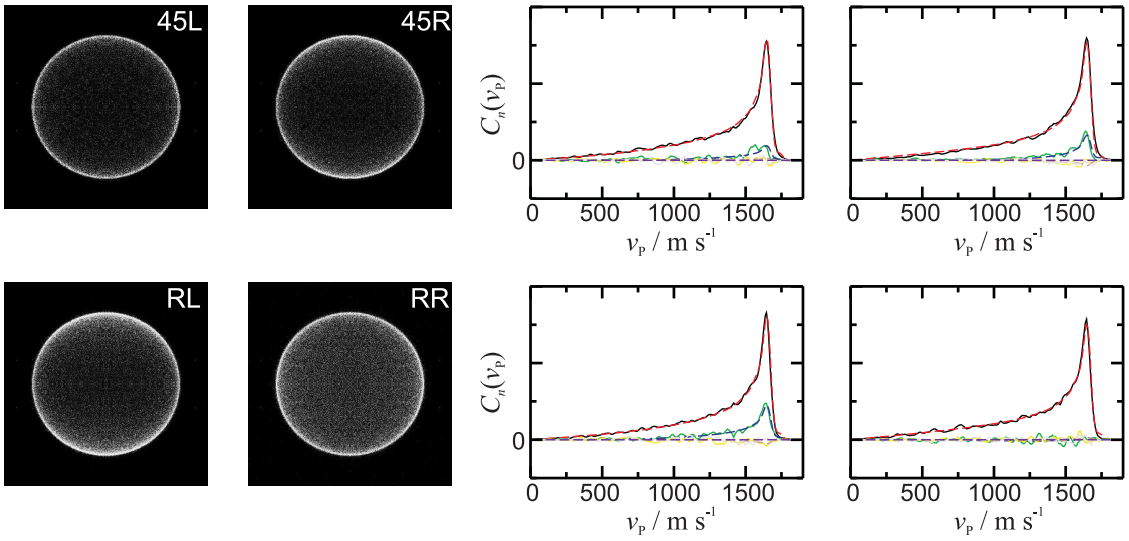

Figure 4.5: Cl($^2P_{3/2}$) ion images, Fourier moments (——) and fits (- - -) for circular geometries using the $^2P_{1/2}$ transition following photodissociation at 355 nm. The Fourier moments are colour coded, C_0 (black), C_2 (green), C_4 (yellow), C_6 (grey).

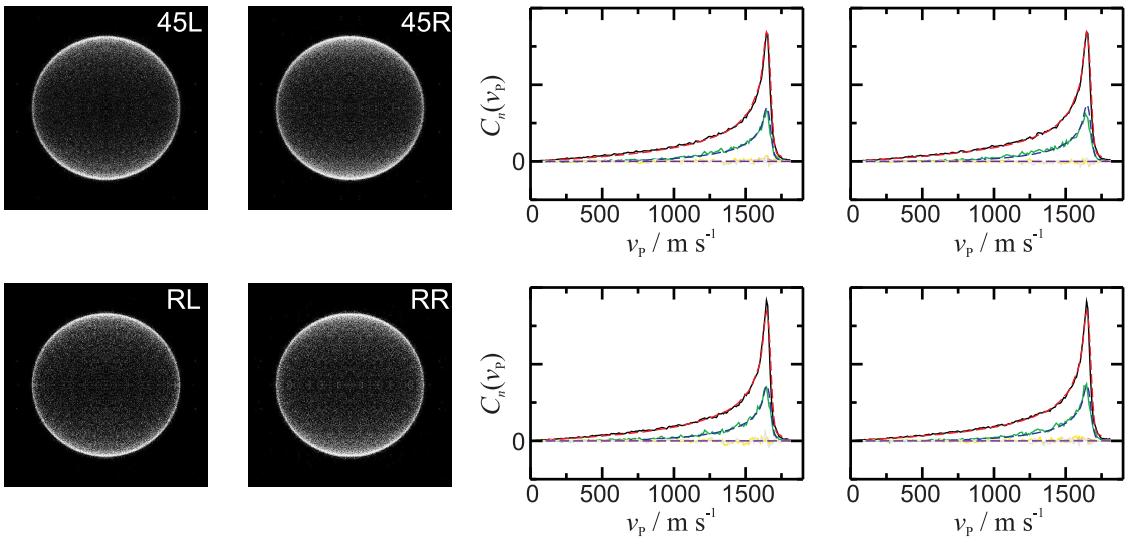

Figure 4.6: Cl($^2P_{3/2}$) ion images, Fourier moments (——) and fits (- - -) for circular geometries using the $^2D_{5/2}$ transition following photodissociation at 355 nm. The Fourier moments are colour coded, C_0 (black), C_2 (green), C_4 (yellow), C_6 (grey).

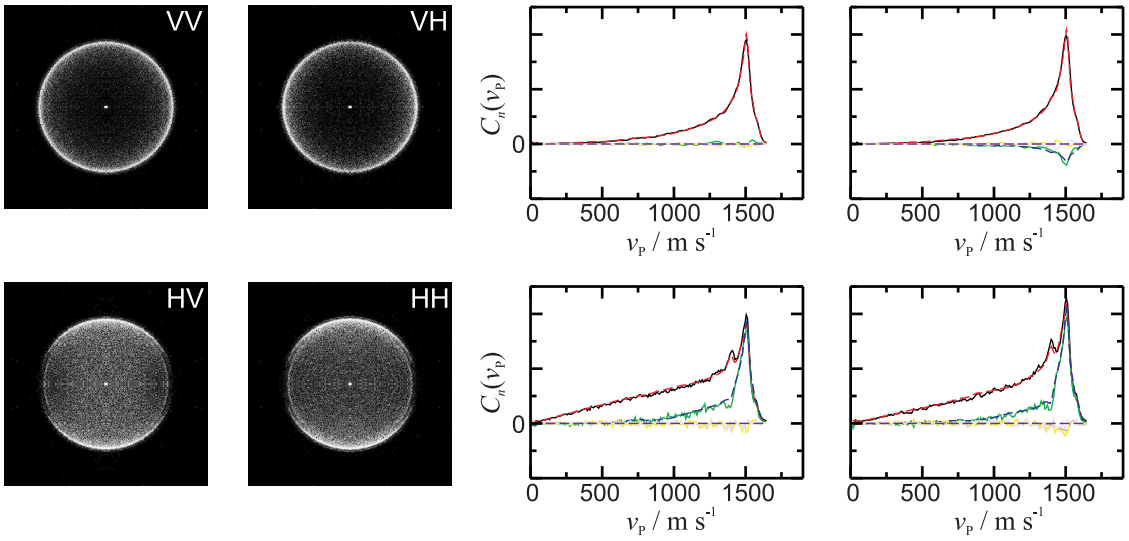

Figure 4.7: Cl($^2P_{3/2}$) ion images, Fourier moments (——) and fits (- - -) for linear geometries using the $^2P_{1/2}$ transition following photodissociation at 376 nm. The Fourier moments are colour coded, C_0 (black), C_2 (green), C_4 (yellow), C_6 (grey).

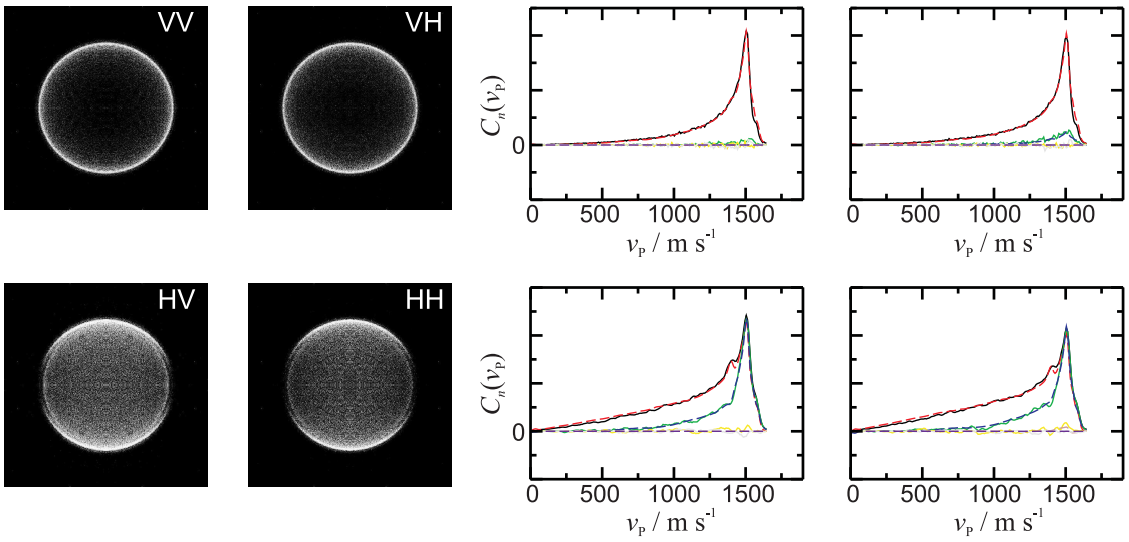

Figure 4.8: Cl($^2P_{3/2}$) ion images, Fourier moments (——) and fits (- - -) for linear geometries using the $^2D_{5/2}$ transition following photodissociation at 376 nm. The Fourier moments are colour coded, C_0 (black), C_2 (green), C_4 (yellow), C_6 (grey).

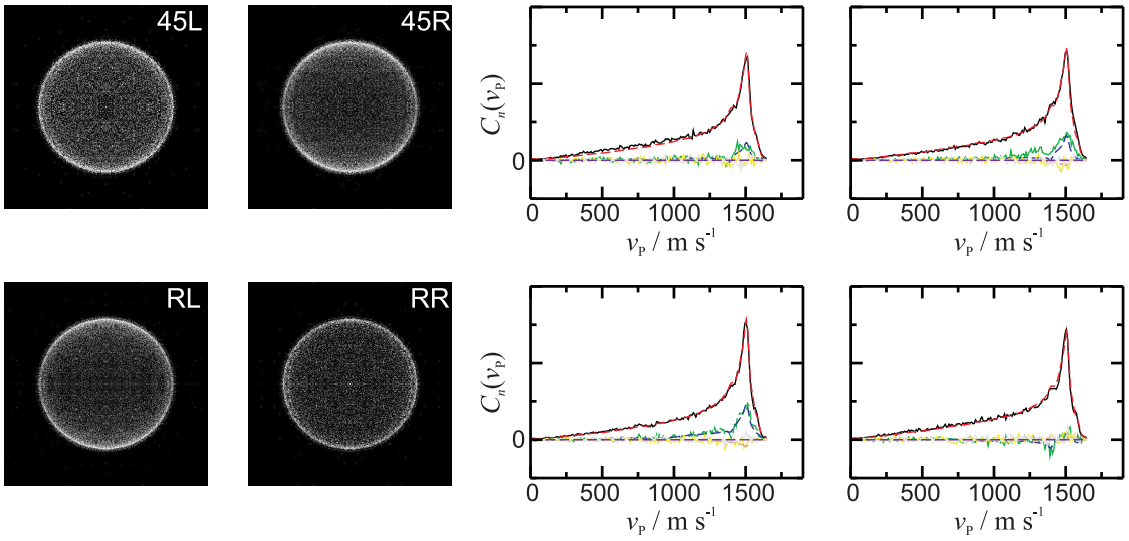

Figure 4.9: Cl($^2P_{3/2}$) ion images, Fourier moments (——) and fits (- - -) for circular geometries using the $^2P_{1/2}$ transition following photodissociation at 376 nm. The Fourier moments are colour coded, C_0 (black), C_2 (green), C_4 (yellow), C_6 (grey).

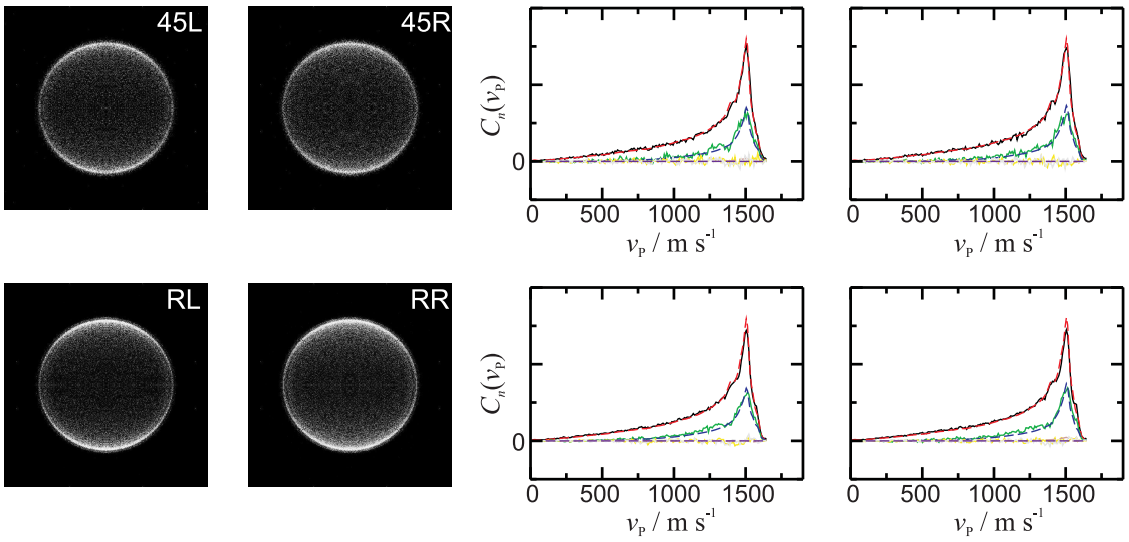

Figure 4.10: Cl($^2P_{3/2}$) ion images, Fourier moments (——) and fits (- - -) for circular geometries using the $^2D_{5/2}$ transition following photodissociation at 376 nm. The Fourier moments are colour coded, C_0 (black), C_2 (green), C_4 (yellow), C_6 (grey).

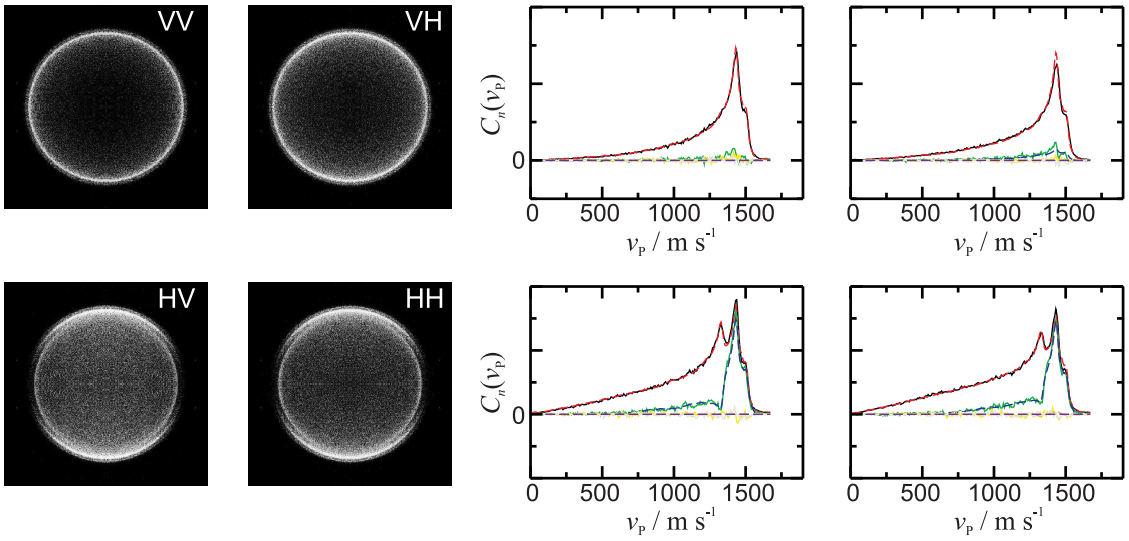

Figure 4.11: Cl($^2P_{3/2}$) ion images, Fourier moments (——) and fits (- - -) for linear geometries using the $^2D_{5/2}$ transition following photodissociation at 384 nm. The Fourier moments are colour coded, C_0 (black), C_2 (green), C_4 (yellow), C_6 (grey).

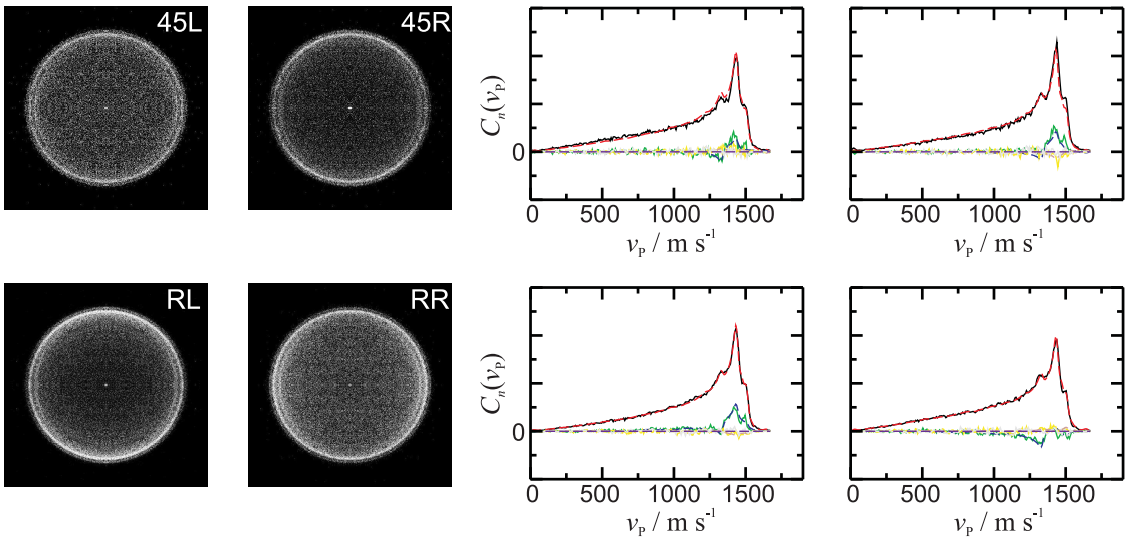

Figure 4.12: Cl($^2P_{3/2}$) ion images, Fourier moments (——) and fits (- - -) for circular geometries using the $^2P_{1/2}$ transition following photodissociation at 384 nm. The Fourier moments are colour coded, C_0 (black), C_2 (green), C_4 (yellow), C_6 (grey).

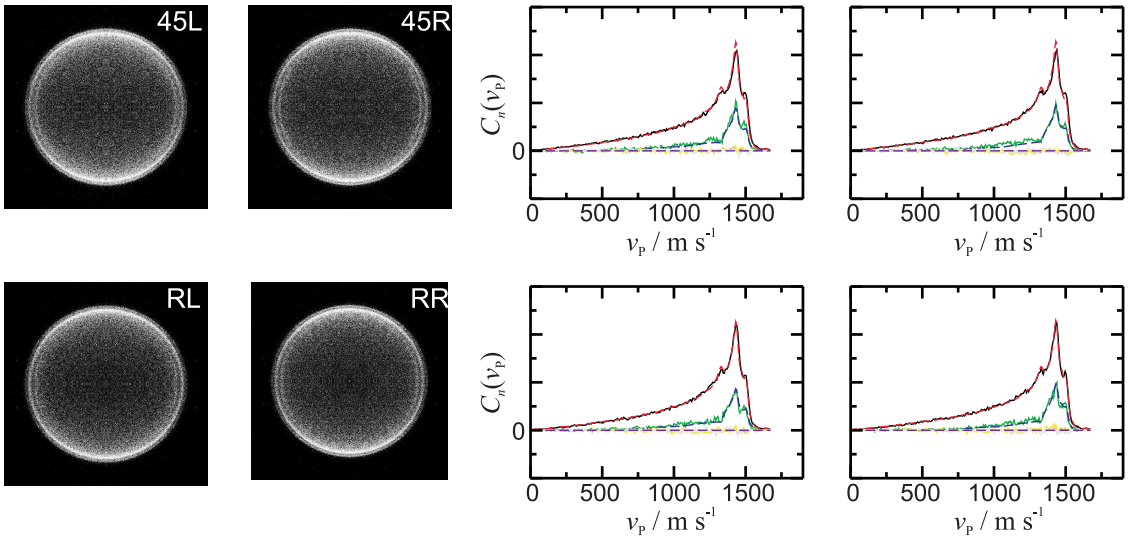

Figure 4.13: Cl($^2P_{3/2}$) ion images, Fourier moments (——) and fits (- - -) for linear geometries using the $^2D_{5/2}$ transition following photodissociation at 384 nm. The Fourier moments are colour coded, C_0 (black), C_2 (green), C_4 (yellow), C_6 (grey).

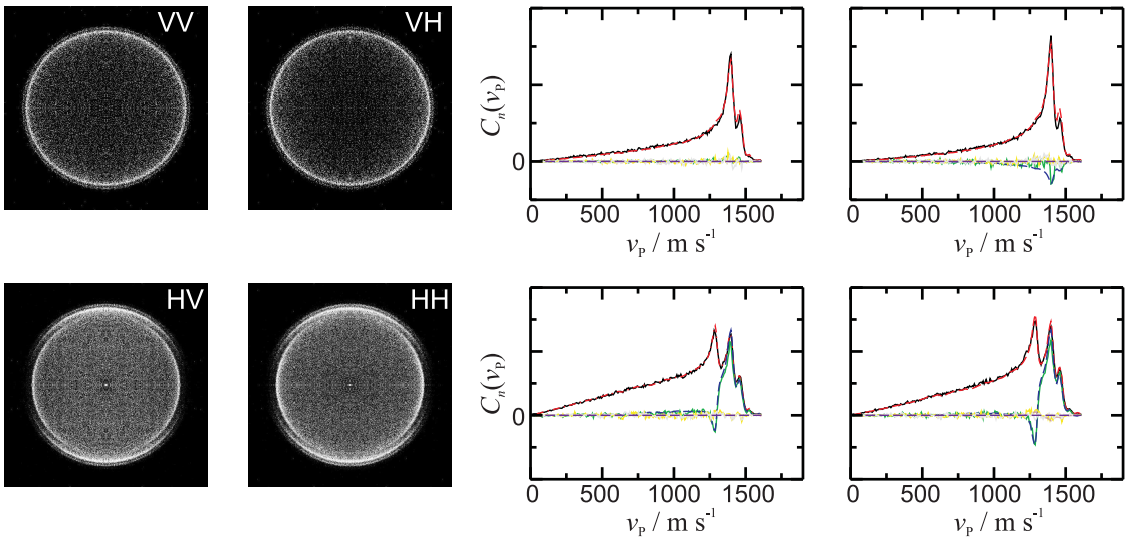

Figure 4.14: Cl($^2P_{3/2}$) ion images, Fourier moments (——) and fits (- - -) for linear geometries using the $^2P_{1/2}$ transition following photodissociation at 389 nm. The Fourier moments are colour coded, C_0 (black), C_2 (green), C_4 (yellow), C_6 (grey).

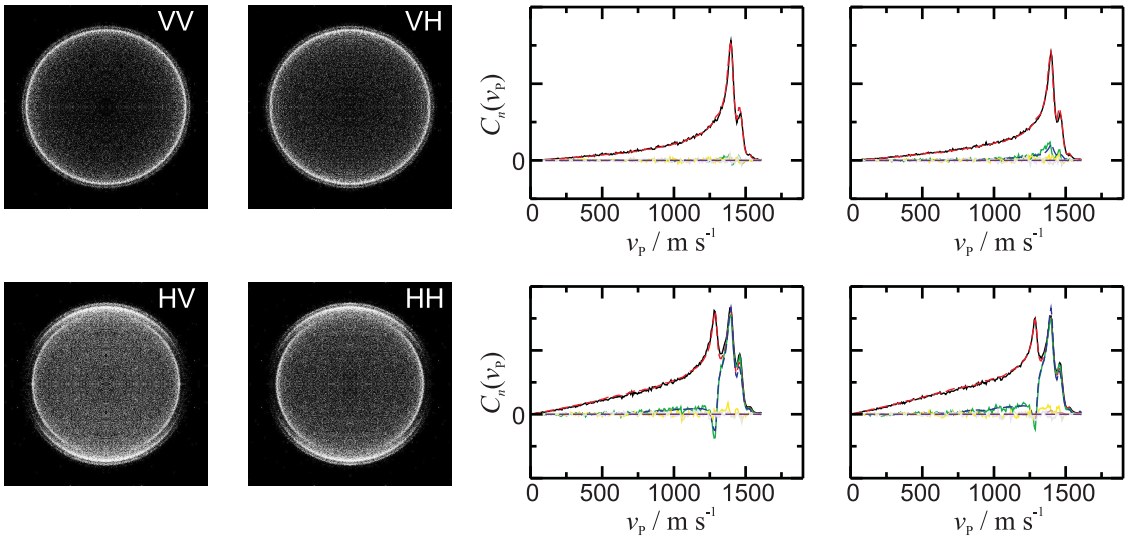

Figure 4.15: Cl($^2P_{3/2}$) ion images, Fourier moments (——) and fits (- - -) for linear geometries using the $^2D_{5/2}$ transition following photodissociation at 389 nm. The Fourier moments are colour coded, C_0 (black), C_2 (green), C_4 (yellow), C_6 (grey).

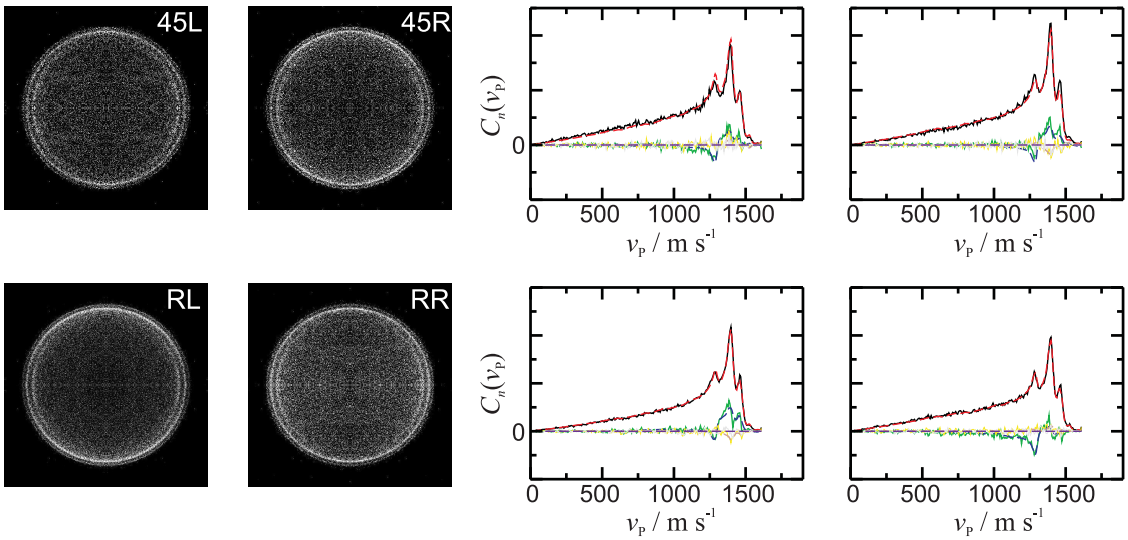

Figure 4.16: Cl($^2P_{3/2}$) ion images, Fourier moments (——) and fits (- - -) for circular geometries using the $^2P_{1/2}$ transition following photodissociation at 389 nm. The Fourier moments are colour coded, C_0 (black), C_2 (green), C_4 (yellow), C_6 (grey).

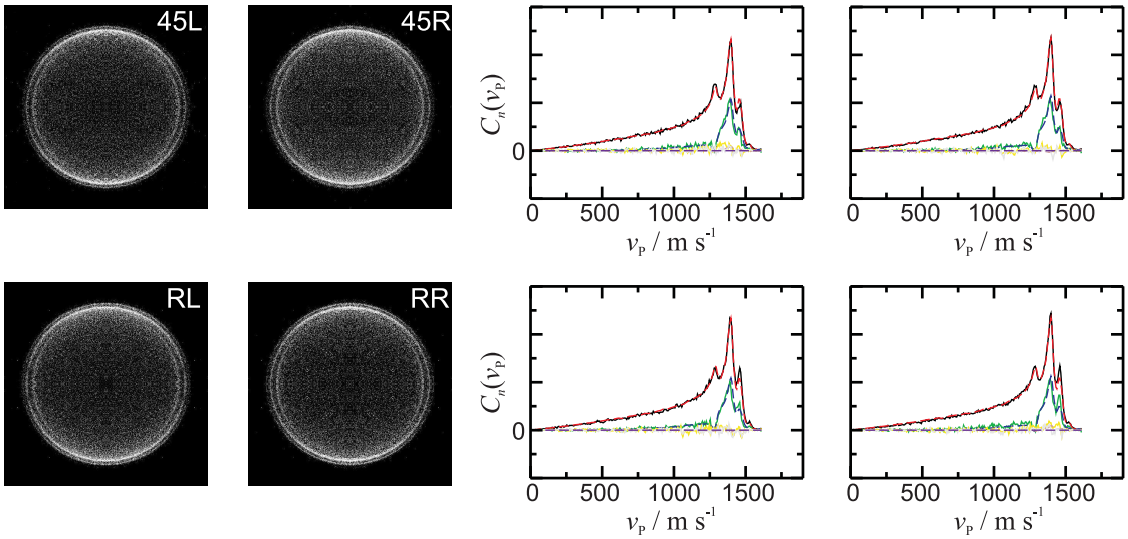

Figure 4.17: Cl($^2P_{3/2}$) ion images, Fourier moments (——) and fits (- - -) for circular geometries using the $^2D_{5/2}$ transition following photodissociation at 389 nm. The Fourier moments are colour coded, C_0 (black), C_2 (green), C_4 (yellow), C_6 (grey).

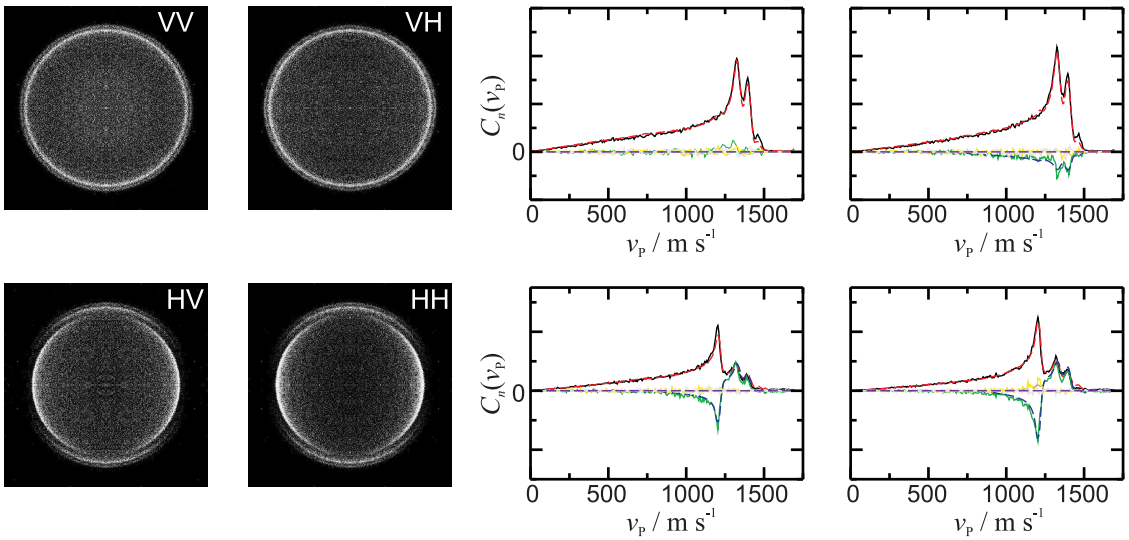

Figure 4.18: Cl($^2P_{3/2}$) ion images, Fourier moments (——) and fits (- - -) for linear geometries using the $^2P_{1/2}$ transition following photodissociation at 398 nm. The Fourier moments are colour coded, C_0 (black), C_2 (green), C_4 (yellow), C_6 (grey).

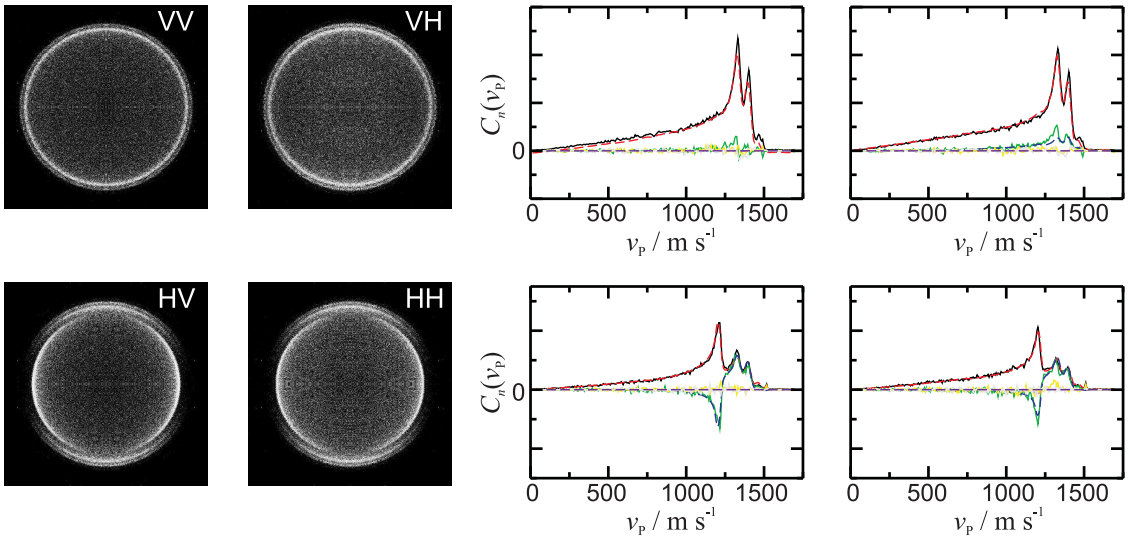

Figure 4.19: Cl($^2P_{3/2}$) ion images, Fourier moments (——) and fits (- - -) for linear geometries using the $^2D_{5/2}$ transition following photodissociation at 398 nm. The Fourier moments are colour coded, C_0 (black), C_2 (green), C_4 (yellow), C_6 (grey).

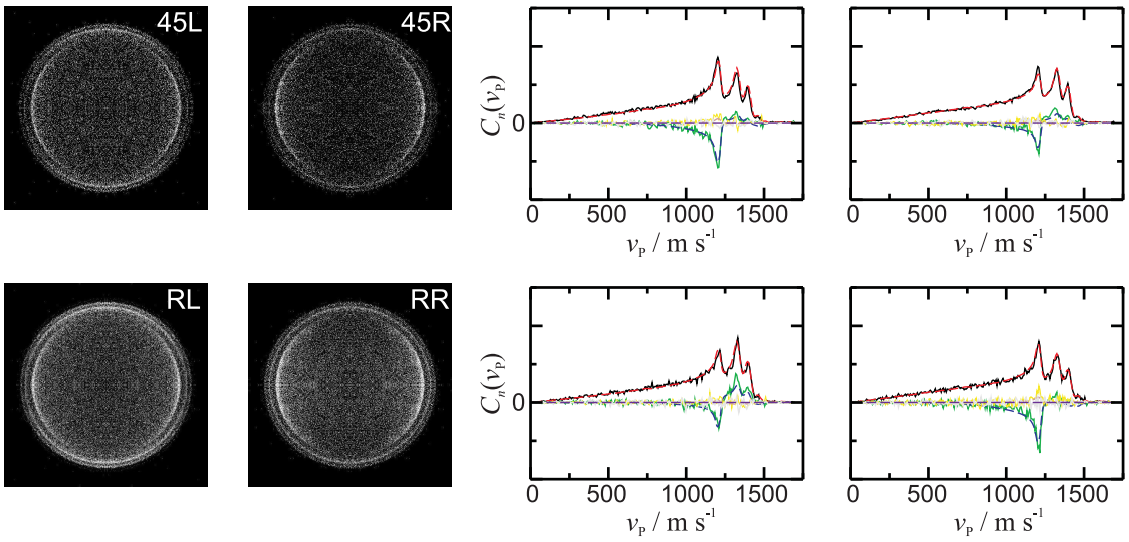

Figure 4.20: Cl($^2P_{3/2}$) ion images, Fourier moments (——) and fits (- - -) for circular geometries using the $^2P_{1/2}$ transition following photodissociation at 398 nm. The Fourier moments are colour coded, C_0 (black), C_2 (green), C_4 (yellow), C_6 (grey).

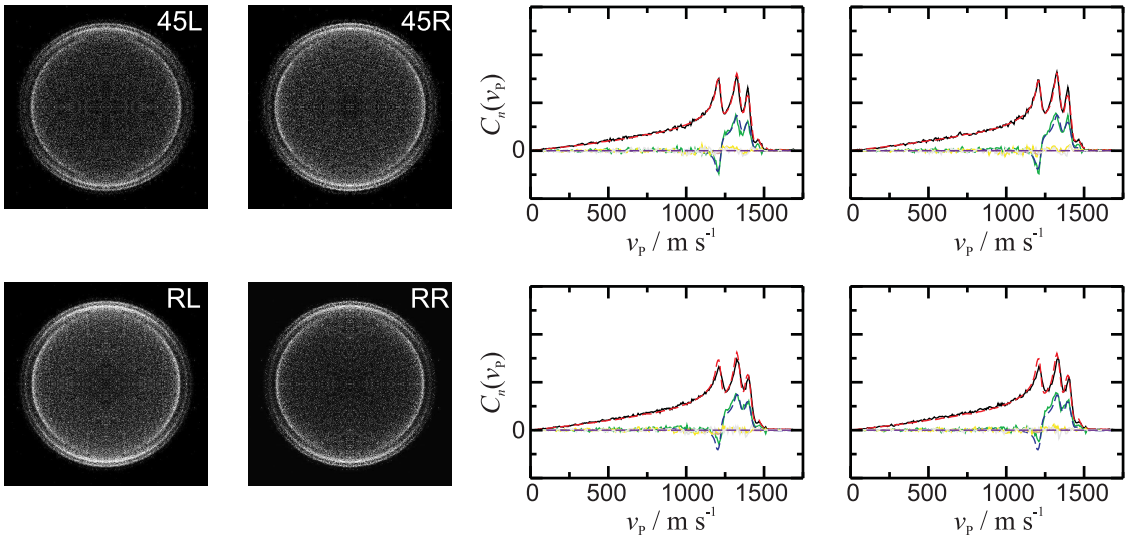

Figure 4.21: Cl($^2P_{3/2}$) ion images, Fourier moments (——) and fits (- - -) for circular geometries using the $^2D_{5/2}$ transition following photodissociation at 398 nm. The Fourier moments are colour coded, C_0 (black), C_2 (green), C_4 (yellow), C_6 (grey).

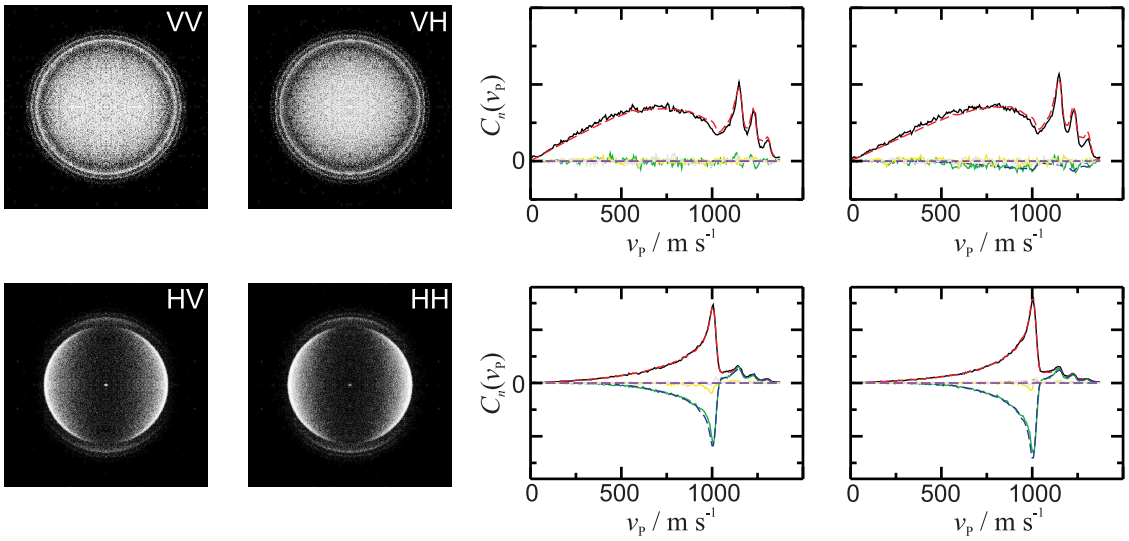

Figure 4.22: Cl($^2P_{3/2}$) ion images, Fourier moments (——) and fits (- - -) for linear geometries using the $^2P_{1/2}$ transition following photodissociation at 420 nm. The Fourier moments are colour coded, C_0 (black), C_2 (green), C_4 (yellow), C_6 (grey).

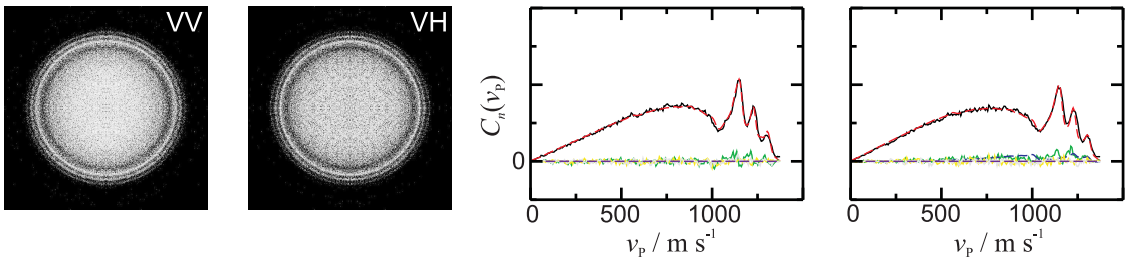

Figure 4.23: Cl($^2P_{3/2}$) ion images, Fourier moments (——) and fits (- - -) for linear geometries using the $^2D_{5/2}$ transition following photodissociation at 420 nm. The Fourier moments are colour coded, C_0 (black), C_2 (green), C_4 (yellow), C_6 (grey).

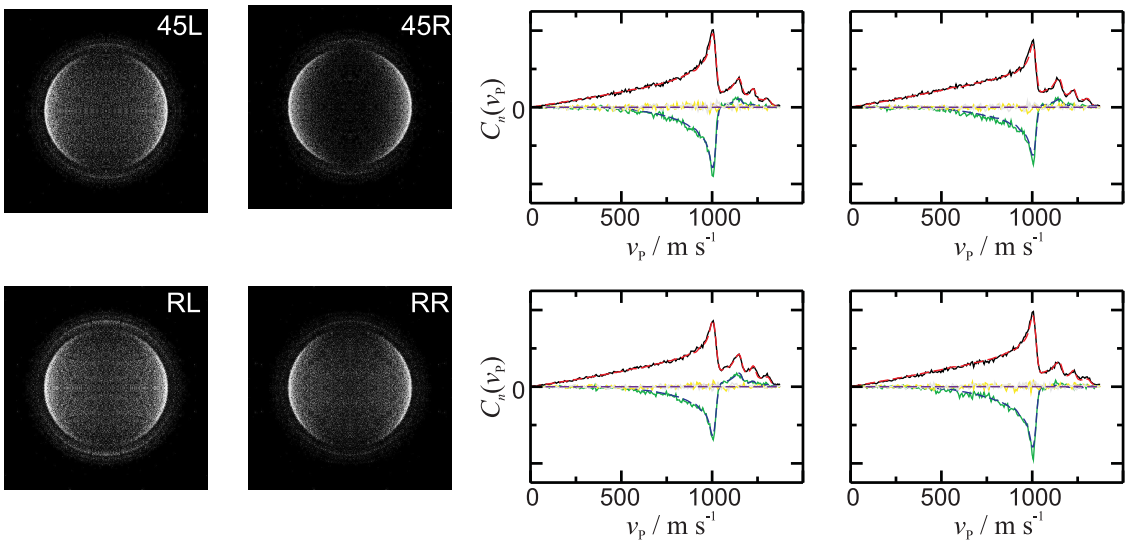

Figure 4.24: Cl($^2P_{3/2}$) ion images, Fourier moments (——) and fits (- - -) for circular geometries using the $^2P_{1/2}$ transition following photodissociation at 420 nm. The Fourier moments are colour coded, C_0 (black), C_2 (green), C_4 (yellow), C_6 (grey).

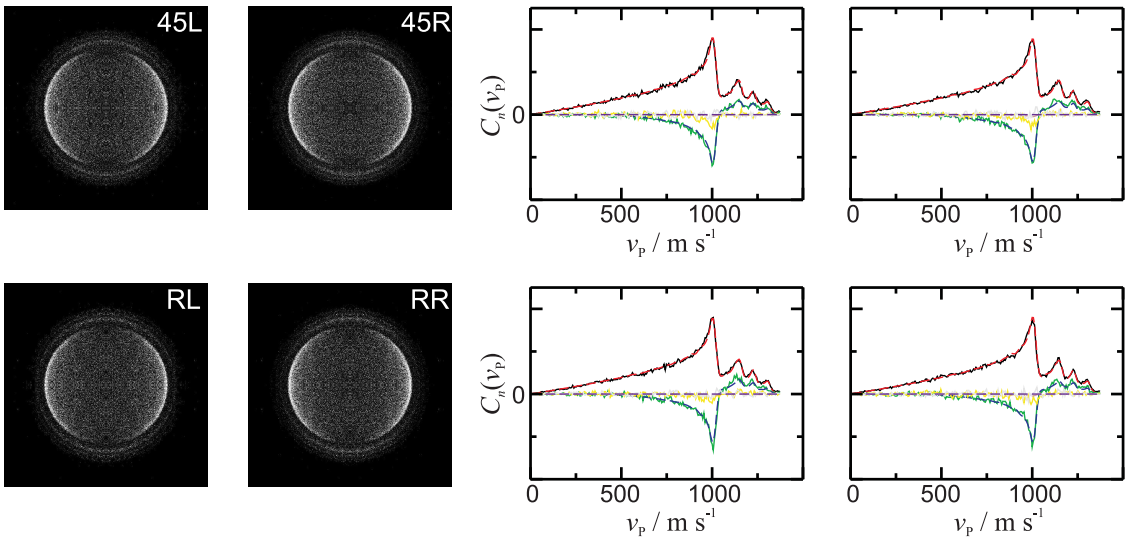

Figure 4.25: Cl($^2P_{3/2}$) ion images, Fourier moments (——) and fits (- - -) for circular geometries using the $^2D_{5/2}$ transition following photodissociation at 420 nm. The Fourier moments are colour coded, C_0 (black), C_2 (green), C_4 (yellow), C_6 (grey).

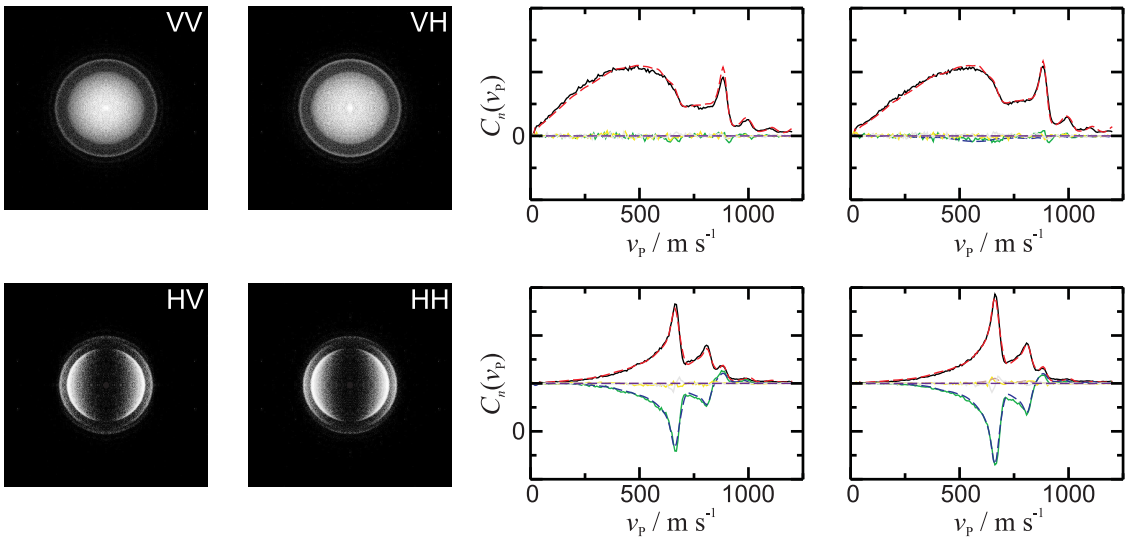

Figure 4.26: Cl($^2P_{3/2}$) ion images, Fourier moments (——) and fits (- - -) for linear geometries using the $^2P_{1/2}$ transition following photodissociation at 450 nm. The Fourier moments are colour coded, C_0 (black), C_2 (green), C_4 (yellow), C_6 (grey).

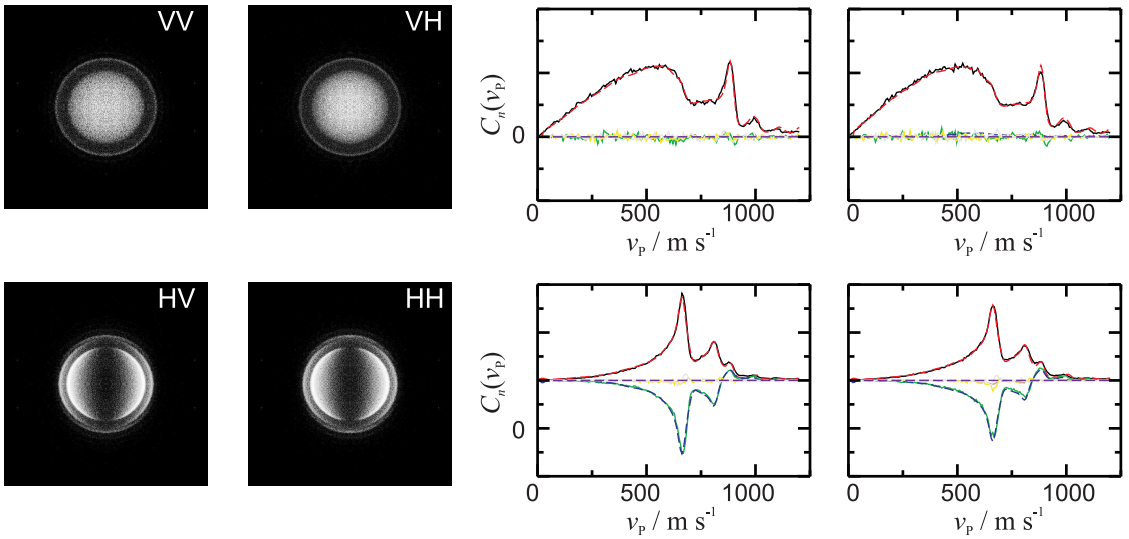

Figure 4.27: Cl($^2P_{3/2}$) ion images, Fourier moments (——) and fits (- - -) for linear geometries using the $^2D_{5/2}$ transition following photodissociation at 450 nm. The Fourier moments are colour coded, C_0 (black), C_2 (green), C_4 (yellow), C_6 (grey).

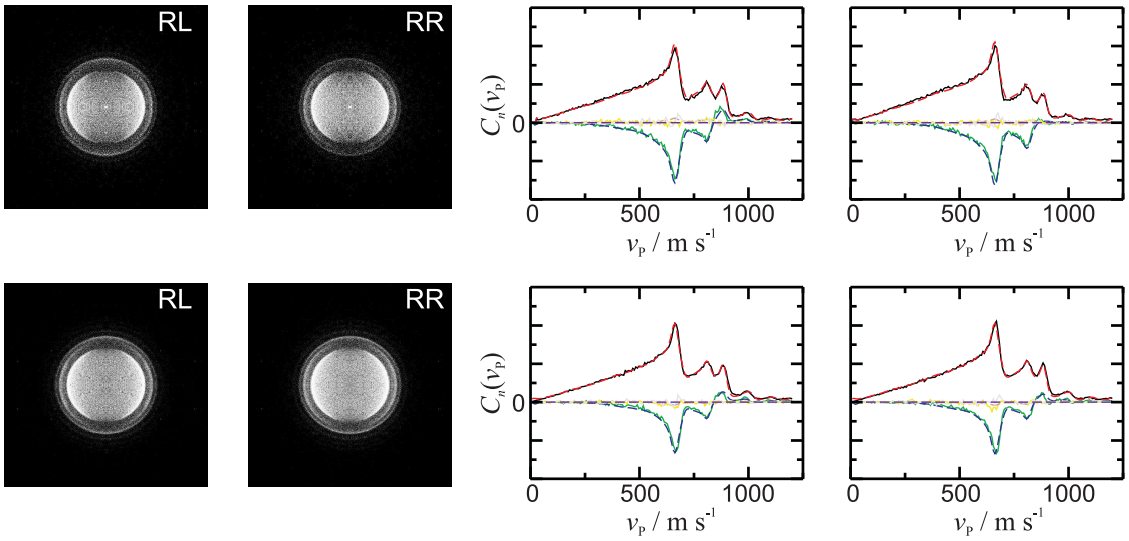

Figure 4.28: Cl($^2P_{3/2}$) ion images, Fourier moments (——) and fits (- - -) for circular geometries using the $^2P_{1/2}$ transition (top) and the $^2D_{5/2}$ transition (bottom) following photodissociation at 450 nm. The Fourier moments are colour coded, C_0 (black), C_2 (green), C_4 (yellow), C_6 (grey).

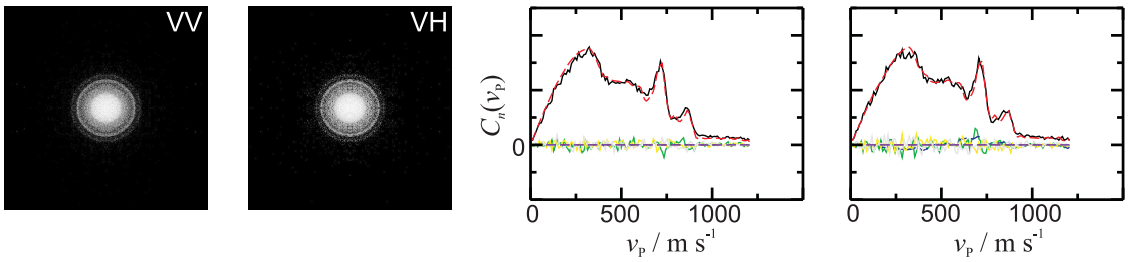

Figure 4.29: Cl($^2P_{3/2}$) ion images, Fourier moments (——) and fits (- - -) for circular geometries using the $^2P_{1/2}$ transition following photodissociation at 470 nm. The Fourier moments are colour coded, C_0 (black), C_2 (green), C_4 (yellow), C_6 (grey).

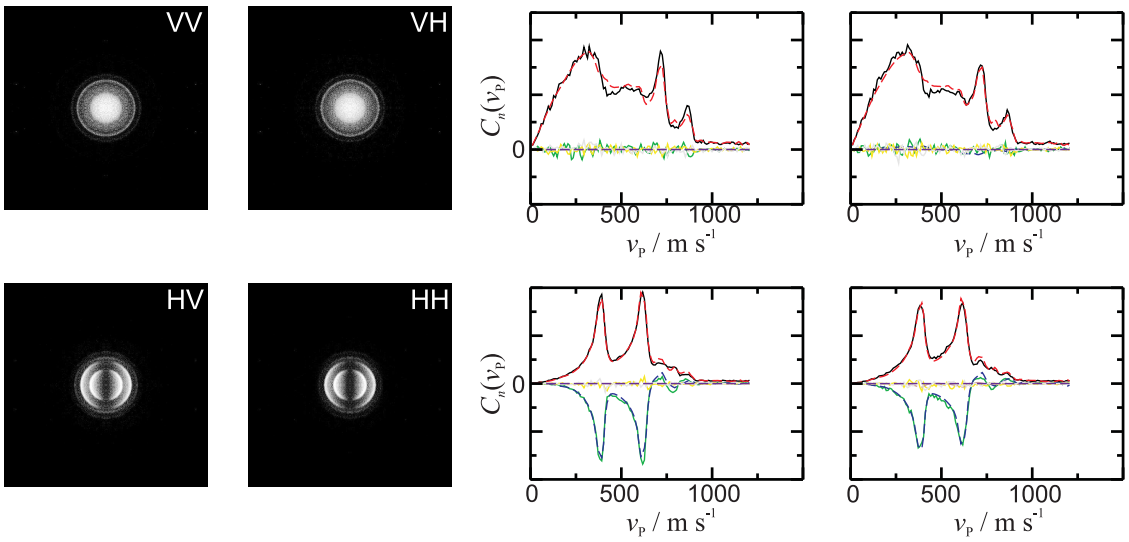

Figure 4.30: Cl(^{2}P$_{3/2}$) ion images, Fourier moments (——) and fits (- - -) for circular geometries using the ^{2}D$_{5/2}$ transition following photodissociation at 470 nm. The Fourier moments are colour coded, C_0 (black), C_2 (green), C_4 (yellow), C_6 (grey).

4.3.2 Discussion

As discussed in Section 1.3 angular momentum polarisation effects can be observed through the differences between ion images collected with the same pump laser polarisation but different probe polarisation. Following photodissociation at 355 nm a single feature is observed in the ion images corresponding to production of the ground state product channel, Cl(^{2}P$_{3/2}$) + Cl(^{2}P$_{3/2}$). The alignment can clearly be seen here by comparison of the isotropic VV geometry with that obtained in a VH geometry, which for the ^{2}P$_{1/2}$ REMPI transition has more intensity at the 'sides' of the image, see Figure 4.3. For the ^{2}D$_{5/2}$ transition, more intensity is seen at the top and bottom of the image, see Figure 4.4. The reason for this effect is due to the linestrength parameters, $\tilde{P}_2$, having opposite signs for the two REMPI transitions, as detailed in Tables 3.4 and 3.5. The electronic orientation can also be clearly seen by inspection of the RL and RR geometries collected *via* the ^{2}P$_{1/2}$ transition. For the ^{2}D$_{5/2}$ transition, which is less sensitive to the orientation, much smaller differences are observed. It should also be noted that, due to the hyperfine

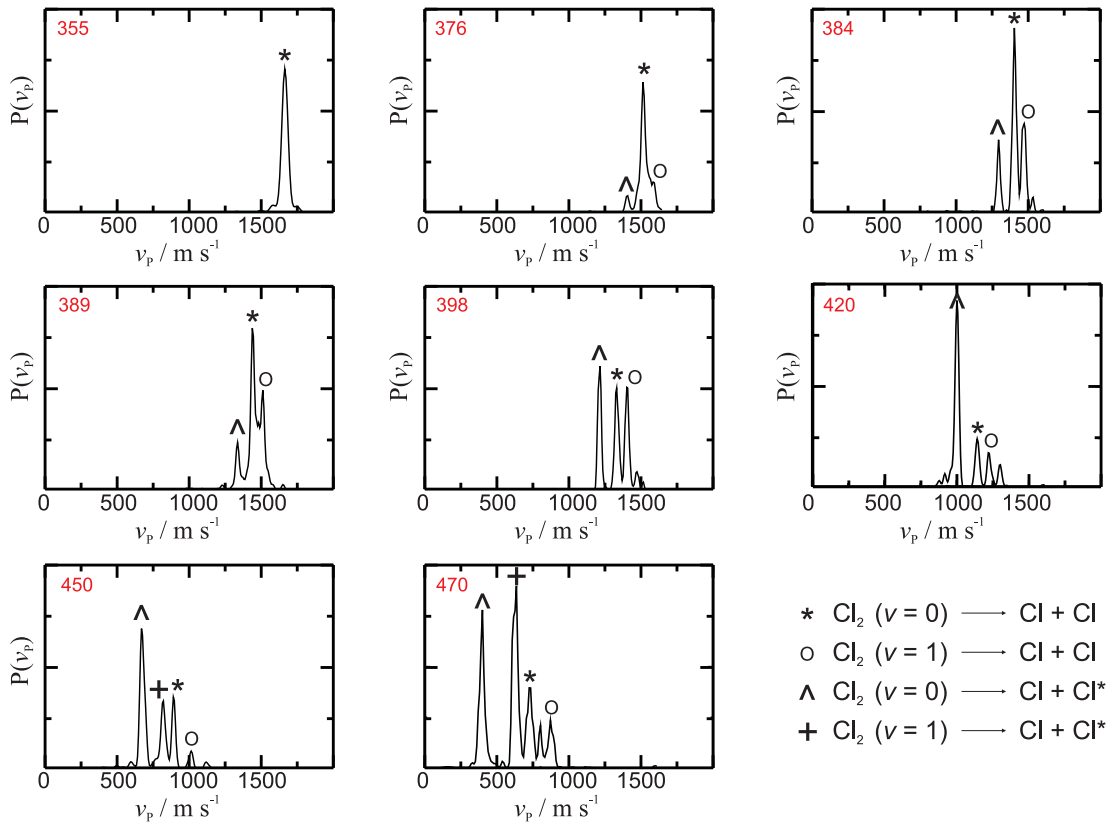

Figure 4.31: Speed distributions, $P(v_P)$, for the $Cl(^2P_{3/2})$ fragments returned from the fits to the experimental Fourier moments. Data shown for wavelengths $355 - 470$ nm.

depolarisation, the experimentally observed alignment will be implicity less than the orientation ($K = 1$) since the alignment ($K = 2$) is more depolarised by coupling to the nuclear spin, $g^{(1)} = 0.5$ vs $g^{(2)} = 0.27$ [52], as detailed in Section 3.5.

The speed distributions returned from the fits to the experimental data are shown in Figure 4.31. At short wavelengths, 355 nm, only one feature is seen in the ion images, which corresponds to the formation of $Cl(^2P_{3/2}) + Cl(^2P_{3/2})$. As the wavelength increases multiple features arise, corresponding to dissociation in both the $Cl(^2P_{3/2}) + Cl(^2P_{3/2})$ and $Cl(^2P_{3/2}) + Cl^*(^2P_{1/2})$ product channels. Furthermore, additional signal from the photodissociation of vibrationally excited parent molecules, $v = 1$, is observed for both product channels, with these results discussed in Section 4.5. At two of the shorter wavelengths, 376 nm and 384 nm, the angu-

lar distributions and polarisation data for the weak excited state product channel could not be reliably extracted from the experimental data. For these wavelengths the ground and excited state product channels are incompletely resolved in the ion images with the intensity dominated by signal arising from the photodissociation into $Cl(^2P_{3/2}) + Cl(^2P_{3/2})$.

Cl*($^2P_{1/2}$)/Cl($^2P_{3/2}$) branching ratio and β

The Cl*($^2P_{1/2}$)/Cl($^2P_{3/2}$) branching ratio has been defined previously as [51]

$$Cl^*/Cl = \frac{\sigma_{Cl^*}}{\sigma_{Cl^*} + 2\sigma_{Cl}}, \tag{4.1}$$

where σ_{Cl^*} and σ_{Cl} represent the sum of the partial cross sections relevant to the ground and excited state product channels, respectively. The factor of two in the denominator arises since two Cl($^2P_{3/2}$) atoms are formed in the ground state channel whereas only one is formed in the excited state channel. The experimental data, as determined from the intensities of the different features seen in the ion images, is shown in Figure 4.32(a) along with the results of the recent theoretical work [50]. Excellent agreement is seen with the previous experimental data from Samartzis *et al.* [148] and the theoretical calculation [50]. The excited state product channel, $Cl(^2P_{3/2}) + Cl^*(^2P_{1/2})$, is shown to become important at wavelengths > 370 nm, and dominates the absorption beyond 400 nm.

Also shown in Figure 4.32 are the spatial anisotropy parameters, β, for dissociation into the two product channels. The measured β parameters for the excited state product channel decrease from a close to limiting parallel transition, $\beta = 1.98$, at long wavelengths to 1.82 at 355 nm, reflecting the mixed nature of the transition in this region. Reassuringly, the β values obtained from measurements of both the Cl($^2P_{3/2}$) and Cl*($^2P_{1/2}$) fragments, at the same wavelength, lie within experimental error of one another. For this channel, measurements made here, Figure 4.32(b), agree quite well with those previously made by Samartzis *et al.* [145]. However, there seems to be a discrepancy in wavelength between the experimental values and

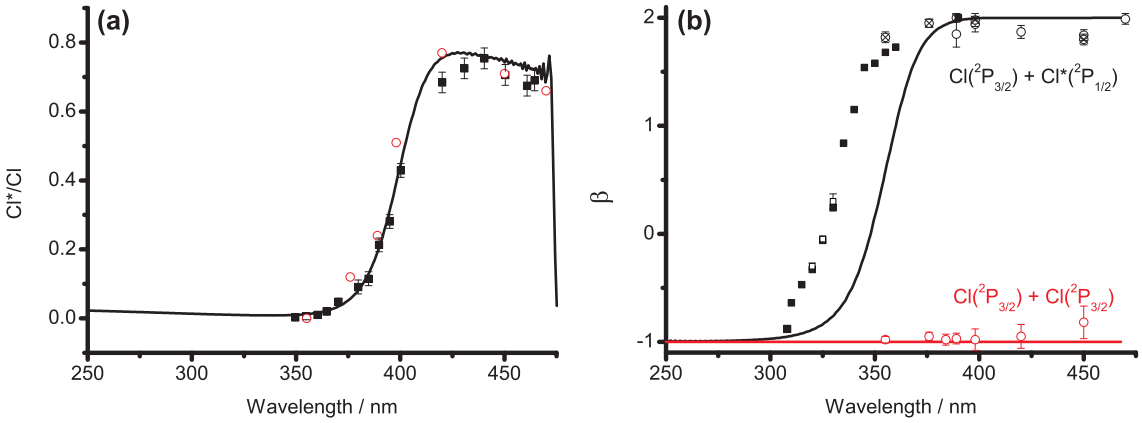

Figure 4.32: **(a)** $Cl^*(^2P_{1/2})/Cl(^2P_{3/2})$ branching ratio determined from theoretical work (——) [50] and compared with experimental data (circles) and the previous results of Samartzis *et al.* (squares) [148]. **(b)** Spatial anisotropy parameter, β, determined from theoretical work (——) for both product channels [50]. Values returned from fits to experimental data represented by circles. Open and crossed circles refer to the $Cl(^2P_{3/2})$ and $Cl^*(^2P_{1/2})$ results, respectively. Previous measurements by Samartzis *et al.* [148] and Ritchie and co-workers [156] represented by solid and open squares, respectively.

theory. This is perhaps surprising since theory seems to reproduce the branching ratio, $Cl^*(^2P_{1/2})/Cl(^2P_{3/2})$, very well. Interestingly, the β parameter determined experimentally reaches a maximum limiting value near 400 nm then decreases somewhat, giving $\beta \sim 1.8$ at 450 nm, confirmed by measurements of both the $Cl(^2P_{3/2})$ and $Cl^*(^2P_{1/2})$ fragments, see Figure 4.32(b). By 470 nm the spatial anisotropy parameter again approaches the limiting value for a pure parallel transition. The possible reasons for these discrepancies between experiment and theory are discussed in Section 4.7 with a view to future work. For the ground state product channel the experimental data is consistent with a wavelength independent $\beta = -1$. The low values of β measured here imply a low rotational temperature of the molecular beam < 10 K.

At long wavelengths the dissociation to give excited state products is believed to arise following an adiabatic dissociation on the $B\,^3\Pi_{0_u^+}$ state potential, resulting in $\beta = 2$. As one moves to shorter wavelengths, however, the excited state channel develops perpendicular character and a sharp reduction in β is seen. Since more

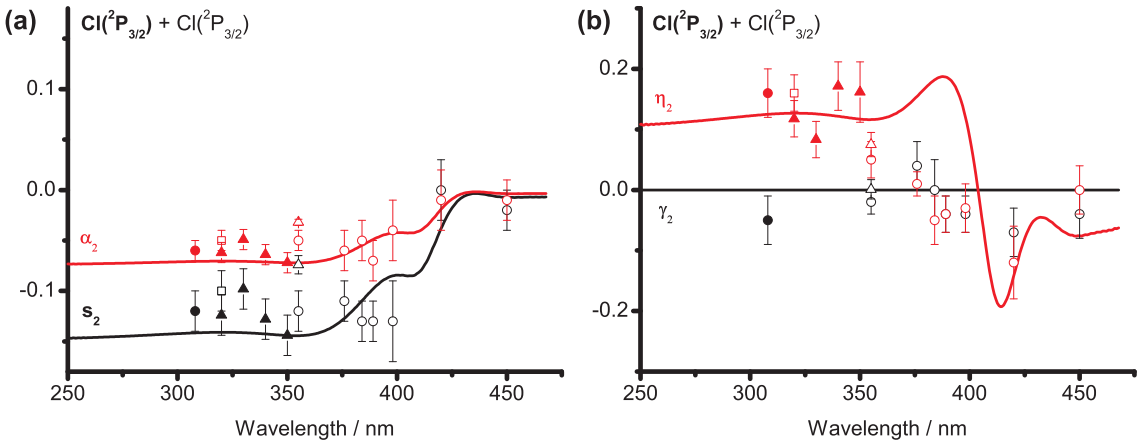

Figure 4.33: Incoherent **(a)** and coherent **(b)** $K = 2$ alignment parameters for the $Cl(^2P_{3/2}) + Cl(^2P_{3/2})$ channel returned from fits to the $Cl(^2P_{3/2})$ Fourier moments. Experimental data represented by open circles and compared to the recent quantum calculation (——) [50]. Previous measurements by Brouard and co-workers at 308 nm (solid circles) [61], Zare and co-workers at 320 nm (squares) [78], Ritchie and co-workers from 320 to 350 nm (solid triangles) [156], and Bracker *et al.* at 355 nm (open triangles) [63] also shown.

than one $\Omega = 1$ state correlates with this channel, measurements of β alone are unable to unravel the subtle mechanism resulting in the formation of these products. Likewise, measurements for the ground state product channel, where $\beta = -1$ across the absorption band, are unable to distinguish which of the $\Omega = 1$ symmetry states are ultimately responsible for dissociation.

$Cl(^2P_{3/2})$ alignment in the $Cl(^2P_{3/2}) + Cl(^2P_{3/2})$ channel

The incoherent alignment parameters s_2 and α_2 returned from the fits to the data are shown in Figure 4.33(a) and compared to the theoretical calculation [50]. The theory predicts that $s_2 = 2\alpha_2$ at all dissociation wavelengths, as expected for a purely perpendicular dissociation channel. The experimental data appear to be in good agreement with the theory with respect to both the signs and magnitude of these parameters. Furthermore, the data is in good accord with the previously reported measurements by Brouard and co-workers at 308 nm [61], Zare and co-workers at 320 nm [78], Ritchie and co-workers from 320 to 350 nm [156], and the

studies at 355 nm [63, 79].

At short wavelengths, $\lambda \leq 360$ nm, the values of the incoherent parameters are near limiting. For an adiabatic dissociation process the incoherent alignment can be predicted by inspection of the expansion coefficients of the molecular wavefunction in the atomic basis at long range [93, 105, 110]. These expansion coefficients, in this case computed by consideration of the long range quadrupole-quadrupole interaction, have been given by Alexander [113]. For the $C\,^1\Pi_{1u}$ state, the molecular wavefunction can be written as

$$\Psi^{el}_{C^1\Pi_{1u}}(\mathbf{r},\mathbf{R}) \xrightarrow{R\to\infty} \left|\frac{3}{2},\frac{1}{2}\right\rangle\left|\frac{3}{2},\frac{1}{2}\right\rangle, \tag{4.2}$$

with the long range expansion coefficient given by

$$T^{C^1\Pi_{1u}}_{\frac{3}{2}\frac{1}{2},\frac{3}{2}\frac{1}{2}} = 1\,. \tag{4.3}$$

As discussed in Section 2.3.2, the expansion coefficients can be used to calculate the asymptotic polarisation in the axial recoil limit. For adiabatic dissociation on the $C\,^1\Pi_{1u}$ state potential, the *molecular* frame polarisation is predicted to be a limiting $a_0^{(2)}(\perp) = -0.8$, which transformed to the *lab* frame gives $s_2 = -0.16$ and $\alpha_2 = -0.08$. In the short wavelength region, $\lambda \leq 360$ nm, theory gives $s_2 = -0.14$ and $\alpha_2 = -0.07$, which is broadly consistent with the picture of *adiabatic* dissociation *via* the $C\,^1\Pi_{1u}$ state. Following the incoherent excitation of an $\Omega = 1$ or -1 component of the $C\,^1\Pi_{1u}$ state, only dissociation on the same substate leads to non-zero values of the dynamical function $f_2(1,1)$, giving rise to the parameters s_2 and α_2 [62, 63, 141].

The reduction in magnitude of these incoherent parameters even in this short wavelength region, however, indicates the involvement of another state. Inspection of Figure 4.33(b) shows that theory predicts the coherent alignment parameter γ_2 to be zero at all dissociation wavelengths, as expected if there is no parallel component to the channel. The parameter η_2, however, which is related to the $f_2(1,-1)$ dynamical function is predicted to be important, even in the short wavelength region. As

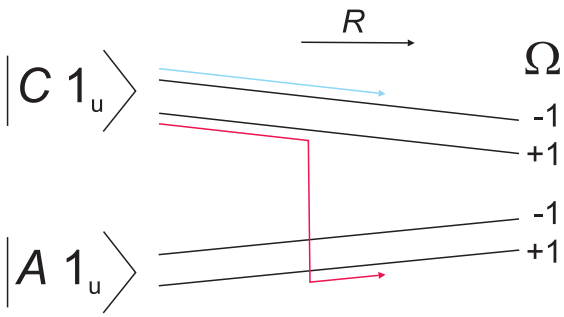

Figure 4.34: Only possible mechanism for non-adiabatic transition leading to non-zero $f_2(1,-1)$. Note that a similar mechanism can be drawn with the non-adiabatic transfer taking place from the $C\,^1\Pi_{1u}$ $\Omega = -1$ substate. This mechanism, however, would be associated with the $f_2(-1,1)$ dynamical function which is related to $f_2(1,-1)$ by symmetry [92]. Adapted from Ref [62].

discussed by Bracker *et al.* it turns out that this parameter can only arise following a non-adiabatic transition from the $C\,^1\Pi_{1u}$ state to the $A\,^3\Pi_{1u}$ state, which must occur in the long range region of the potentials where the energy separation between the *adiabatic* curves is small [63, 66, 141].

There are several possibilities for dissociation following coherent excitation of the $\Omega = \pm 1$ substates of the $C\,^1\Pi_{1u}$ state, both of which being equally populated from the initial excitation step. The molecule may dissociate *via* the same substates, *via* a coherent superposition of $A\,^3\Pi_{1u}$ $\Omega = \pm 1$ or *via* a coherent superposition of the $C\,^1\Pi_{1u}$ $\Omega = \pm 1$ and $A\,^3\Pi_{1u}$ $\Omega = \mp 1$ substates, with the latter the only mechanism for production of non-zero η_2 [62]. This mechanism is shown schematically in Figure 4.34, with interference between the two pathways responsible for the variation in η_2 as a function of wavelength. As the dissociation wavelength increases the magnitudes of the incoherent parameters s_2 and α_2 decrease, which can be taken to mean a rise in the relative importance of the non-adiabatic transition to the $A\,^3\Pi_{1u}$ state, as outlined above. As discussed by Brouard and co-workers, at longer wavelengths the optical transition to the $C\,^1\Pi_{1u}$ state would occur to less repulsive parts of the potential, see Figure 4.1, resulting in progressively slower timescales associated with the dissociation, facilitating the non-adiabatic transition [61]. The experimental data for the η_2 parameter seem to be in reasonable accord with the

quantum calculation with, barring a discrepancy in the position, the change in sign observed as the wavelength is increased. In addition, the 355 nm measurements are in good agreement with the previously reported values by Bracker *et al.* [63].

More surprisingly, however, are the experimental measurements of small but non-zero values of the γ_2 parameter, which is related to the $f_2(1,0)$ dynamical function, at several dissociation wavelengths. A very small but non-zero value of this parameter has previously been reported by Brouard and co-workers following photodissociation at 308 nm [61]. The implications for appearance of the γ_2 parameter are that a parallel, $\Omega = 0$, state is somehow involved in the dissociation mechanism. An $\Omega = 0$ state may be involved in the dissociation either through Coriolis ($\Delta\Omega = \pm 1$) coupling of the $C\,^1\Pi_{1u}$ state with an $\Omega = 0$ state or more directly by optical excitation from the ground state. Given that the experimental β parameters are so close to limiting, any parallel component to the excitation process must necessarily be very small. It is interesting to note, however, that consideration of the extremum values of the γ_2 parameter, which for $J = \frac{3}{2}$ are given by [84]

$$\gamma_2^{\text{extr}} = \pm 0.16 \left[\frac{(1+\beta)(2-\beta)}{2} \right]^{1/2}, \tag{4.4}$$

show that even for a spatial anisotropy parameter β of -0.9, the magnitude of the parameter γ_2 can be as high as ~ 0.06. The implications of these measurements are discussed in more detail below with regards to the electronic orientation.

$Cl(^2P_{3/2})$ orientation in the $Cl(^2P_{3/2})$ + $Cl(^2P_{3/2})$ channel

Strong orientation has been observed for the $Cl(^2P_{3/2}) + Cl(^2P_{3/2})$ channel, clearly visible in the raw ion images recorded using circularly polarised pump and probe radiation. Theory predicts that both low order, $K = 1$, and high order, $K = 3$, orientation are important in this channel, however, only the low order orientation has been reported previously.

The incoherent orientation parameters, α_1 and α_3, are shown in Figure 4.35.

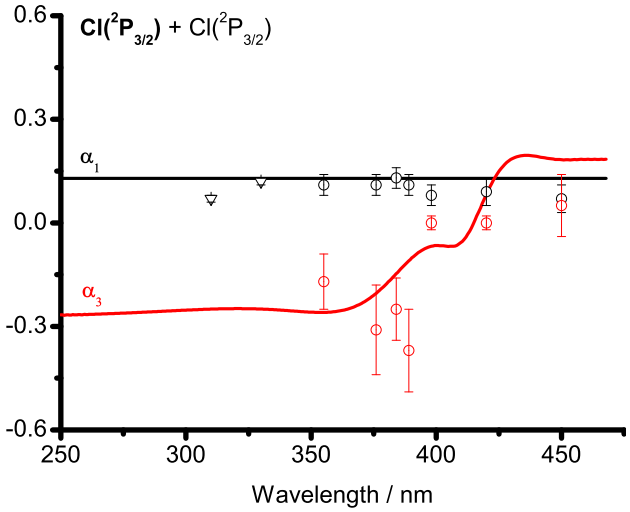

Figure 4.35: Incoherent $K = 1$ and 3 orientation parameters for the $Cl(^2P_{3/2}) + Cl(^2P_{3/2})$ channel returned from fits to the $Cl(^2P_{3/2})$ Fourier moments. Experimental data represented by open circles and compared to the recent quantum calculation (——) [50], and previous measurements by Zare and co-workers (triangles) [142].

α_1 is seen to be wavelength independent, taking a value of ~ 0.13, with excellent agreement seen between experiment and theory. The value of $\alpha_1 \sim 0.13$ can be understood since incoherent excitation to, and adiabatic dissociation on both of the potentials believed to be important in this channel, $A\,^3\Pi_{1u}$ and $C\,^1\Pi_{1u}$, would be expected to give $\alpha_1 = 0.13$ based on long range interactions [113]. Unfortunately, however, this means that measurements of the α_1 parameter, like those for the spatial anisotropy parameter, are rather insensitive to the non-adiabatic dynamics occurring in this product channel.

The parameter α_3, however, does show some wavelength dependence. In fact the α_3 parameter shows a similar wavelength dependence to the incoherent alignment parameters s_2 and α_2. In the case of alignment the reduction in magnitude of these incoherent parameters as the wavelength increases was taken to be indicative of the importance of non-adiabatic effects. For the incoherent orientation parameter, α_3, the same reasoning must be applied. The short wavelength measurements of α_3 seem to be in good agreement with the quantum calculation [50], and the reduction

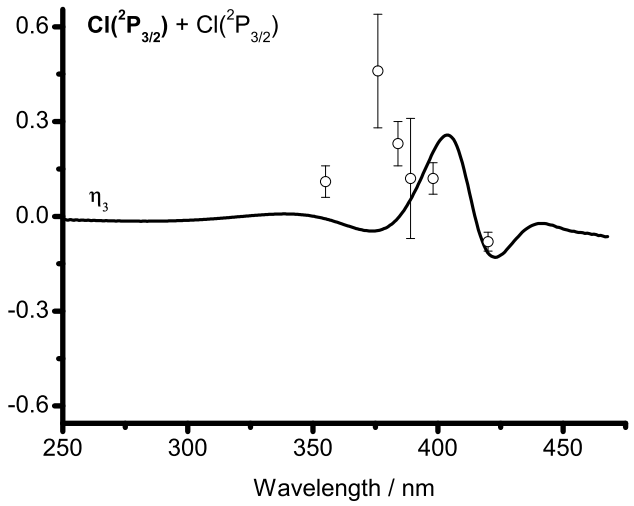

Figure 4.36: Coherent η_3 orientation parameter for the $Cl(^2P_{3/2}) + Cl(^2P_{3/2})$ channel returned from fits to the $Cl(^2P_{3/2})$ Fourier moments. Experimental data represented by open circles and compared to the recent quantum calculation (——) [50].

in magnitude with increasing wavelength is also seen experimentally.

The coherent parameter η_3, related to the $f_3(1,-1)$ dynamical function, is predicted to be non-zero. Non-zero values of this parameter, like η_2, indicate interference between the $C\,^1\Pi_{1u}$ state and $A\,^3\Pi_{1u}$ state dissociation pathways. As mentioned previously the non-adiabatic transition between these two states becomes increasingly important in the long wavelength region of the spectrum, which is reflected in the wavelength dependence of η_3, as shown in Figure 4.36.

Theory predicts that the coherent parameters γ_K and γ'_K should be zero since, as discussed previously, the channel is believed to be fully perpendicular in character. The experimental data detailed in Table 4.6, however, indicate non-zero $\gamma'_{1,3}$ parameters. The manifestation of these parameters can be seen in differences between images recorded in 45L and 45R geometries. As discussed above with regards to the alignment of the ground state product channel, these coherent parameters indicate the involvement of some $\Omega = 0$ component in the dissociation channel. In particular there are two mechanisms that could give rise to such coherent parameters

- Spin-orbit coupling of the ground state to higher triplet *gerade* states allowing a

necessarily weak optical transition to take place to the $\Omega = 0$ states correlating with the ground state product channel, see Figure 4.2.

- Coriolis coupling ($\Delta\Omega = \pm 1$) between one of the *ungerade* $\Omega = 1$ states with the *ungerade* $\Omega = 0$ potential correlating with the ground state channel.

The first such mechanism, in which a spin-forbidden transition takes place to either the $^3\Pi_u(0_u^+)$ or the higher energy $^3\Sigma_u^+(0_u^-)$ state, perhaps weakly allowed *via* spin-orbit coupling between the ground state and triplet states of *gerade* character, is similar to the mechanism which gives rise to the excitation of the $B\,^3\Pi_{0_u^+}$ state, important in the excited state product channel. It should be noted that the excited $^3\Pi_u(0_u^+)$ and $^3\Sigma_u^+(0_u^-)$ states, with the second derived from excitation of the $5\sigma_g$ bonding molecular orbital, were not included in the recent dynamics calculation [50]. The absence of these states should not, however, affect the results of the recent calculation since there are no electronic transition moments associated with these states [51]. The second mechanism which could give rise to a non-zero parallel component in the dissociation is coupling of $\Omega = \pm 1$ and $\Omega = 0$ states due to rotation of the nuclear framework, termed Coriolis coupling. It is interesting to note that Coriolis couplings of the $C\,^1\Pi_{1u}$ and/or $A\,^3\Pi_{1u}$ states with the $B\,^3\Pi_{0_u^+}$ state, important in the excited channel dissociation, were found to be negligible for parent rotational temperatures as high as 300 K [139, 142].

Cl($^2P_{3/2}$) alignment in the Cl($^2P_{3/2}$) + Cl*($^2P_{1/2}$) channel

The excited state product channel makes a significant contribution to the photodissociation at wavelengths > 370 nm, as shown in Figure 4.32(a). At long wavelengths the theoretical calculation predicts that limiting values are taken by the incoherent alignment parameters, $s_2 = -0.16$ and $\alpha_2 = 0.16$, with zero contributions arising from coherent processes, as shown in Fig 4.37(a). These values, as well as indicating a pure parallel transition (since $s_2 = -\alpha_2$), are predictable based on the long range expansion coefficients assuming a fully adiabatic dissociation takes place on the $B\,^3\Pi_{0_u^+}$ state potential. In the long wavelength region the experimental results

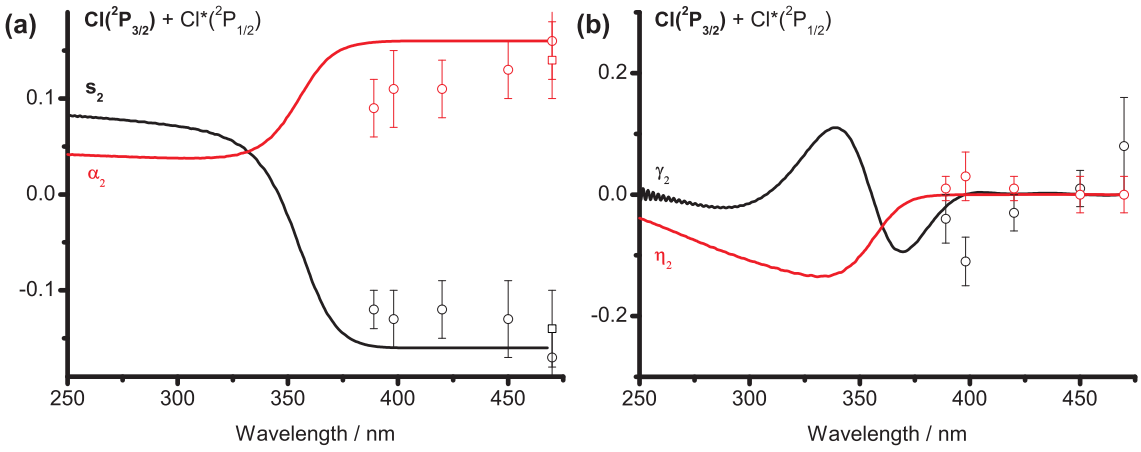

Figure 4.37: Incoherent **(a)** and coherent **(b)** $K = 2$ alignment parameters for the $Cl(^2P_{3/2}) + Cl^*(^2P_{1/2})$ channel returned from fits to the $Cl(^2P_{3/2})$ Fourier moments. Experimental data represented by open circles and compared to the recent quantum calculation (——) [50]. Previous measurements by Zare and co-workers (squares) [78] also shown.

are consistent with this picture, and in good agreement with the previously reported values by Zare and co-workers [78] and Samartzis *et al.* [148].

At around 400 nm the magnitudes of these incoherent parameters are reduced, indicating that the dissociation can no longer be described as a purely adiabatic process taking place on the $B\,^3\Pi_{0_u^+}$ state potential. Zare and co-workers [78] have previously given a mechanism for the dissociation into this channel based on electronic orientation measurements of the co-fragment, $Cl^*(^2P_{1/2})$. Their mechanism involves $C\,^1\Pi_{1u}$ state excitation followed by a non-adiabatic transition to the $(3)^3\Sigma^+_{1u}$ state, with some additional contribution arising following a further non-adiabatic transition to the $(4)^3\Delta_{1u}$ state.

The molecular wavefunctions in the atomic basis for the three states can be written as

$$\Psi^{el}_{B0_u^+}(\mathbf{r},\mathbf{R}) \xrightarrow{R\to\infty} \frac{1}{2}\left[\left|\frac{3}{2},\frac{1}{2}\right\rangle\left|\frac{1}{2},\frac{-1}{2}\right\rangle - \left|\frac{1}{2},\frac{-1}{2}\right\rangle\left|\frac{3}{2},\frac{1}{2}\right\rangle - \left|\frac{3}{2},\frac{-1}{2}\right\rangle\left|\frac{1}{2},\frac{1}{2}\right\rangle + \left|\frac{1}{2},\frac{1}{2}\right\rangle\left|\frac{3}{2},\frac{-1}{2}\right\rangle\right]$$

$$\Psi^{el}_{(3)^3\Sigma^+_{1u}}(\mathbf{r},\mathbf{R}) \xrightarrow{R\to\infty} \frac{1}{\sqrt{2}}\left[\left|\frac{3}{2},\frac{3}{2}\right\rangle\left|\frac{1}{2},\frac{-1}{2}\right\rangle + \left|\frac{1}{2},\frac{-1}{2}\right\rangle\left|\frac{3}{2},\frac{3}{2}\right\rangle\right]$$

$$\Psi_{(4)^3\Delta_{1u}}(\mathbf{r},\mathbf{R}) \xrightarrow{R\to\infty} \frac{1}{\sqrt{2}}\left[\left|\frac{3}{2},\frac{1}{2}\right\rangle\left|\frac{1}{2},\frac{1}{2}\right\rangle + \left|\frac{1}{2},\frac{1}{2}\right\rangle\left|\frac{3}{2},\frac{1}{2}\right\rangle\right]. \tag{4.5}$$

Inspection of the long range coefficients enables prediction of the atomic alignment, $a_0^{(2)}$, based on adiabatic dissociation on each of the above states. For the $B\,^3\Pi_{0_u^+}$ state $a_0^{(2)} = -0.8$, giving $s_2 = -0.16$ and $\alpha_2 = 0.16$ in the lab frame as mentioned above. For the $(3)^3\Sigma^+_{1u}$ state $a_0^{(2)} = 0.8$, giving $s_2 = 0.16$ and $\alpha_2 = 0.08$, while for the $(4)^3\Delta_{1u}$ state $a_0^{(2)} = -0.8$. This value is the same as for the $B\,^3\Pi_{0_u^+}$ state, however, in this case $s_2 = -0.16$ and $\alpha_2 = -0.08$ since this state would be associated with a perpendicular rather than parallel transition.

The experimental results show a decrease in the magnitude of the parameters for wavelengths $< 400\,\text{nm}$, as mentioned above. The trends in the experimental and theoretical data are therefore consistent, based on the above adiabatic polarisation arguments, with the picture of non-adiabatic transfer from the $C\,^1\Pi_{1u}$ to $(3)^3\Sigma^+_{1u}$ state as being the dominant mechanism for production of $\text{Cl}(^2\text{P}_{3/2}) + \text{Cl}^*(^2\text{P}_{1/2})$ in the short wavelength region.

The coherent parameters γ_2 and η_2 are also predicted to be important in the short wavelength region, as shown in Figure 4.37(b). The non-zero values taken by the parameter γ_2, which is related to the $f_2(1,0)$ dynamical function, are consistent with an interference between the $B\,^3\Pi_{0_u^+}$ and $(3)^3\Sigma^+_{1u}/(4)^3\Delta_{1u}$ state dissociation pathways. The manifestation of η_2, on the other hand, is consistent with interference between the $(3)^3\Sigma^+_{1u}$ and $(4)^3\Delta_{1u}$ states. The present study is the first to observe coherent alignment effects for this dissociation channel. The experimental measurements of the electronic alignment for this channel are in reasonable accord with the theoretical calculation and support the mechanism given by Zare and co-workers [78].

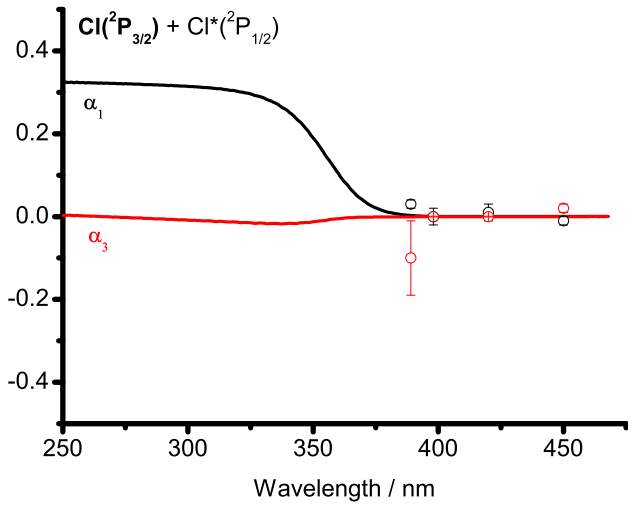

Figure 4.38: Incoherent $K = 1$ and 3 orientation parameters for the $Cl(^2P_{3/2}) + Cl^*(^2P_{1/2})$ channel returned from fits to the $Cl(^2P_{3/2})$ Fourier moments. Experimental data represented by open circles and compared to the recent quantum calculation (——) [50].

$Cl(^2P_{3/2})$ orientation in the $Cl(^2P_{3/2})$ + $Cl^*(^2P_{1/2})$ channel

The incoherent orientation parameters α_1 and α_3 for the excited state state product channel are shown in Figure 4.38 along with theoretical values for comparison. At long wavelengths, > 400 nm, there is no orientation. In this region, as discussed above with respect to the electronic alignment of $Cl(^2P_{3/2})$ in this channel, the dissociation can be viewed as proceeding adiabatically on the $B\,^3\Pi_{0_u^+}$ state potential. Since a pure parallel transition results in zero orientation within the framework of the axial recoil approximation [92] this result is understood.

Moving to shorter wavelengths both α_1 and α_3 are seen to take non-zero values, with theory predicting a positive α_1 and a small, negative α_3. In this region, the spatial anisotropy parameter, β, decreases indicating a perpendicular state is involved in the dissociation. The positive value of $\alpha_1 \sim 0.3$ reached at ~ 330 nm implies a molecular frame orientation of $a_0^{(1)}(\perp) \sim 0.6$. By inspection of the long range expansion coefficients, the dominant $\Omega = 1$ contribution to the dissociation channel must therefore come from the $(3)^3\Sigma_{1u}^+$ state, which is in agreement with the findings of Zare and co-workers [78] and Yabushita *et al.* [151] and with the above discussion

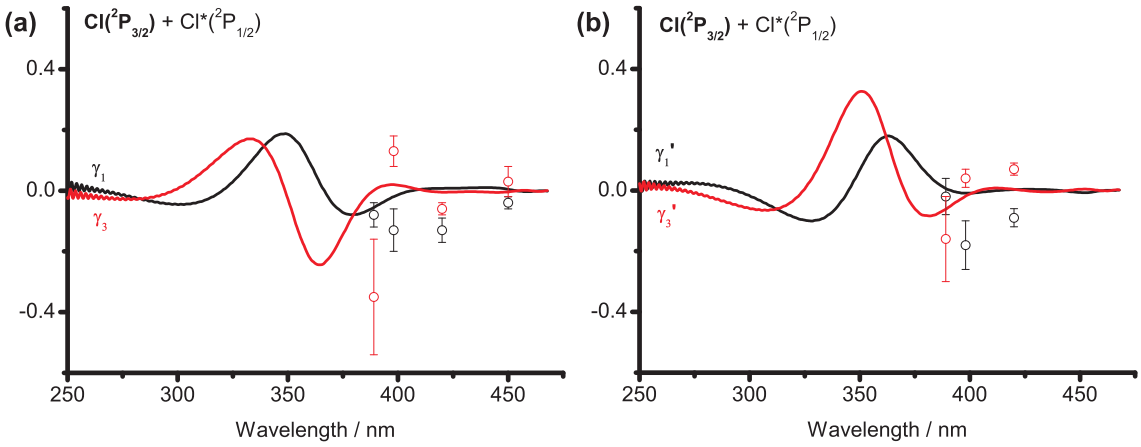

Figure 4.39: Coherent γ_K **(a)** and γ'_K **(b)** $K = 1$ and 3 orientation parameters for the $Cl(^2P_{3/2}) + Cl^*(^2P_{1/2})$ channel returned from fits to the $Cl(^2P_{3/2})$ Fourier moments. Experimental data represented by open circles and compared to the recent quantum calculation (——) [50].

regarding the electronic alignment for this dissociation channel. The value predicted by theory, $a_0^{(1)}(\perp) \sim 0.6$, is somewhat less than the limiting $a_0^{(1)}(\perp) = 0.78$ expected for adiabatic dissociation on the $(3)^3\Sigma_{1u}^+$ state potential [113]. Since in this short wavelength region the spatial anisotropy parameter, $\beta = -1$, another $\Omega = 1$ state must make a contribution to the dissociation. The only other $\Omega = 1$ state correlating with this dissociation channel is the $(4)^3\Delta_{1u}$ state which, in the adiabatic limit, gives a much smaller $a_0^{(1)}(\perp)$ of 0.26. The incoherent orientation parameters are therefore consistent with an additional non-adiabatic transition to the $(4)^3\Delta_{1u}$ state, as first described by Zare and co-workers [78].

For this dissociation channel, as opposed to the ground state channel, coherent orientation parameters are predicted to arise as a result of interference between parallel, $\Delta\Omega = 0$, and perpendicular, $\Delta\Omega = \pm 1$, dissociation pathways. Non-zero values are found at shorter wavelengths, where the β parameter decreases from its limiting value of 2, as shown in Figure 4.39. At the wavelengths studied here, the orientation of the $Cl(^2P_{3/2})$ fragment only just begins to be important. Nevertheless, non-zero values of the coherent orientation parameters are seen, for the first time, in the shorter wavelength measurements.

The spatial anisotropy parameters, β, and angular momentum alignment and orientation parameters for dissociation to both the ground and excited state product channels reported following measurements of the $Cl(^2P_{3/2})$ fragment are summarised in Tables 4.5 and 4.6.

	Wavelength / nm				
Parameter	389	398	420	450	470
β	1.85(12)	1.94(7)	1.87(6)	1.84(5)	1.99(5)
s_2	-0.12(2)	-0.13(3)	-0.12(3)	-0.13(4)	-0.17(3)
α_2	0.09(3)	0.11(4)	0.11(3)	0.13(3)	0.16(4)
γ_2	-0.04(4)	-0.11(4)	-0.03(3)	0.01(3)	0.08(8)
η_2	0.01(2)	0.03(4)	0.01(2)	0.00(3)	0.00(3)
α_1	0.03(1)	-0.00(2)	0.01(2)	-0.01(1)	-
γ_1	-0.08(4)	-0.13(7)	-0.13(4)	-0.04(2)	-
γ_1'	-0.02(6)	-0.18(8)	-0.09(3)	-	-
α_3	-0.10(9)	0.00(0)	-0.00(0)	0.02(1)	-
γ_3	-0.35(23)	0.13(5)	-0.06(2)	0.03(5)	-
γ_3'	-0.16(14)	0.04(3)	0.07(2)	-	-
η_3	-0.35(22)	0.19(19)	0.01(1)	-	-

Table 4.5: Spatial anisotropy and angular momentum polarisation parameters for the $Cl(^2P_{3/2})$ fragments from the excited state product channel returned from the fits to experimental data. Errors (1σ) in the last digit(s) are given in parenthesis.

	Wavelength / nm						
Parameter	355	376	384	389	398	420	450
β	-0.98(3)	-0.95(4)	-0.98(5)	-0.97(5)	-0.98(10)	-0.95(11)	-0.82(15)
s_2	-0.12(2)	-0.11(2)	-0.13(2)	-0.13(2)	-0.13(4)	0.00(3)	-0.02(2)
α_2	-0.05(1)	-0.06(2)	-0.05(2)	-0.07(2)	-0.04(3)	-0.01(3)	-0.01(2)
γ_2	-0.02(2)	0.04(4)	0.00(5)	-0.04(3)	-0.04(3)	-0.07(4)	-0.04(4)
η_2	0.05(3)	0.01(2)	-0.05(4)	-0.04(3)	-0.03(4)	-0.12(6)	0.00(4)
α_1	0.11(3)	0.11(3)	0.13(3)	0.11(3)	0.08(3)	0.09(4)	0.07(4)
γ_1	-0.05(3)	-0.07(2)	-0.02(3)	-0.04(1)	-0.02(3)	-0.04(3)	-0.02(5)
γ_1'	-0.04(3)	-0.06(4)	-0.01(3)	0.02(4)	-0.02(4)	0.03(4)	-
α_3	-0.17(8)	-0.31(13)	-0.25(9)	-0.37(12)	0.00(2)	0.00(2)	0.05(9)
γ_3	-0.02(2)	-0.21(16)	-0.25(9)	0.14(26)	0.02(1)	0.12(4)	0.24(30)
γ_3'	0.14(7)	-0.08(17)	0.33(14)	0.26(15)	0.12(5)	0.03(1)	-
η_3	0.11(5)	0.46(18)	0.23(7)	0.12(19)	0.12(5)	-0.08(3)	-

Table 4.6: Spatial anisotropy and angular momentum polarisation parameters for the $Cl(^2P_{3/2})$ fragments from the ground state product channel returned from the fits to experimental data. Errors (1σ) in the last digit(s) are given in parenthesis.

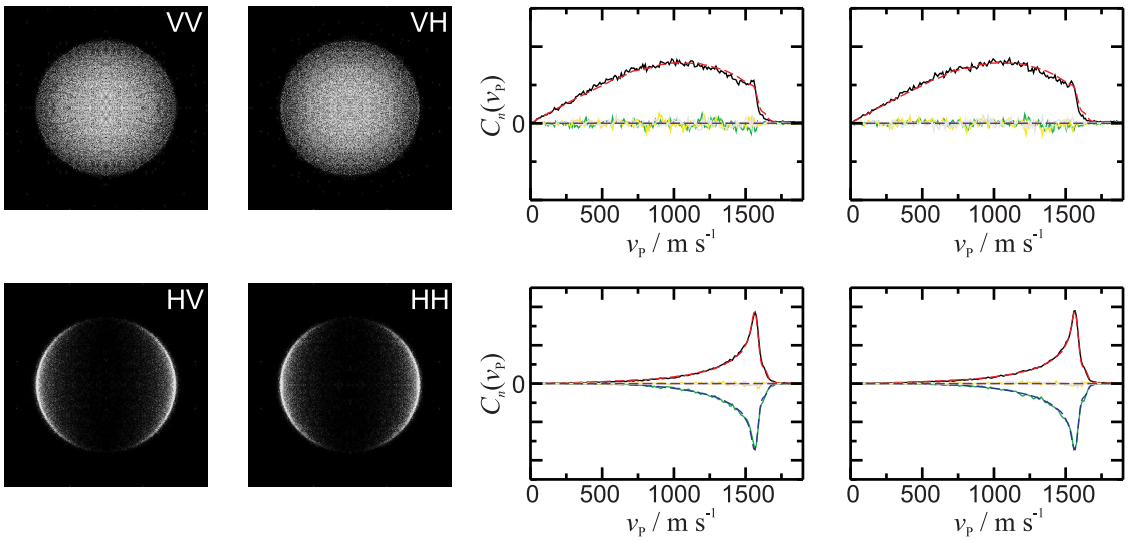

Figure 4.40: $Cl^*(^2P_{1/2})$ ion images, Fourier moments (——) and fits (- - -) for linear geometries using the $^2P_{3/2}$ transition following photodissociation at 355 nm. The Fourier moments are colour coded, C_0 (black), C_2 (green), C_4 (yellow), C_6 (grey).

4.4 The $Cl^*(^2P_{1/2})$ fragment

4.4.1 Experimental results

Following photodissociation of Cl_2 at 355, 376, 389, 398, and 450 nm, pump-probe images of the $Cl^*(^2P_{1/2})$ fragment were collected using the (2+1) REMPI transition *via* the $^2P_{3/2}$ state at 236.4 nm. This (2+1) REMPI transition was chosen as it is sensitive to the $K = 1$ orientation. Images were collected using a variety of pump-probe geometries using both linearly and circularly polarised pump and probe laser radiation. For a particular photolysis wavelength, the Fourier moments extracted from all pump-probe geometries were fit globally. For data collected at 398 and 450 nm only geometries using linearly polarised radiation were collected. For these wavelengths only the spatial anisotropy parameter, β, is presented. The ion images, Fourier moments and fits to the data are shown in Figures 4.40 to 4.47, in order of increasing photolysis wavelength.

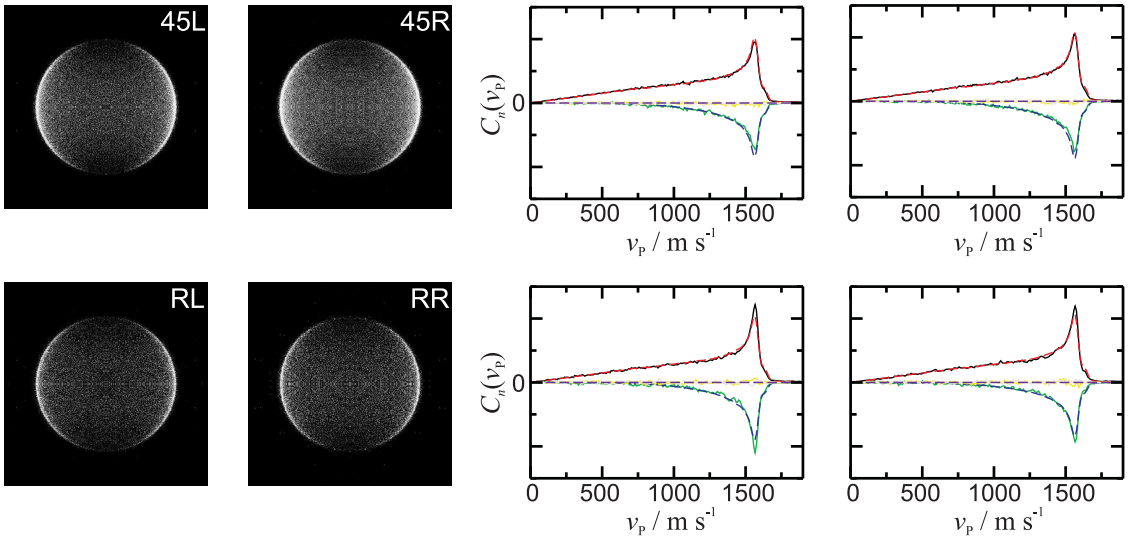

Figure 4.41: Cl*($^2P_{1/2}$) ion images, Fourier moments (——) and fits (- - -) for circular geometries using the $^2P_{3/2}$ transition following photodissociation at 355 nm. The Fourier moments are colour coded, C_0 (black), C_2 (green), C_4 (yellow), C_6 (grey).

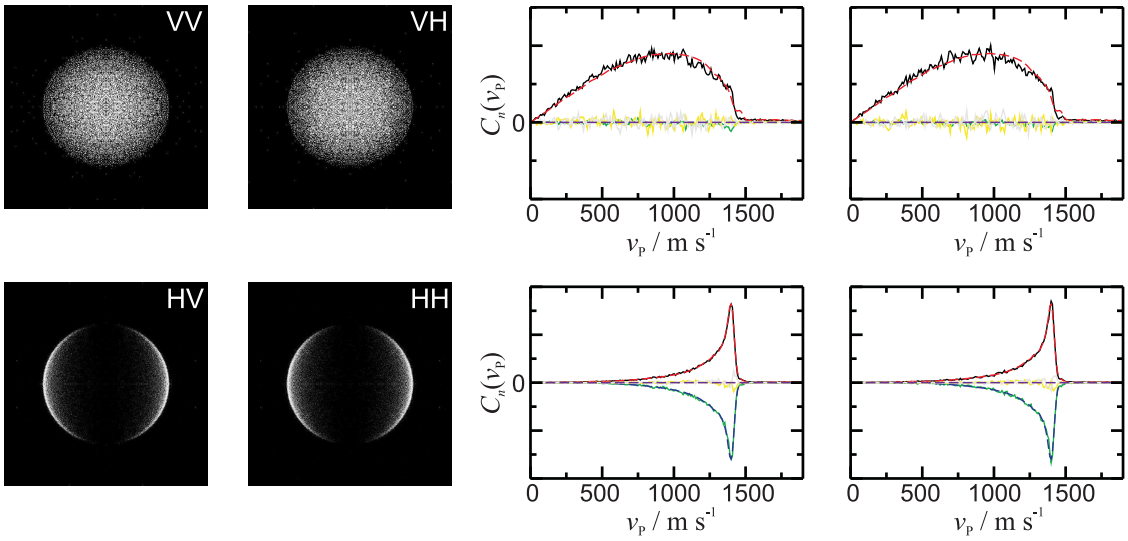

Figure 4.42: Cl*($^2P_{1/2}$) ion images, Fourier moments (——) and fits (- - -) for linear geometries using the $^2P_{3/2}$ transition following photodissociation at 376 nm. The Fourier moments are colour coded, C_0 (black), C_2 (green), C_4 (yellow), C_6 (grey).

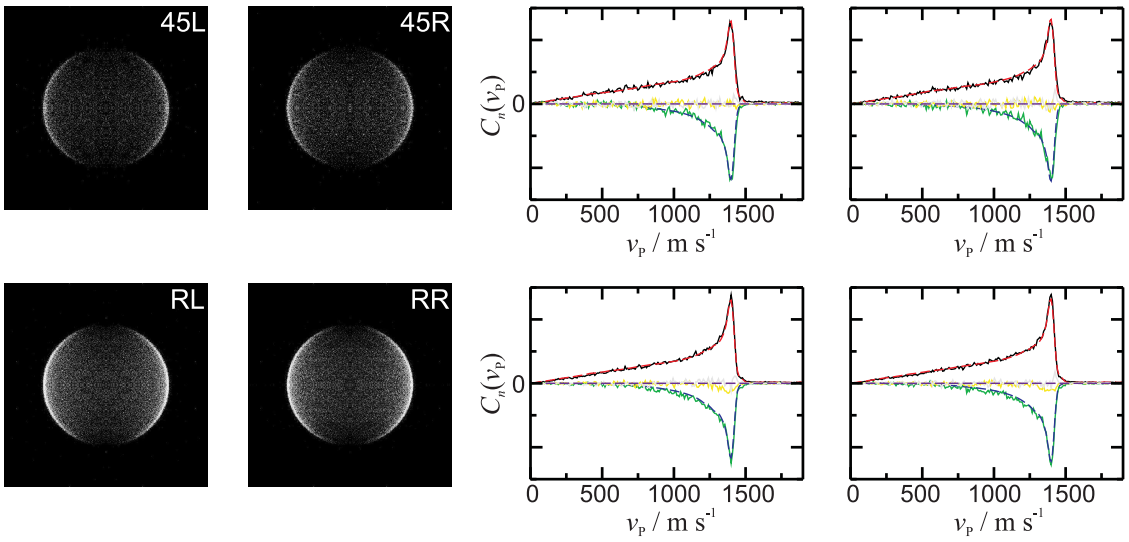

Figure 4.43: Cl*($^2P_{1/2}$) ion images, Fourier moments (——) and fits (- - -) for circular geometries using the $^2P_{3/2}$ transition following photodissociation at 376 nm. The Fourier moments are colour coded, C_0 (black), C_2 (green), C_4 (yellow), C_6 (grey).

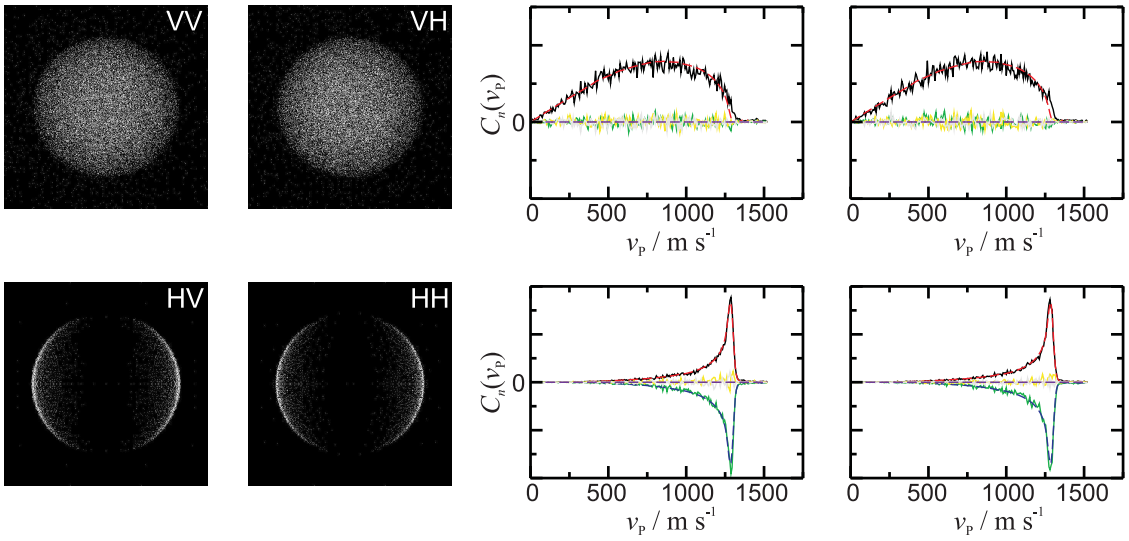

Figure 4.44: Cl*($^2P_{1/2}$) ion images, Fourier moments (——) and fits (- - -) for linear geometries using the $^2P_{3/2}$ transition following photodissociation at 389 nm. The Fourier moments are colour coded, C_0 (black), C_2 (green), C_4 (yellow), C_6 (grey).

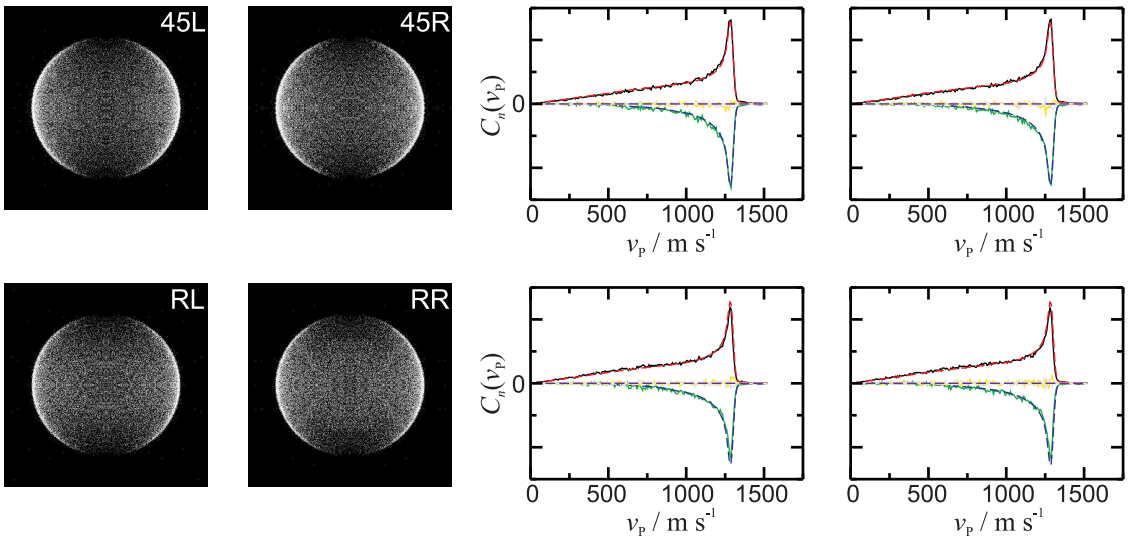

Figure 4.45: Cl*($^2P_{1/2}$) ion images, Fourier moments (——) and fits (- - -) for circular geometries using the $^2P_{3/2}$ transition following photodissociation at 389 nm. The Fourier moments are colour coded, C_0 (black), C_2 (green), C_4 (yellow), C_6 (grey).

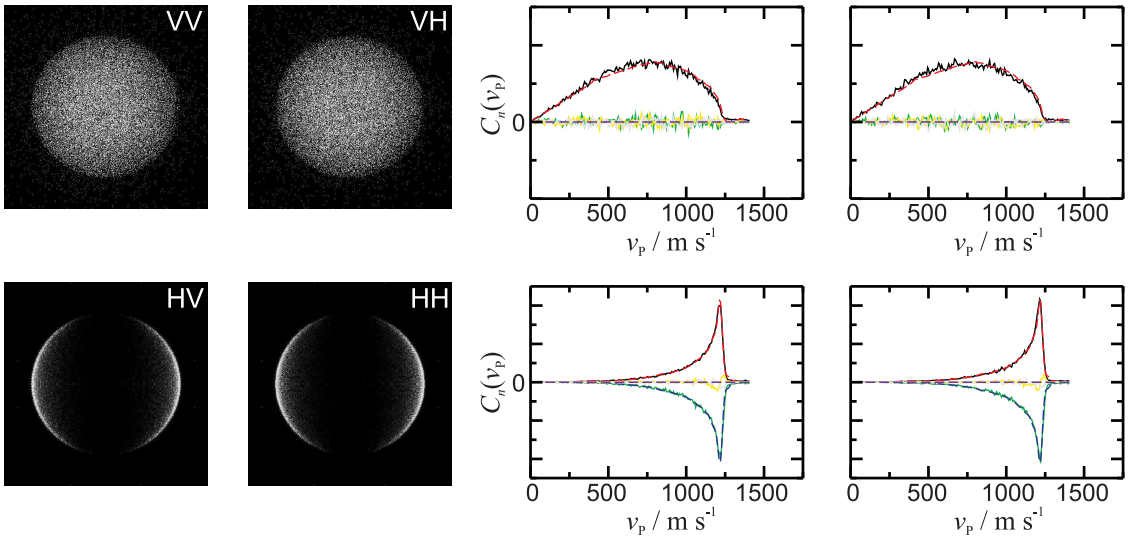

Figure 4.46: Cl*($^2P_{1/2}$) ion images, Fourier moments (——) and fits (- - -) for linear geometries using the $^2P_{3/2}$ transition following photodissociation at 398 nm. The Fourier moments are colour coded, C_0 (black), C_2 (green), C_4 (yellow), C_6 (grey).

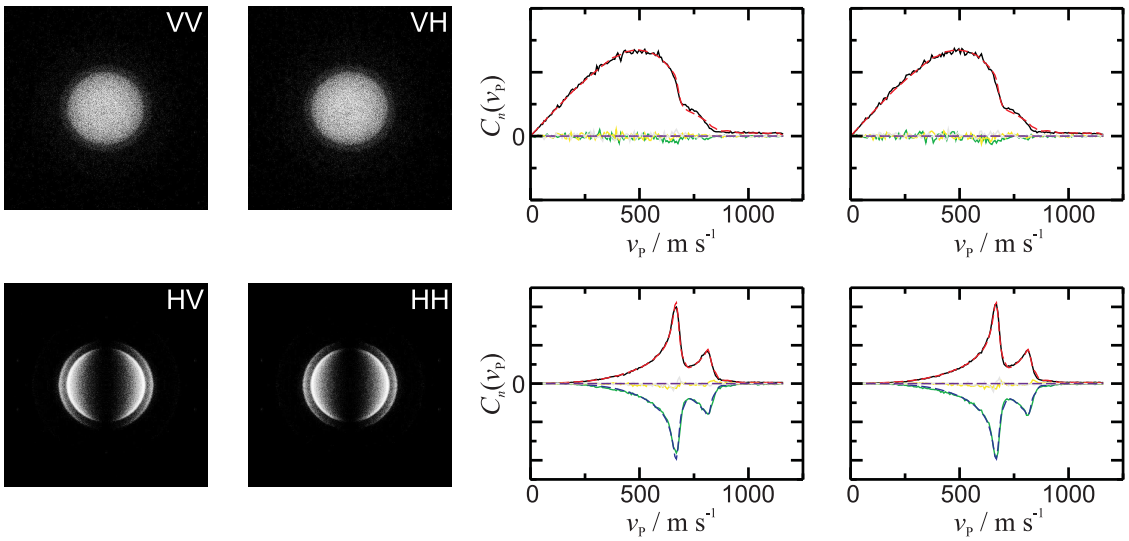

Figure 4.47: $Cl^*(^2P_{1/2})$ ion images, Fourier moments (——) and fits (- - -) for linear geometries using the $^2P_{3/2}$ transition following photodissociation at 450 nm. The Fourier moments are colour coded, C_0 (black), C_2 (green), C_4 (yellow), C_6 (grey).

4.4.2 Discussion

Following photodissociation at wavelengths below 450 nm only one feature is observed in the $Cl^*(^2P_{1/2})$ ion images corresponding to dissociation into the $Cl(^2P_{3/2})$ + $Cl^*(^2P_{1/2})$ channel. At 450 nm two features are seen in the ion images corresponding to dissociation into the $Cl(^2P_{3/2})$ + $Cl^*(^2P_{1/2})$ channel following excitation of Cl_2 $v = 0$ and $v = 1$. The spatial anisotropy parameters, β, returned from the fits to the experimental Fourier moments are presented in Figure 4.32 and have been discussed previously, in Section 4.3.2, with respect to measurements made on the $Cl(^2P_{3/2})$ co-fragment.

At the wavelengths used here the $Cl^*(^2P_{1/2})$ photofragment is somewhat less interesting than the ground state $Cl(^2P_{3/2})$ fragment. At the longer wavelengths probed only the spatial anisotropy parameter was determined since in this region the excited state channel predominantly arises following adiabatic dissociation on the $B\,^3\Pi_{0_u^+}$ state potential. For a purely parallel transition no orientation of the electronic angular momentum is possible and since $J = \frac{1}{2}$ for this fragment there cannot

be alignment. At two of the shorter wavelengths, however, low order orientation was observed.

Following photodissociation at 355 nm and 376 nm, small but non-zero values of the coherent γ_1' parameters are found for the $Cl^*(^2P_{1/2})$ fragment. This parameter arises following quantum mechanical interference between the $B\,^3\Pi_{0_u^+}$ and $(3)^3\Sigma_{1u}^+$ state pathways giving rise to the excited state product channel. γ_1' is related to the molecular frame $\mathrm{Im}[a_1^{(1)}(\parallel,\perp)]$ parameter, as detailed in Table 2.1. This molecular frame parameter has been modelled theoretically by Yabushita *et al.* [151] using the Youngs double slit method to estimate the phase difference, $\Delta\phi$, between the parallel, $B\,^3\Pi_{0_u^+}$ state, and perpendicular, $(3)^3\Sigma_{1u}^+$ state, dissociation pathways. Using the model, the $\mathrm{Im}[a_1^{(1)}(\parallel,\perp)]$ parameter could be expressed as [151]

$$\mathrm{Im}[a_1^{(1)}(\parallel,\perp)] \propto \sqrt{(1+\beta)\left(1-\frac{\beta}{2}\right)}\sin(\Delta\phi). \tag{4.6}$$

The $\mathrm{Im}[a_1^{(1)}(\parallel,\perp)]$ parameter for the $^{35}Cl^*(^2P_{1/2})$ and $^{37}Cl^*(^2P_{1/2})$ fragments, as calculated by Yabushita *et al.* [151] using Equation (4.6) is shown in Figure 4.48. Also shown are the previous results from Zare and co-workers [149], and recent measurements from Ritchie and co-workers [156], for both the $^{35}Cl^*(^2P_{1/2})$ and $^{37}Cl^*(^2P_{1/2})$ fragments. The $\mathrm{Im}[a_1^{(1)}(\parallel,\perp)]$ parameter calculated by Yabushita *et al.* [151] is in qualitative agreement with the previous results for both isotopes by Zare and co-workers, and the recent results from Ritchie and co-workers [156], correctly predicting the phase shift due to the different de Broglie wavelengths associated with the $^{35}Cl^*(^2P_{1/2})$ and $^{37}Cl^*(^2P_{1/2})$ fragments. The results for the shorter wavelength measurements made here show the same trend as the previous experimental work. Results from the recent theoretical calculation [50] show the same oscillatory structure but appear somewhat shifted in wavelength relative to the experimental results made here and the previously reported values by Zare and co-workers [149]. This discrepancy in wavelength is perhaps unsurprising given the differences in the theoretical and experimental β parameters, as discussed in Section 4.3.2. A wavelength

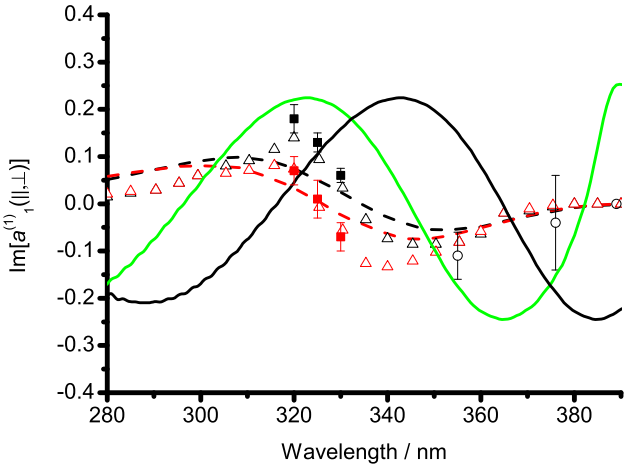

Figure 4.48: $\mathrm{Im}[a_1^{(1)}(\|,\perp)]$ parameter for the $Cl^*(^2P_{1/2})$ fragments in the $Cl(^2P_{3/2}) + Cl^*(^2P_{1/2})$ product channel. The solid black line represents the recent theoretical work [50]. The solid green line shows a shift of 20 nm to shorter wavelengths (see text for details). Experimental data returned from fits to Fourier moments represented by circles. Also shown is the $\mathrm{Im}[a_1^{(1)}(\|,\perp)]$ parameter reported from the theoretical work by Yabushita *et al.* for $^{35}Cl^*(^2P_{1/2})$ (black dashed) and $^{37}Cl^*(^2P_{1/2})$ (red dashed) fragments. Previous measurements by Zare and co-workers [149] and Ritchie and co-workers [156] represented by triangles and squares, respectively, for $^{35}Cl^*(^2P_{1/2})$ (black) and $^{37}Cl^*(^2P_{1/2})$ (red).

shift of 20 nm is required to the brings the experimental and theoretical β parameters into better agreement, see Figure 4.32, and a similar shift here improves the agreement between the experimental and theoretical work. Table 4.7 summaries the spatial anisotropy and angular momentum orientation parameters returned from the fits to the experimental Fourier moments for the $Cl^*(^2P_{1/2})$ fragments.

Unlike the orientation parameters, α_K and γ_K, which may arise following photodissociation using circularly polarised light and result from the helicity of the dissociation photon, the orientation parameter γ_1', and therefore $\mathrm{Im}[a_1^{(1)}(\|,\perp)]$, is produced following photodissociation using linearly polarised light and is related to the alignment of the photolysis photon [84]. Using a classical description of two orthogonal oscillations Zare and co-workers provided an instructive discussion on the manifestation of such electronic orientation following photolysis using linearly polarised light [149]. Following a parallel transition the transition dipole moment oscillates along the bond axis, whereas following a perpendicular transition the dipole

	Wavelength / nm				
Parameter	355	376	389	398	450
β	1.82(5)	1.95(4)	2.00(4)	1.98(6)	1.80(5)
α_1	-0.02(2)	-0.00(2)	-	-	-
γ_1	-0.21(16)	-0.07(7)	-	-	-
γ_1'	0.05(4)	0.01(4)	-	-	-

Table 4.7: Spatial anisotropy and angular momentum polarisation parameters for the $Cl^*(^2P_{1/2})$ fragments from the excited state product channel returned from the fits to experimental data. Errors (1σ) in the last digit(s) are given in parenthesis.

oscillates back and forth perpendicular to this axis. When a mixed transition is excited, composed of both parallel and perpendicular transitions, both the parallel and perpendicular oscillations take place with a fixed initial phase relationship. The parallel and perpendicular components sample different potential energy curves as the internuclear separation increases, which gives rise to a phase shift in the parallel and perpendicular motions. Both transitions ultimately converge to the same asymptotic photofragment product channel with result that the overall phase difference gives rise to a helicity in the electronic charge distribution [149]. Measurements of such helicity, and therefore phase difference, provide a very sensitive test of the potentials sampled on route to dissociation.

4.5 Photodissociation of Cl_2 ($v = 1$)

The photodissociation of vibrationally excited Cl_2 ($v = 1$) has been investigated both theoretically and experimentally. In this section theoretical results from time-dependent wavepacket calculations performed on a set of *ab initio* potentials [51] are presented. Additionally, experimental results are presented for dissociation into

both the ground and excited state product channels. The $v = 1$ results are compared to those obtained for the dissociation of vibrational ground state molecules.

4.5.1 Theoretical details

Using the methodology set out in Section 2.4.1 time-dependent wavepacket calculations have been performed on the set of *ab initio* potentials calculated by Buenker and co-workers [51]. The calculations presented here are an extension of the work by Johnsen *et al.* [50] to vibrationally excited Cl_2 molecules. Similar detailed calculations, in which all angular momentum polarisation parameters are determined, have previously only been performed for the photodissociation of the hydrogen halides [95, 101, 102]. As for Ref [50], the calculation was performed on a set of

State	Adiabatic correlation
$^3\Pi_u(2_u)$	$Cl(^2P_{3/2}) + Cl(^2P_{3/2})$
$A^3\Pi_u(1_u)$	$Cl(^2P_{3/2}) + Cl(^2P_{3/2})$
$C^1\Pi_u(1_u)$	$Cl(^2P_{3/2}) + Cl(^2P_{3/2})$
$^3\Delta_u(3_u)$	$Cl(^2P_{3/2}) + Cl(^2P_{3/2})$
$B^3\Pi_u(0_u^+)$	$Cl(^2P_{3/2}) + Cl^*(^2P_{1/2})$
$^3\Sigma_u^+(1_u)$	$Cl(^2P_{3/2}) + Cl^*(^2P_{1/2})$
$^3\Delta_u(2_u)$	$Cl(^2P_{3/2}) + Cl^*(^2P_{1/2})$
$^3\Delta_u(1_u)$	$Cl(^2P_{3/2}) + Cl^*(^2P_{1/2})$
$^3\Sigma_u^+(1_u)$	$Cl^*(^2P_{1/2}) + Cl^*(^2P_{1/2})$

Table 4.8: Ungerade electronic states of the Cl_2 molecule correlating with two ^2P_J fragments included in the dynamics calculations. Hunds case (c) labels are given in parenthesis.

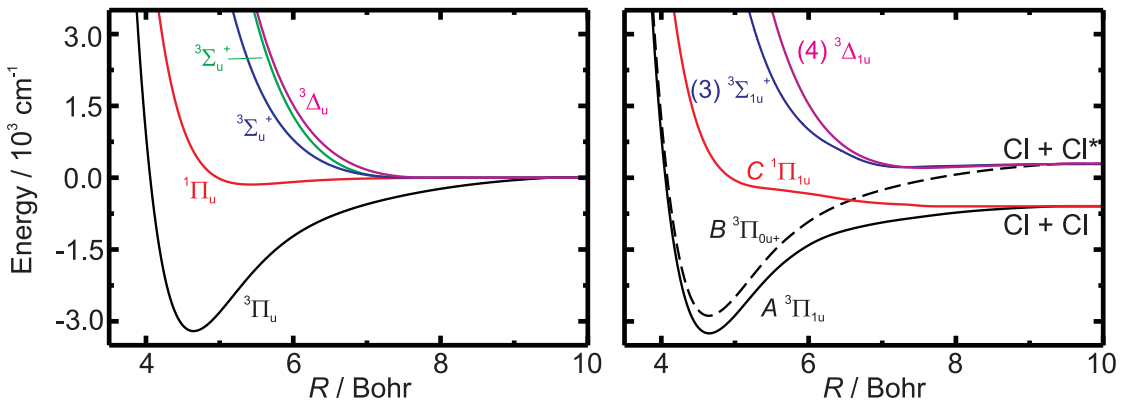

Figure 4.49: Relevant diabatic (left) and adiabatic (right) potentials for electronically excited states [51] included in the dynamics calculation.

10 *ab initio* potential energy curves [51]. The potentials included in the calculation, in both the diabatic and adiabatic representations, are shown in Figure 4.49 and listed in Table 4.8. Constant (R independent) values of the *ab initio* transition dipole moments [51] in the adiabatic representation were used in the calculation, as listed in Table 4.9. As discussed in Section 2.4.1, the wavepackets were propagated using the Chebychev method for the time evolution operator $\exp\{-i\hat{H}t/\hbar\}$ [117]. Damping of the wavepackets was performed by using a complex absorbing potential. The details of all parameters used to perform the dynamical calculation are provided in Table 4.10.

State	TDM / Debye
$A\,^3\Pi_{1u}$	0.021
$B\,^3\Pi_{0_u^+}$	0.060
$C\,^1\Pi_{1u}$	0.347
$(3)^3\Sigma_{1u}^+$	0.010

Table 4.9: *Ab initio* transition dipole moments (TDM) [51] used in the dynamics calculation.

Parameter	Value
Total propagation time / fs	32768
Time step /fs	0.5
No. of grid points	2048
Grid spacing / Bohr	0.0075
Grid range / Bohr	3.2-18.5
Analysis distance / Bohr	15.0
Start of damping potential /Bohr	15.5
Damping parameter / Bohr	0.0594
No. of Chebychev polynomials	14

Table 4.10: Parameters used in the dynamics calculation.

4.5.2 Results

Partial Cross Sections

The partial cross sections for all states correlating with the $Cl(^2P_{3/2}) + Cl(^2P_{3/2})$ and $Cl(^2P_{3/2}) + Cl^*(^2P_{1/2})$ channels, calculated from the square of the T matrix elements returned from the dynamics calculation, are shown in Figure 4.50. Superimposed on the same plot are the partial cross sections following the photodissociation of Cl_2 ($v = 0$) as calculated by Johnsen *et al.* [50]. The partial cross sections give the probability the photofragment will be found in a specific adiabatic state following photodissociation and Figure 4.51(a) and (b) show the cross sections relevant for dissociation into the ground and excited state product channels, respectively.

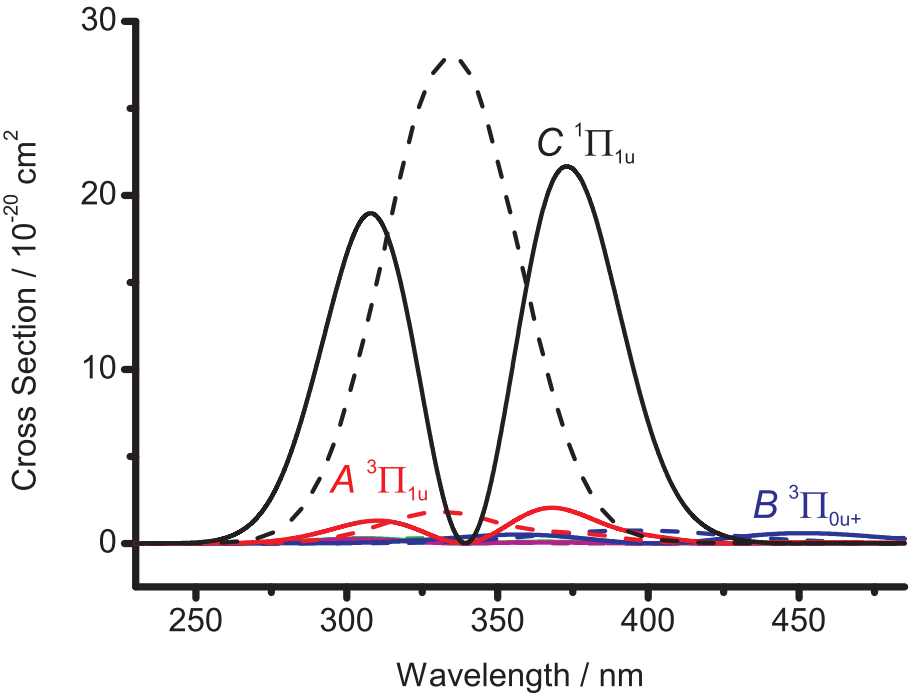

Figure 4.50: Partial cross sections for all states included in full $v = 1$ calculation (——) compared with the $v = 0$ results (- - -) [50].

The same states significant for the dissociation of Cl_2 ($v = 0$) are found to be important in the dissociation of $v = 1$ molecules. The partial cross sections themselves and the wavelengths at which they become important change significantly, however, compared to $v = 0$. Most strikingly, as a consequence of the reflection principle discussed in Section 1.2.2, the partial cross sections for all states possess a node following dissociation from $v = 1$. The node appears since the dissociation is a direct process and the shape of the partial cross sections are mostly determined from the nuclear wavefunction of the ground electronic state. In this direct dissociation process the shape of the partial cross sections ultimately comes from a reflection of the square of the $v = 1$ nuclear wavefunction. As such, the cross sections for the $v = 1$ calculation possess a minimum near the position of the maximum in the $v = 0$ cross sections.

For dissociation to the ground state product channel only the $C\,^1\Pi_{1u}$ and $A\,^3\Pi_{1u}$ states are important. The partial cross sections for these two states, Figure 4.51(a),

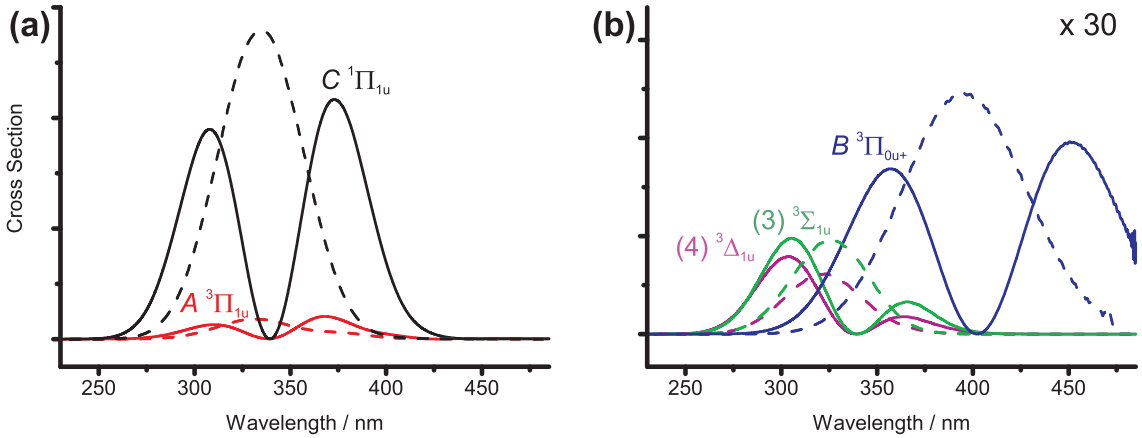

Figure 4.51: **(a)** Partial cross sections for states correlating with the ground state product channel. **(b)** Close up of partial cross sections for states correlating with the excited state product channel. $v = 1$ (——) results compared to $v = 0$ (- - -).

possess a node at around 340 nm. Furthermore, the cross section for the $C\,^1\Pi_{1u}$ state is seen to be significant at much longer (and shorter) wavelengths compared to the dissociation from $v = 0$, which has implications for the branching into the two product channels. For the excited state product channel the $B\,^3\Pi_{0_u^+}$, $(3)^3\Sigma_{1u}^+$ and $(4)^3\Delta_{1u}$ states are important, with population in the latter two arising following photoexcitation to the $C\,^1\Pi_{1u}$ state. Since dissociation on the $(3)^3\Sigma_{1u}^+$ and $(4)^3\Delta_{1u}$ state potentials comes following a non-adiabatic transition from the $C\,^1\Pi_{1u}$ state, the node in the partial cross sections appear at the same wavelength as that for the $C\,^1\Pi_{1u}$ state. The partial cross section for the $B\,^3\Pi_{0_u^+}$ state, shown in Figure 4.51(b), extends to much longer wavelengths than that for $v = 0$ dissociation. Interestingly, the partial cross sections for the $(3)^3\Sigma_{1u}^+$ and $(4)^3\Delta_{1u}$ states are somewhat different in shape to those for all other states. In particular, for these two states larger cross sections are seen on the short wavelength side of the node whereas for all other states the opposite is true, illustrating the increasing importance of the non-adiabatic transition from the $C\,^1\Pi_{1u}$ to $(3)^3\Sigma_{1u}^+$ state at shorter wavelengths.

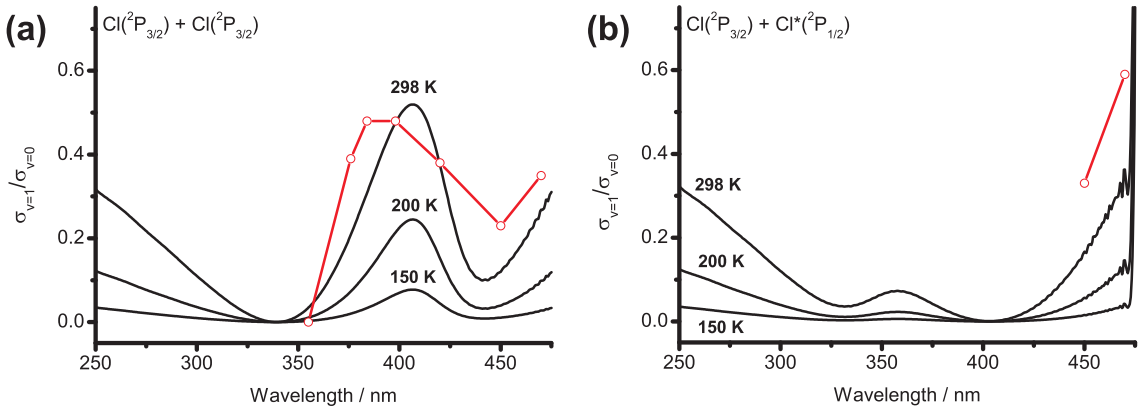

Figure 4.52: Ratio of partial cross sections for $v = 0$ and $v = 1$ calculations, $\sigma_{v=1}/\sigma_{v=0}$ (black), and experimental $(v = 1)/(v = 0)$ ratio (red) determined from intensities of the $v = 1$ and $v = 0$ signals in the ion images. Simulations based on vibrational temperatures of 150, 200 and 298 K. Data shown in **(a)** and **(b)** correspond to the ground and excited state product channels, respectively.

Vibrational 'temperature' of the molecular beam

Surprisingly large signal levels identified as arising from the photodissociation of Cl_2 $(v = 1)$ have been observed experimentally. Attempts have therefore been made to assign the likely vibrational temperature associated with the molecular beam using a combination of both experiment and theory. The partial cross sections, or rather, the sum of the partial cross sections relevant to the dissociation into the ground and excited state product channels have been determined from both the $v = 0$ and $v = 1$ calculations. Using the ratio of these two quantities, $\sigma_{v=1}/\sigma_{v=0}$, with the σ_v weighted by the vibrational populations, therefore allows simulation of this characteristic of the molecular beam. The experimental $(v = 1)/(v = 0)$ ratio was calculated using the intensity of the relevant features in the experimental ion images. Reassuringly, the ratio of the theoretical partial cross sections, $\sigma_{v=1}/\sigma_{v=0}$, was found to qualitatively follow the wavelength dependent behaviour observed experimentally. In particular, a 'vibrational temperature' of 298 K appeared to model the experimental data reasonably well, as shown in Figure 4.52.

The simulations suggest that there is little or no cooling of the vibrational degree of freedom in the molecular beam. As discussed in Section 4.3.2, in relation

to the near limiting spatial anisotropy parameters, β, observed for the ground state product channel, the rotational degrees of freedom are cooled efficiently, with the experimental data consistent with low rotational temperatures, $< 10\,\mathrm{K}$. In general, cooling of the rotational degrees of freedom is much more efficient than for vibrations in supersonic molecular beams. Aside from hydrogen, which has a very large rotational constant, the rotational energy of the molecules in a molecular beam is equilibrated within $\sim$ tens of collisions and the energy removed from rotation converted to translational energy along the propagation direction of the beam [157]. For vibrations of energy $> k_{\mathrm{B}}T$ it may take an order of magnitude more collisions for the vibrational energy to be equilibrated and the cooling of these in a molecular beam can therefore be very inefficient [157].

Cl*(^{2}P$_{1/2}$)/Cl(^{2}P$_{3/2}$) branching ratio and β parameter

Figure 4.53(a) displays the theoretical Cl*(^{2}P$_{1/2}$)/Cl(^{2}P$_{3/2}$) branching ratio, as defined in Equation (4.1), for the $v = 1$ calculation. Also shown are the previously reported theoretical values for the photodissociation of Cl_2 ($v = 0$) [50]. The excited state product channel becomes significant at much longer wavelengths, $\sim 420\,\mathrm{nm}$, relative to the dissociation from $v = 0$ where Cl*(^{2}P$_{1/2}$) starts to increase near 370 nm. Furthermore, the slope of Cl*(^{2}P$_{1/2}$)/Cl(^{2}P$_{3/2}$) is much steeper for the $v = 1$ species, reflecting the gradients of the partial cross sections for the $C\,^1\Pi_{1u}$ and $B\,^3\Pi_{0_u^+}$ states in the region $420 - 440\,\mathrm{nm}$, and ultimately gives rise to relatively more excited state products in the long wavelength region. The sharp spike in the branching ratio near 340 nm can be understood in terms of the nodes in the partial cross sections correlating with the ground state product channel, see Figure 4.51. At 340 nm the partial cross sections for both the $C\,^1\Pi_{1u}$ and $A\,^3\Pi_{1u}$ states are zero and only the $B\,^3\Pi_{0_u^+}$ state contributes to the dissociation. Since the $B\,^3\Pi_{0_u^+}$ state is associated with the excited state product channel a sharp peak is observed in the Cl*(^{2}P$_{1/2}$)/Cl(^{2}P$_{3/2}$) branching ratio. Reassuringly, as with the $v = 0$ data, the experimental measurements appear to be in good agreement with the theoretically

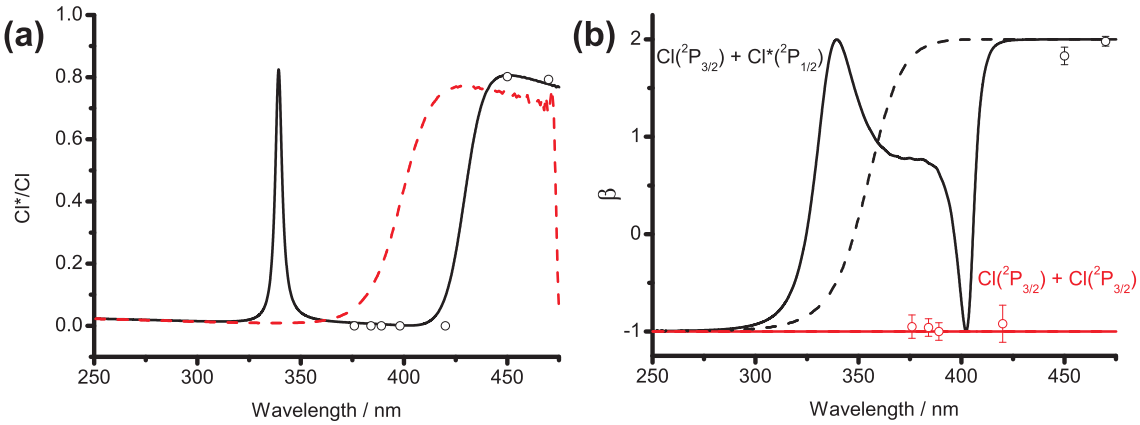

Figure 4.53: **(a)** Branching ratio, $Cl^*(^2P_{1/2})/Cl(^2P_{3/2})$, for $v = 1$ (——) and $v = 0$ (- - -). **(b)** Spatial anisotropy parameter, β, for $v = 1$ (——) and $v = 0$ (- - -). Experimental data represented by open circles.

predicted branching ratio.

The spatial anisotropy parameter, β, for both dissociation channels is shown in Figure 4.53(b). Like the dissociation of Cl_2 ($v = 0$), the angular distribution of the ground state product channel is seen to be wavelength independent and characterised by $\beta = -1$. Experimental measurements for this dissociation channel at all wavelengths are in good accord with the theory, all within error of the predicted limiting value. For the excited state product channel the β parameter is wavelength dependent, reaching a limiting parallel transition value at long wavelengths, similar to the dissociation of Cl_2 ($v = 0$). Near 400 nm the β parameter for this channel suddenly drops from a limiting +2 to −1. At this wavelength a node appears in the partial cross section for the $B\,^3\Pi_{0_u^+}$ state, Figure 4.51, with the only non-zero contributions to the dissociation channel arising from the $(3)^3\Sigma_{1u}^+$ and $(4)^3\Delta_{1u}$ states. Both of these $\Omega = 1$ states arise following a perpendicular transition to the $C\,^1\Pi_{1u}$ state which therefore results in a β of −1 at this wavelength. Moving to shorter wavelengths β increases quickly reaching positive values, reflecting the relative importance of the $B\,^3\Pi_{0_u^+}$, $(3)^3\Sigma_{1u}^+$ and $(4)^3\Delta_{1u}$ states, again reaching a limiting value of +2 at 340 nm. At this wavelength, as mentioned above with regards to the spin-orbit branching ratio, a node appears in the partial cross section for the $C\,^1\Pi_{1u}$ state

and thus for both the $(3)^3\Sigma^+_{1u}$ and $(4)^3\Delta_{1u}$ states, and only the parallel character $B\,^3\Pi_{0^+_u}$ state makes a contribution to the dissociation. Beyond 340 nm, the β parameter declines sharply to -1 as the short wavelength wing of the $B\,^3\Pi_{0^+_u}$ state partial cross section decreases to zero.

Given the low $Cl^*(^2P_{1/2})/Cl(^2P_{3/2})$ branching ratio at wavelengths > 420 nm, dissociation of Cl_2 ($v = 1$) into the excited state product channel was only observed experimentally at two wavelengths, both in the long wavelength tail of the absorption. The experimental data at 470 nm is in good agreement with the theoretical value of $+2$ with the value determined for dissociation at 450 nm slightly smaller at 1.82, but in agreement with the results for $v = 0$.

$Cl(^2P_{3/2})$ alignment in the $Cl(^2P_{3/2})$ + $Cl^*(^2P_{1/2})$ channel

At wavelengths > 420 nm the dissociation into the excited state product channel can be viewed as an adiabatic process taking place on the $B\,^3\Pi_{0^+_u}$ state potential. In this region the theoretical spatial anisotropy parameter $\beta = 2$ and only non-zero incoherent polarisation parameters are expected. The values of s_2 and α_2, -0.16 and 0.16, respectively, are consistent with this picture and zero contributions are found to arise from coherent processes. The experimental data in this region are in excellent agreement with theory.

Moving to shorter wavelengths the magnitudes of both s_2 and α_2 decrease sharply reaching a minimum near 400 nm. As mentioned previously with regards to the $Cl^*(^2P_{1/2})/Cl(^2P_{3/2})$ branching and β parameter, a node appears in the partial cross section for the $B\,^3\Pi_{0^+_u}$ state near this wavelength. In the region $340 - 400$ nm the incoherent parameters follow the same trend as a function of wavelength as seen for the spatial anisotropy parameter, Figure 4.53(b), reflecting the relative importance of the $B\,^3\Pi_{0^+_u}$, $(3)^3\Sigma^+_{1u}$ and $(4)^3\Delta_{1u}$ states to the dissociation in this region. Both parallel-perpendicular and perpendicular-perpendicular coherent parameters show oscillatory structure in this region, resulting from interferences between the different routes taken to the dissociation channel.

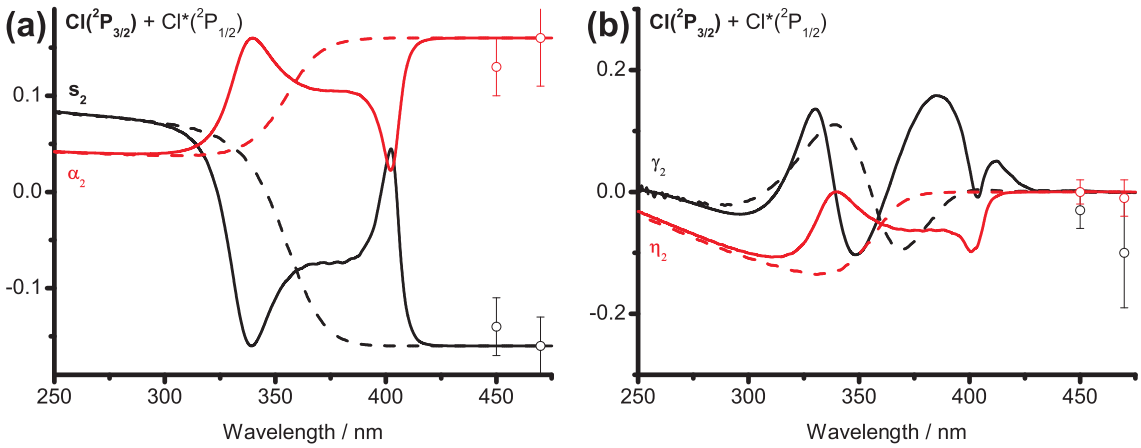

Figure 4.54: Incoherent **(a)** and coherent **(b)** $K = 2$ alignment parameters for $v = 1$ (——) and $v = 0$ (- - -) dissociation into the excited state product channel. Experimental data returned from fits to $Cl(^2P_{3/2})$ Fourier moments represented by open circles.

At 340 nm the node in the $(3)^3\Sigma^+_{1u}$ and $(4)^3\Delta_{1u}$ state partial cross sections means the dissociation occurs adiabatically on the $B\,^3\Pi_{0^+_u}$ state potential and so s_2 and α_2 reach limiting values. The coherent parameters γ_2 and η_2 both go to zero at this wavelength, as shown in Figure 4.54(b), illustrating the adiabatic nature of the process. Below 300 nm contributions to the dissociation channel from the $B\,^3\Pi_{0^+_u}$ state are very small and the coherent γ_2 parameter approaches zero. Here only the perpendicular $(3)^3\Sigma^+_{1u}$ and $(4)^3\Delta_{1u}$ states are involved and so $s_2 = 2\alpha_2$, with non-zero values of η_2 also predicted.

$Cl(^2P_{3/2})$ polarisation in the $Cl(^2P_{3/2})$ + $Cl(^2P_{3/2})$ channel

The $K = 2$ alignment for the ground state product channel is shown in Figure 4.55. Similar to the dissociation of Cl_2 ($v = 0$), at short wavelengths the dissociation may be viewed as a mostly adiabatic process taking place on the $C\,^1\Pi_{1u}$ state potential. Below 325 nm the incoherent parameter s_2 is close to the limiting value of -0.16, with $s_2 = 2\alpha_2$, as expected following adiabatic dissociation on the perpendicular $C\,^1\Pi_{1u}$ state potential. The sharp structure seen at 340 nm is a consequence of the node in the partial cross section for the $C\,^1\Pi_{1u}$ state. Interestingly, the incoherent

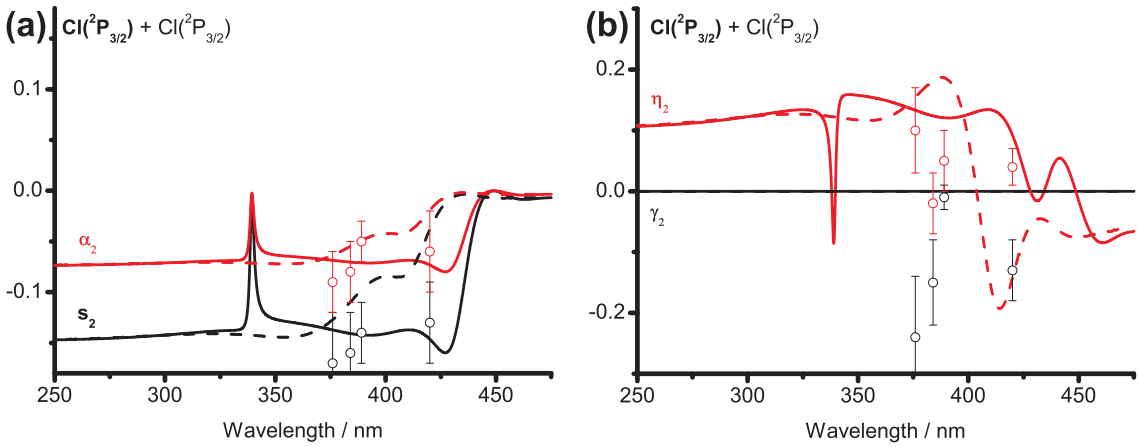

Figure 4.55: Incoherent **(a)** and coherent **(b)** $K = 2$ alignment parameters for $v = 1$ (——) and $v = 0$ (- - -) dissociation into the ground state product channel. Experimental data returned from fits to $Cl(^2P_{3/2})$ Fourier moments represented by open circles.

parameters s_2 and α_2 appear symmetrical for ~ 75 nm either side of the node at 340 nm, reflecting the double structure in the partial cross sections, Figure 4.51. Around 425 nm the incoherent parameters decrease in magnitude. This reduction takes place at much longer wavelengths than that seen for Cl_2 ($v = 0$). The decrease in magnitude of the incoherent parameters for $v = 0$ was understood to reflect the increasing importance of the non-adiabatic pathway to the dissociation. For $v = 1$ the decrease of s_2 and α_2 to 0 occurs much more rapidly than the gradual decrease seen for $v = 0$. The experimental measurements of these parameters are in excellent agreement with the theoretical values.

Similar to Cl_2 ($v = 0$) theory predicts no parallel $\Omega = 0$ state is involved in the dissociation into the ground state product channel and therefore $\gamma_2 = 0$. The η_2 parameter, which arises from interference between the $C\,^1\Pi_{1u}$ and $A\,^3\Pi_{1u}$ state pathways, shows similar short wavelength behaviour to that following $v = 0$ dissociation. The change in sign of this parameter, however, occurs at longer wavelengths than observed for $v = 0$, reflecting the differences in the importance of the $C\,^1\Pi_{1u}$ to $A\,^3\Pi_{1u}$ state non-adiabatic transition as discussed above with respect to the incoherent alignment parameters. The experimental data seems to be in reasonable accord

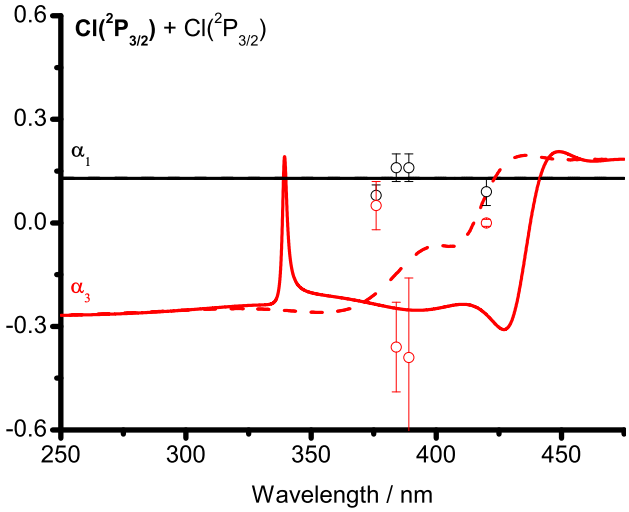

Figure 4.56: Incoherent $K = 1$ and 3 orientation parameters for $v = 1$ (——) and $v = 0$ (- - -) dissociation into the ground state product channel. Experimental data returned from fits to $Cl(^2P_{3/2})$ Fourier moments represented by open circles.

with theory, although in less good agreement than for the incoherent parameters.

Both $K = 1$ and $K = 3$ incoherent orientation have been measured experimentally for dissociation into $Cl(^2P_{3/2}) + Cl(^2P_{3/2})$, as shown in Figure 4.56. The α_1 parameter is wavelength independent since only the $C\,^1\Pi_{1u}$ and $A\,^3\Pi_{1u}$ states are involved in the dissociation, as discussed in Section 4.3.2 with regards to the orientation for dissociation of $v = 0$. The α_3 parameter, however, like the incoherent alignment parameters is symmetrical about the node at 340 nm, reflecting the symmetry of the partial cross sections. At longer wavelengths this parameter decreases in magnitude as a result of the increasing importance of the non-adiabatic effects.

Table 4.11 summarises the angular and angular momentum polarisation data returned from the fits to the $Cl(^2P_{3/2})$ Fourier moments.

4.6 Summary

The photodissociation of molecular chlorine has been investigated at a range of energies from close to the peak in the absorption spectrum, 355 nm, out to the long wavelength region, 470 nm. Experimentally, the velocity map ion imaging technique has

	Wavelength / nm					
Parameter	376	384	389	420	450	470
β	-0.95(12)	-0.96(9)	-1.00(9)	-0.92(19)	1.83(9)	1.98(5)
s_2	-0.17(5)	-0.16(4)	-0.14(3)	-0.13(4)	-0.14(3)	-0.16(3)
α_2	-0.09(3)	-0.08(3)	-0.05(2)	-0.06(4)	0.13(3)	0.16(5)
γ_2	-0.24(10)	-0.15(7)	-0.01(2)	-0.13(5)	-0.03(3)	-0.10(9)
η_2	0.10(7)	-0.02(5)	0.05(5)	0.04(3)	0.00(2)	-0.01(3)
α_1	0.08(3)	0.16(4)	0.16(4)	0.09(4)	0.03(2)	-
γ_1	-0.07(4)	-0.03(4)	-0.09(5)	0.00(2)	-0.08(8)	-
γ_1'	0.05(7)	-0.02(4)	0.01(5)	0.00(5)	-	-
α_3	0.05(7)	-0.36(13)	-0.39(23)	0.00(1)	-0.05(14)	-
γ_3	0.31(16)	-0.15(5)	-0.38(26)	0.04(1)	-0.37(33)	-
γ_3'	0.16(39)	0.05(3)	0.51(33)	0.08(2)	-	-
η_3	-0.19(10)	0.36(9)	0.09(23)	0.02(1)	-	-

Table 4.11: Spatial anisotropy and angular momentum polarisation parameters for the $Cl(^2P_{3/2})$ fragments from the returned from the fits to experimental Fourier moments. For wavelengths $376-420$ nm data shown for the ground state product channel. For 450 nm and 470 nm data corresponds to the excited state product channel. Errors (1σ) in the last digit(s) are given in parenthesis.

been used to probe the speed, angular and angular momentum distributions of the resulting atomic fragments. Both $Cl(^2P_{3/2})$ and $Cl^*(^2P_{1/2})$ species have been probed with the electronic alignment and orientation of both the $Cl(^2P_{3/2}) + Cl(^2P_{3/2})$ and $Cl(^2P_{3/2}) + Cl^*(^2P_{1/2})$ product channels investigated.

The experimental results presented here have been compared to the recent time dependent wavepacket calculations [50] performed on a set of high level *ab initio* potentials [152]. The calculations provide the first prediction of all angular momentum polarisation information amenable to the Cl_2 system. From this detailed study high order, $K = 3$, polarisation was predicted to be important for the $Cl(^2P_{3/2})$ photofragments. The current work provides the first experimental measurements of such orientation moments. In general good agreement was found between experiment and theory, and the previous experimental measurements, with any discrepancies discussed in Section 4.7 with a view to future work.

The data presented here generally support the previously made assertions regarding the subtle mechanisms by which the Cl_2 molecule dissociates. The $Cl(^2P_{3/2}) + Cl(^2P_{3/2})$ product channel dominates the short wavelength region with excitation to and adiabatic dissociation on the $C\,^1\Pi_{1u}$ state potential giving rise to the majority of the products. As the wavelength increases a significant non-adiabatic transition from the $C\,^1\Pi_{1u}$ to $A\,^3\Pi_{1u}$ state takes place, with the effects of this encoded in both the experimental and theoretical polarisation parameters. At the other end of the absorption spectrum the $Cl(^2P_{3/2}) + Cl^*(^2P_{1/2})$ channel dominates with excitation to and adiabatic dissociation occurring on the $B\,^3\Pi_{0_u^+}$ state potential. At shorter wavelengths perpendicular components to the dissociation channel become important. In particular, a non-adiabatic transition from the $C\,^1\Pi_{1u}$ to $(3)^3\Sigma_{1u}^+$ state takes place and results in the $Cl(^2P_{3/2}) + Cl^*(^2P_{1/2})$ channel developing purely perpendicular character. Moreover, an additional transition takes place to the $(4)^3\Delta_{1u}$ state giving rise to coherent polarisation resulting from two perpendicular electronic transitions. Where the $B\,^3\Pi_{0_u^+}$, $(3)^3\Sigma_{1u}^+$ and $(4)^3\Delta_{1u}$ state dissociation pathways overlap, significant interference effects result.

Furthermore, both experimental and theoretical work has been presented regarding the photodissociation of vibrationally excited Cl_2. Although the electronic states involved in the photodissociation of Cl_2 ($v = 1$) were found to be the same as for Cl_2 ($v = 0$), significant differences were found regarding the observables. The differences were discussed in terms of the partial cross sections for dissociation into the two product channels. Good agreement was found between the experimental measurements, the first presented for $v = 1$, and the theoretical calculations. Using a combination of both theory and experiment it was discovered that negligible cooling of the vibrational degree of freedom takes place in the molecular beam.

4.7 Future work

The results presented here point to several possibilities regarding future experimental and theoretical work. Although in good general agreement with theory, the experimental polarisation data for dissociation into the ground state product channel carry the fingerprints of a parallel, $\Omega = 0$, state. No such state has previously been discussed, and could only arise through two mechanisms. Either a direct excitation could take place to one of the two $\Omega = 0$ states correlating with the product channel or a Coriolis type coupling, $\Delta\Omega = \pm 1$, could give rise to population in one of these states as the dissociation proceeds. The second mechanism could be investigated relatively easily by monitoring the dissociation as a function of the rotational temperature of the molecular beam.

Another slight discrepancy with theory was found at 450 nm, where the measured spatial anisotropy seemed to be somewhat smaller than the limiting values predicted by theory. It would be useful to know whether this measurement reflected the experimental conditions at this particular wavelength, namely the rotational temperature of the molecular beam, or the underlying dissociation dynamics, since this would have strong implications for the underlying mechanism, currently understood to be adiabatic dissociation on the $B\,^3\Pi_{0_u^+}$ state potential. A disagreement between experiment and theory was found regarding the position at which the spa-

tial anisotropy parameter, β, starts to decrease from its limiting value of +2 in the excited state product channel. While the theory appears to predict correctly both the $Cl^*(^2P_{1/2})/Cl(^2P_{3/2})$ branching ratio and the shape of the experimentally observed decrease in β, the wavelength at which this takes place is shifted somewhat. Further electronic structure studies would therefore be useful in order to understand this effect.

Regarding the photodissociation of vibrationally excited Cl_2 it would be interesting to investigate the dynamics at shorter wavelengths than probed here. In particular, it would useful to study the region around 340 nm where a node appears in both partial cross sections of the states correlating with the $Cl(^2P_{3/2}) + Cl(^2P_{3/2})$ product channel. At this wavelength a sharp peak in the $Cl^*(^2P_{1/2})/Cl(^2P_{3/2})$ branching ratio is expected as all molecules dissociate to the excited state product channel. Measurements in this region would prove a stringent test of the current *ab initio* potentials.

In the present study, the coherences describing the correlations between photofragments in different M_J levels have been investigated. By using femtosecond techniques, however, it may be possible to probe coherences between the $Cl(^2P_J)$ spin-orbit states of the photofragments in future experimental studies. Further possibilities for new experiments on this system include the investigation of electronic polarisation effects following the photodissociation of a coherently prepared sample of Cl_2 in $v = 0$ and $v = 1$. In addition, the current theoretical treatment of polarisation effects in photodissociation deals with the case in which only one of the photofragments is detected. It may be possible, however, to use ion imaging techniques to probe the electronic polarisation of the two fragments born in coincidence. In a system such as Cl_2, in which determination of all T matrix elements through the detection of only one fragment is possible, this may not reveal new information. However, in a general sense, the detection of both fragments atomic polarisation could reveal fascinating new information on molecular photodissociation.

Chapter 5

Photodissociation of CS_2 : the $S(^1D_2)$ channel

In this chapter experimental results on the photodissociation of CS_2 at several wavelengths are presented. The results come from two sets of experiments, the first corresponding to dissociation at 193.3 nm, and the second regarding the state-to-state dissociation at lower energies close to the $S(^1D_2)$ channel threshold. Whereas the results at 193.3 nm follow electronic excitation above the barrier to linearity in the $(^1B_2)^1\Sigma_u^+$ state, the state-to-state results are relevant to excitation below this energetic barrier. In this region the structured features in the absorption spectrum correspond to vibronic transitions taking place to the combined bending and symmetric stretching levels in the excited state. Given the low bending frequency of ground state CS_2, transitions also take place starting from excited bending levels in the ground electronic state, giving rise to rich absorption structure. In this chapter the results of experiments following excitation of different features in the absorption spectrum are compared and contrasted. Comparisons are also drawn with the photodissociation of the isovalent molecule OCS.

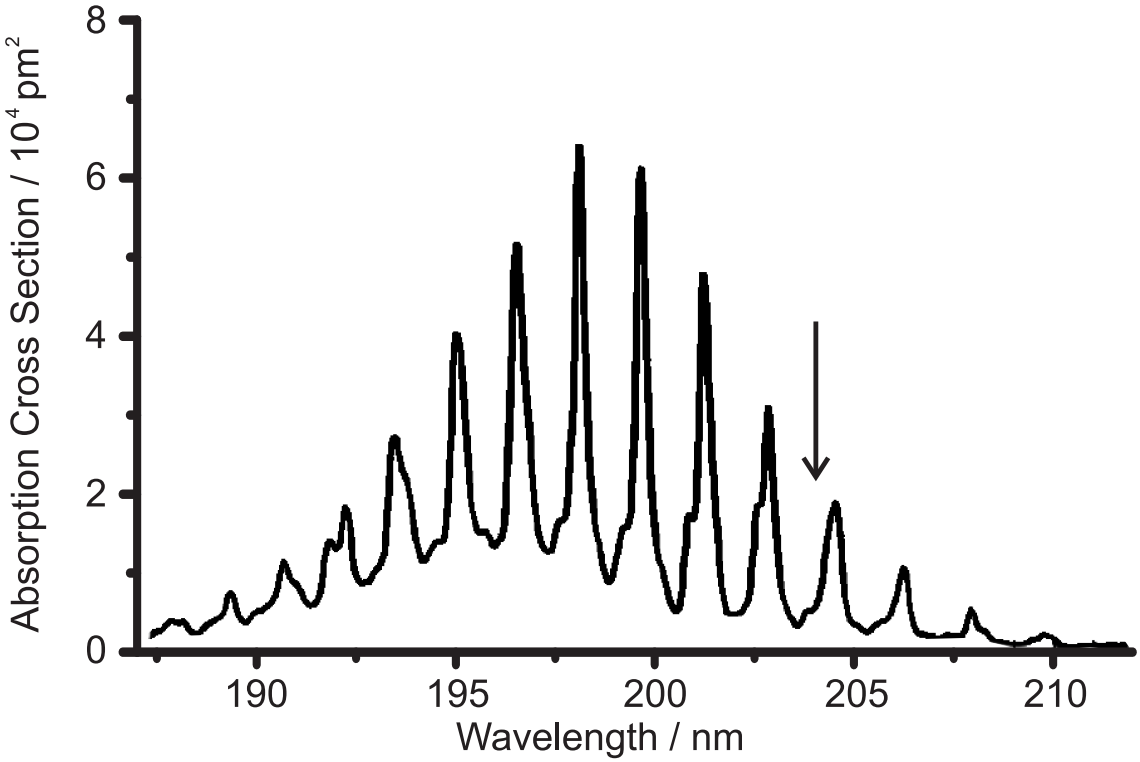

Figure 5.1: 300 K ultraviolet absorption spectrum of CS_2, corresponding to the $^1B_2(^1\Sigma_u^+) \leftarrow \widetilde{X}^1\Sigma_g^+$ transition. The barrier to linearity in the $^1B_2(^1\Sigma_u^+)$ state is located near 204 nm, as indicated by the arrow. Adapted from Ref [168].

5.1 Background

Extensive spectroscopic literature dating back to the 1960s exists on the ultraviolet absorption of CS_2 in the region $43{,}000 - 54{,}000\,\mathrm{cm}^{-1}$ [158–167], corresponding to the transition from the linear $...(\pi_g)^4\ \widetilde{X}\ ^1\Sigma_g^+$ ground state to the $...(\pi_g)^3\ (\pi_u^*)^1\ ^1\Sigma_u^+(^1B_2)$ excited state in a fully allowed parallel ($\Delta\Omega = 0$) transition. The intense absorption band is shown in Figure 5.1. Analysis of the absorption spectra show that the equilibrium geometry of the excited electronic state changes at higher energies, $\sim 49{,}000\,\mathrm{cm}^{-1}$, from bent to linear nuclear configurations, with these two regions of the $^1\Sigma_u^+(^1B_2)$ potential separated by an energetic barrier to linearity [158, 165]. Above the barrier to linearity the spectrum appears to consist of a series of bands separated by $\sim 410\,\mathrm{cm}^{-1}$, consistent with progressions in the near degenerate symmetric stretching and bending modes of the excited state, ν_1 and ν_2, respectively, and

in the bending mode of the ground state, ν_2''. Unfortunately, however, the features in the absorption spectrum are not well described using a simple harmonic picture. Furthermore, since the three modes are near degenerate, $\nu_1 \sim \nu_2 \sim \nu_2'' \simeq 400\,\mathrm{cm}^{-1}$, and of the same symmetry species in the C_{2v} point group, at energies below the barrier ($< 204\,\mathrm{nm}$) this leads to a highly complicated, perturbed and irregularly spaced absorption spectrum.

The low energy region of the absorption spectrum lies close to the energetic threshold for dissociation into the $CS(X^1\Sigma^+) + S(^1D_2)$ product channel, where the CS_2 molecule may be described as a near-prolate symmetric top allowing the quantum number K to be used [159]. K represents the projection of total (electronic + vibrational, $[\Lambda + l]$) angular momentum on the figure axis, also referred to as the a-axis. For the linear ground state, the electronic angular momentum, $\Lambda = 0$, so that $K'' = l''$. For a parallel type transition the selection rule $\Delta K = K' - K'' = 0$ [169] means that the projection quantum number K' must be equal to the vibrational angular momentum in the ground electronic state, $K' = l''$. Absorption bands are labelled with the greek letters Σ, Π, Δ *etc.* for transitions arising from $K''(= l) = 0, 1$ and 2 levels. Vibrational angular momentum may arise due to excitation of a degenerate vibrational mode [169], which for linear CS_2 restricts the source of this angular momentum to the bending mode, ν_2''. The manifestation of vibrational angular momentum, l, in the case of a triatomic may be intuitively visualised by superimposing the two degenerate, perpendicular, bending motions with a certain phase shift, as illustrated in Figure 5.2. As shown, the nuclei will move around the axis in a circular motion giving rise to an angular momentum about the figure axis.

The $^1\Sigma_u^+(^1B_2)$ state is predissociative, and there are two energetically accessible product channels following excitation with the wavelengths used here, leading to sulfur atoms of singlet and triplet spin multiplicity

$$CS_2 + h\nu \longrightarrow CS(X^1\Sigma^+) + S(^1D_2) \tag{5.1}$$

$$CS_2 + h\nu \longrightarrow CS(X^1\Sigma^+) + S(^3P_{2,1,0})\,. \tag{5.2}$$

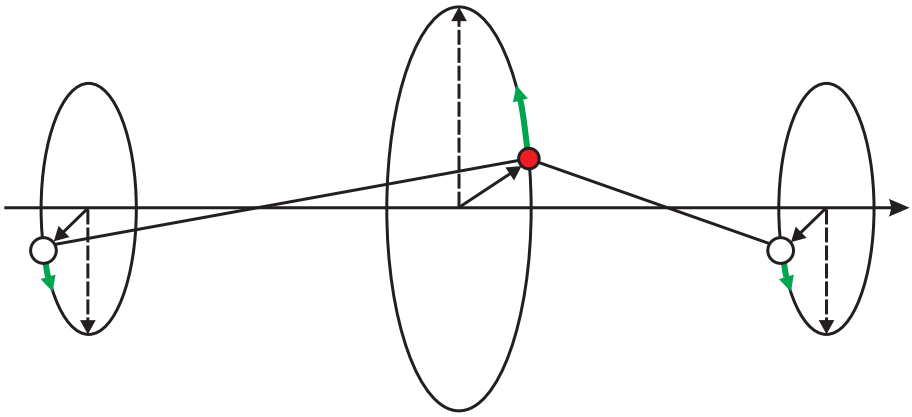

Figure 5.2: Schematic illustration of the source of vibrational angular momentum in a triatomic molecule. The two degenerate bending modes are represented by the solid and dashed arrows. Adapted from Ref [169].

In both cases, the CS co-fragment is formed in its electronic ground state, $X(^1\Sigma^+)$. The majority of work on CS_2 dissociation has been carried out at 193.3 nm, however, there have also been a few studies where the excitation has taken place below the barrier to linearity. The previous work is summarised in the following sections.

Previous work below the barrier

Hepburn and co-workers performed a detailed photodissociation study at wavelengths across the absorption band from $198 - 214$ nm [170, 171]. Their study was carried out by dissociating a jet cooled sample of CS_2 seeded in He using a tuneable dye laser system with detection of the $S(^1D_2)$ and $S(^3P_2)$ photofragments using laser induced fluorescence (LIF). The resulting photofragment excitation (PHOFEX) spectra showed drastic differences depending on whether the $S(^1D_2)$ or $S(^3P_J)$ atomic species were probed. In particular, the major products following excitation of Σ bands were found to be $S(^3P_2)$ species, with the $S(^3P_2)/S(^1D_2)$ branching ratio of 1.96 ± 0.17 at higher energies (198 nm) in good agreement with previous work at 193.3 nm [172]. Relative to excitation of a Σ band, significantly more $S(^1D_2)$ photofragments were observed when a Π band was excited. Furthermore, analysis of their PHOFEX spectra indicated much shorter lifetimes associated with these

hot bands [170, 171]. The overall picture led to the description of a mode specific dissociation, with K enhancing both the dissociation rate and the $S(^1D_2)/S(^3P_2)$ electronic branching ratio [170, 171]. Based on some preliminary *ab initio* work, Hepburn and co-workers suggested a mechanism for producing $S(^1D_2)$ atoms [171] involving photoexcitation to the $^1\Sigma_u^+(^1B_2)$ state, followed by crossing to a purely repulsive state of $^1\Pi_g$ symmetry. As the molecule bends, the $^1\Pi_g$ state splits into a $^1A_2$ + $^1B_2$ Renner-Teller pair in C_{2v} geometries, and an avoided crossing results between the photo-excited $^1B_2$ state and the $^1B_2$ component derived from the Π state. The overall picture was therefore of a conical intersection between these two states [171], and passage through this conical intersection could then allow predissociation into $CS(X^1\Sigma^+)$ + $S(^1D_2)$. The recent *ab initio* calculations by Bisgaard *et al.* are in agreement with this picture and point to an additional conical intersection with a $^1\Delta_u$ state further along the dissociation co-ordinate [173]. The $^1B_2$ components derived from the Σ and Π states are shown in Figure 5.3. Until recently, no information was available about the states giving rise to triplet products, although one expects spin-orbit coupling of the $^1\Sigma_u^+(^1B_2)$ excited state with triplet states of Σ_g^- or Π_g symmetry to give rise to these products. The schematic potential energy curves by Townsend *et al.* are qualitatively in agreement with this picture [174]. Slices through the *ab initio* potentials calculated by Stolow and co-workers are shown in Figure 5.4 including the repulsive $^3\Pi_g$ state [173].

In their laser induced fluorescence (LIF) study Liou *et al.* investigated the dissociation following excitation at 210 nm. The authors reported a lifetime of 4.4 ps for the level accessed at 210 nm and observed the $CS(X^1\Sigma^+)$ fragments in vibrational levels up to $v = 6$, with the higher vibrational levels necessarily arising from dissociation to the triplet channel [175]. In a later study, Liou *et al.* used the stimulated emission pumping (SEP) technique to prepare specific rotational levels in the excited state. In this study, also concerning the band at 210 nm, comparisons were made between the dissociation process initiated from the vibrationless ground state (0,0,0) with that from a highly vibrationally excited ground state (3,18,0). The predissoci-

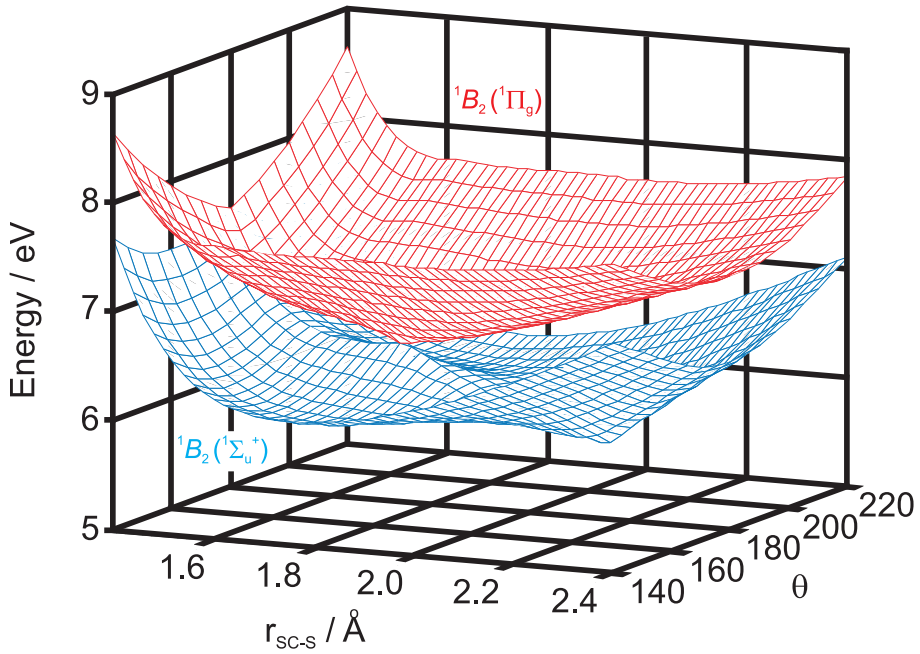

Figure 5.3: *Ab initio* $^1B_2$ potentials derived from the excited Σ and Π states as a function of asymmetric stretching co-ordinate and bending angle, see text for details. The other CS bond length is fixed at 1.55 Å. Adapted from Ref [173].

ation was found to be twice as fast for the photodissociation of vibrationally excited ground state molecules, relative to dissociation following excitation of (0,0,0) [176].

By using a heated supersonic nozzle, Chen *et al.* were able to investigate the effects of hot band excitation on the dissociation in the region 210 − 216 nm [177]. Predissociation lifetimes and $S(^1D_2)/S(^3P_2)$ branching ratios were determined from photofragment excitation (PHOFEX) and laser induced fluorescence (LIF) spectra. The use of a heated nozzle allowed bands with up to $K = 2$ to be observed for the upper vibrational states accessed. Chen *et al.* reported a strong dependence of both the lifetime and branching ratios on the quantum number K. In particular they found that the lifetimes decreased and $S(^1D_2)/S(^3P_2)$ branching ratio increased with increasing K [177]. The authors concluded that predissociation of CS_2 giving rise to the $S(^1D_2)$ channel occurs through more bent nuclear geometries than that for the $S(^3P_J)$ channel [177].

In a more recent ion imaging study, Lin and co-workers recorded (1+1) REMPI

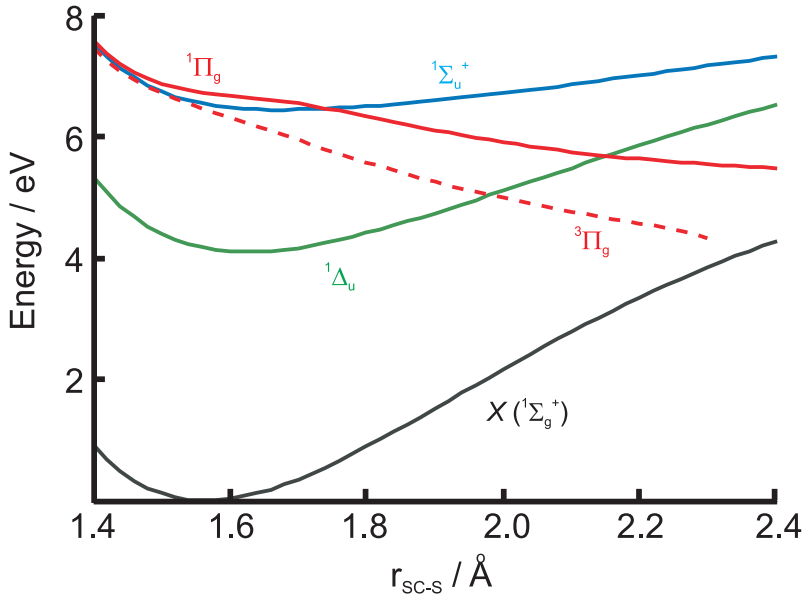

Figure 5.4: Slices, at linearity, through the potentials relevant to $S(^1D_2)$ channel dissociation as a function of asymmetric stretching co-ordinate. Adapted from Ref [173].

spectra of jet cooled CS_2 [178]. The (1+1) REMPI process consists of excitation to the $^1\Sigma_u^+(^1B_2)$ state followed by a one-photon ionisation, with the spectra generated in this manner therefore similar to true absorption spectra. Analysis of their (1+1) REMPI spectra gave rise to excited state lifetimes in the range $0.3 - 3$ ps, in accord with previous lifetime measurements [171, 179, 180]. The authors also recorded ion images of both the CS and S fragments at two dissociation wavelengths, 210.25 nm and 212.54 nm, which were assigned as the (1,3,0) $\leftarrow$ (0,1^1,0) and (2,0,0) $\leftarrow$ (0,0,0) transitions, respectively. Although the authors did not use a state selective detection method they reported values of the anisotropy parameter, β, of ~ 0.8 for the $S(^3P_J)$ channel at both dissociation wavelengths and values of ~ 1.3 and ~ 1.1 for 210.25 and 212.54 nm dissociation to the $S(^1D_2)$ channel, respectively. Analysis of the CS_2 (1+1) REMPI spectrum revealed lifetimes of 1.5 ± 0.3 and 2.7 ± 0.4 ps following excitation at 210.25 nm and 212.54 nm, respectively [178].

Previous work above the barrier

Absorption at 193.3 nm excites close to a peak in the absorption spectrum that is believed to belong to a progression in the combined symmetric stretching and bending modes of the quasi-linear molecule [158, 166]. Photodissociation at the argon fluoride excimer wavelength has been the subject of numerous experimental studies using a variety of different techniques. Unfortunately, despite the attention paid to the dissociation at 193.3 nm, considerable disagreement remains in the literature regarding many of the experimental observables. Branching ratios for production of ground and excited state sulfur atoms, $S(^3P_J)/S(^1D_2)$, have been reported to range from as low as 0.25 to as high as 6.0 [23, 172, 174, 181–185], although the more recent ion imaging studies suggest values of 1.5 ± 0.4 and 1.6 ± 0.3 [186, 187]. These values are somewhat smaller than the previously accepted branching ratio of 2.8 ± 0.3 measured by Waller and Hepburn [172], which was in good agreement with the results of two time of flight mass spectrometry (TOF MS) studies [188, 189]. For the singlet channel the $CS(X^1\Sigma^+)$ products can be formed in vibrational levels up to $v_{\max} = 5$, while for the triplet channel they can be vibrationally excited up to $v_{\max} = 13$, and, broadly speaking, there is consensus regarding the energy partitioning in the two channels. For the singlet channel, several studies have reported the distribution among CS vibrational levels to reach maxima around $v = 2$ [186] or $v = 3$ [172, 181, 188, 189]. For the triplet channel, $S(^3P_J)$ kinetic energy distributions are found to be broader and much less structured than for the singlet channel, implying maxima in the CS co-fragment vibrational populations in the range $7 \leq v \leq 10$ [172, 181, 188, 189]. Some limited data concerning the rotational distributions of $CS(X^1\Sigma^+)$ is also available and is discussed in Section 5.3.1 with respect to the experimentally determined $S(^1D_2)$ speed distribution.

Angular distributions of the $S(^1D_2)$ and $S(^3P_J)$ atomic products formed at 193.3 nm have also been reported in several studies, although there is some degree of disagreement in these measurements. For the singlet channel, the reported values of the spatial anisotropy parameter, β, range from 0.2, corresponding to an

almost isotropic angular distribution, to an almost limiting value of ~ 2, while for the triplet channel the reported values range from 0.2 to 1 [172, 174, 186, 187, 190]. Where the β parameter has been used to infer the lifetime, this disagreement has inevitably led to uncertainty in this property, with reported values ranging from $0.6 - 2.0$ ps. Direct measurements of the lifetimes near 200 nm suggest that the dissociation is associated with a shorter timescale, approaching 180 fs at 194 nm [191]. The more recent time resolved photoelectron spectroscopy studies of Stolow and co-workers, also at wavelengths around 200 nm, support these shorter dissociation lifetimes [173, 174], and in the first of these papers Townsend *et al.* highlight the discrepancies in the lifetime obtained from observations of the translational anisotropy, β, alone [174]. Several authors have previously noted the incompatibility between the direct measurements of the lifetime and those determined indirectly based on estimates of β [171, 186].

5.2 Results for dissociation at 193.3 nm

5.2.1 Ion images and fits

Two REMPI transitions were used to collect ion images in several pump-probe geometries, giving a total of 14 experimental images. The summed and processed ion images obtained using the $^1F_3 \leftarrow ^1D_2$ and $^3P_1 \leftarrow ^1D_2$ (2+1) REMPI transitions are shown in Figures 5.5 to 5.8. The Fourier moments (coefficients) and the simultaneous global fit to all the experimental moments are shown alongside the images.

5.3 Discussion

5.3.1 Speed distribution

The speed distribution, $P(v_P)$, returned from the global fit, shown in Figure 5.9(a), contains information about the internal energy distribution of the diatomic co-

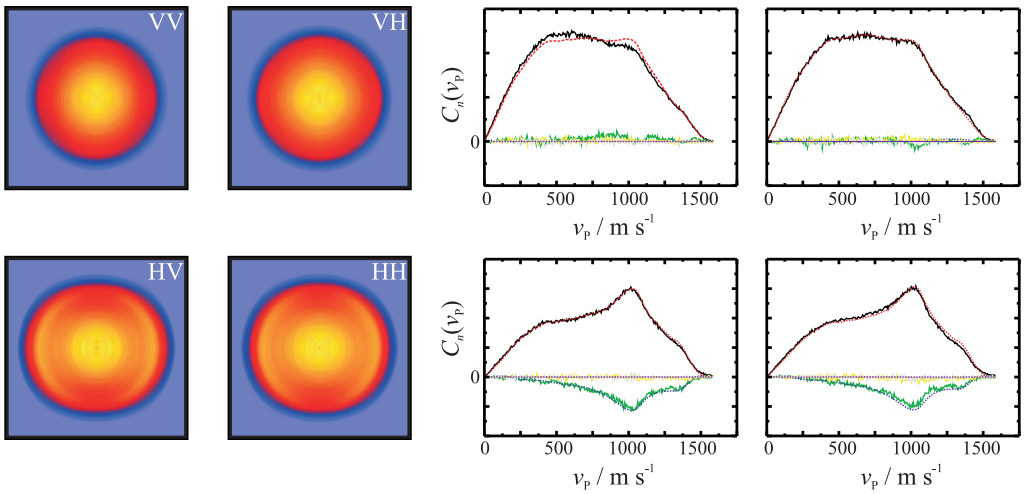

Figure 5.5: Ion images (false colour), Fourier moments (——), and fits (- - -) for the $S(^1D_2)$ atomic products probed *via* the $^1F_3$ intermediate state. The Fourier moments are colour coded, C_0 (black), C_2 (green), C_4 (yellow), and C_6 (grey). Data shown for photolysis at 193.3 nm.

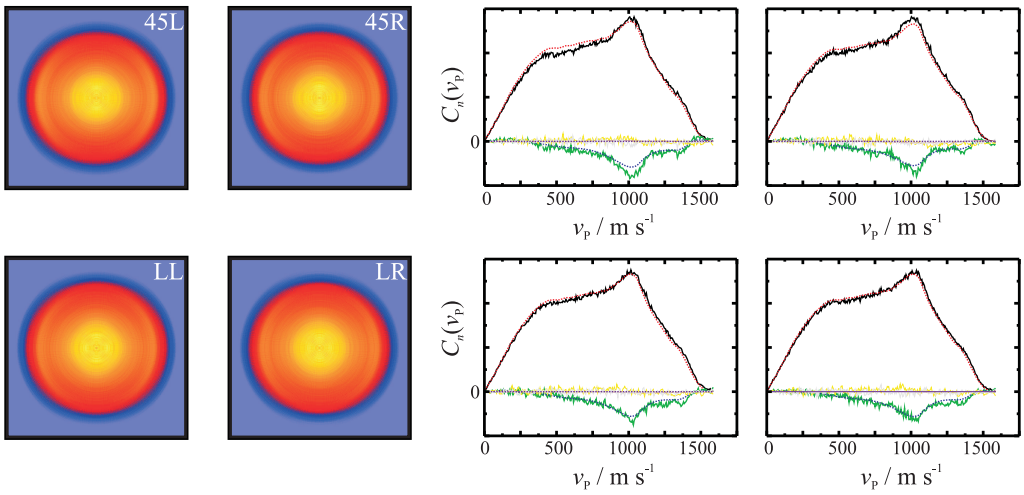

Figure 5.6: Ion images (false colour), Fourier moments (——), and fits (- - -) for the $S(^1D_2)$ atomic products probed *via* the $^1F_3$ intermediate state. The Fourier moments are colour coded, C_0 (black), C_2 (green), C_4 (yellow), and C_6 (grey). Data shown for photolysis at 193.3 nm.

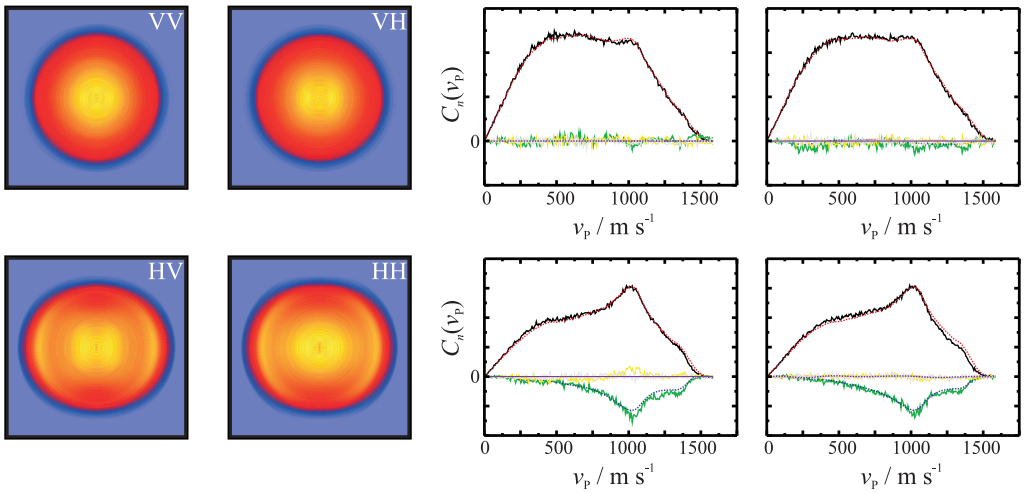

Figure 5.7: Ion images (false colour), Fourier moments (——), and fits (- - -) for the $S(^1D_2)$ atomic products probed *via* the $^3P_1$ intermediate state. The Fourier moments are colour coded, C_0 (black), C_2 (green), C_4 (yellow), and C_6 (grey). Data shown for photolysis at 193.3 nm.

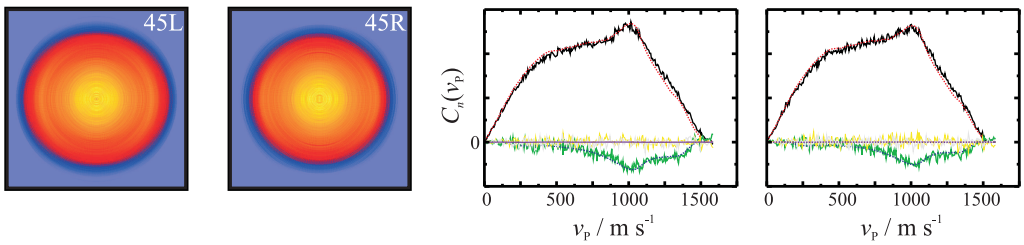

Figure 5.8: Ion images (false colour), Fourier moments (——), and fits (- - -) for the $S(^1D_2)$ atomic products probed *via* the $^3P_1$ intermediate state. The Fourier moments are colour coded, C_0 (black), C_2 (green), C_4 (yellow), and C_6 (grey). Data shown for photolysis at 193.3 nm.

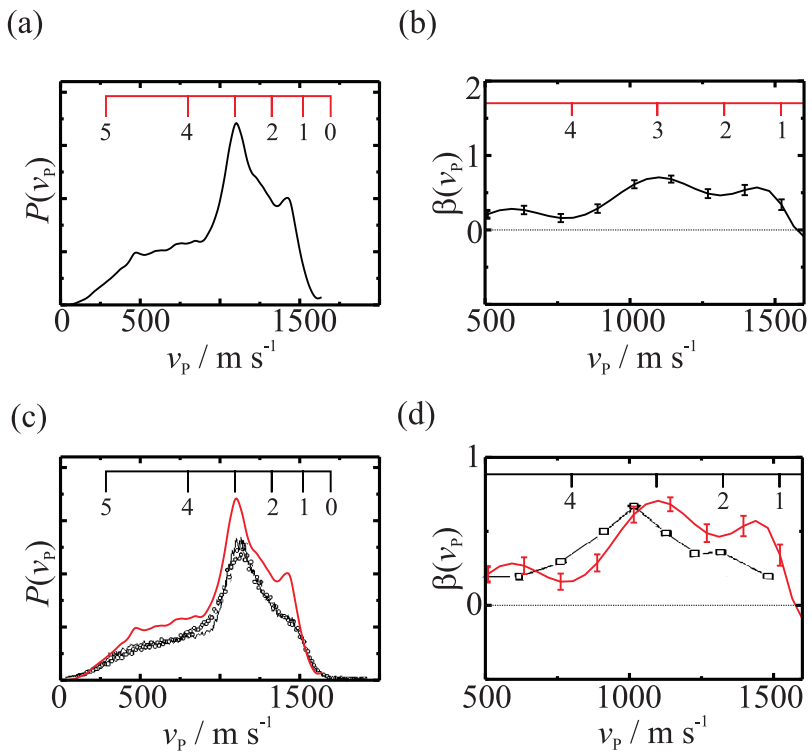

Figure 5.9: Speed distribution (a) and speed dependence of the spatial anisotropy (b) for the $S(^1D_2)$ products returned from the fit to the experimental data. The speed distribution and translational anisotropy shown in (a) and (b) are superimposed on the results obtained by Kitsopoulos *et al.* [186] in (c) and (d).

fragment $CS(v, J)$ that accompanies the $S(^1D_2)$ atomic products. The distribution peaks around $v = 2$ or 3, in good agreement with previous work at this wavelength [172, 181, 182, 186, 188, 189, 192]. The speed distribution determined in the present work is also superimposed on that obtained in the slice imaging study of Kitsopoulos and co-workers [186] in Figure 5.9(c), and demonstrates the excellent agreement between the two studies.

As discussed in the introduction, speed (or kinetic energy) distributions from the 193.3 nm photolysis of CS_2 have been reported widely in the literature [172, 181, 182, 186–189, 192]. Through laser induced fluorescence (LIF) and TOF MS measurements, Yang *et al.* estimated the $CS(v, J)$ distribution to peak at $v = 3$ [181], with this conclusion broadly echoed in several later studies [172, 182, 188, 189, 193].

Although the authors did not analyse the rotational distributions in detail, it was noted that there appeared to be little dependence on vibrational state, assigning an average rotational energy of $\sim 1225\,\mathrm{cm}^{-1}$ for $v = 4$ [181]. A later photofragment translational spectroscopy study by Frey and Felder, with a much improved energy resolution, revealed structure that appeared to represent well defined vibrational features, particularly at translational energies below the onset of $S(^1D_2)$ production [190]. Subsequent LIF measurements by Butler *et al.* indicated the rotational distributions for each of the CS vibrational levels to be bimodal [192]. Similar findings were presented later by McCrary *et al.* [182], and since both studies involved the detection of diatomic fragments formed in coincidence with both $S(^1D_2)$ and $S(^3P_J)$, it was suggested that the bimodality may reflect differences in the potential energy surfaces (PESs) that give rise to the singlet and triplet atomic products [182].

Through simulations of the speed distribution obtained from the universal detection of both the $S(^1D_2)$ and $S(^3P_J)$ atomic products, Suits and co-workers estimate that the vibrational distribution of the CS fragments reaches a maximum at $v = 3$ [188]. In the same simulation, average rotational energies of between 525 and $875\,\mathrm{cm}^{-1}$ were suggested for each of the vibrational levels [188]. In their recent slice imaging study, Kitsopoulos *et al.* assigned the maximum in the $P(v_P)$ distribution to either the $v = 2$ or $v = 3$ vibrational level of the co-fragment [186]. It was argued that assignment of the maximum to $v = 2$ implied high rotational excitation ($J \sim 30$) for $v = 0$ to 2, and lower rotational excitation ($J \sim 20$) for the higher vibrational levels ($v = 3$ to 5) [186].

A more recent ion imaging study by Jackson and co-workers reported a bimodal kinetic energy distribution with peaks in $P(E_T)$ below $350\,\mathrm{cm}^{-1}$ and $2798\,\mathrm{cm}^{-1}$ [187]. These findings, however, have not been supported by any of the previous studies, nor by the present work. Jackson and co-workers emphasise the potential influences of multi-photon effects on results recorded using focussed 193.3 nm radiation [187]. However, in the present study the photolysis source was focussed $\sim 5\,\mathrm{cm}$ beyond the laser-interaction region. In addition, the laser power was sufficiently low, *via* use of

a neutral density filter, such that no CS^+ ions were observed on the TOF spectrum during $S(^1D_2)$ image acquisition.

Simulations of the experimentally measured kinetic energy release distribution have been carried out with the aim of gaining a more quantitative estimate of the degree of vibrational and rotational excitation of the diatomic co-fragment. The simulations assume a Gaussian envelope in rotational population in level J, with these rotational distributions transformed into the velocity space of the recoiling $S(^1D_2)$ atom. Each rotational envelope was then used as a basis function and, after convolution with a detection sensitivity function, fit to the experimental distribution using a genetic algorithm routine similar to that described in Section 3.5.5. Figure 5.10 shows the best fit to the experimental kinetic energy distribution, and includes the rotational envelopes for each of the CS vibrational levels. The vibrational populations derived from this fit were $P(v = 0 : 1 : 2 : 3 : 4) = 0.18 : 0.17 : 0.32 : 0.15 : 0.18$. Apart from the extra population in $v = 0$, the distribution agrees well with previous work [181]. The slight excess population in $v = 0$ may be due to the photodissociation of vibrationally excited parent molecules in the molecular beam, which would result in a shift in the kinetic energy distribution to higher kinetic energies. The simulations also return estimates for the rotational distributions of each vibrational state. These are all found to be quite narrow, with Gaussian widths of $15 - 25\,J$, and peaks at values in the range 45 to 31 as the vibrational state varies from $v = 0$ to $v = 4$. These values seem to be in reasonable accord with previous estimates [181, 186, 188].

It is worth noting that the degree of $CS(X^1\Sigma^+)$ rotational excitation observed here is significantly smaller than that observed for the $CO(X^1\Sigma^+)$ fragments born in the photodissociation of OCS at 248 nm [194]. Unlike the case of CS_2, where excitation at 193.3 nm takes place above the barrier to linearity in the $^1\Sigma_u^+(^1B_2)$ state, photon absorption by OCS at 248 nm is formally forbidden at linear configurations, which may be one reason for the higher rotational excitation observed for the latter. Another possibility is that the differences can be described entirely on electronic

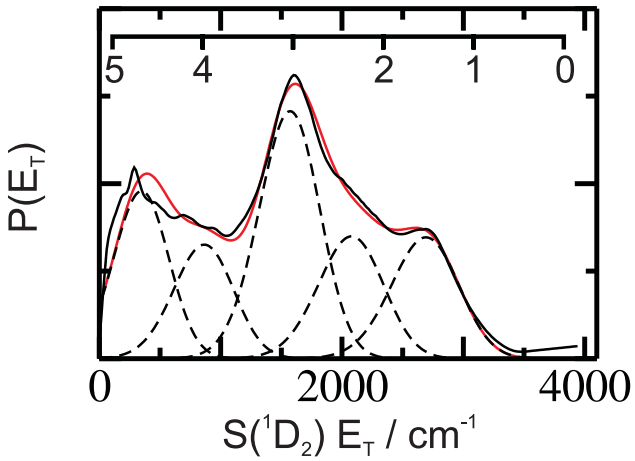

Figure 5.10: $S(^1D_2)$ kinetic energy release distribution (black) and fit (red) using a basis of Gaussian population distributions in J for each vibrational state. Also shown are the fitted vibrational envelopes for $v = 0$ to 4 (- - -).

structure grounds, as discussed by Bersohn and co-workers [195]. For the current system, highly vibrationally excited diatomic fragments are formed, whereas OCS dissociation gives rise to CO predominantly in $v = 0$. In OCS the chromophore, non-bonding electron, is almost exclusively on the S atom, with the CO bond therefore not affected by the absorption process. Following the electronic excitation in CS_2, however, both bonds are stretched, since the non-bonding electrons on both S atoms contribute to the absorption process. Since only one of the CS bonds breaks in the dissociation process, the diatomic fragment is strongly vibrationally excited [195].

5.3.2 Spatial anisotropy parameter, β

The speed dependence of the spatial anisotropy is plotted in Figure 5.9(b). It is mildly structured, with maxima that may correlate with the vibrational levels of the CS cofragment. The β parameter returned from the fit to the experimental data is positive at all speeds, as expected for a parallel transition, with a speed averaged value of $\beta \sim 0.44$. Several previous studies have probed the angular distribution of products resulting from dissociation at 193.3 nm [172, 181, 184, 186, 187, 190]. The mildly structured β value observed here, with a speed averaged value of ~ 0.44, is

in quantitative agreement with the ion-imaging study of Kitsopoulos *et al.* [186] (see Figure 5.9(d)), and is also close to the most recent of the molecular beam TOF MS studies by McGivern *et al.* [188]. Several previous studies have found the same trend of increasing β with increasing translational energy, however, the structure observed in the present study is most consistent with the recent results of Kitsopoulos *et al.* [186]. Both Frey and Felder and Suits and co-workers have indicated the importance of the expansion conditions on the reported values of β [188, 190]. Most studies, including the present one, have been carried out in the inert carrier gas, He, while neat CS_2 was used in the study by Jackson and co-workers [187]. Less good agreement is found with the anisotropy parameters reported in earlier studies by Yang *et al.* [181], and Waller and Hepburn [172].

In the axial recoil diatomic limit, the angular distribution for a parallel ($\Delta\Omega = 0$) transition gives the spatial anisotropy parameter, β, a limiting value of 2. The reduction in magnitude from limiting values may be due to several factors, including rotation of the parent molecule prior to dissociation, bending motions during dissociation, and non-axial recoil effects. It is interesting to compare the translational anisotropy with the larger speed averaged value of ~ 0.78 observed in the photodissociation of OCS at 248 nm [194]. As noted in Section 5.3.1 with regards to the $S(^1D_2)$ speed distribution, for OCS excitation takes place to a bent excited state in a transition that is formally forbidden at linear geometries, resulting in CO products with a large amount of rotational excitation and little vibrational excitation [194]. In contrast, and as discussed in Section 5.1, the optical transition relevant to 193.3 nm studies of CS_2 is formally allowed at linearity, and is believed to excite a quasi-linear electronic state of the molecule. Further comparisons with OCS, with particular reference to the excitation schemes in the two systems, are discussed in Section 5.3.3 in relation to $S(^1D_2)$ polarisation effects.

Kitsopoulos *et al.* [186] have pointed out that it is hard to interpret the experimentally determined values of β with what is known about the lifetime of the CS_2 $^1\Sigma_u^+(^1B_2)$ state excited around 193.3 nm. As noted in Section 5.1, direct lifetime

measurements at wavelengths as low as 194 nm suggest lifetimes on the order of 180 fs. A lifetime of around 500 fs, for example, would only reduce β for a parallel transition from +2 to around +1 for a 300 K rotational distribution, and about +1.7 for a 50 K rotational temperature, a conservative estimate of the beam temperature of the present experiments. Furthermore, assuming the simulations of the speed distributions are correct, the rotational excitation of the $CS(X^1\Sigma^+)$ fragments are not high enough to lead to significant non-axial recoil effects, and hence significant deviation of β from its limiting value. This is in contrast with the case of OCS photodissociation at 248 nm, where the CO rotational excitation for the singlet channel is so high as to cause significant non-axial recoil [194].

In the recent time-resolved photoelectron study of aligned CS_2 at 201.2 nm, Bisgaard *et al.* coherently excited a combination of symmetric stretching and bending levels in the $^1\Sigma_u^+(^1B_2)$ state with a femtosecond pulse [173]. In their study, changes in the character of the excited electronic wavefunction with stretching and bending of the CS_2 nuclear framework were used to account for observed oscillatory, time dependent, changes in the photoelectron angular distribution [173]. In the present work, carried out using nanosecond lasers, this quantum beat phenomena would not be observed. In the present case it is better to think of the excited state system as of mixed $^1\Sigma_u^+(^1B_2)$ $-^1\Pi_g(^1B_2)$ character at non-linear geometries, with the nature of the initial mixture dependent on the vibronic band excited. It seems plausible to assume that knowledge of the precise details of the excitation process, as opposed to arguments constructed purely by consideration of the lifetime, would allow a full interpretation of the reduction in β from its limiting value of +2. While it remains possible that a number of the factors outlined above may play a role in reducing β from its limiting value, it is clear that interpreting this behaviour solely in terms of a lifetime effect is not appropriate in this case. As will be discussed in Section 5.3.3, this description is consistent with the $S(^1D_2)$ electronic polarisation measurements.

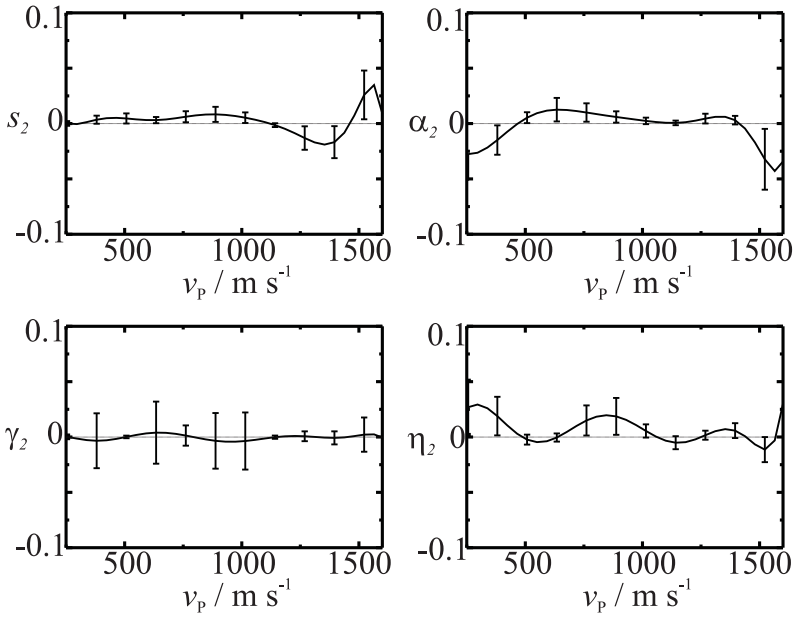

Figure 5.11: Speed dependent $K = 2$ angular momentum alignment parameters returned from the fits to the data for the $S(^1D_2)$ products following dissociation at 193.3 nm.

5.3.3 Angular momentum polarisation

Given the large $S(^1D_2)$ polarisation effects observed in the photodisscoation of OCS at 248 nm [194], the $S(^1D_2)$ fragments in the present study are surprisingly found to be completely unpolarised, as shown in Figure 5.11 where the speed dependence of the low rank $K = 2$ alignment parameters are plotted. In addition, the speed averaged values of all laboratory frame polarisation parameters returned from the fit to the experimental data are listed in Table 5.1. Several factors could contribute to experimentally observed $S(^1D_2)$ depolarisation. As with the β parameter, the magnitude of some of the laboratory frame polarisation parameters can be reduced by rotation of the parent molecule prior to dissociation [84, 197]. Furthermore, recent theory by Vasyutinskii and co-workers, applicable to both diatomic and linear triatomic molecules, indicates that for broad band incoherent excitation in the high J limit several of the polarisation parameters tend to zero for slow predissociation with respect to rotation of the parent molecule [84, 198]. Specifically, only the even

Parameter	$S(^1D_2)$	$S(^3P_2)$	$S(^3P_1)$	$S(^3P_0)$
β	0.441(23)	0.298(27)	0.358(17)	0.406(23)
s_2	-0.001(1)	0.007(3)	0.019(4)	-
α_2	0.001(1)	-0.001(5)	0.033(7)	-
γ_2	-0.001(4)	-0.009(6)	0.079(17)	-
η_2	0.004(4)	-0.003(4)	0.046(12)	-
s_4	0.001(1)	-0.000(1)	-	-
α_4	-0.000(1)	0.000(3)	-	-
γ_4	0.001(1)	0.001(2)	-	-
η_4	0.001(2)	0.001(2)	-	-
α_1	0.003(4)	0.001(2)	-0.005(9)	-
γ_1	0.015(16)	-0.001(2)	0.005(7)	-
γ_1'	-0.014(15)	0.017(11)	0.018(26)	-
α_3	-0.000(3)	0.002(15)	-	-
γ_3	-0.002(11)	0.000(17)	-	-
γ_3'	0.011(11)	0.000(4)	-	-

Table 5.1: Speed averaged polarisation parameters returned from fit to the $S(^1D_2)$ experimental data following dissociation at 193.3 nm. Also shown are the polarisation parameters for the $S(^3P_J)$ products taken from Ref [196]. Errors (1σ) are given in parenthesis and refer to the errors in the final digits reported.

rank parameters s_K, α_K, and η_K, and the odd rank moment γ_K should survive to give non-zero values [84, 198]. However, although these effects could theoretically contribute to the experimental findings they do not, alone, explain why in the present

case all the $S(^1D_2)$ polarisation parameters are zero within experimental error.

The recent *ab initio* calculations of the excited potential energy surfaces of CS_2 by Bisgaard *et al.* (see Figure 5.3) indicate that motion on the surfaces involved in the dissociation to $S(^1D_2)$ + $CS(X^1\Sigma^+)$ may be non-trivial, possibly involving two conical intersections on route to the asymptotic products [173]. Therefore, it seems plausible to assume that these intersections have some effect on the character of the dissociating wavefunction, and therefore the observed atomic orbital polarisation effects. It should be noted, however, that the mechanism for production of $S(^1D_2)$ atoms from OCS dissociation at 248 nm also involves passage through a conical intersection, with large $S(^1D_2)$ polarisation effects observed [199].

In both CS_2 and OCS the state(s) accessed *via* photon absorption are derived from a single electron $\pi \rightarrow \pi^*$ promotion. However, a possibility for the large differences in $S(^1D_2)$ polarisation effects comes from the contrasting excitation pathways in the two systems. In the case of OCS, as discussed in Section 5.3.1, photon absorption is formally forbidden at linear nuclear configurations, and the excitation at 248 nm is believed to predominantly access a state of A' symmetry with a small contribution from an A'' state (C_s point group). These are derived from the $^1\Delta$ and $^1\Sigma^-$ states, respectively, at linearity. This is in contrast to the case of CS_2, where it is the $^1\Sigma_u^+(^1B_2)$ state that is accessed. The transition to the corresponding $^1\Sigma^+$ state in OCS occurs at shorter wavelengths $\sim$ 153 nm compared to $\sim$ 197 nm in CS_2 [163]. A further complication in CS_2 exists in that the excited state accessed, $^1\Sigma_u^+(^1B_2)$, is heavily mixed with the $^1\Pi_g(^1B_2)$ state at non-linear geometries. Unlike the Σ^-, Δ, and Σ^+ states discussed above, the $^1\Pi_g$ state is derived from $\sigma \rightarrow \pi^*$ promotion.

Consideration must also be given to long range effects between the two recoiling fragments. In the following, the absence of observable atomic polarisation is discussed in the light of a long range interaction model [124], which, although approximate, has proved a useful tool in understanding the origin of polarisation effects in various triatomic systems [59, 124–127, 199]. The model [59, 124], see Section 2.4.2,

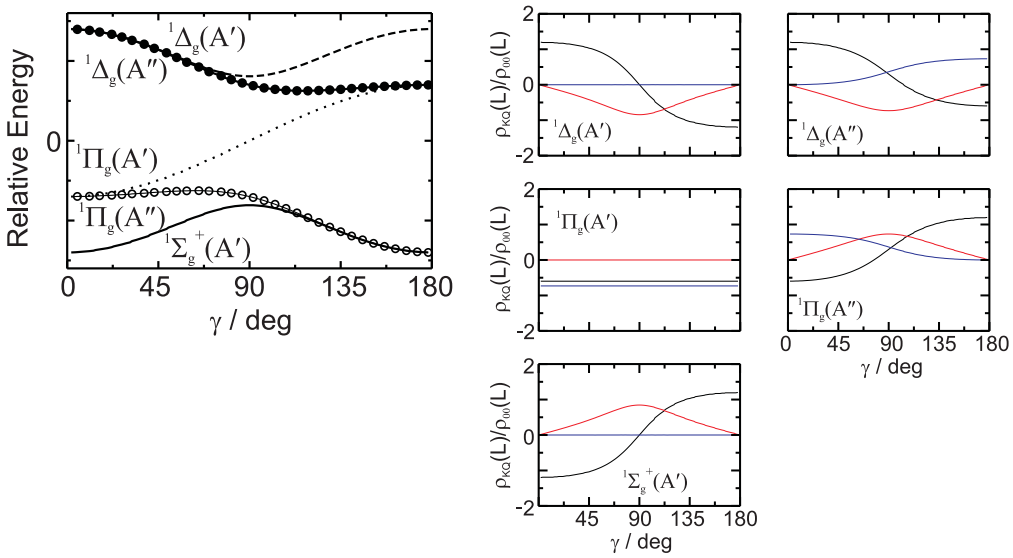

Figure 5.12: Predicted long range potentials for the $S(^1D_2)$ + $CS(X^1\Sigma^+)$ channel based on the (long range) dipole-quadrupole interaction (left). Shown on the right are the polarisation moments associated with dissociation on each of the five surfaces, ρ_{20} (black), ρ_{21} (red), and ρ_{22} (blue). Adapted from Refs [194] and [86].

has been described in detail in a recent review article [86], and considers the case where the potential in the long range region is determined solely by first order electrostatic interactions between the diatomic and atomic fragments. Cuts through the long range potential surfaces are generated as a function of Jacobi angle, γ, which then allow calculation of the dependence of the molecular frame photofragment state multipoles, ρ_{KQ}, describing the orbital polarisation of the system, for evolution on each of the surfaces. The potentials are evaluated at an arbitrary critical distance, R_c, which is not determined by the model after which point the fragments are assumed to lose all contact.

As described in Section 5.1, and similar to the OCS system mentioned above, CS_2 predissociates into $S(^1D_2)$ and the closed shell diatomic $CS(X^1\Sigma^+)$ co-fragment. The symmetry of the molecular states in the long range region is therefore determined entirely by the orbital occupancy of the atomic fragment. The closed shell $CS(X^1\Sigma^+)$ diatomic possesses both a dipole and quadrupole moment, 6.53×10^{-30} C m [200] and -8.3×10^{-40} C m^2 [201], respectively, whereas the $S(^1D_2)$ atomic fragment possesses

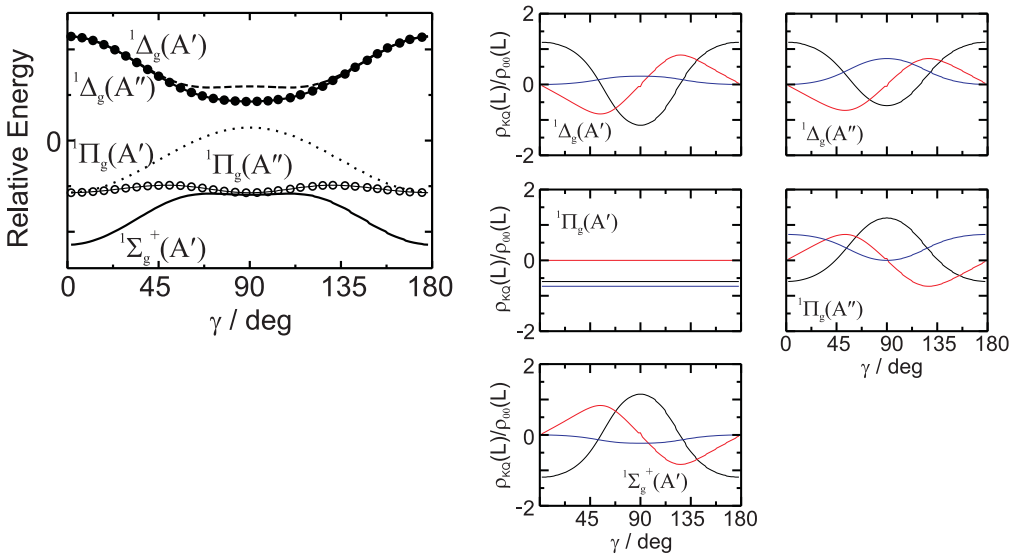

Figure 5.13: Predicted long range potentials for the $S(^1D_2)$ + $CS(X^1\Sigma^+)$ channel based on the (long range) quadrupole-quadrupole interaction (left). Shown on the right are the polarisation moments associated with dissociation on each of the five surfaces, ρ_{20} (black), ρ_{21} (red), and ρ_{22} (blue). Adapted from Refs [194] and [86].

only a quadrupole, $9.9 \times 10^{-40}\,\mathrm{C\,m^2}$ [202]. Although the dipole-quadrupole interaction must dominate at sufficiently large values of R, both the dipole-quadrupole and the quadrupole-quadrupole interactions might be important in determining the polarisation of the S-atom in the $CS(X^1\Sigma^+)$ + $S(^1D_2)$ system.

The dipole-quadrupole and quadrupole-quadrupole contributions to the long range electrostatic potentials are shown in Figures 5.12 and 5.13. The linear SCS configuration corresponds to $\gamma = 0°$, while 180° coincides with a linear CSS configuration. The relative energy ordering of the states at long range has been chosen to be consistent with the $CO(X^1\Sigma^+)$ + $S(^1D_2)$ system, as the signs of both interaction terms are the same. Evaluated at a large separation of 5 Å, the interaction terms have values of $69.9\,\mathrm{cm^{-1}}$ and $-8.9\,\mathrm{cm^{-1}}$ for the dipole-quadrupole and quadrupole-quadrupole, respectively. One important difference between the $CS(X^1\Sigma^+)$ + $S(^1D_2)$ and the $CO(X^1\Sigma^+)$ + $S(^1D_2)$ system is that the CS dipole moment is an order of magnitude larger than that for CO. Therefore, it seems plausible to assume that the $CS(X^1\Sigma^+)$ + $S(^1D_2)$ dipole-quadrupole interaction might dominate in the long

range region at which the polarisation of the atom is established. This is in contrast to the case of $CO(X^1\Sigma^+)$ + $S(^1D_2)$ where at 5 Å the dipole-quadrupole and quadrupole-quadrupole terms are of similar magnitude, $3.9\,cm^{-1}$ and $-7.0\,cm^{-1}$, respectively. The polarisation moments associated with dissociation on each of the surfaces are shown alongside the potentials in Figures 5.12 and 5.13 and also appear in Refs [86, 106, 194]. For example, for the Δ state shown in Figure 5.12, a positive value of the moment ρ_{20} is predicted at $\gamma = 0°$ for both the dipole-quadrupole and quadrupole-quadrupole interactions. This is consistent with a preferential alignment of J parallel to $\mathbf{z}$ since the Δ state is derived from population in $M_J = \pm 2$ only. Likewise ρ_{20} for the Σ and Π states are negative at 0°, indicating alignment of J perpendicular to $\mathbf{z}$ [86]. These states are derived from population in the $M_J = \pm 1$ and 0 levels for Π and Σ, respectively.

As γ increases from 0° the molecular system bends away from linearity, and this gives rise to mixing between states of the same symmetry species, A' or A'' in the C_s point group. Avoided crossings necessarily result, and are most evident at $\gamma = 90°$ in the quadrupole-quadrupole surfaces. Notice that the energy ordering of the states, see Figure 5.13, and the polarisation moments they give rise to, switch round between $\gamma = 0°$ and 180° in the case of the dipole-quadrupole interaction. Recall that, unlike OCS [194], this is likely to be the dominant interaction at long range for CS_2. A crude estimate of the Jacobi angles sampled during the dissociation process can be made by comparison of the time taken to reach the critical distance, here taken as 5 Å, with the classical period of rotation of the CS molecule. Assuming that the fragments born at the peak of the speed distribution, corresponding to around $v = 2$, $J = 37$ in $CS(X^1\Sigma^+)$, result from a direct process, the time taken to reach the critical distance can be estimated to be $t_{diss} \sim 2.6 \times 10^{-13}$ s, assuming that the relative velocity of the fragments remains constant during the dissociation. Furthermore, if the CS moiety behaves as a free rotor, the classical period of rotation is $\tau_{rot} \sim 5.4 \times 10^{-13}$ s. This means that CS could rotate about half a period as the fragments separate. One might expect the sampling of Jacobi angles particularly

for $S(^1D_2)$ fragments formed in coincidence with high rotational angular momenta $CS(X^1\Sigma^+)$ diatomics to be nearly uniform in γ. Any sampling of $\gamma > 0°$ inevitably means some mixing between states of the same symmetry. A possible consequence of the mixing is that the orbital polarisation, described by the ρ_{KQ} functions, becomes scrambled at long range.

Another difference between the current study and that of the $CO(X^1\Sigma^+)$ + $S(^1D_2)$ system is that while in the latter case the diatomic co-fragment was born vibrationally cold [194], in the present study the CS diatomic can populate levels up to $v = 5$. The dipole moment of $CS(X^1\Sigma^+)$, like its $CO(X^1\Sigma^+)$ counterpart, actually changes sign as the C-S bond length increases [200]. Although extension of the diatomic C-S bond for levels up to $v = 5$ is not large enough to change the sign of the dipole [203], it is sufficiently large to reduce the magnitude of the $C^{\delta-}S^{\delta+}$ dipole by $\sim 50\%$ [200]. If one considers the maximum extension of the C-S bond during a $v = 3$ vibration, then the dipole moment is reduced to $5.09 \times 10^{-30}\,\mathrm{C\,m}$. This puts the value of the dipole-quadrupole interaction energy at $54.7\,\mathrm{cm}^{-1}$. Based on these estimates, however, it seems likely that this change in dipole-quadrupole interaction with CS vibration is probably too small to account for the lack of $S(^1D_2)$ polarisation observed here.

The interpretation of the experimental results using the long range interaction model is necessarily qualitative. If the simulation of the speed distribution is to be believed, then it seems possible that there may be some rotational scrambling effects on the $S(^1D_2)$ polarisation in the long range region. However, arguments based on the long range potentials do not appear to account for the fact that while S-atom polarisation is not observed in the singlet channel, it is found in the triplet channel, in particular for $S(^3P_1)$ species, as detailed in Table 5.1 [196]. It therefore seems more likely that the complicated motion along the dissociation co-ordinate, with the multiple conical intersections encountered, in addition to the nature of the excitation process itself, are the more likely source of the interesting observation of the lack of $S(^1D_2)$ polarisation.

5.4 State-to-state results

5.4.1 CS_2 (1+1) REMPI spectrum

The (1+1) REMPI spectra generated by electronically gating the CCD camera over the CS_2^+ peak in the TOF spectrum and scanning the pump laser in a one-colour experiment is shown in Figure 5.14. The spectrum is compared to the (1+1) REMPI spectra previously reported by Beatty *et al.* [204] and Lin and co-workers [178] in Figure 5.15. The bands in the spectrum are labelled as far as possible based on previously made assignments [159, 204], as listed in Table 5.2.

5.4.2 Photofragment excitation (PHOFEX) spectra

Photofragment excitation spectra were generated in a two colour experiment by scanning the photolysis (pump) laser with the probe laser fixed in order to selectively detect the $S(^1D_2)$ products. The $S(^1D_2)$ fragments were ionised using the (2+1) REMPI transition *via* the $^1F_3$ state at 288.1 nm. The $S(^1D_2)$ excitation spectrum is shown in Figure 5.16 alongside that of the $S(^3P_2)$ fragments and the CS_2 (1+1) REMPI spectra for comparison.

5.4.3 Ion images and fits

Ion images of the $S(^1D_2)$ atomic fragments were recorded following photodissociation at nine wavelengths, as listed in Table 5.2 and indicated in Figure 5.14. For each photolysis wavelength images were recorded in four pump-probe geometries using the (2+1) REMPI transition *via* the $^1F_3$ state at 288.1 nm. The ion images, Fourier moments and fits for all transitions are shown in Figures 5.17−5.25. The ion images for each dissociation wavelength show two major features corresponding to the formation of the diatomic co-fragment in the $v = 0$ and 1 vibrational levels.

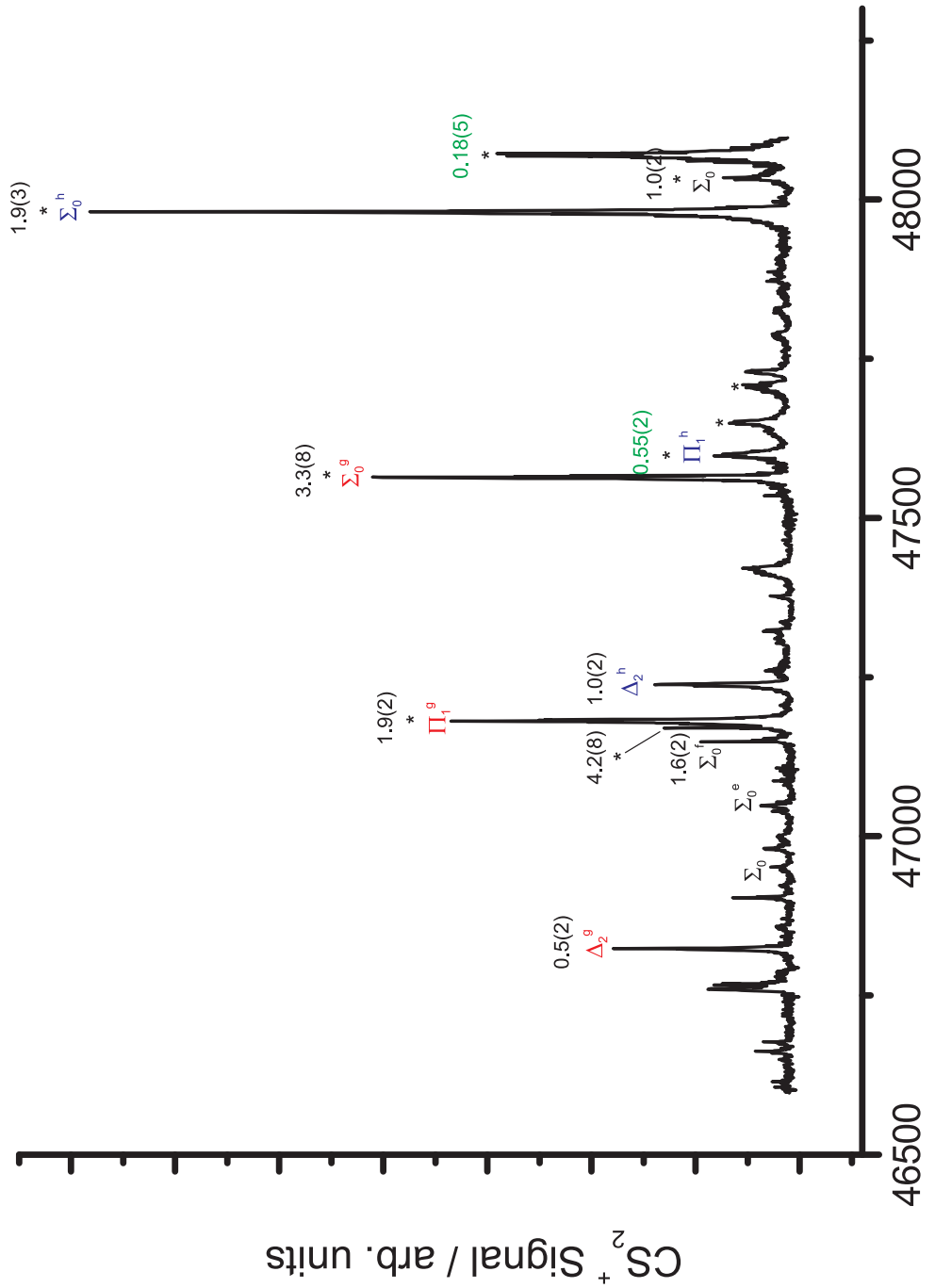

Figure 5.14: Experimental CS_2 (1+1) REMPI spectra. Band type assignments (Σ, Π) are taken from the work of Douglas and Zanon [159] and Beatty *et al.* [204]. The superscripts e, f, g and h denote the excited state vibrational level and the subscripts 0 and 1 refer to the number of quanta in the bending mode of ground state CS_2. The peaks marked with an asterisk indicate the transitions studied herein. The numbers in black and green indicate the lifetimes, in picoseconds, associated with each transition taken from the work of Beatty *et al.* [204] and Hepburn and co-workers [171], respectively.

Energy / cm^{-1}	Label	Assignment	Lifetime[171] / ps	Lifetime[178] / ps	Lifetime[204] / ps	$S(^3P_2)/S(^1D_2)$[171]
48071	(a)	-	-	-	-	1.3(3)
48034	(b)	Σ_0	1.0(2)	1.6(2)	1.0(2)	3.3(7)
47980	(c)	Σ_0^h	1.4(2)	2.5(3)	1.9(3)	4.1(9)
47709	(d)	-	-	-	-	-
47648	(e)	-	-	-	-	-
47597	(f)	Π_1^h	0.6(15)	-	-	1.1(2)
47564	(g)	Σ_0^g	2.8(3)	1.5(3)	3.3(8)	6.1(1)
47181	(h)	Π_1^g	1.2(3)	2.0(3)	1.9(2)	2.4(5)
47170	(i)	-	-	-	-	-

Table 5.2: Energies, assignments [159, 204] and lifetimes of the transitions studied in Section 5.4.3. Lifetimes taken from the work of Hepburn and co-workers [171], Beatty *et al.* [204], and Lin and co-workers [178]. The superscript g and h designate the excited state vibrational level and the subscripts 0 and 1 refer to the number of quanta in the bending mode of ground state CS_2. The labels (a−i) are used in the following sections.

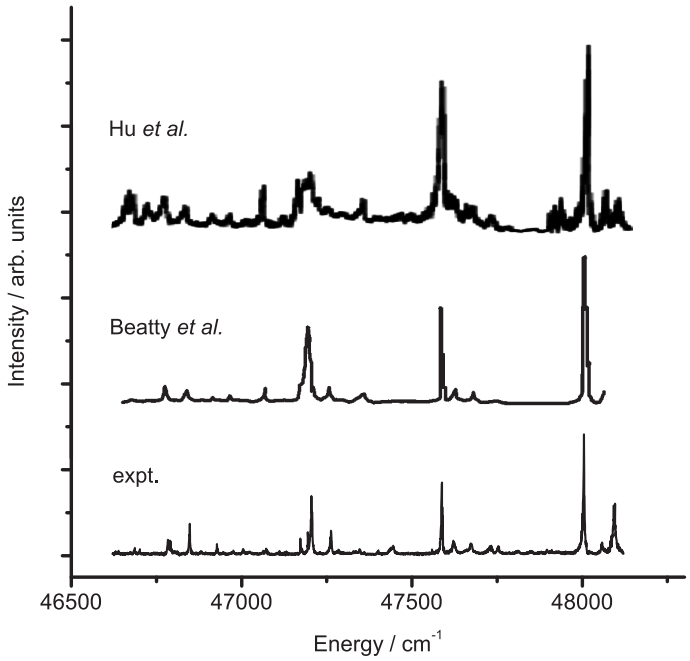

Figure 5.15: CS_2 (1+1) REMPI spectra. The bottom trace shows the experimentally determined spectrum, while the middle and top traces show the spectra reported by Beatty *et al.* [204] and Lin and co-workers [178], respectively.

5.5 Discussion

5.5.1 Spectra

The CS_2 (1+1) REMPI spectrum, Figure 5.14, is produced by one photon excitation to and ionisation from the $^1\Sigma_u^+(^1B_2)$ state. The spectrum generated in this manner shows rich absorption structure, with progressions in the combined symmetric stretching and bending modes of the excited state, ν_1 and ν_2, respectively. In addition, due to the low frequency bending mode of ground state CS_2, $\nu_2'' \sim 400\,\mathrm{cm}^{-1}$, hot bands are also observed due to vibrationally excited parent molecules. The assignments of the various bands, along with previously determined excited state lifetimes, are provided in Table 5.2.

The CS_2 (1+1) REMPI spectrum is compared with that obtained in two previous studies by Beatty *et al.* [204] and Lin and co-workers [178] in Figure 5.15. The spectrum is seen to be in excellent agreement with the spectra generated by Beatty *et al.*, and in reasonable accord with the measurements by Lin and co-workers,

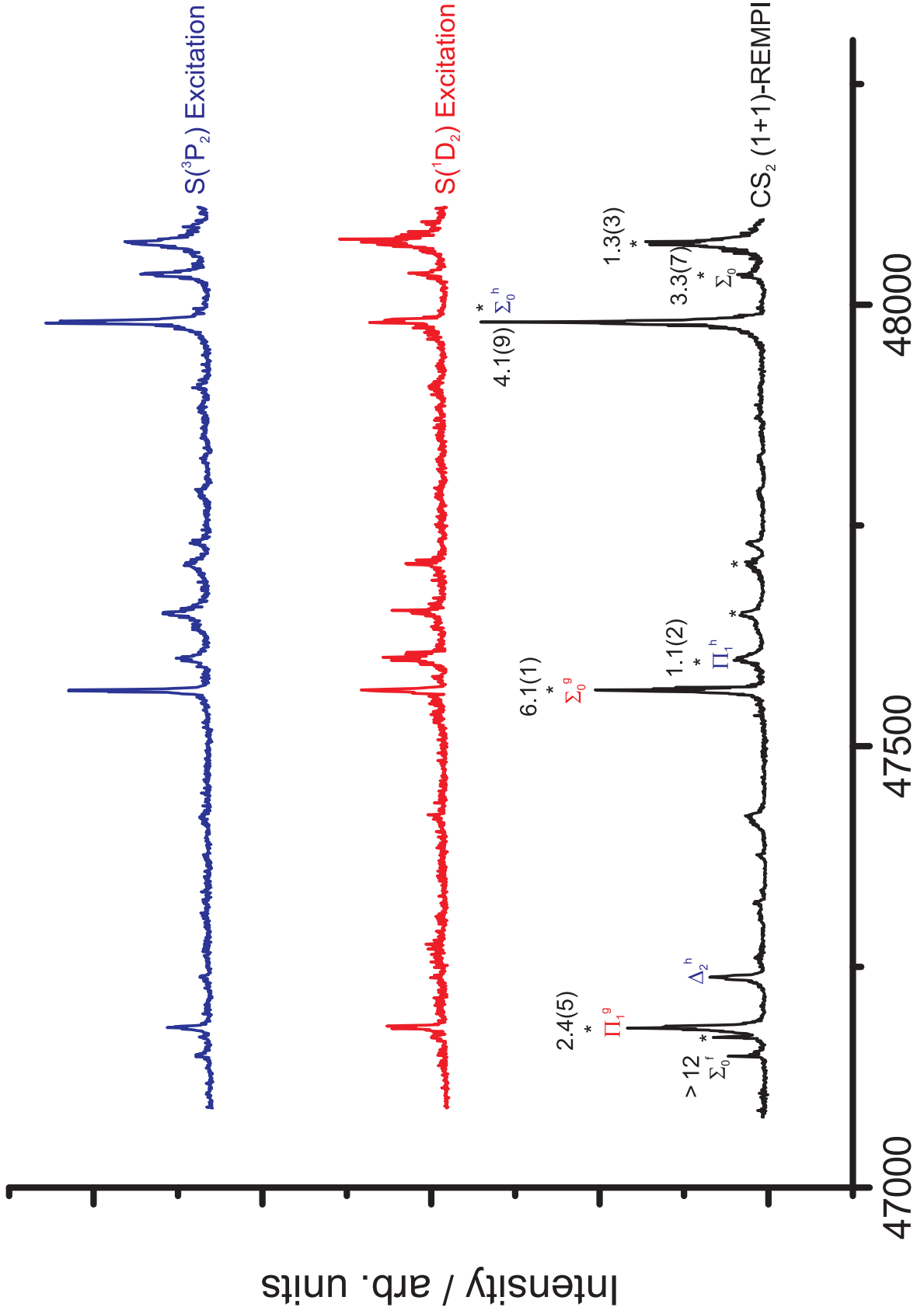

Figure 5.16: Excitation spectra for $S(^1D_2)$ and $S(^3P_2)$ fragments (middle and top) compared to CS_2 (1+1) REMPI spectrum (bottom). The numbers refer to the $S(^3P_2)/S(^1D_2)$ branching ratio taken from the study by Hepburn and co-workers [171].

with any discrepancies perhaps attributable to different expansion conditions of the molecular beams used in the three experiments. Lin and co-workers also point to the possibility of clusters of parent CS_2 molecules as responsible for the unassigned peaks in their spectra [178]. In the study by Beatty *et al.* [204], two different expansions were used, firstly using He as the buffer, and secondly using a 5 : 1 mixture of argon:butane [204]. The latter mixture was used in order to facilitate cooling of the vibrational degrees of freedom in the parent beam. In their study Beatty *et al.* observed drastic differences in the spectrum obtained using argon:butane compared to that obtained using He as the buffer gas, with significant reductions in the intensities of bands arising from vibrationally excited precursor molecules [204]. Additionally, through a full rotational analysis of their spectra, Beatty *et al.* were also able to evaluate the lifetimes of the different transitions. The authors showed that Π and Δ bands were associated with shorter lifetimes than those for Σ bands, supporting the previous conclusions by Hepburn and co-workers [170, 171, 204]. The spectral analysis by Lin and co-workers revealed lifetimes in general agreement with those obtained by Beatty *et al.* although the trend in lifetime with K was not observed [178]. Table 5.2 summarizes the assignments and lifetimes of the different features in the (1+1) REMPI spectrum.

Figure 5.16 compares the $S(^1D_2)$ and $S(^3P_2)$ photofragment excitation spectra with the CS_2 (1+1) REMPI spectrum. The spectrum for the $S(^3P_2)$ fragments more closely resembles the CS_2 (1+1) REMPI spectrum. This is perhaps unsurprising since dissociation to give triplet S-atoms is known to be the dominant dissociation pathway. The $S(^1D_2)$ spectrum, however, does show significant differences to both the $S(^3P_2)$ excitation and CS_2 (1+1) REMPI spectra. In particular, the $S(^1D_2)$ spectrum appears to show an enhancement of the Π over Σ bands, relative to that obtained for the $S(^3P_2)$ species, most notably in the region $\sim$ 47,600 cm^{-1}. This observation is in good agreement with the conclusions drawn by Hepburn and co-workers [170, 171, 204] and Chen *et al.* [177], as discussed in Section 5.1.

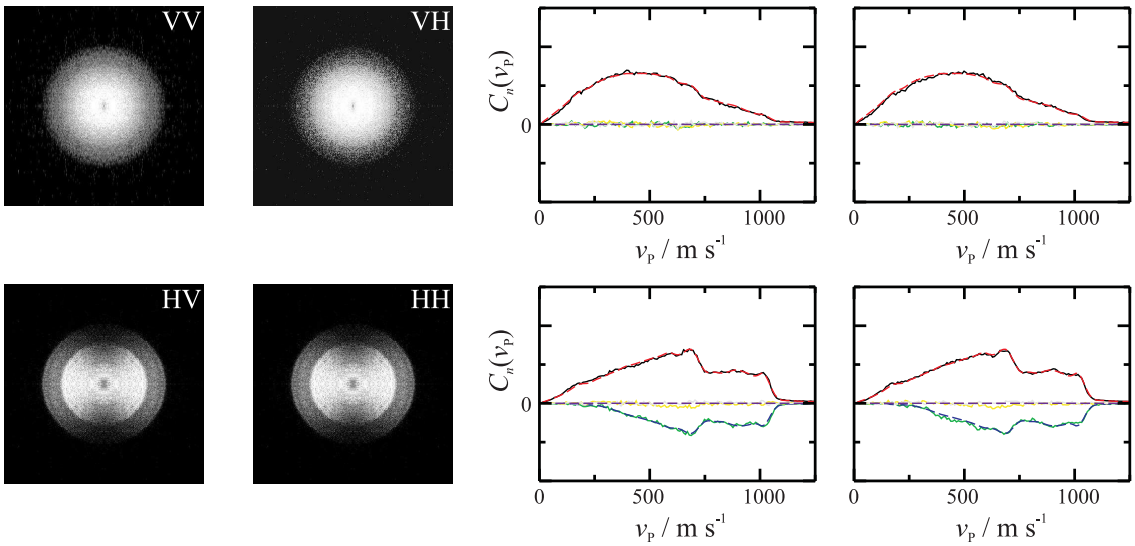

Figure 5.17: Ion images (left), Fourier moments (——), and fits (- - -) (right) for the $S(^1D_2)$ atomic products probed *via* the $^1F_3$ intermediate state. The Fourier moments are colour coded, C_0 (black), C_2 (green), C_4 (yellow), C_6 (grey). $S(^1D_2)$ data collected following excitation *via* band (a), see Table 5.2.

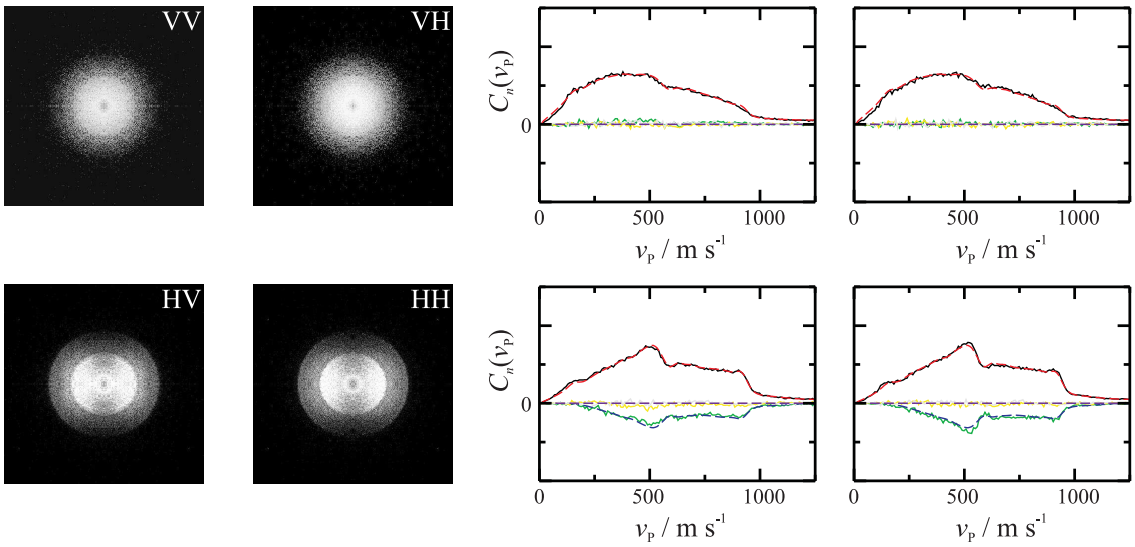

Figure 5.18: Ion images (left), Fourier moments (——), and fits (- - -) (right) for the $S(^1D_2)$ atomic products probed *via* the $^1F_3$ intermediate state. The Fourier moments are colour coded, C_0 (black), C_2 (green), C_4 (yellow), C_6 (grey). $S(^1D_2)$ data collected following excitation *via* band (b), see Table 5.2.

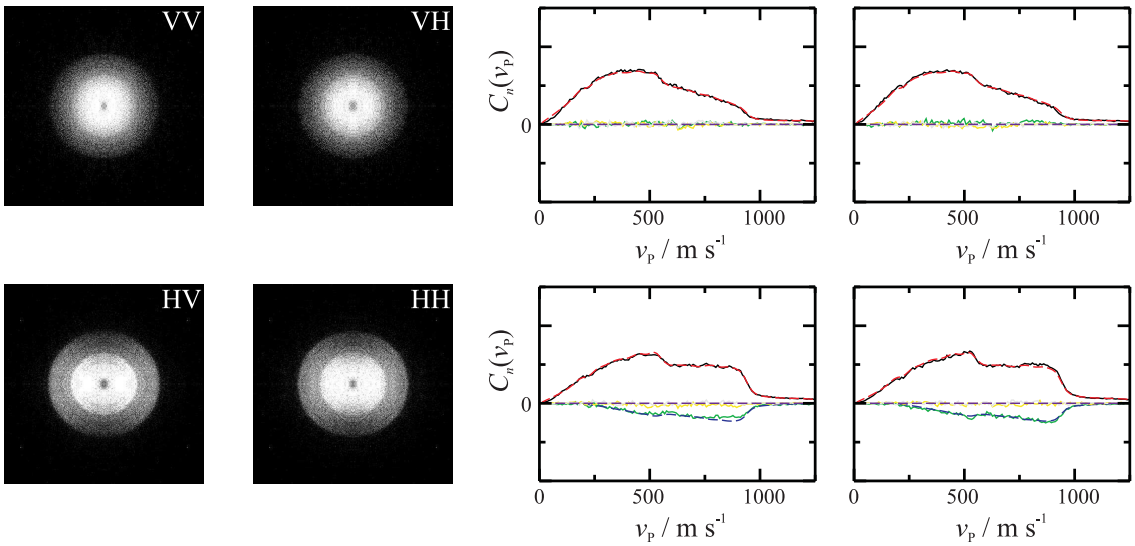

Figure 5.19: Ion images (left), Fourier moments (——), and fits (- - -) (right) for the $S(^1D_2)$ atomic products probed *via* the $^1F_3$ intermediate state. The Fourier moments are colour coded, C_0 (black), C_2 (green), C_4 (yellow), C_6 (grey). $S(^1D_2)$ data collected following excitation *via* band (c), see Table 5.2.

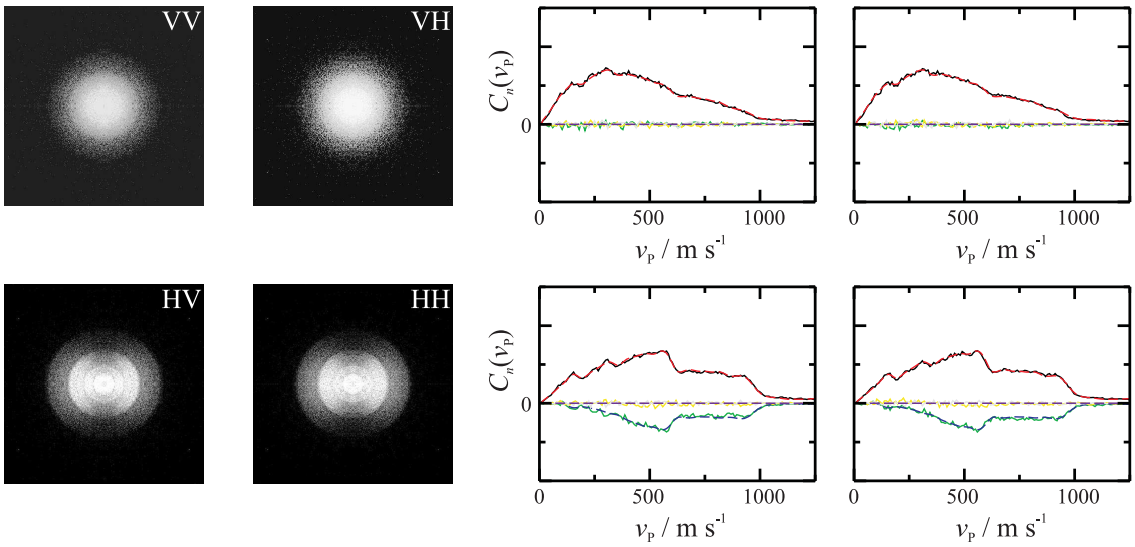

Figure 5.20: Ion images (left), Fourier moments (——), and fits (- - -) (right) for the $S(^1D_2)$ atomic products probed *via* the $^1F_3$ intermediate state. The Fourier moments are colour coded, C_0 (black), C_2 (green), C_4 (yellow), C_6 (grey). $S(^1D_2)$ data collected following excitation *via* band (d), see Table 5.2.

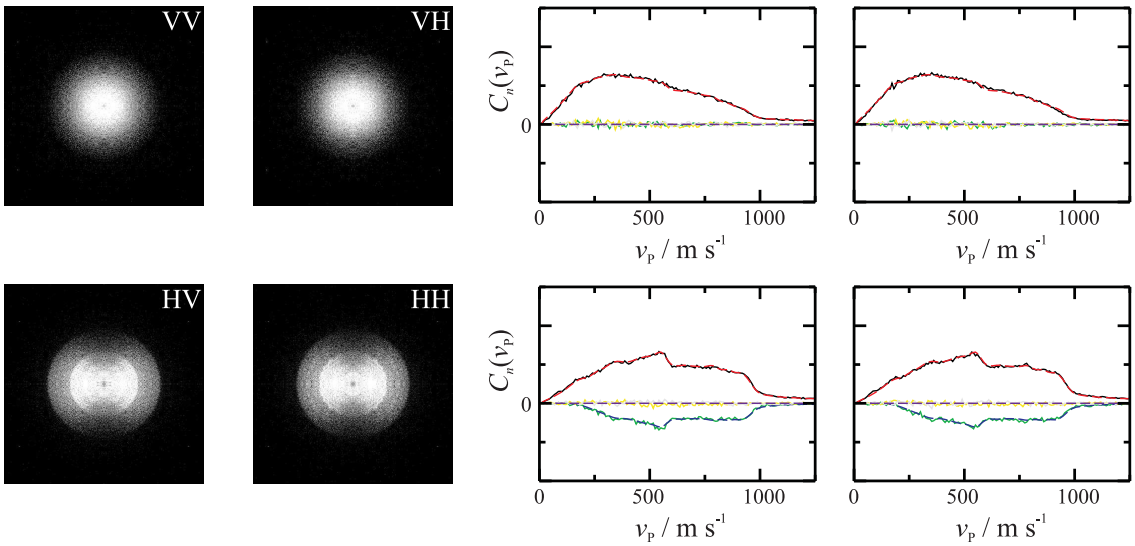

Figure 5.21: Ion images (left), Fourier moments (——), and fits (- - -) (right) for the $S(^1D_2)$ atomic products probed *via* the $^1F_3$ intermediate state. The Fourier moments are colour coded, C_0 (black), C_2 (green), C_4 (yellow), C_6 (grey). $S(^1D_2)$ data collected following excitation *via* band (e), see Table 5.2.

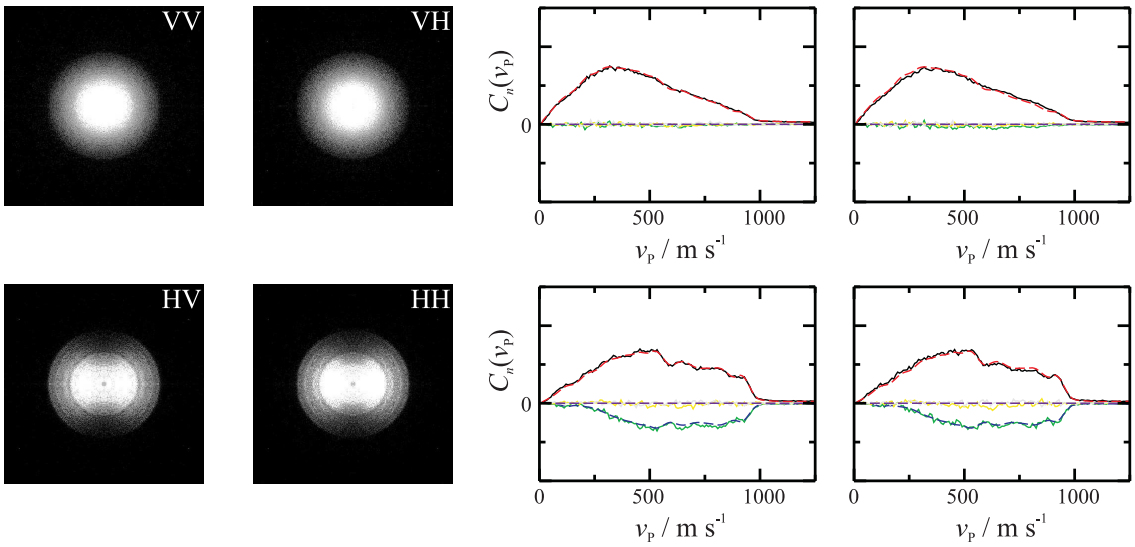

Figure 5.22: Ion images (left), Fourier moments (——), and fits (- - -) (right) for the $S(^1D_2)$ atomic products probed *via* the $^1F_3$ intermediate state. The Fourier moments are colour coded, C_0 (black), C_2 (green), C_4 (yellow), C_6 (grey). $S(^1D_2)$ data collected following excitation *via* band (f), see Table 5.2.

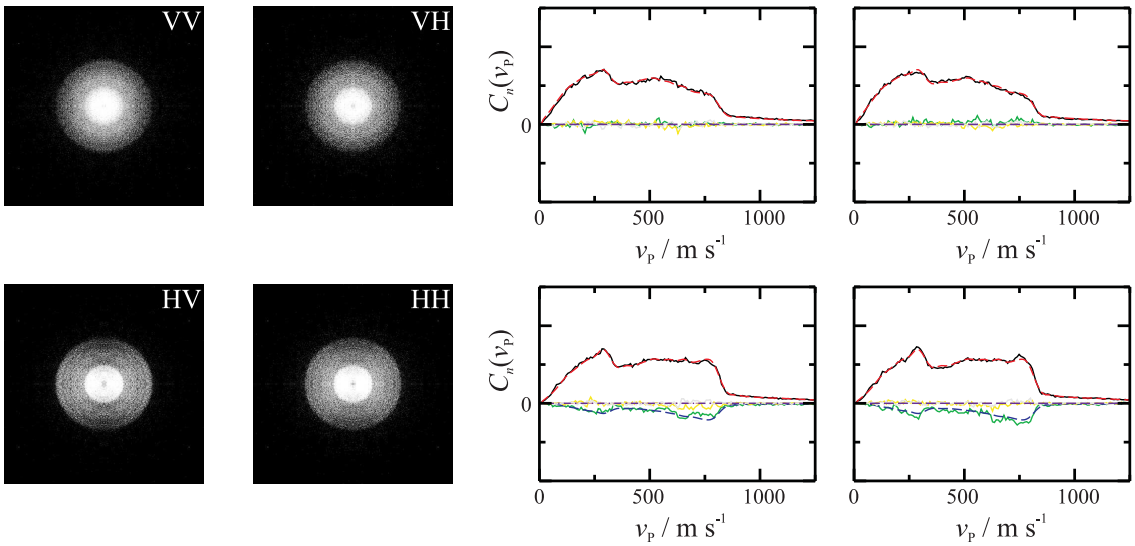

Figure 5.23: Ion images (left), Fourier moments (——), and fits (- - -) (right) for the $S(^1D_2)$ atomic products probed *via* the $^1F_3$ intermediate state. The Fourier moments are colour coded, C_0 (black), C_2 (green), C_4 (yellow), C_6 (grey). $S(^1D_2)$ data collected following excitation *via* band (g), see Table 5.2.

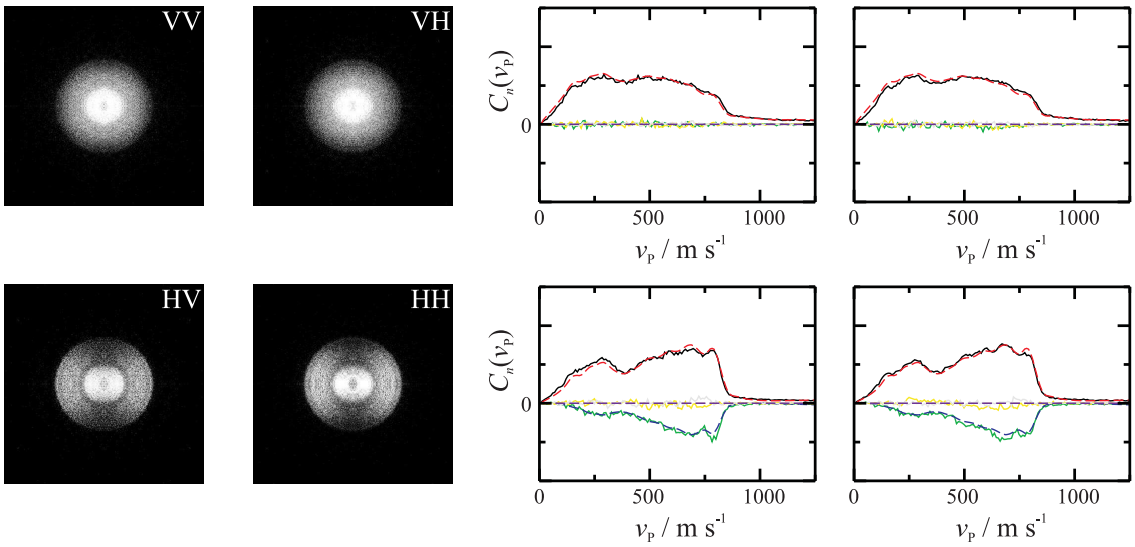

Figure 5.24: Ion images (left), Fourier moments (——), and fits (- - -) (right) for the $S(^1D_2)$ atomic products probed *via* the $^1F_3$ intermediate state. The Fourier moments are colour coded, C_0 (black), C_2 (green), C_4 (yellow), C_6 (grey). $S(^1D_2)$ data collected following excitation *via* band (h), see Table 5.2.

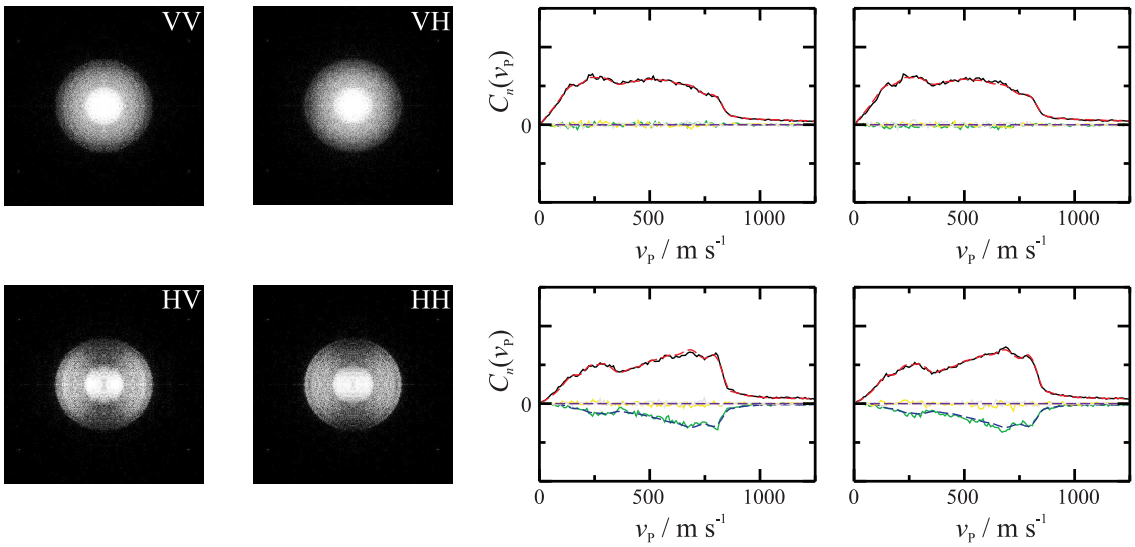

Figure 5.25: Ion images (left), Fourier moments (——), and fits (- - -) (right) for the $S(^1D_2)$ atomic products probed *via* the $^1F_3$ intermediate state. The Fourier moments are colour coded, C_0 (black), C_2 (green), C_4 (yellow), C_6 (grey). $S(^1D_2)$ data collected following excitation *via* band (i), see Table 5.2.

5.5.2 Speed distributions

The speed distributions, $P(v_P)$, generated by the fits to experimental Fourier moments for all dissociation wavelengths, presented in Figure 5.26, show two major features which appear at velocities consistent with $S(^1D_2)$ formed in coincidence with $CS(X^1\Sigma^+)$ $v = 0$ and 1. For several photodissociation wavelengths further rotational structure is observed, but only partially resolved. The HH ion images were additionally analysed using the pBASEX method of Garcia *et al.* [205]. This analysis procedure allowed slightly higher resolution speed distributions to be obtained and could be performed since the ion images show no evidence of angular momentum alignment. The slices through the 3D scattering distribution and speed distributions obtained using this method are shown in Figure 5.27, along with the distributions obtained following the Fourier moment analysis, for all photodissociation wavelengths, demonstrating the excellent agreement between the two analysis schemes.

In order to investigate the internal energy distributions further, the speed dis-

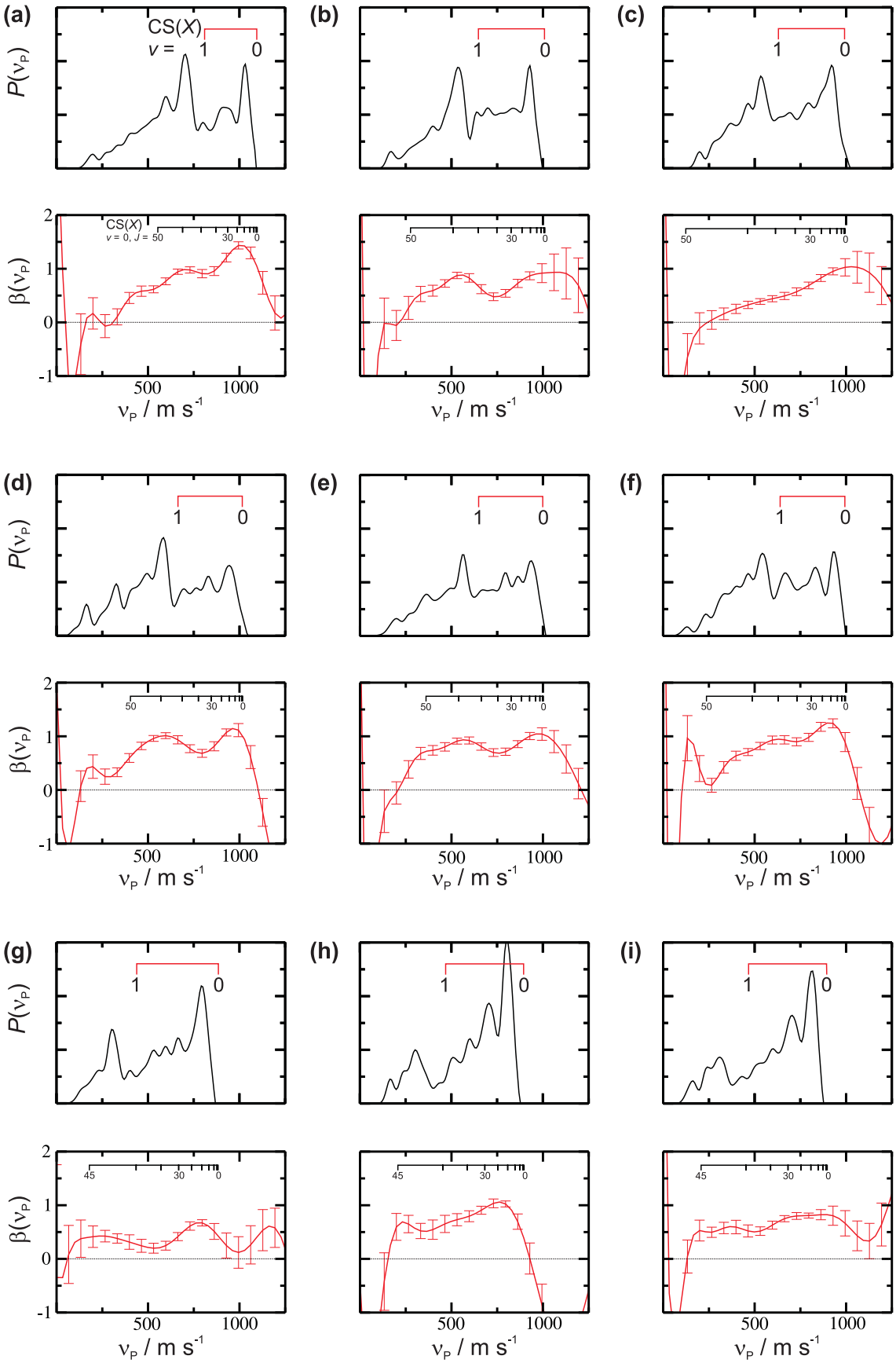

Figure 5.26: Speed distributions (top) and speed dependence of the spatial anisotropy parameter, β, (bottom) for the $S(^1D_2)$ products returned from the fits to the experimental Fourier moments. $S(^1D_2)$ data shown for transitions detailed in Table 5.2.

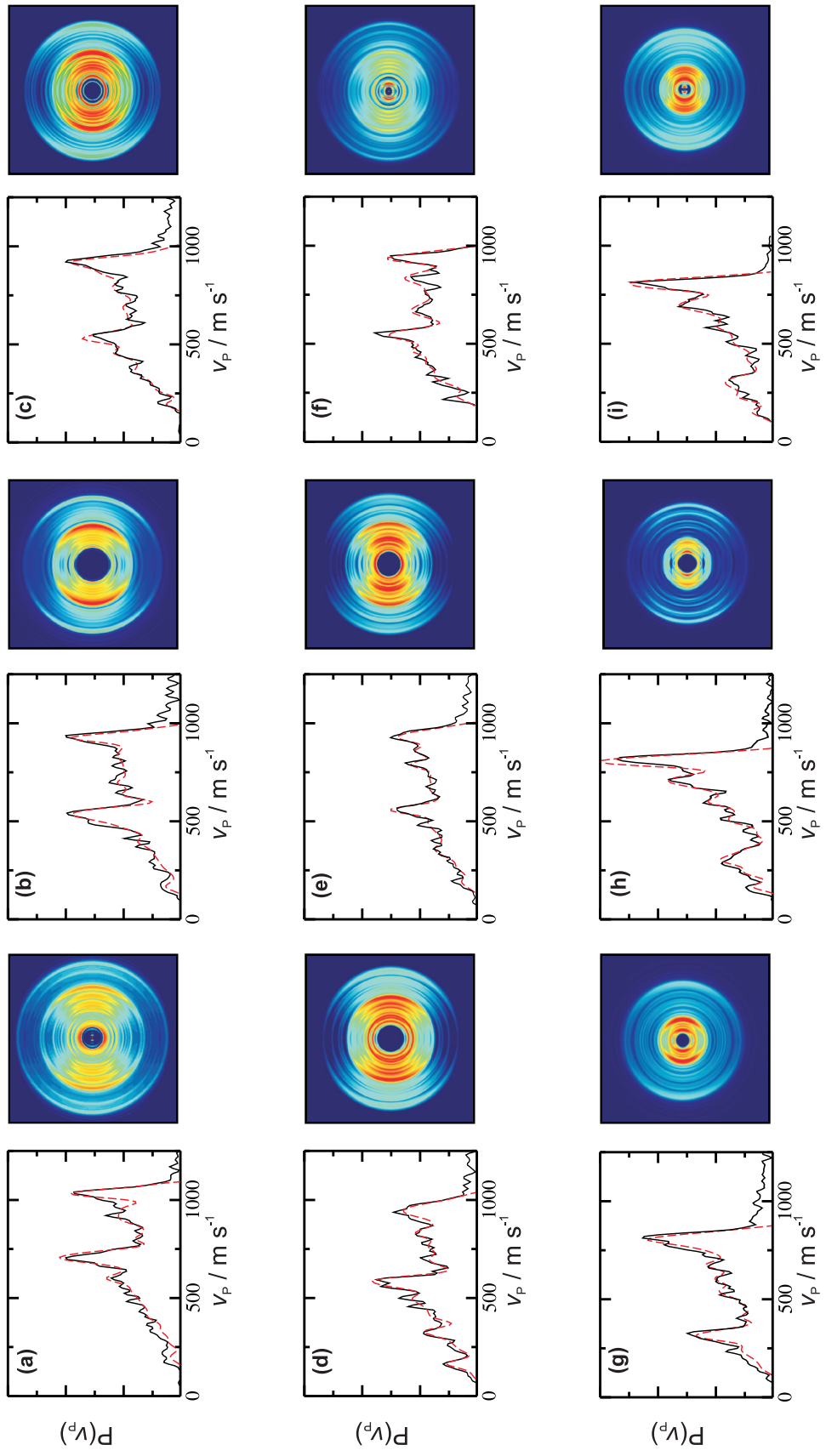

Figure 5.27: Speed distributions returned from fits to Fourier moments (- - -) and Abel inversion (——) (left) and Abel inversion of crushed ion image *via* pBASEX [205] (right). $S(^1D_2)$ data shown for transitions detailed in Table 5.2.

tributions, $P(v_P)$, were transformed into $S(^1D_2)$ kinetic energy distributions and simulated with a series of Gaussian functions, one for each rotational level of the CS co-fragment. The central position of the Gaussian functions were calculated given the dissociation energy of CS_2 and the rotational constant of $CS(X^1\Sigma^+)$. The simulated distribution was fit to the kinetic energy distribution using a genetic algorithm technique similar in spirit to the fitting technique used to treat the raw experimental data. Unfortunately, the fitting program was unable to distinguish the high J CS(X $v = 0$) from the low J CS(X $v = 1$) products occuring at similar kinetic energy release. The *average* behaviour of the $CS(X^1\Sigma^+)$ rotational populations, $P(J_{CS})$, generated from these fits, however, follows a general trend given by the well-known prior distribution for a statistical distribution among product states. The prior-expectation probability of an individual rovibrational level is given by [4]

$$P^o(v, J) \propto (2J + 1)(E_{\text{avl}} - E_\nu - E_J)^{1/2} \tag{5.3}$$

where E_{avl}, E_ν, and E_J refer to the available, internal $CS(X^1\Sigma^+)$ vibrational and rotational energies, respectively. In order to simulate the experiment the Gaussian basis functions for each rovibrational level of the CS co-fragment were weighted with the prior distribution, Equation (5.3), and the resulting distribution superimposed onto the $S(^1D_2)$ kinetic energy distributions, as shown in Figure 5.28. The resulting simulations, although unable to account for the oscillations in the kinetic energy distributions, strongly suggest that on average the distribution amongst $CS(X^1\Sigma^+)$ vibrational and rotational states is statistical.

Mechanistic implications

The implications for this observation are that the CS_2 molecule becomes trapped in a deep potential well and the PES does not possess a barrier to dissociation in the exit channel. It is therefore worth revisiting the previously suggested mechanism for photolysis, see Section 5.1, involving dissociation on the repulsive $^1\Pi_g$ state, and the *ab initio* potentials of Stolow and co-workers shown in Figures 5.3 and 5.4 [173].

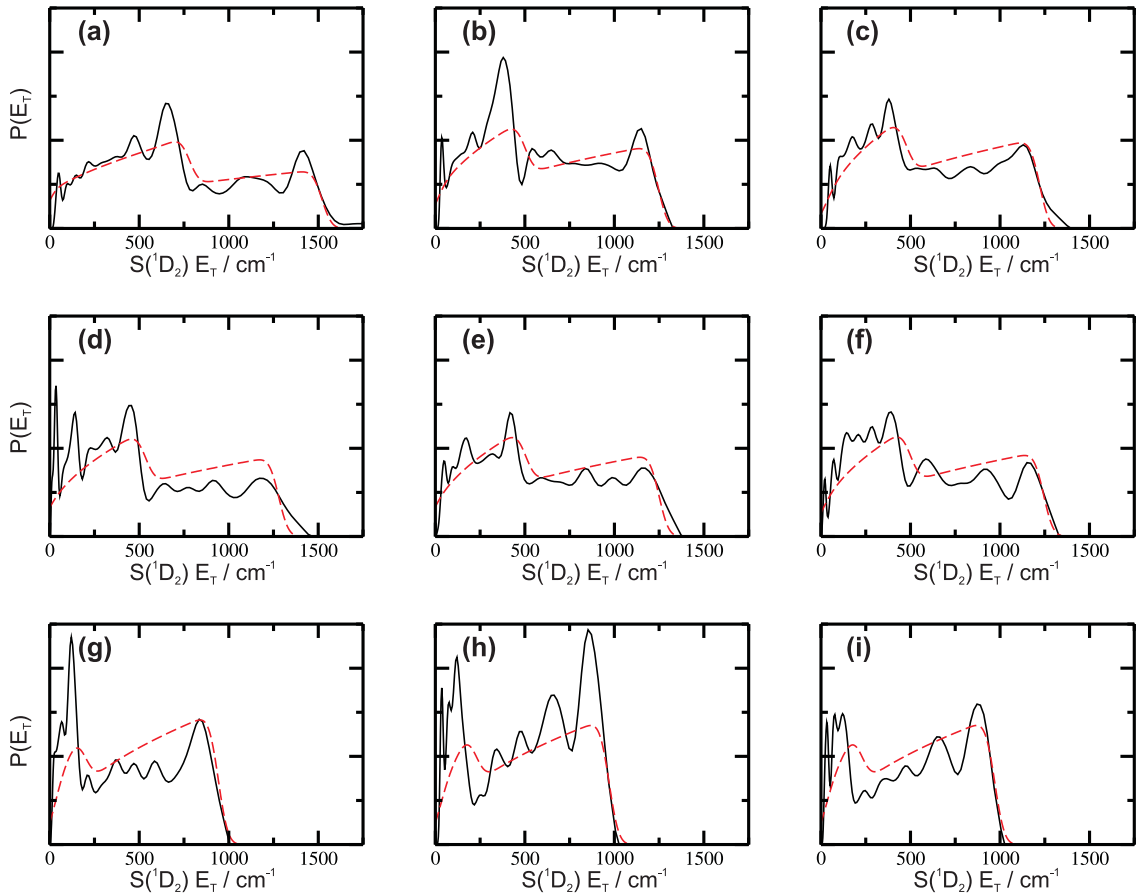

Figure 5.28: $S(^1D_2)$ kinetic energy distibutions (——) and simulations based on the statistical prior distribution (- - -), see text for details. $S(^1D_2)$ data shown for transitions detailed in Table 5.2.

At the low energies of the present experiments, the excitation takes place below the barrier to linearity in the $^1B_2(^1\Sigma_u^+)$ state, and therefore reaches the double well part of the $^1B_2(^1\Sigma_u^+)$ state potential, as viewed along the bending co-ordinate. The excitation is not energetic enough to reach the position of the conical intersection with the $^1B_2(^1\Pi_g)$ state, as illustrated in Figure 5.3.

The statistical product state distributions may indicate that dissociation ultimately occurs on the ground state potential energy surface. It may be possible to explain these observations, for example, in terms of a heterogeneous predissociation following a Coriolis interaction between the electronic and rotational motions. The photoexcited state is of B_2 electronic symmetry and rotation about the x-axis (in

the C_{2v} point group) transforms as b_2 symmetry. Through the electronic-rotation interaction a radiationless transition could take place to a surface of A_1 symmetry, since $B_2 \otimes b_2 = A_1$. A rotationally induced transition may therefore give rise to population in the ground state PES, which transforms as A_1 in C_{2v}. Another possibility is that rotation about the figure axis, which transforms as b_1, could give rise to a transition to a state of A_2 symmetry, since $B_2 \otimes b_1 = A_2$. Recall that the $^1\Pi_g$ state splits into the $A_2 + B_2$ Renner-Teller pair upon bending away from linearity. Unfortunately, however, no information on this state is available to confirm whether dissociation on the A_2 potential would be likely to give rise to statistical product state distributions.

When rotation is not important, an interaction between the electronic and vibrational motions could also give rise to dissociation on the ground state potential. In the excited $^1B_2$ state the coupled symmetric stretching and bending modes both transform as the totally symmetric representation, A_1, and the vibronic states accessed would therefore be of B_2 symmetry. At bent configurations the ground electronic state is A_1 and the asymmetric stretch is described by b_2 symmetry, with the overall vibronic species also B_2. Through the interaction between electronic and vibrational motions a non-radiative transition could therefore transfer population to the ground state. While the above discussion remains speculative, it at least seems clear from the kinetic energy distributions, for both the $K = 0$ and 1 levels, that following excitation below the barrier to linearity the CS_2 molecule ultimately dissociates on a potential which has a rather deep well, high density of states and no exit channel barrier.

The observations of statistical $CS(X^1\Sigma^+)$ product state distributions are in no way at odds with the mode specific dissociation behaviour as discussed by Hepburn and co-workers [170, 171, 204] and Chen *et al.* [177], since measurements made in these studies reflect a different part of the overall dissociation process. Whereas the $CS(v, J)$ distributions indicate, on average, a statistical partitioning of energy when molecules reach the potential on which dissociation finally takes place, the

measurements of $S(^1D_2)/S(^3P_2)$ branching ratios are sensitive to a more dynamical process governing the relative importance of the $S(^1D_2)$ and $S(^3P_2)$ dissociation pathways.

Origin of the oscillatory structure

The $CS(v, J)$ product state distributions seem to fit well on average with a statistical description of the dissociation. However, the distributions presented in Figure 5.28 also show some intruiging oscillatory structure, which is reproduced in several bands. In the region of the absorption spectrum studied excitation takes place to levels with ~ 4 quanta in the combined bending and stretching modes. Therefore, one possibility for the origin of the structure is that it represents a reflection of the transition state wavefunction onto the product rotational state distributions, $P(J_{CS})$.

In a fast and direct dissociation process rotational distributions of the diatomic co-fragment can represent either a direct reflection of the initial ground state wavefunction, or, alternatively, can reflect the initial wavefunction modified somewhat by the anisotropy of the excited state potential [5]. For an indirect process the molecule may survive for many vibrational periods before dissociation eventually occurs *via* some dynamical process, by which time the identity of the initial ground state wavefunction may have been completely 'forgotten' by the system. In this case, however, it is still possible for the wavefunction at the transition state to be mapped onto the product rotational distributions [5].

Reisler and co-workers have developed a model to account for the oscillations in the NO rotational distributions following the photodissociation of NOCl *via* the T_1 state [206, 207]. Their model, a modification of a Franck-Condon treatment for mapping of the parent bending wavefunctions onto the diatomic rotational distributions, was able to account for the experimentally observed multimodal NO $P(J)$ distributions [206, 207]. In a Franck-Condon treatment the rotational distributions of the diatomic fragment are simply determined by the Franck-Condon factors, in this case the square of the overlap between the bending wavefunction at the transition state,

$\Psi^*_{\rm bend}$, and the wavefunctions of the free diatomic fragment, $Y_{20}(\gamma, 0)$ [5]

$$P(J) = \left|\left\langle Y_{J0}(\gamma, 0)|\Psi^*_{\rm bend}(\gamma)\right\rangle\right|^2. \tag{5.4}$$

For NOCl dissociation, the NO rotational distributions derived from the harmonic oscillator bending wavefunctions at the transition state were found to be modified by the torque generated by the angular anisotropy of the excited state potential energy surface. In particular, it was found that the torque resulted in a shift in the NO rotational distributions, which are symmetric about $J = 0$ in the Franck-Condon limit, to higher (or lower) J. The rotational distributions were modelled by [206, 207]

$$P_n(J) = F(J - J_1(T)) + F(-J - J_1(T))\,, \tag{5.5}$$

with

$$F(x) = H_n^2\left(\alpha'^{1/2}\hbar x\right)\exp\left(-\alpha'\hbar^2x^2\right)\,, \tag{5.6}$$

where H_n is the $n^{\rm th}$ order Hermite polynomial, ω is the bending frequency, $\alpha' = (I\omega\hbar)^{-1}$, and I is the bending moment of inertia with $I^{-1} = \left[\frac{1}{\mu r^2}\right] + \left[\frac{1}{mR^2}\right]$. The parameter $J_1(T)$ determines the shift in the rotational distributions from the Franck-Condon limit as a result of the change in the bending angle during dissociation. By using ω, the bending frequency at the transition state, and $J_1(T)$ as adjustable parameters, Reisler and co-workers were able to successfully reproduce the multimodal NO $P(J)$ distributions [206, 207].

In the $^1\Sigma_u^+(^1B_2)$ state of CS_2 the symmetric stretching and bending modes are coupled, and therefore a modified Franck-Condon treatment may not be directly applicable. Furthermore, the precise details of the dissociation following excitation of the $^1\Sigma_u^+(^1B_2)$ state are unknown at present, although possible mechanisms were discussed above. However, in order to assess, at least qualitatively, whether the multimodal distributions observed here could be the result of a reflection of the transition state wavefunction, assumed to be at the $^1\Sigma_u^+(^1B_2)$ state, Equations (5.5) and (5.6) have been used to model the CS rotational distributions assuming four

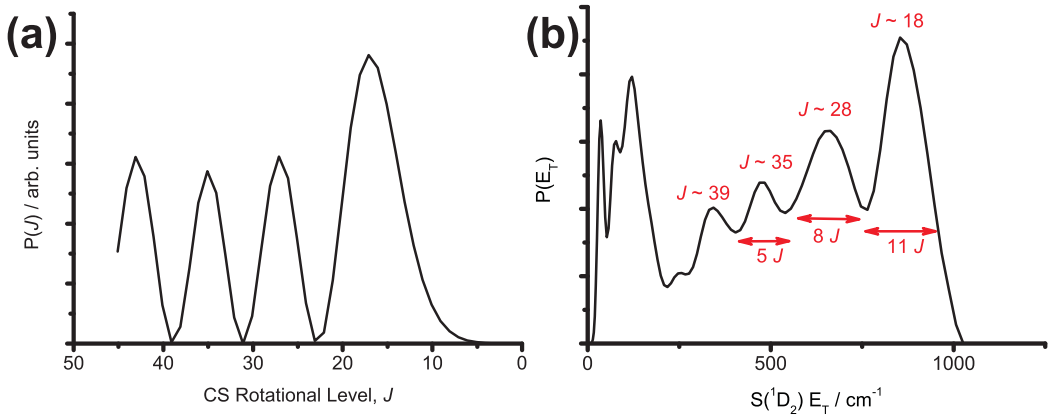

Figure 5.29: **(a)** CS rotational distributions, P(J), calculated using the modified Franck-Condon model (see text for details). **(b)** $S(^1D_2)$ kinetic energy distribution for dissociation *via* transition (h), with the widths and positions of the multiple peaks given in terms of the rotational angular momentum, J, of CS.

quanta in the $^1\Sigma_u^+(^1B_2)$ bending mode. Using the equilibrium value of the Jacobi length, R, and of the bending frequency in the $^1\Sigma_u^+(^1B_2)$ state, $\omega \sim 400\,\mathrm{cm}^{-1}$, the CS $P(J)$ distributions were modelled with $J_1(T)$ an adjustable parameter.

The CS $P(J)$ distribution calculated using the modified Franck-Condon model is shown in Figure 5.29. Also shown is the $S(^1D_2)$ kinetic energy distribution observed following excitation *via* transition (h). The best agreement between the model and the experimental data was found with $J_1(T) \sim 35$. The CS P(J) distributions calculated using the model are cut off for $J > 47$ as these states are inaccessible on energetic grounds. The positions of the peaks in the $S(^1D_2)$ kinetic energy distribution at $J \sim 18, 28, 35, 39$ appear to be in reasonable accord with those predicted by the model $J \sim 17, 27, 35, 43$. Furthermore, the widths of the peaks determined by the model, $\Delta J \sim 10$ for the lowest J peak and $\Delta J \sim 5$ for the others, also appear comparable to the widths of the structures seen in the $S(^1D_2)$ kinetic energy distribution. Finally, the model also predicts that the most intense peak should correspond to the lowest J, consistent with the experimental data.

From the above discussion it appears plausible that the oscillations seen in the CS rotational distributions may result from a reflection of the transition state wavefunction. The position of the peaks in the CS P(J) distribution also indicate a

modest torque is generated by changes in the bending angle during dissociation. As mentioned above, the modified Franck-Condon model can only be used here qualitatively since the bending and stretching modes in the $^1\Sigma_u^+(^1B_2)$ are strongly mixed, and the details of the potentials sampled on route to dissociation have yet to be worked out.

If the oscillations in the product state distributions do indeed represent a reflection of the transition state wavefunction, it is perhaps surprising that on average they seem to fit so well with a statistical prior distribution. Schinke has discusssed two limiting cases for dissociations that proceed *via* a long lived intermediate such that memory of the initial ground state wavefunction is lost by the system [5]. In particular, for a dissociation that proceeds *via* a narrow transition state separating the reactants and products, Schinke has shown that the product rotational distributions can reflect the (bending) wavefunction of the molecule at the transition state. On the other hand, where the transition state is very broad the product state distributions are frequently found to be statistical [5]. For the case of CS_2 photolysis the $CS(v, J)$ product state distributions exhibit features expected from both limiting types of process, dynamical and statistical, as outlined above. This may indicate that the dissociation lies in between these two limiting extremes or that there are two competeing processes involved, giving rise to the features observed in the $CS(v, J)$ distributions. It is interesting to note, therefore, that there appears to be a continuum background to the first absorption band. The possibility of the oscillatory structure in the $CS(v, J)$ product state distributions representing a reflection of the transition state wavefunction is discussed further in Section 5.6, with respect to future work.

5.5.3 Spatial anisotropy parameter, β

The speed dependence of the spatial anisotropy parameters, $\beta(v_P)$, for all photodissociation wavelengths studied herein are shown in Figure 5.26. The parameters are all positive, consistent with a parallel-type transition. A general trend of decreasing

β with increasing internal excitation of the $CS(X^1\Sigma^+)$ co-fragment is apparent for all dissociation wavelengths.

A number of factors must be considered before attempts can be made to explain the values of the anisotropy parameters measured in the current work. Firstly, consideration must be given to the precise nature of the excitation process, and, in particular, the rotational details of the rovibronic transition, *i.e.* P, Q or R-branch excitation. Secondly, the anisotropy will depend on the geometry and lifetime of the vibronic level acessed *via* the optical process. Finally, consideration should also be given to the prospect of non-axial or transverse components to the recoil direction. In the following paragraphs the likely importance to the measured β parameters from the above mentioned factors are discussed.

For a symmetric top molecule the β parameter following P, Q and R-branch excitation has been shown to be given by [198, 208, 209]

$$\beta(P) = \left[\frac{J_i(J_i+1) - 3K_i}{J_i(2J_i+1)}\right] \tag{5.7}$$

$$\beta(Q) = -\left[\frac{J_i(J_i+1) - 3K_i}{J_i(J_i+1)}\right]$$

$$\beta(R) = \left[\frac{(J_i+1)(J_i+2) - 3K_i}{(J_i+1)(2J_i+1)}\right],$$

where J_i refers to the initial rotational angular momentum of the parent molecule and K represents the projection on the figure axis. Since the rotational temperature of the molecular beam is believed to be $< 10\,\mathrm{K}$, only a small number of rotational levels of the parent molecule, J_i, may be expected to be populated in the molecular beam. The dependence of β on initial rotational level for P, Q, and R-branches, as calculated from Equation (5.7), are shown in Figure 5.30 for both $K = 0$ and $K = 1$. As seen from inspection of Figure 5.30, at low J_i the β parameter for a symmetric top molecule depends strongly on the exact nature of the transition. A

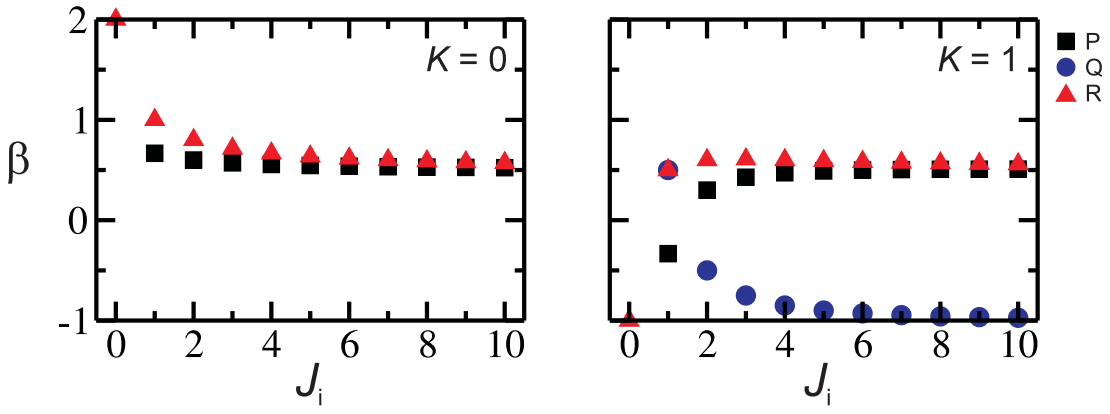

Figure 5.30: Spatial anisotropy parameter, β, for symmetric top molecule as a function of the initial rotational angular momentum, J_i. $K = 0$ shown on left and $K = 1$ on right.

particularly striking example is the change in β of 1 for $K = 0$ R-branch excitation from $J_i = 0$ to 1. In the present work the rotational transitions optically excited are incompletely resolved, due to the low rotational constant of CS_2 in both the ground and excited states, $B \sim 0.1\,\mathrm{cm}^{-1}$. The precise details of the possible overlapping transitions, taking into account a rotational temperature of $\sim 10\,\mathrm{K}$, that may be associated with each dissociation wavelength are detailed in Table 5.3, and, perhaps, illustrate the difficulty in interpreting the angular distribution for this system even in the absence of other factors.

For work carried out in this region, close to the $S(^1D_2)$ threshold, little energy is available to the products. In cases where the kinetic energy release is small and the rotational excitation of the diatomic fragment is large, non-axial or transverse components to the recoil direction should be expected. Therefore, it is not unreasonable to expect that non-axial recoil effects make an important contribution to the measured angular distribution. In order to attempt to quantify this effect the spatial anisotropy for the photodissociation, following excitation *via* band (a), was modelled classically using the method introduced by Reisler and co-workers [91]. This non-axial recoil model has been sucessfully applied to several triatomic photodissociation cases, including, for example, NO_2 [91] and OCS [194]. The important

Energy / cm^{-1}	Label	Rotational Lines
48032.91	(b)	R(0)
47980.76	(c)	R(6, 8),R(14)
47562.48	(g)	R(4)

Table 5.3: Overlapping rotational transitions based on laser spectral bandwidth of $0.2\,cm^{-1}$. Only transitions with previous band origin measurements [204] are shown.

parameters for the model, which is based on angular momentum conservation, are shown schematically in Figure 5.31. In the following the important parameters in the model are described.

Angular momentum conservation dictates that

$$J_{CS_2} = J_{CS} + J_S + \ell\,, \tag{5.8}$$

where J_{CS_2}, J_{CS}, and J_S refer to the total angular momentum of the parent molecule, the CS and the S photofragments, respectively, and ℓ refers to the orbital angular momentum of the system. In the classical model J_{CS_2} and J_S are neglected and so the magnitude of the orbital angular mometum $|\ell| \approx |J_{CS}|$ such that

$$|\ell| = \mu v_{rel} b = \hbar\sqrt{J_{CS}(J_{CS}+1)}\,, \tag{5.9}$$

where the impact parameter, b, is shown in Figure 5.31, and μ and v_{rel} are the reduced mass and relative speed of the atom-diatom system. Rotation of the co-fragment is assumed to be established at some Jacobi distance, R_r. The impact parameter and Jacobi length can then be related to the angle, α', describing the deflection from linearity, *via* $\alpha' = \sin^{-1}(b/R_r)$. The spatial anisotropy may then be written as

$$\beta \simeq 2P_2(\cos\chi')\,, \tag{5.10}$$

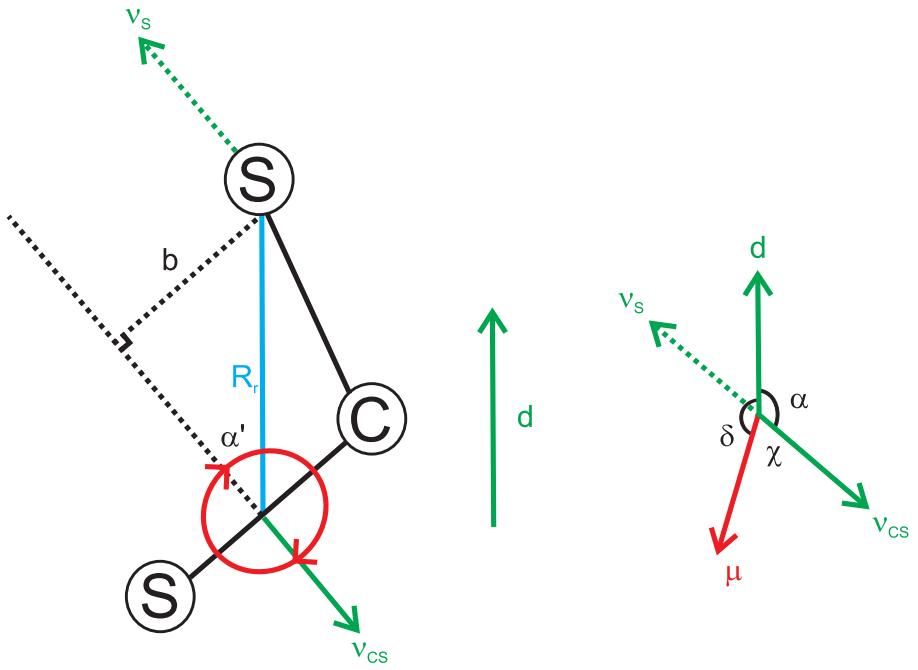

Figure 5.31: Parameters used to classically model the spatial anisotropy parameter, β, as a function of the rotational excitation of the diatomic co-fragment. On the left the exit impact parameter, b, and Jacobi length, R_r, at which CS rotation is established are defined. Also shown is d which indicates the direction of R at the moment of excitation. On the right the angles α, δ, and χ are defined. Adapted from Refs [47, 194].

where the angle, χ', refers to the angle between v_S and μ. This angle, $\chi' = 180° - \chi$, may also be written as $\chi' = \delta - \alpha'$ if all vectors are co-planar, see Figure 5.31. By using R_r and δ as adjustable parameters, the spatial ansiotropy, β, can be modelled as a function of the rotational angular momentum of the diatomic co-fragment, J_{CS}.

The spatial anisotropy parameter, β, following photodissociation *via* transition (a) shows strong speed dependence, see Figure 5.26, decreasing quickly from a maxima of $\sim$ 1.4 as J_{CS} increases. Using the methodology set out above, the speed dependence of β for this transition could be successfully modelled by allowing the transition dipole moment, μ, to be deflected away from the initially linear SCS axis. In particular a small tilt angle, δ, of 155° and a Jacobi length, R_r, of 2.79 Å allowed suitable modelling of the experimental measurement. Comparison of the experimental data with the classical model is shown in Figure 5.32. Perhaps reassuringly,

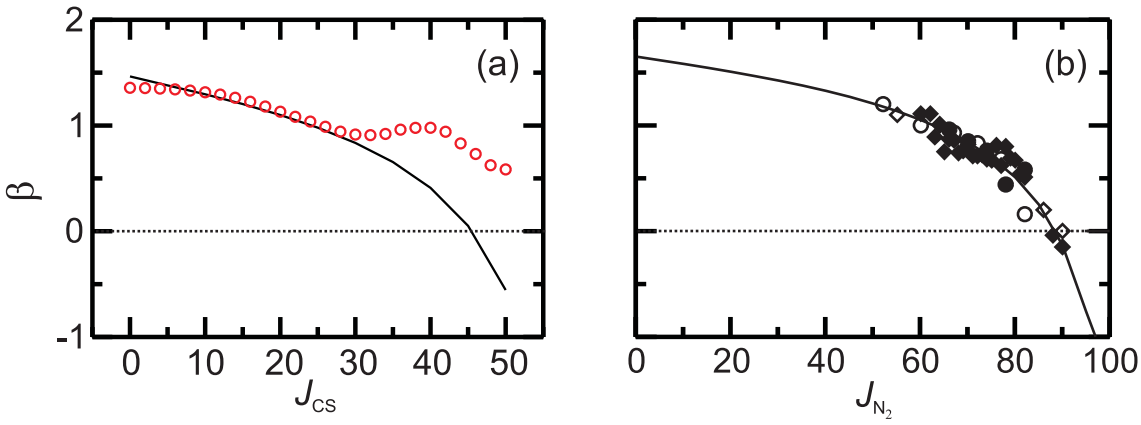

Figure 5.32: Modelling of the spatial ansiotropy parameter as a function of the rotational angular momentum of the CS diatomic (left). Model parameters are R_r = 2.79 Å and $\delta = 155°$, see text for details. Experimental data represented by the red circles. Shown on the right is the model (——) applied to the N_2O system [47, 194], in which similar parameters were applied. Experimental points from Refs [124, 210–212].

the Jacobi length, R_r, used to model the spatial anisotropy parameter corresponds to that found for the equilibrium Jacobi length of CS_2 in the excited $^1B_2$ state. Moreover, the modest deflection of the transition dipole moment and the Jacobi length used to model the speed dependence of β are very similar to the parameters which were successfully used to treat the isovalent molecule N_2O [47], as shown in Figure 5.32, perhaps indicating that similar torques would be generated in the both dissociations. It should be noted that the disagreement between the classical model and experimental measurements for $J_{CS} > 40$ is attributable to the onset of the production of CS ($v = 1$), which overlaps with the production of high rotation $v = 0$ photofragments in the velocity distribution, making it difficult to extract a β value for the $v = 0$ and $v = 1$ levels separately.

The experimentally measured spatial anisotropy will depend on numerous factors, discussed above, making quantitative assertions about this parameter difficult. However, the measurements for photodissociation resulting in the highest kinetic energy release seem to be successfully reproduced using a classical model to account for non-axial recoil. It therefore seems plausible to assume that non-axial effects

will be even more important for the lower kinetic energy release (longer wavelength) measurements. In addition, the similarity between the parameters used to model the non-axial recoil for CS_2 and N_2O lend further support to this analysis.

5.6 Summary and future work

Following dissociation above the barrier to linearity, at 193.3 nm, the $CS(X^1\Sigma^+)$ fragments are found to be produced with a high degree of vibrational excitation. This is in stark contrast to the dissociation of the OCS system at 248 nm, which results in little or no vibrational excitation in the diatomic fragment. For OCS, the spatial anisotropy could be successfully modelled classically, taking into account the effects of non-axial recoil. For CS_2 at 193.3 nm, however, the rotational excitation is too low to cause significant non-axial recoil. Furthermore, it is difficult to interpret the β parameter solely in terms of the lifetime of the excited state. More likely, the nature of the excitation process itself holds the key to the interpretation of β. Interestingly, no orbital polarisation, alignment or orientation, was observed in the $S(^1D_2)$ products. Attempts were made to interpret this in terms of the long range interactions between the $S(^1D_2)$ and $CS(X^1\Sigma^+)$ fragments. It seems more probable, however, that the complicated motion along the dissociation co-ordinate, in addition to the precise nature of the excitation ultimately give rise to this observation.

Below the barrier to linearity in the excited state, intriguing behaviour has been observed. Firstly, it seems that the $S(^3P_2)/S(^1D_2)$ branching ratio is highly dependent on the vibrational state accessed following absorption. In particular, PHOFEX spectra presented here seem to add further support to the mode specificity described by Hepburn and co-workers [170, 171, 204]. It was also found that the $CS(X^1\Sigma^+ v,J)$ internal energy distributions were well described, on average, by a statistical prior distribution. The statistical product state distributions were taken to indicate that dissociation, following excitation below the barrier to linearity in the $^1\Sigma_u^+(^1B_2)$ state, occurs on the ground state potential energy surface. It was suggested that either coupling between the electronic and vibrational or electronic and rotational motions

could result in a radiationless transition to the ground electronic state. Interesting oscillatory structure was also observed in the product state distributions. Although difficult to understand, it was suggested that the origin of this structure could arise through a mapping of the transition state wavefunction onto the $CS(X^1\Sigma^+)$ product rotational distributions. Finally, the angular distibutions were found to be successfully modelled by taking into account non-axial recoil effects. The parameters used to model β were found to be similar to those previously applied to N_2O [47], perhaps indicating similarity in the dissociation geometries accessed in the two systems.

Overall there seems to be plenty of scope for further studies on this interesting system. One possibility is to evaluate the product state distributions in the $S(^1D_2)$ channel at even lower energies. Excited state species would then be produced with fewer quanta in the combined symmetric stretching and bending modes, giving rise to different transition state wavefunctions. Additionally, since the measurements made here seem to point to rather different dynamics occurring far above and below the barrier to linearity, it would be interesting to investigate the dissociation around the position of this barrier $\sim 204\,\text{nm}$. Finally, investigation of the dissociation dynamics following excitation completely off-resonance would enable one to see if contributions from bound-continuum and bound-bound excitation processes are made to the dissociation processes studied here.

Chapter 6

Photodissociation of CS_2 : the $S(^3P_J)$ channel

In this chapter experimental results on the photodissociation of CS_2 at several wavelengths are presented. The results were obtained by probing the three spin-orbit states of the $S(^3P_J)$ photofragments following excitation below the barrier to linearity in the $^1\Sigma_u^+(^1B_2)$ state. Compared to dissociation into $CS(X^1\Sigma^+)$ + $S(^1D_2)$, as discussed in Chapter 5, much more energy is available to the diatomic co-fragment in the $CS(X^1\Sigma^+)$ + $S(^3P_J)$ channel. Experimental data is presented following the excitation of three vibronic bands in the highly structured absorption spectrum. Results for dissociation into this spin-forbidden channel are compared with those following excitation above the barrier to linearity in the $^1\Sigma_u^+(^1B_2)$ state and also to the dissociation of the isovalent molecule OCS.

6.1 Background

As discussed in Chapter 5, most experimental studies have been performed following excitation at 193.3 nm, above the barrier to linearity in the $^1\Sigma_u^+(^1B_2)$ state. At these energies the spin-forbidden dissociation into $CS(X^1\Sigma^+)$ + $S(^3P_J)$ gives rise to highly vibrationally excited diatomic photofragments. Energetically, the $CS(X^1\Sigma^+)$ fragments can populate levels up to $v_{\max} = 13$, with several studies pointing to

the maximum in the vibrational population being in the range $v = 7 - 10$ [172, 181, 188, 189]. As mentioned in Chapter 5, several studies have probed the angular distribution of the triplet S-atoms following dissociation at 193.3 nm [172, 174, 186, 187, 190]. Although there is some discrepancy between previous results, the most recent ion imaging studies appear to be in good agreement. From these studies the β parameter is found to be similar for each $S(^3P_J)$ spin-orbit level, characterised by a speed averaged value of ~ 0.4 [186, 196]. The magnitude of β is similar to that obtained following the spin-allowed dissociation into $CS(X^1\Sigma^+) + S(^1D_2)$ providing an indication that the singlet and triplet products arise following excitation to a common electronically excited state, and subsequently follow similar dissociation dynamics.

$S(^3P_J)$ spin-orbit populations have also been reported by several groups, and are found to be highly non-statistical, with $S(^3P_2) : S(^3P_1)$ reported to be $\sim 3 : 1$ [172, 188, 189, 196]. As discussed in Section 2.2.2, non-statistical spin-orbit populations indicate that the dissociation cannot be described in the 'statistical' or 'diabatic' limit. In the diabatic limit, one assumes that complete mixing takes place between the asymptotic potentials and the spin-orbit branching ratio is simply determined by the degeneracy of the fine-structure levels. The $(J = 2) : (J = 1)$ ratio of $1.7 : 1$ predicted from the degeneracies of the fine-structure levels indicates that the dissociation at 193.3 nm may be closer to the adiabatic limit. Furthermore, in the diabatic limit the speed distributions, $P(v_P)$, for each of the spin-orbit states would be expected to be the same. Results from two imaging studies at 193.3 nm [186, 196], however, indicate that the distribution for the $J = 2$ level is significantly different from that of the $J = 0$ and 1 species, and provides a further indication that the dissociation at 193.3 nm is not well described in the diabatic limit.

Interesting polarisation effects have also been observed for the triplet S-atoms following dissociation at 193.3 nm [196]. As with the $S(^1D_2)$ products discussed in Chapter 5, the $S(^3P_2)$ fragments were shown to be unpolarised, however, significant alignment effects were observed for the $S(^3P_1)$ species. Similar incoherent alignment

effects in the molecular frame have also been reported following the dissociation of the triatomic molecule OCS at 248 nm [194]. In particular, the $J = 2$ states for both systems were found to be characterised by isotropic M_J populations while for $J = 1$ a preferential population was reported in the $M_J = \pm 1$ levels [194, 196]. The similarities between the polarisation data may indicate that a similar mechanism is responsible for the photofragment alignment effects in both cases.

There have been comparatively few studies on the dissociation at lower energies, below the barrier to linearity in the $^1\Sigma_u^+(^1B_2)$ state. However, as discussed in Chaper 5, several studies have pointed to a mode specificity in this wavelength region. In particular, dissociation following excitation of $K > 0$ levels in the $^1\Sigma_u^+(^1B_2)$ state were found to be characterised by a higher $S(^1D_2)/S(^3P_2)$ branching ratio and a faster dissociation rate than for $K = 0$ levels [170, 171, 175–177]. In Chapter 5 it was suggested that for $K > 0$ dissociation the $S(^1D_2)$ products arise following a Coriolis interaction between electronic and rotational motions. For dissociation to the triplet channel Hepburn and co-workers have reported yields of the $S(^3P_J)$ spin-orbit states. The results following excitation of the Σ bands appear similar to that observed at 193.3 nm, giving a $(J = 2) : (J = 1)$ ratio of $\sim 3 : 1$, however, following excitation of Π bands this ratio was found to be near $1 : 1$ [170]. The differences in the spin-orbit branching ratios for the excitation of $K > 0$ levels perhaps indicates a different dissociation mechanism than following $K = 0$ excitation.

Compared to the singlet potentials, less information is available on the triplet surfaces giving rise to $CS(X^1\Sigma^+) + S(^3P_J)$ products. The most recent *ab initio* work presented by Bisgaard *et al.* [173] points to a surface of $^3\Pi_g$ symmetry at linearity as that giving rise to triplet S-atoms. 1D slices through the potentials are shown in Figure 5.4. At linearity two triplet states of Σ_g and Π_g symmetry correlate adiabatically with the $S(^3P_J)$ asymptote, although no information is available on the former.

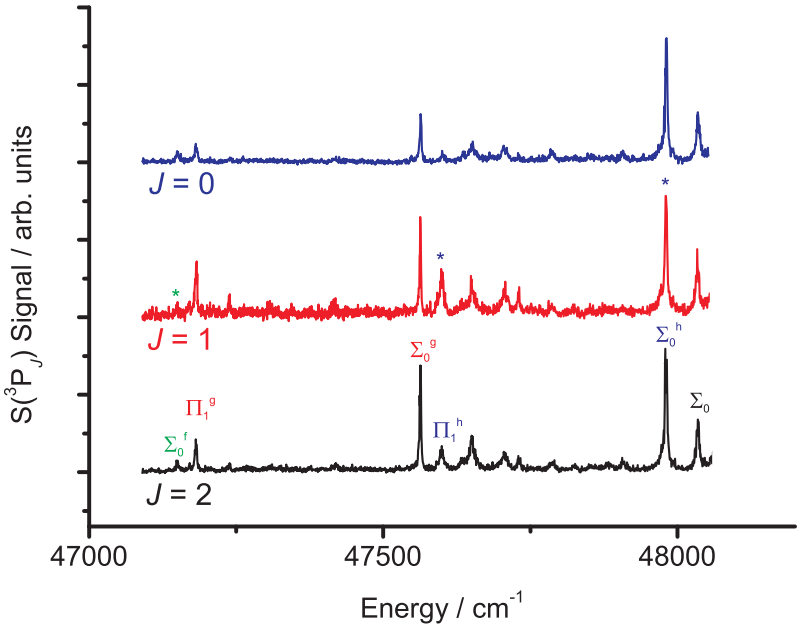

Figure 6.1: $S(^3P_J)$ photofragment excitation spectra for $J = 2$ (bottom), $J = 1$ (middle) and $J = 0$ (top) species. Band assignments are taken from the work of Douglas and Zanon [159]. The superscripts f, g and h designate the excited vibrational state and the subscripts 0 and 1 refer to the number of quanta in the bending mode of ground state CS_2. The bands labelled with an asterisk indicate the transitions studied in the current work.

6.2 Results

6.2.1 Spectra

Photofragment excitation spectra were generated in a two colour experiment by scanning the photolysis (pump) laser with the probe laser fixed in order to selectively detect the $S(^3P_J)$ products. The $S(^3P_2)$, $S(^3P_1)$ and $S(^3P_0)$ fragments were ionised using the (2+1) REMPI transitions *via* the $S(^3P_1)$, $S(^3P_2)$ and $S(^3P_2)$ intermediate states at 308.1, 310.0 and 310.8 nm, respectively. The three spectra are shown in Figure 6.1.

For two of the photolysis wavelengths used, corresponding to the Σ_0^h and Π_1^h transitions, REMPI scans, in which the total ion signal was recorded as a function of the probe wavelength, were performed in order to elucidate the relative spin-orbit populations for the triplet channel. The relative linestrengths for the three

REMPI transitions are unknown but believed to be approximately the same [172, 189, 213]. By integrating over each individual peak, the ratio of population in the three spin-orbit states could be estimated. The spin-orbit populations obtained from the REMPI spectra are detailed in Table 6.1, although given the uncertainty in the relative linestrengths of the REMPI transitions the estimates of the spin-orbit populations may be associated with large errors.

	Expt.			Starrs *et al.*		
Band Position / cm^{-1}	$S(^3P_2)$	$S(^3P_1)$	$S(^3P_0)$	$S(^3P_2)$	$S(^3P_1)$	$S(^3P_0)$
47980 (Σ_0^h)	3.3(9)	1.0(4)	2.1(7)	3.1	1.0	1.2
47597 (Π_1^h)	1.7(6)	1.4(6)	1.0(4)	1.0	1.0	< 1

Table 6.1: Populations of the $S(^3P_J)$ spin-orbit levels following excitation of the Σ_0^h and Π_1^h transitions (left). Also shown (right) are previous results from Hepburn and co-workers [170].

6.2.2 Ion images and fits

Ion images of the $S(^3P_2)$, $S(^3P_1)$ and $S(^3P_0)$ photofragments were recorded following excitation of the three bands indicated in Figure 6.1. Ion images of the $S(^3P_0)$ fragments were recorded using the (2+1) REMPI transition *via* the $S(^3P_2)$ intermediate state at 310.8 nm. For the $S(^3P_0)$ species, which cannot be polarised, ion images were recorded in the HH and VV pump-probe geometries. Images of the $S(^3P_1)$ fragments were recorded using the (2+1) REMPI transition *via* the $S(^3P_2)$ intermediate state at 310.0 nm. The images were recorded using linearly polarised pump and probe radiation. In addition, following excitation of the Σ_0^h transition, ion images were also recorded using circularly polarised pump and probe radiation. For the $S(^3P_2)$ species, ion images were collected *via* the $S(^3P_1)$ intermediate state in the (2+1) REMPI transition at 308.1 nm. Ion images, Fourier moments and fits to the $S(^3P_2)$, $S(^3P_1)$ and $S(^3P_0)$ data are presented in Figures 6.2 to 6.11 in order of increasing photolysis wavelength.

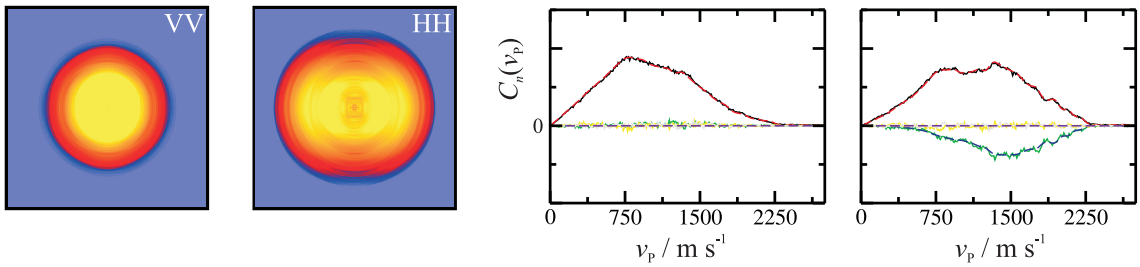

Figure 6.2: Ion images (false colour), Fourier moments (——), and fits (- - -) for the $S(^3P_0)$ atomic products probed *via* the $S(^3P_2)$ intermediate state. The Fourier moments are colour coded, C_0 (black), C_2 (green), C_4 (yellow), C_6 (grey). $S(^3P_0)$ data collected following excitation of the Σ_0^h transition.

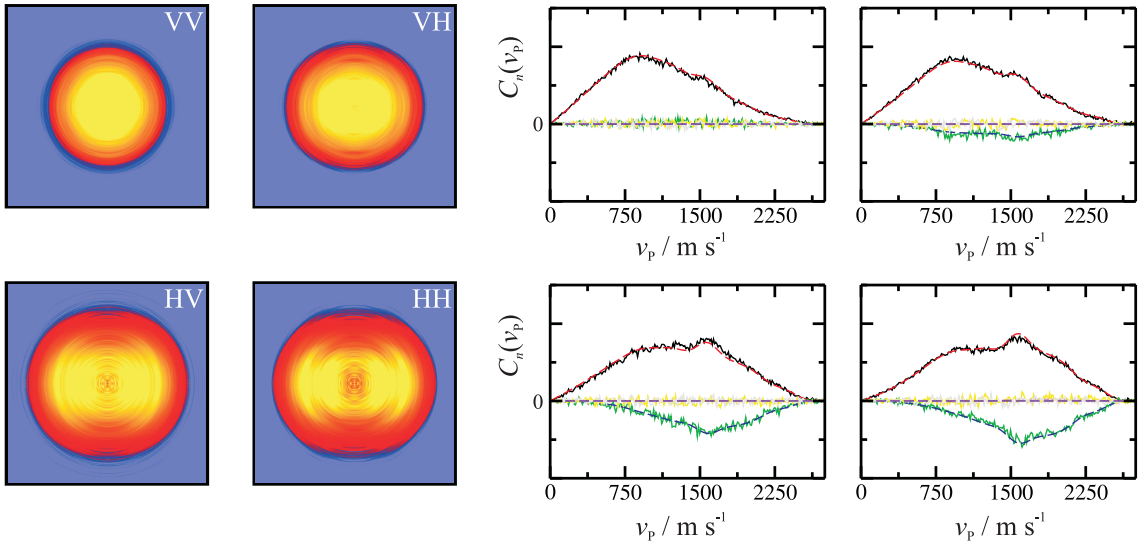

Figure 6.3: Ion images (false colour), Fourier moments (——), and fits (- - -) for the $S(^3P_1)$ atomic products probed *via* the $S(^3P_2)$ intermediate state. The Fourier moments are colour coded, C_0 (black), C_2 (green), C_4 (yellow), C_6 (grey). $S(^3P_1)$ data collected following excitation of the Σ_0^h transition.

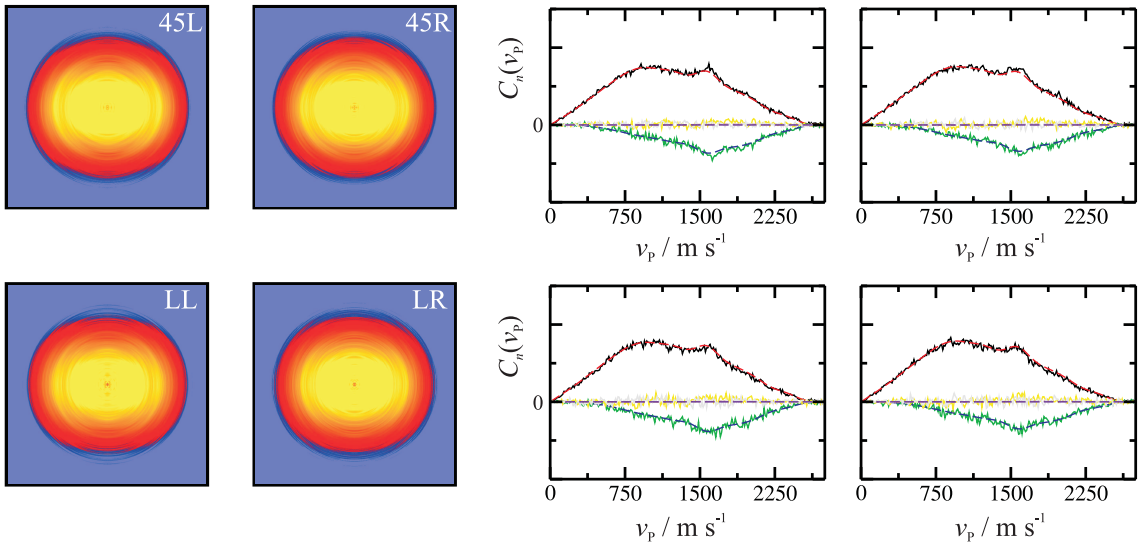

Figure 6.4: Ion images (false colour), Fourier moments (——), and fits (- - -) for the $S(^3P_1)$ atomic products probed *via* the $S(^3P_2)$ intermediate state. The Fourier moments are colour coded, C_0 (black), C_2 (green), C_4 (yellow), C_6 (grey). $S(^3P_1)$ data collected following excitation of the Σ_0^h transition.

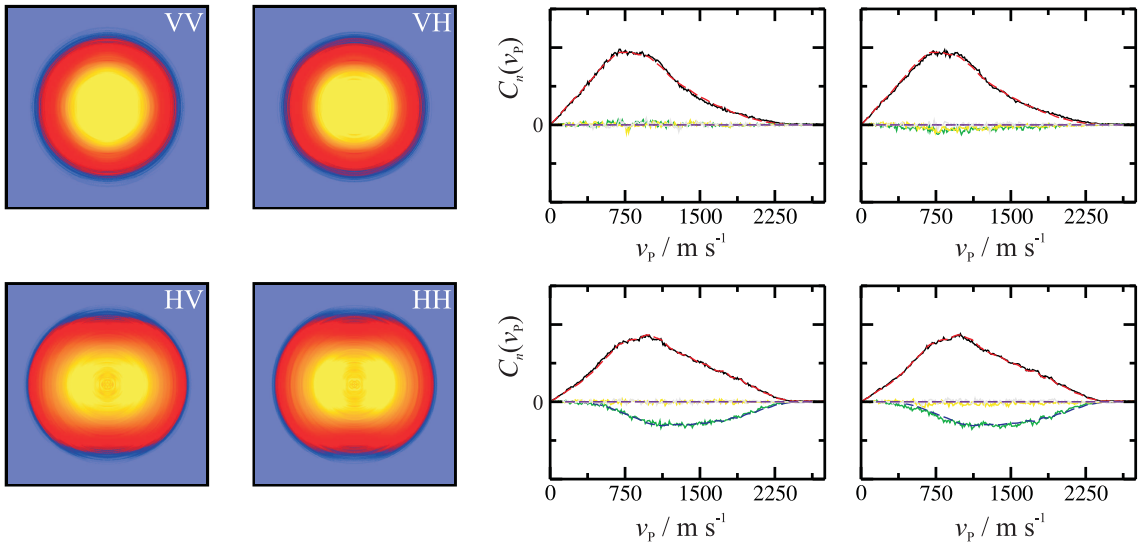

Figure 6.5: Ion images (false colour), Fourier moments (——), and fits (- - -) for the $S(^3P_2)$ atomic products probed *via* the $S(^3P_1)$ intermediate state. The Fourier moments are colour coded, C_0 (black), C_2 (green), C_4 (yellow), C_6 (grey). $S(^3P_2)$ data collected following excitation of the Σ_0^h transition.

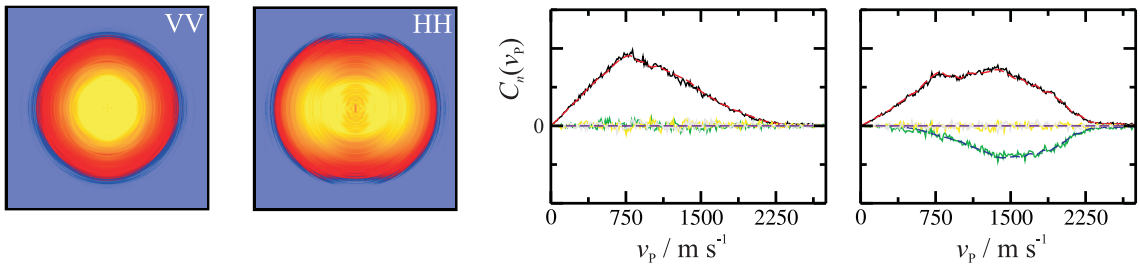

Figure 6.6: Ion images (false colour), Fourier moments (——), and fits (- - -) for the $S(^3P_0)$ atomic products probed *via* the $S(^3P_2)$ intermediate state. The Fourier moments are colour coded, C_0 (black), C_2 (green), C_4 (yellow), C_6 (grey). $S(^3P_0)$ data collected following excitation of the Π_1^h transition.

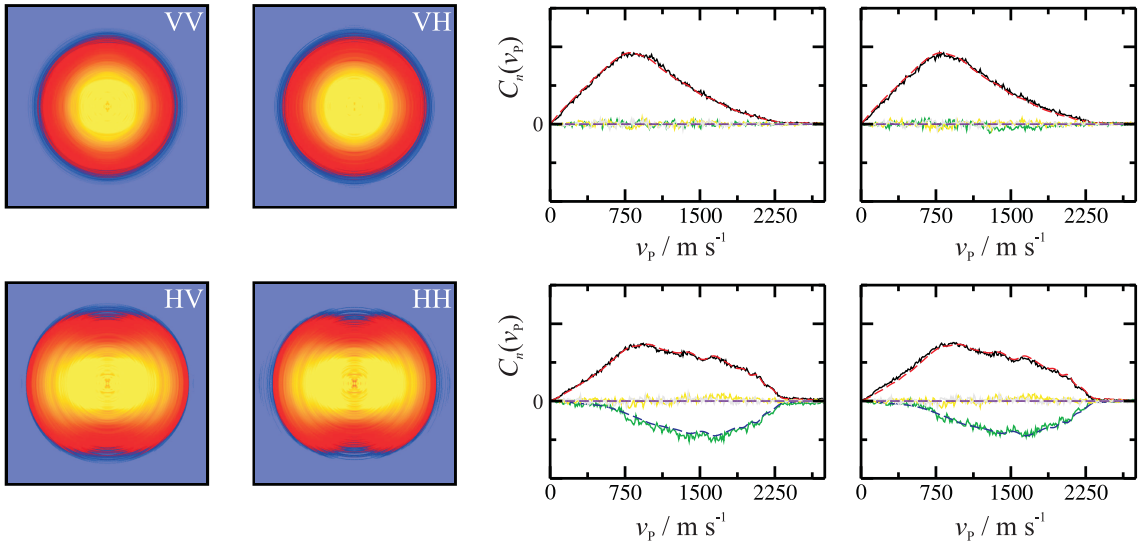

Figure 6.7: Ion images (false colour), Fourier moments (——), and fits (- - -) for the $S(^3P_1)$ atomic products probed *via* the $S(^3P_2)$ intermediate state. The Fourier moments are colour coded, C_0 (black), C_2 (green), C_4 (yellow), C_6 (grey). $S(^3P_1)$ data collected following excitation of the Π_1^h transition.

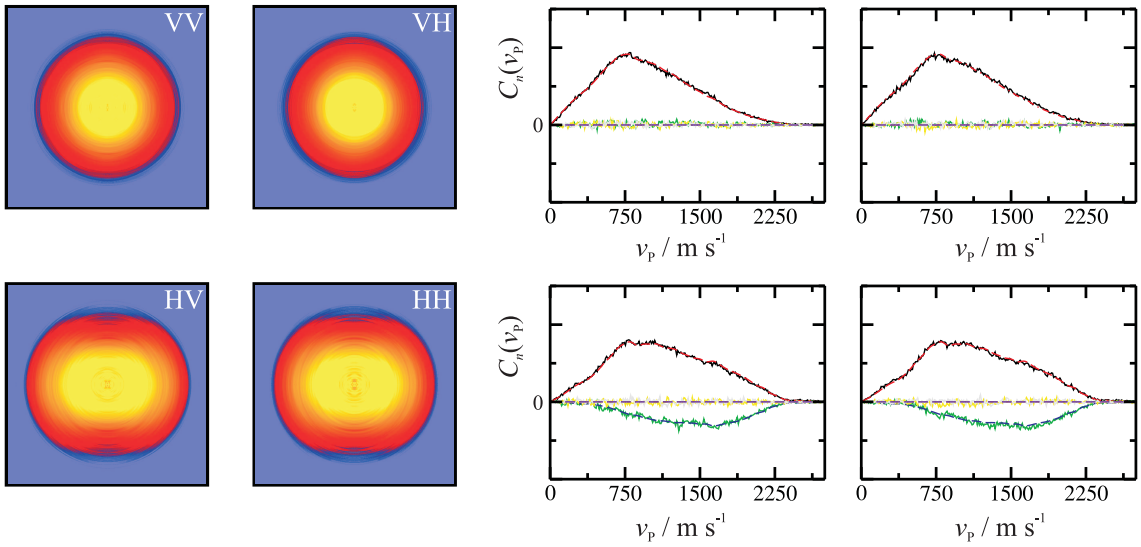

Figure 6.8: Ion images (false colour), Fourier moments (——), and fits (- - -) for the $S(^3P_2)$ atomic products probed *via* the $S(^3P_1)$ intermediate state. The Fourier moments are colour coded, C_0 (black), C_2 (green), C_4 (yellow), C_6 (grey). $S(^3P_2)$ data collected following excitation of the Π_1^h transition.

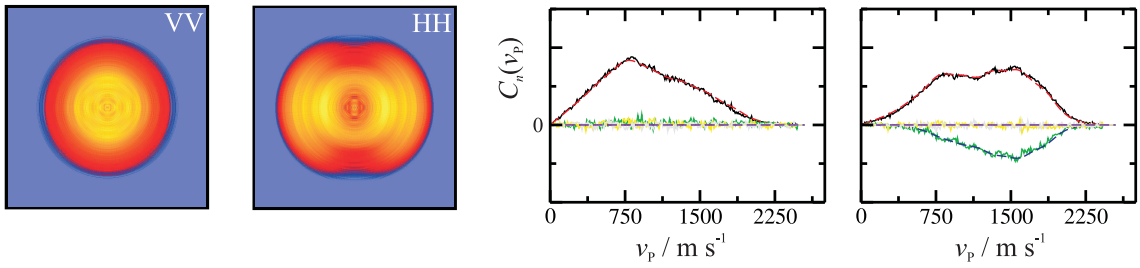

Figure 6.9: Ion images (false colour), Fourier moments (——), and fits (- - -) for the $S(^3P_0)$ atomic products probed *via* the $S(^3P_2)$ intermediate state. The Fourier moments are colour coded, C_0 (black), C_2 (green), C_4 (yellow), C_6 (grey). $S(^3P_0)$ data collected following excitation of the Σ_0^f transition.

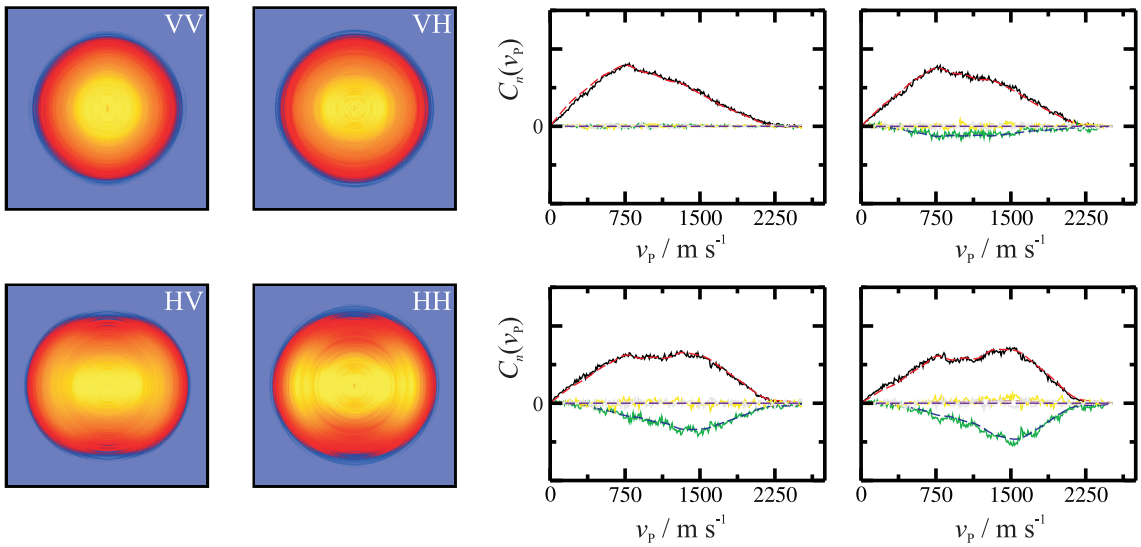

Figure 6.10: Ion images (false colour), Fourier moments (——), and fits (- - -) for the $S(^3P_1)$ atomic products probed *via* the $S(^3P_2)$ intermediate state. The Fourier moments are colour coded, C_0 (black), C_2 (green), C_4 (yellow), C_6 (grey). $S(^3P_1)$ data collected following excitation of the Σ_0^f transition.

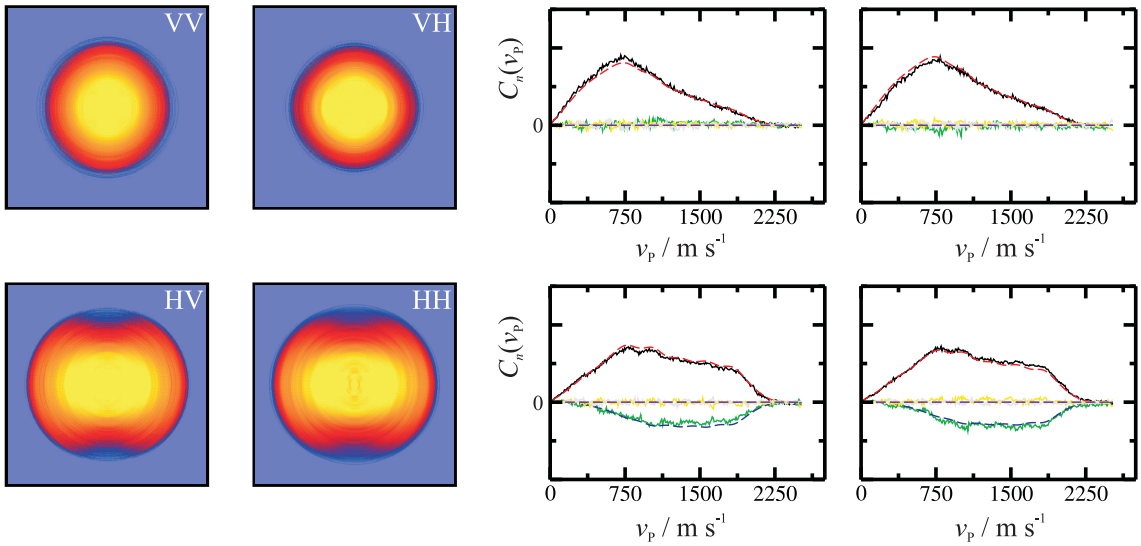

Figure 6.11: Ion images (false colour), Fourier moments (——), and fits (- - -) for the $S(^3P_2)$ atomic products probed *via* the $S(^3P_1)$ intermediate state. The Fourier moments are colour coded, C_0 (black), C_2 (green), C_4 (yellow), C_6 (grey). $S(^3P_2)$ data collected following excitation of the Σ_0^f transition.

6.3 Discussion

6.3.1 Spectra

The $S(^3P_J)$ photofragment excitation spectra, shown in Figure 6.1, are qualitatively similar for the three spin-orbit levels. The main difference between the $S(^3P_2)$ and $S(^3P_1)$ spectra appears to be the relative intensity of the Π_1^h band located at 47,597 cm^{-1}. This band in particular, and also the Π_1^h band at 47,150 cm^{-1}, appears to be more significant for the $S(^3P_1)$ species, relative to the nearby Σ bands. The $S(^3P_0)$ spectrum appears quite similar to that obtained for $S(^3P_2)$, aside from the reduction in intensity of the Σ_0^g band for $S(^3P_0)$.

REMPI spectra have also been used to estimate the populations of the $S(^3P_J)$ spin-orbit levels following excitation *via* the Σ_0^h and Π_1^h transitions, as detailed in Table 6.1. The spin-orbit populations estimated here appear to be in good accord with previously reported values by Hepburn and co-workers [170]. Following excitation *via* the Σ_0^h transition the $(J = 2) : (J = 1)$ ratio of $\sim 3 : 1$ is very similar to that observed following photodissociation at 193.3 nm, above the barrier to linearity in the $^1\Sigma_u^+(^1B_2)$ state [172, 188, 189, 196]. For the Π_1^h transition, however, the $S(^3P_1)$ species are much more important, giving a near 1 : 1 branching ratio. Hepburn and co-workers have also provided the $S(^3P_J)$ yields for several more vibronic bands [170]. Their data appear to suggest a more general trend in that excitation of Σ bands results in a $(J = 2) : (J = 1)$ ratio close to 3 : 1, while following excitation of Π bands the ratio is closer to 1 : 1. The spin-orbit populations for both transitions are found to be highly non-statistical, cf. $1.7 : 1 : 0.3$ for $J = 2 : 1 : 0$. As mentioned in Section 6.1, in relation to the previous work at 193.3 nm, non-statistical spin-orbit population indicate that the dynamics of formation of $S(^3P_J)$ are not well-described in the statistical or diabatic limit, and an adiabatic description of the dissociation process may be more appropriate. The implications from these measurements are discussed further in Section 6.3.3 in relation to the polarisation of triplet S-atoms.

6.3.2 Speed distributions and β parameters

The speed distributions for the three $S(^3P_J)$ spin-orbit species returned from the fits to the experimental data are shown in Figure 6.12 for the three photolysis wavelengths. Compared to the singlet channel, much more energy is available to the photofragments upon dissociation. The CS diatomic co-fragment can, for example, be vibrationally excited up to $v_{\max} = 9$, compared to only $v_{\max} = 1$ for $CS(X^1\Sigma^+) + S(^1D_2)$. The distributions show some unresolved structure indicating appreciable population in the $CS(X^1\Sigma^+)$ $v = 0 - 9$ vibrational levels.

The speed distributions obtained for the three transitions studied are qualitatively similar, however, small differences are observed between the distributions obtained following Π and Σ band excitation. For the Π transition the distributions for each of the three spin-orbit levels appear quite similar. For both the Σ transitions, however, the distributions of the $J = 1$ and 0 levels are very similar, while that for $J = 2$ has more intensity for slow ($v_P < 1000\,\mathrm{m\,s^{-1}}$) photofragments. The distributions obtained following Σ band excitation are qualitatively similar to those obtained following dissociation above the barrier to linearity, at 193.3 nm [196], which are also shown in Figure 6.12. In the sudden or diabatic limit, the three $S(^3P_J)$ speed distributions would be expected to be the same, and, therefore, the differences in $P(v_P)$ for different J indicates some degree of adiabaticity in the dissociation process.

As discussed in Chapter 5 regarding measurements made on the $S(^1D_2)$ product channel, several factors may be important in understanding the values of the spatial anisotropy parameters measured here. These factors include the precise details of the excitation process, the lifetime of the excited state and non-axial recoil effects. The speed dependence of the spatial anisotropy parameters, $\beta(v_P)$, are presented in Figure 6.12 alongside the speed distributions, $P(v_P)$. For 193.3 nm excitation, see Section 5.3.2, it was suggested that an interpretation of β solely in terms of the lifetime of the $^1\Sigma_u^+(^1B_2)$ state seemed inappropriate in this case. Furthermore, effects of non-axial recoil should be less important here than in the $S(^1D_2)$ channel due to the differences in energy available to the fragments in the two channels.

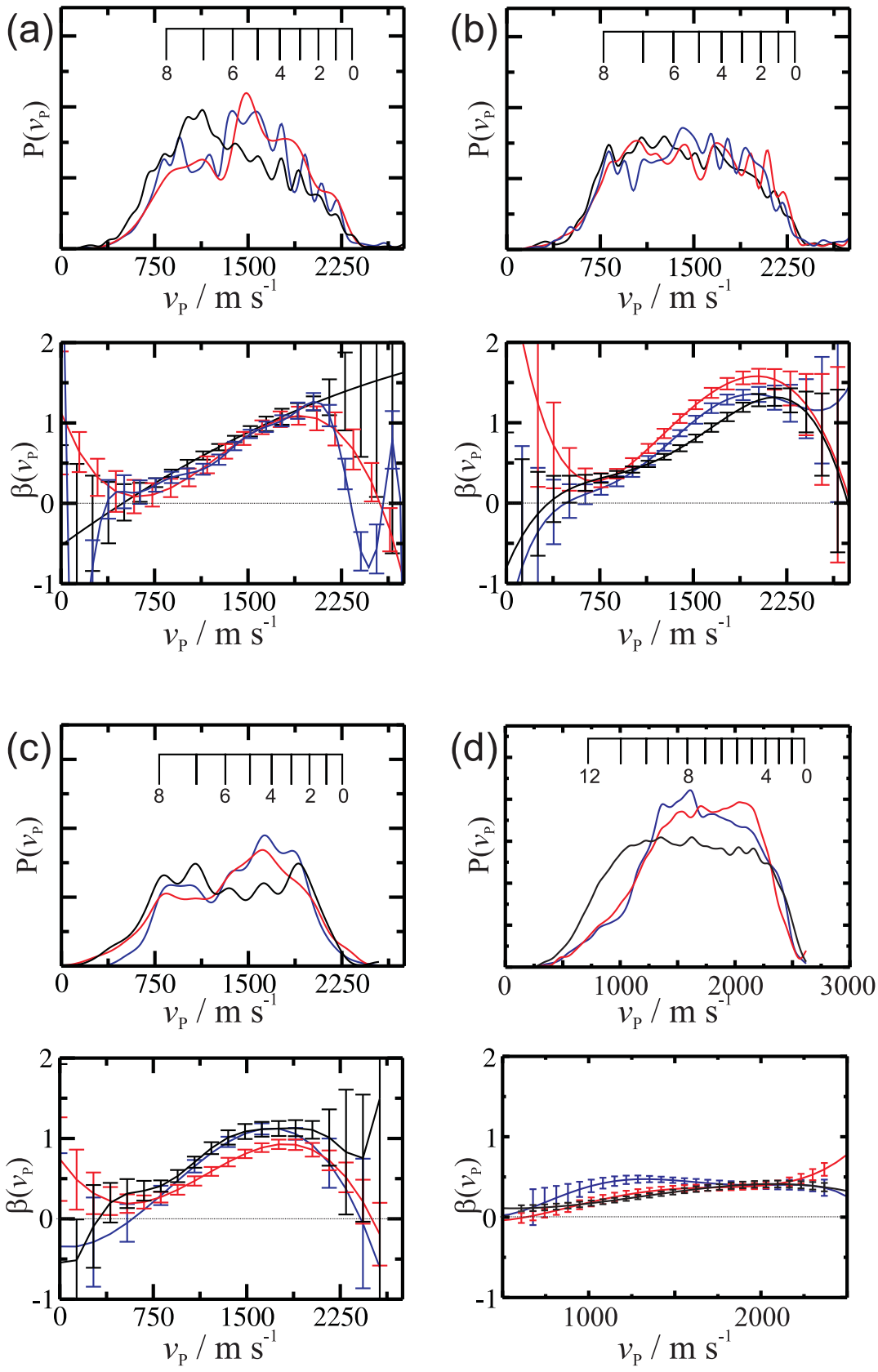

Figure 6.12: Speed distributions (top) and speed dependence of the spatial anisotropy parameter (bottom) for the three spin-orbit levels returned from the fits to the Fourier moments, $S(^3P_2)$ (black), $S(^3P_1)$ (red) and $S(^3P_0)$ (blue). Data shown in **(a)**, **(b)** and **(c)** corresponds to excitation of the Σ_0^h, Π_1^h and Σ_0^f bands, while **(d)** shows results reported at 193.3 nm [196].

For the three photolysis wavelengths studied the magnitude of the $\beta(v_P)$ parameter is similar for each of the spin-orbit levels, and similar to that observed for the singlet channel dissociation. As found following dissociation above the barrier at 193.3 nm [196], this provides an indication that the singlet and triplet products arise following excitation to a common electronically excited state, and may subsequently follow similar dissociation dynamics. The $\beta(v_P)$ parameters are somewhat larger than that observed for the triplet channel dissociation at 193.3 nm, and all show the trend of decreasing magnitude with increasing vibrational excitation of the diatomic co-fragment.

6.3.3 Angular momentum polarisation

Given the similarities in $\beta(v_P)$ for the singlet and triplet channels, it seems likely that the two products share a common excitation pathway. One might anticipate near-zero angular momentum polarisation effects for the triplet channel, as observed for the $S(^1D_2)$ products (see Chapter 5), and indeed this is found to be the case for all fragments following excitation of the Π_1^h transition. It is surprising, therefore, that significant polarisation effects have been observed for the $S(^3P_1)$ spin-orbit species for both of the Σ bands studied here. Furthermore, the $S(^3P_2)$ species for these bands, like the $S(^1D_2)$ fragments, are found to be completely unpolarised. The results following excitation of the Σ bands are very similar to those obtained following dissociation at 193.3 nm.

The speed dependence of the rank $K = 2$ alignment parameters for the $S(^3P_1)$ spin-orbit levels are shown in Figures 6.13 and 6.14 following Σ_0^h and Σ_0^f band excitation, respectively. A complete list of the speed averaged laboratory frame polarisation parameters for the $S(^3P_1)$ products for both transitions is also provided in Table 6.2. The polarisation measurements made here are also compared to those following 193.3 nm photolysis [196] and the dissociation of OCS at 248 nm [194], as detailed in Table 6.2. Similar to the $S(^3P_1)$ fragments generated in the dissociation of OCS, following excitation of the Σ_0^f band large contributions to the polarisation

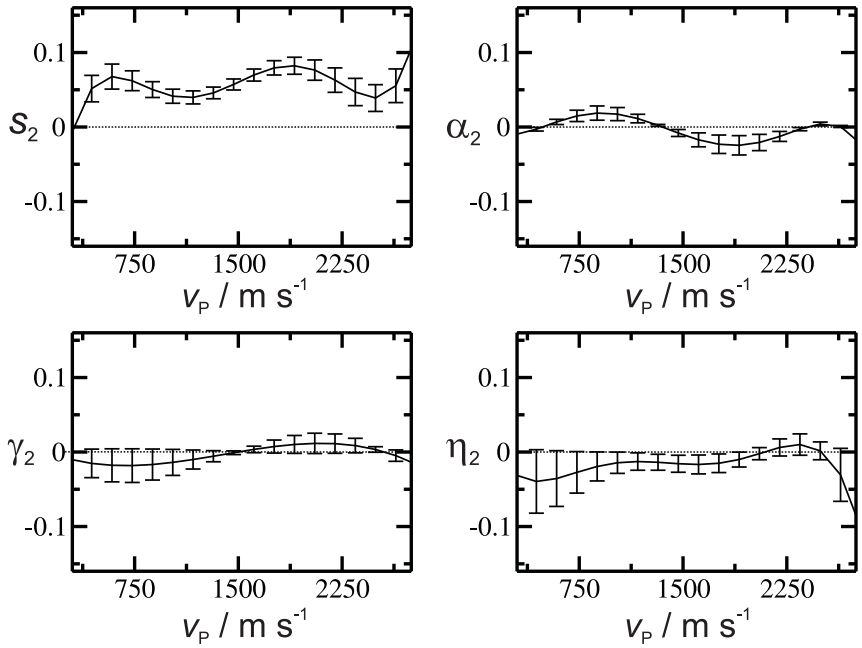

Figure 6.13: Speed dependence of the $K = 2$ alignment parameters returned from the fits to the Fourier moments. Data shown for excitation of the Σ_0^h band.

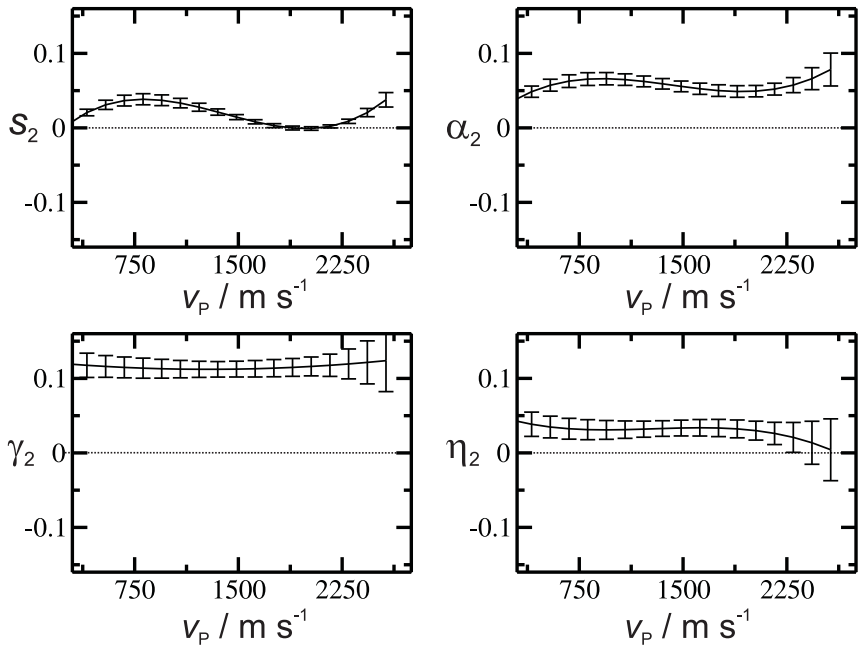

Figure 6.14: Speed dependence of the $K = 2$ alignment parameters returned from the fits to the Fourier moments. Data shown for excitation of the Σ_0^f band.

are found from the coherent alignment parameters γ_2 and η_2. For Σ_0^f excitation the two data sets are in very close agreement, while for Σ_0^h and Π_1^h excitation they are less so (see further below). As described by Vasyutinskii and co-workers, a pure parallel transition in a diatomic or linear triatomic molecule should result in s_2 and α_2 parameters of equal magnitude but opposite sign [63, 66, 84]. In addition, for slow predissociation (in the high J limit), the parameter α_2 should be reduced by a factor of 4 from its limiting axial recoil value [84, 198]. Furthermore, in the slow predissociation limit all the rank $K = 2$ parameters, excluding s_2, are known to be reduced from their axial recoil limiting values [84, 197]. However, for the $S(^3P_1)$ products following Σ_0^f excitation, α_2 is found to be much larger than s_2, and both γ_2 and η_2 are large. These observations lend support to the view that the reduction of β and the polarisation parameters from their limiting values is not primarily due to the long lifetime of the electronically excited CS_2 parent molecule.

The diagonal elements of the density matrix may be used to determine the molecular frame M_J populations, for which $\mathbf{z}||v$. For $S(^3P_1)$ the populations are determined by the values of the parameters s_2 and α_2. Plots of scattering angle averaged molecular frame M_J populations provided in Figure 6.15 indicate an alignment of $J \perp v$, *i.e.* a preferential population of the $M_J = \pm 1$ sub-levels in the molecular frame for $S(^3P_1)$. The absence of polarisation of the $J = 2$ products implies that the M_J populations for these products are almost equal. The M_J populations for both $J = 1$ and $J = 2$ photofragments determined here for both Σ transitions are very similar to those found for OCS at 248 nm, and to the results following dissociation of CS_2 at 193.3 nm. For $J = 2$, differences which do exist between the polarisation parameters for the two systems concern primarily the coherent terms γ_2 and η_2, which do not contribute to the M_J populations. The similarities in the polarisation data for OCS and CS_2 as outlined above may indicate an exit channel effect is ultimately responsible for the electronic polarisation in both cases.

A complete theoretical treatment of electronic polarisation effects following triatomic dissociation is not available at present. However, approximate 'fast' or di-

Parameter	Σ_0^h	Σ_0^f	193.3 nm[196]	OCS 248 nm[194]
β	0.70(4)	0.66(2)	0.36(2)	0.32(1)
s_2	0.061(6)	0.017(3)	0.019(4)	0.018(1)
α_2	-0.005(3)	0.056(6)	0.033(7)	0.038(4)
γ_2	-0.002(3)	0.11(10)	0.079(17)	0.081(6)
η_2	-0.014(11)	0.032(5)	0.046(12)	0.031(4)
α_1	0.015(17)	-	-0.005(9)	-0.001(1)
γ_1	-0.016(17)	-	0.005(7)	0.000(1)
γ_1'	-0.039(21)	-	0.018(26)	-0.001(1)

Table 6.2: Speed averaged polarisation parameters returned from fit to the $S(^3P_1)$ experimental data following Σ_0^h and Σ_0^f excitation. Also shown are the polarisation parameters for the $S(^3P_1)$ products following dissociation at 193.3 nm [196] and from the dissociation of OCS at 248 nm [194]. Errors (1σ) are given in parenthesis and refer to the errors in the final digits reported.

abatic models have proved useful for describing the origin of polarisation effects in the triatomic molecules N_2O and SO_2. Some of these models have been the subject of recent review [86], where a detailed discussion may be found. In the diabatic, fast recoil limit, assuming the electron spin is unpolarised, the alignment of the $S(^3P_2)$ species should be approximately equal in magnitude but opposite sign to that of the $S(^3P_1)$ species [59, 125]. Statistical spin-orbit populations should also be observed [125], clearly in disagreement with the experimental findings. It would appear from these polarisation measurements that dissociation of CS_2 to generate triplet S-atoms is closer to the adiabatic limit. An adiabatic model, similar to that used to interpret the triplet S-atom polarisation effects in OCS dissociation [194] is discussed below.

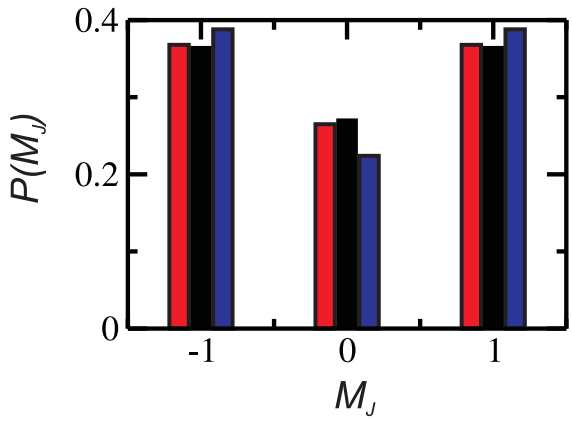

Figure 6.15: Populations of the magnetic sublevels, $P(M_J)$, in the molecular frame for the $S(^3P_1)$ species. Data shown following excitation of the Σ_0^h band (red), at 193.3 nm (black) [196] and the Σ_0^f band (blue).

Adiabatic model

An adiabatic correlation diagram is shown in Figure 6.16, which connects the molecular states of the linear CS_2 molecule with atomic states in the long range region by conservation of the projection quantum number, Ω. A similar diagram has been constructed for the triplet channel arising from the photodissociation of OCS [194]. The correlation diagram connects molecular states of triplet spin multiplicity and therefore applies only to the part of the dissociation process taking place after the spin-orbit interaction has coupled the singlet photo-excited state to the repulsive state. At linearity two triplet states converge on the $CS(X^1\Sigma^+)$ + $S(^3P_J)$ asymptote, the $^3\Sigma_g^-$ and the $^3\Pi_g$ states. The $^3\Sigma_g^-$ state lies higher in energy at short range, and is assumed to lie higher in energy in the long range for linear SCS based on the signs of the quadrupole-quadrupole and dipole-quadrupole interactions [196]. Assuming that axial recoil takes place, the value of the quantum number Ω transforms into the value of M_J.

The correlation diagram allows prediction of the spin-orbit and M_J populations assuming the dissociation takes place adiabatically on a single surface. From inspection of Figure 6.16, it can be seen that for dissociation at linearity on the $^3\Pi_g$ surface the adiabatic correlation diagram predicts an isotropic angular momentum

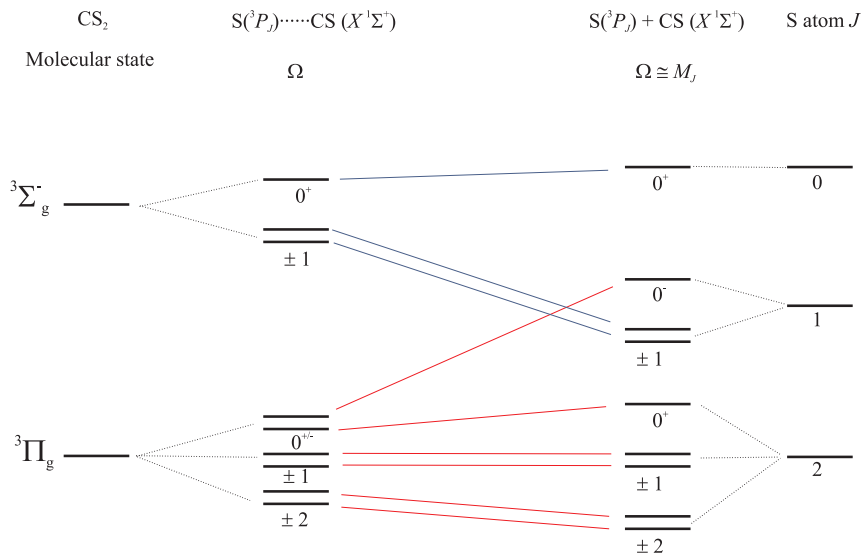

Figure 6.16: Adiabatic correlation diagram (at linearity) connecting the molecular and atomic states characterized by the total angular momentum projection quantum number Ω. Adapted from Ref [194].

distribution for the $J = 2$ spin-orbit species, in agreement with the experimental observations. Recall that it was the $^3\Pi_g$ surface that Bisgaard *et al.* suggest is responsible for triplet S-atom production based on their *ab initio* calculations [173], see Figure 5.4. However, the model also predicts that dissociation on the $^3\Pi_g$ state at linearity should lead to population only in the $M_J = 0$ magnetic sub-level of the $J = 1$ species, in contrast to the preferential population of $M_J = \pm 1$ levels found in the present study. Furthermore, the spin-orbit populations predicted from the model, $P(J = 2) : P(J = 1) : P(J = 0) = 5 : 1 : 0$, disagree with the experimental findings for all transitions studied. An adiabatic correlation diagram is also presented for bent (C_s) configurations of the CS_2 molecule in Figure 6.17. The correlation diagram for dissociation on the $^3A'$ and $^3A''$ components derived from the $^3\Pi_g$ state at bent configurations, however, predicts the same results for the polarisation of the $J = 2$ and $J = 1$ species, as well as the spin orbit populations.

It is possible that the preferential population of the $M_J = \pm 1$ component of the $J = 1$ spin-orbit state could occur because of a crossing between states arising from the $^3\Pi_g$ and $^3\Sigma_g^-$ states at some point along the dissociation co-ordinate. Although

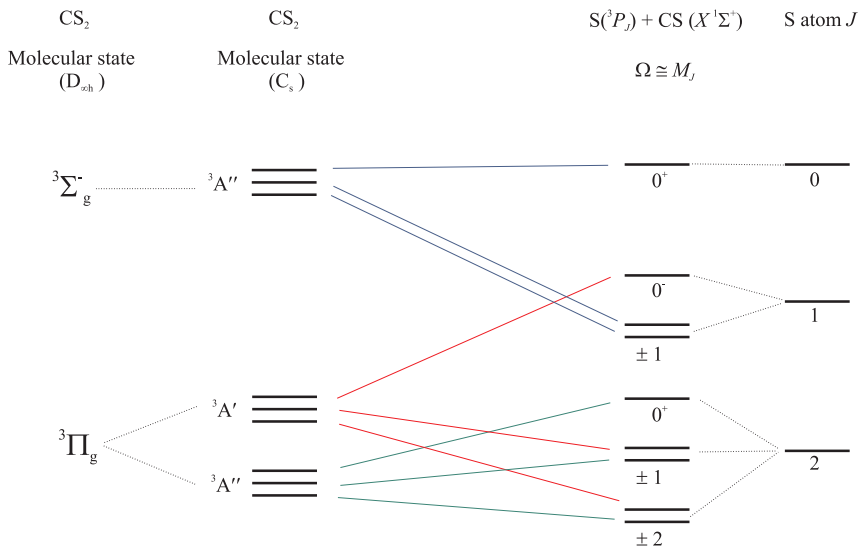

Figure 6.17: Adiabatic correlation diagram (bent) connecting the molecular and atomic states. Adapted from Ref [194].

the latest *ab initio* calculations of Bisgaard *et al.* [173] point to intersystem crossing between the photoexcited $^1\Sigma_u^+$ and the $^3\Pi_g$ states as the origin of the triplet products, both the details of this crossing and the subsequent dissociation pathway are yet to be worked out. It should also be born in mind that the population and polarisation of the spin-orbit states of $S(^3P_J)$ might be better described by an intermediate picture of the dynamics, rather than by the limiting diabatic or adiabatic pictures described above. Whatever the explanation for the polarisation of the $J = 1$ products in CS_2, it seems highly likely that a similar mechanism is also at play in the triplet channel of the photodissociation of OCS.

6.4 Summary

Results have been presented for dissociation into the spin-forbidden triplet channel following excitation below the barrier to linearity in the $^1\Sigma_u^+(^1B_2)$ state. In this region the population of the $S(^3P_J)$ fine-structure levels has been shown to vary with the vibronic band excited. In particular, following Σ band excitation the majority of triplet S-atoms are $S(^3P_2)$, whereas for Π band excitation the population

in $J = 2$ and $J = 1$ are similar. Furthermore, the speed distributions, $P(v_P)$, of the $S(^3P_J)$ species are also different following excitation of the Σ and Π bands. For Σ band excitation the distributions for the $J = 1$ and 0 levels are very similar, and significantly different to that observed for $J = 2$. The differences in $P(v_P)$ with J and the highly non-statistical spin-orbit populations indicate some degree of adiabaticity in the dissociation process. Unlike the speed distributions of the $S(^1D_2)$ products, see Chapter 5, the $S(^3P_J)$ distributions, while dependent on the vibronic band excited, do not appear to significantly change following excitation above and below the barrier to linearity in the $^1\Sigma_u^+(^1B_2)$ state.

Interesting polarisation effects of the triplet S-atoms have also been observed. For Σ band excitation, the $S(^3P_2)$ fragments are found to be unpolarised and the $S(^3P_1)$ species show a preference for the $M_J = \pm 1$ sub-levels. These observations are very similar to the results following dissociation at 193.3 nm, above the barrier to linearity in the $^1\Sigma_u^+(^1B_2)$ state. Furthermore, the spin-orbit populations and speed distributions are also very close to the results at 193.3 nm. Following excitation of the Π band, all $S(^3P_J)$ fragments are found to be unpolarised. The differences in spin-orbit population, speed distributions and polarisation data perhaps indicates that a somewhat different dissociation mechanism results following Π band excitation. Attempts have been made to interpret the polarisation data in terms of adiabatic dissociation on the two surfaces correlating asymptotically with $CS(X^1\Sigma^+) + S(^3P_J)$. While successfully predicting an isotropic angular momentum distribution for $J = 2$, it is more difficult to account for the spin-orbit populations and $S(^3P_1)$ polarisation based on this simple model. Little information is available on the surfaces giving rise to the triplet channel but since the non-zero incoherent alignment measured here is very similar to that observed following the dissociation of OCS at 248 nm, it seems likely that a similar mechanism, at least in the asymptotic region, may be responsible for the polarisation in the two systems.

Bibliography

[1] F. London, *Z. Elektrochem.*, **35**, 552 (1929).

[2] H. Eyring and M. Polanyi, *Z. Physik. Chemie. B.*, **12**, 279 (1931).

[3] M. G. Evans and M. Polanyi, *Trans. Faraday Soc.*, **35**, 178 (1939).

[4] R. D. Levine and R. B. Bernstein, *Molecular Reaction Dynamics and Chemical Reactivity*, Oxford University Press, 1987.

[5] R. Schinke, *Photodissociation Dynamics*, Cambridge University Press, 1993.

[6] M. Brouard, *Reaction Dynamics*, Oxford University Press, 1998.

[7] M. Brouard and C. Vallance, Eds., *Tutorials in Molecular Reaction Dynamics*, Royal Society of Chemistry, 2010.

[8] M. Born and R. Oppenheimer, *Zur Quantentheorie der Molekeln*, **84**, 457 (1927).

[9] B. Retail and A. J. Orr-Ewing, In *Tutorials in Molecular Reaction Dynamics*, M. Brouard and C. Vallance, Eds., 2010, chapter 4, pages 88–115.

[10] G. Herzberg, *Molecular Spectra and Molecular Structure I. Spectra of Diatomic Molecules*, D. Van Nostrand Company, Ltd., 2nd ed., 1950.

[11] F. F. Crim, *J. Phys. Chem.*, **100**, 12725 (1996).

[12] R. L. Vander Wal, J. L. Scott, F. F. Crim, K. Weide, and R. Schinke, *J. Chem. Phys.*, **94**, 3548 (1991).

[13] R. J. Van Brunt and R. N. Zare, *J. Chem. Phys.*, **48**, 4304 (1968).

[14] M. J. Sabety-Dvonik and R. J. Cody, *J. Chem. Phys.*, **66**, 125 (1977).

[15] R. J. Cody, M. J. Sabety-Dvonik, and W. M. Jackson, *J. Chem. Phys.*, **66**, 2145 (1977).

[16] H. Zacharias, M. Geilhaupt, K. Meier, and K. H. Welge, *J. Chem. Phys.*, **74**, 218 (1981).

[17] T. G. Slanger, W. K. Bischel, and M. J. Dyer, *J. Chem. Phys.*, **79**, 2231 (1983).

[18] C. B. McKendrick, C. Fotakis, and R. J. Donovan, *J. Photochem.*, **20**, 175 (1982).

[19] P. T. Knepp, A. C. Terentis, and S. H. Kable, *J. Chem. Phys.*, **103**, 194 (1995).

[20] N. Changlong, L. Hua, and J. Pfab, *J. Phys. Chem.*, **97**, 7458 (1993).

[21] R. P. Baker, M. L. Costen, G. Hancock, G. A. D. Ritchie, and D. Summerfield, *Phys. Chem. Chem. Phys.*, **2**, 661 (2000).

[22] J. A. Harrison, X. Yang, M. Roesslein, and J. R. Huber, *J. Phys. Chem.*, **98**, 12260 (1994).

[23] G. Dornhoefer, W. Hack, and W. Langel, *J. Phys. Chem.*, **88**, 3060 (1984).

[24] P. Andresen, G. S. Ondrey, B. Titze, and E. W. Rothe, *J. Chem. Phys.*, **80**, 2548 (1984).

[25] P. Andresen, G. S. Ondrey, and B. Titze, *Phys. Rev. Lett.*, **50**, 486 (1983).

[26] R. Schinke, V. Engle, P. Andresen, D. Häusler, and G. G. Balint-Kurti, *Phys. Rev. Lett.*, **55**, 1180 (1985).

[27] D. Häusler, P. Andresen, and R. Schinke, *J. Chem. Phys.*, **87**, 3949 (1987).

[28] R. L. Vander Wal, J. L. Scott, and F. F. Crim, *J. Chem. Phys.*, **94**, 1859 (1991).

[29] M. Brouard, S. R. Langford, and D. E. Manolopoulos, *J. Chem. Phys.*, **101**, 7458 (1994).

[30] D. F. Plusquellic, O. Votava, and D. J. Nesbitt, *J. Chem. Phys.*, **109**, 6631 (1998).

[31] A. J. Alexander, *J. Chem. Phys.*, **118**, 6234 (2003).

[32] Y.-P. Chang, M. Brouard, R. Cireasa, T. Perkins, and S. A. Seamons, *Phys. Chem. Chem. Phys.*, **13**, 8213 (2011).

[33] R. N. Dixon, *J. Chem. Phys.*, **85**, 1866 (1986).

[34] G. E. Busch, R. T. Mahoney, R. I. Morse, and K. R. Wilson, *J. Chem. Phys.*, **51**, 449 (1969).

[35] G. E. Busch, J. F. Cornelius, R. T. Mahoney, R. I. Morse, D. W. Schlosser, and K. R. Wilson, *Rev. Sci. Instum.*, **41**, 1066 (1970).

[36] G. E. Busch, R. T. Mahoney, R. I. Morse, and K. R. Wilson, *J. Chem. Phys.*, **51**, 837 (1969).

[37] G. E. Busch and K. R. Wilson, *J. Chem. Phys.*, **56**, 3638 (1972).

[38] G. E. Busch and K. R. Wilson, *J. Chem. Phys.*, **56**, 3626 (1972).

[39] G. E. Busch and K. R. Wilson, *J. Chem. Phys.*, **56**, 3655 (1972).

[40] M. N. R. Ashfold and J. D. Howe, *Annu. Rev. Phys. Chem.*, **45**, 57 (1994).

[41] D. W. Chandler and P. L. Houston, *J. Chem. Phys.*, **87**, 1445 (1987).

[42] A. J. R. Heck and D. W. Chandler, *Annu. Rev. Phys. Chem.*, **46**, 335 (1995).

[43] N. H. Abel, *J. Reine. Angew. Math.*, **1**, 153 (1826).

[44] W. C. Wiley and I. H. McLaren, *Rev. Sci. Instum.*, **26**, 1150 (1955).

[45] A. T. J. B. Eppink and D. H. Parker, *Rev. Sci. Instr.*, **68**, 3477 (1997).

[46] B.-Y. Chang, R. C. Hoetzlein, J. A. Mueller, J. D. Geiser, and P. L. Houston, *Rev. Sci. Instr.*, **69**, 1665 (1998).

[47] F. Quadrini, *Atomic Angular Momentum Polarisation in Molecular Photodissociation* DPhil thesis, Oxford University, (2007).

[48] M. N. R. Ashfold, N. H. Nahler, A. J. Orr-Ewing, O. P. J. Vieuxmaire, R. L. Toomes, T. N. Kitsopoulos, I. A. Garcia, D. A. Chestakov, S.-M. Wu, and D. H. Parker, *Phys. Chem. Chem. Phys.*, **8**, 26 (2006).

[49] R. D. Levine and R. B. Bernstein, *Molecular Reaction Dynamics and Chemical Reactivity*, Cambridge University Press, 2005.

[50] A. Johnsen, *Ion Imaging: Applications and Extensions* DPhil thesis, Oxford University, (2010).

[51] D. B. Kokh, A. B. Alekseyev, and R. J. Buenker, *J. Chem. Phys.*, **120**, 11549 (2004).

[52] R. N. Zare, *Angular Momentum, Understanding Spatial Aspects in Chemistry and Physics*, John Wiley & Sons, New York, 1988.

[53] G. G. Balint-Kurti and M. Shapiro., *Chem. Phys.*, **61**, 137 (1981).

[54] G. G. Balint-Kurti and M. Shapiro, *Advances in Chem. Phys.*, **60**, 403 (1985).

[55] E. Merzbacher, *Quantum Mechanics*, Vol. 1 & 2, John Wiley & Sons, New York, 1970.

[56] C. Cohen-Tannoudji, B. Diu, and F. Laloe, *Quantum Mechanics*, Wiley, New York, 1977.

[57] R. Loudon, *The Quantum Theory of Light*, Oxford University Press, 1983.

[58] M. J. Bass, M. Brouard, A. P. Clark, and C. Vallance, *J. Chem. Phys.*, **117**, 8723 (2002).

[59] M. Brouard, R. Cireasa, A. P. Clark, T. J. Preston, C. Vallance, G. C. Groenenboom, and O. S. Vasyutinskii, *J. Phys. Chem. A.*, **108**, 7965 (2004).

[60] M. Brouard, A. P. Clark, C. Vallance, and O. S. Vasyutinskii, *J. Chem. Phys.*, **119**, 771 (2003).

[61] M. J. Bass, M. Brouard, A. P. Clark, C. Vallance, and B. Martínez-Haya, *Phys. Chem. Chem. Phys.*, **5**, 856 (2003).

[62] A. S. Bracker, E. R. Wouters, A. G. Suits, Y. T. Lee, and O. S. Vasyutinskii, *Phys. Rev. Lett.*, **80**, 1626 (1998).

[63] A. S. Bracker, E. R. Wouters, A. G. Suits, and O. S. Vasyutinskii, *J. Chem. Phys.*, **110**, 6749 (1999).

[64] M. Ahmed, D. S. Peterka, A. S. Bracker, O. S. Vasyutinskii, and A. G. Suits, *J. Chem. Phys.*, **110**, 4115 (1999).

[65] A. G. Smolin, O. S. Vasyutinskii, O. P. J. Vieuxmaire, M. N. R. Ashfold, G. G. Balint-Kurti, and A. J. Orr-Ewing, *J. Chem. Phys.*, **124**, 094305 (2006).

[66] E. R. Wouters, M. Ahmed, D. S. Peterka, A. S. Bracker, A. G. Suits, and O. S. Vasyutinskii, In *Imaging in Chemical Dynamics*, A. G. Suits and R. E. Continetti, Eds., 2000, chapter 15, pages 238–284.

[67] Yu. Ralchenko, A. E. Kramida, J. Reader, and NIST ASD Team (2010), Nist atomic spectra database (version 4.0) `http://physics.nist.gov/asd`, 2011.

[68] H. S. W. Massey, *Rep. Prog. Phys.*, **12**, 248 (1949).

[69] Y.-L. Huang and R. J. Gordon, *J. Chem. Phys.*, **94**, 2640 (1991).

[70] M. C. G. N. van Vroonhoven and G. C. Groenenboom, *J. Chem. Phys.*, **116**, 1954 (2002).

[71] M. C. G. N. van Vroonhoven and G. C. Groenenboom, *J. Chem. Phys.*, **116**, 1965 (2002).

[72] B. Buijsse, W. J. van der Zande, A. T. J. B. Eppink, D. H. Parker, B. R. Lewis, and S. T. Gibson, *J. Chem. Phys.*, **108**, 7229 (1998).

[73] S. Chen, W. Zhou, and J. Zhang, *Chem. Phys. Lett.*, **418**, 328 (2006).

[74] W. Zhou, Y. Yuan, S. Chen, and J. Zhang, *J. Chem. Phys.*, **123**, 054330 (2005).

[75] C.-W. Hsu, C.-L. Liao, Z.-X. Ma, P. J. H. Tjossem, and C. Y. Ng, *Chem. Phys. Lett.*, **199**, 78 (1992).

[76] Y.-L. Huang and R. J. Gordon, *J. Chem. Phys.*, **93**, 868 (1990).

[77] A. P. Clark, *Velocity Mapping of Elementary Photodissociation Reactions* DPhil thesis, Oxford University, (2006).

[78] T. P. Rakitzis, S. A. Kandel, A. J. Alexander, Z. H. Kim, and R. N. Zare, *J. Chem. Phys.*, **110**, 3351 (1999).

[79] T. P. Rakitzis and T. N. Kitsopoulos, *J. Chem. Phys.*, **116**, 9228 (2002).

[80] P. L. Houston, *J. Phys. Chem.*, **91**, 5388 (1987).

[81] G. E. Hall and P. L. Houston, *Ann. Rev. Phys. Chem.*, **40**, 375 (1989).

[82] J. P. Simons, *J. Phys. Chem.*, **88**, 1287 (1984).

[83] J. A. Beswick, In *Computational Chemistry: structure, interactions and reactivity*, S. Fraga, Ed., 1992, chapter 3, pages 400–402.

[84] A. G. Suits and O. S. Vasyutinskii, *Chem. Rev.*, **108**, 3706 (2008).

[85] A. P. Clark, M. Brouard, F. Quadrini, and C. Vallance, *Phys. Chem. Chem. Phys.*, **8**, 5591 (2006).

[86] M. Brouard, R. Cireasa, A. P. Clark, F. Quadrini, and C. Vallance, In *Gas Phase Molecular Reaction and Photodissociation Dynamics*, K. C. Lin and P. D. Kleiber, Eds., Transworld Research Network, 2007, chapter 7, pages 269–331.

[87] R. N. Zare, *Molecular Fluorescence and Photodissociation* PhD thesis, Harvard University, (1964).

[88] C. Jonah, *J. Chem. Phys.*, **55**, 1915 (1971).

[89] S. Yang and R. Bersohn, *J. Chem. Phys.*, **61**, 4400 (1974).

[90] T. Nagata, T. Kondow, K. Kuchitsu, G. W. Loge, and R. N. Zare, *Mol. Phys.*, **50**, 49 (1983).

[91] A. V. Demyanenko, V. Dribinski, H. Reisler, H. Meyer, and C. X. W. Qian, *J. Chem. Phys.*, **111**, 7383 (1999).

[92] L. D. A. Siebbeles, M. Glass-Maujean, O. S. Vasyutinskii, J. A. Beswick, and O. Roncero, *J. Chem. Phys.*, **100**, 3610 (1994).

[93] O. S. Vasyutinskii, *Opt. Spectrosk.*, **54**, 524 (1983).

[94] K. Blum, *Density Matrix Theory and Applications*, Plenum Press, New York, 2nd ed., 1996.

[95] G. G. Balint-Kurti, A. J. Orr-Ewing, J. A. Beswick, A. Brown, and O. S. Vasyutinskii, *J. Chem. Phys.*, **116**, 10760 (2002).

[96] G. G. Balint-Kurti, A. Brown, and O. S. Vasyutinskii, *Physica Scripta.*, **73**, C76 (2006).

[97] Y. B. Band, K. F. Freed, and S. J. Singer, *J. Chem. Phys.*, **84**, 3762 (1986).

[98] G. Parlant and D. R. Yarkony, *J. Chem. Phys.*, **110**, 363 (1999).

[99] A. G. Smolin, O. S. Vasyutinskii, G.G. Balint-Kurti, and A. Brown, *J. Phys. Chem. A*, **110**, 5371 (2006).

[100] G. G. Balint-Kurti, R. N. Dixon, and C. C. Marston, *J. Chem. Soc. Faraday Trans.*, **86**, 1741 (1990).

[101] A. Brown, G. G. Balint-Kurti, and O. S. Vasyutinskii, *J. Phys. Chem. A*, **108**, 7790 (2004).

[102] A. G. Smolin, O. S. Vasyutinskii, G. G. Balint-Kurti, and A. Brown, *J. Phys. Chem. A*, **110**, 5371 (2006).

[103] B. V. Picheyev, A. G. Smolin, and O. S. Vasyutinskii, *J. Phys. Chem. A*, **101**, 7614 (1997).

[104] A. G. Smolin, O. S. Vasyutinskii, E. R. Wouters, and A. G. Suits, *J. Chem. Phys.*, **121**, 6759 (2004).

[105] O. S. Vasyutinskii, *Sov. Phys. JETP.*, **54**, 855 (1981).

[106] M. Brouard, R. Cireasa, A. P. Clark, G. C. Groenenboom, G. Hancock, S. J. Horrocks, F. Quadrini, G. A. D. Ritchie, and C. Vallance, *J. Chem. Phys.*, **125**, 133308 (2006).

[107] A. S. Bracker, E. R. Wouters, A. G. Suits, and O. S. Vasyutinskii, *J. Chem. Phys.*, **110**, 6749 (1999).

[108] T. P. Rakitzis and R. N. Zare, *J. Chem. Phys.*, **110**, 3341 (1999).

[109] T. P. Rakitzis, G. E. Hall, M. L. Costen, and R. N. Zare, *J. Chem. Phys.*, **111**, 8751 (1999).

[110] J. A. Beswick and O. S. Vasyutinskii, *Comments At. Mol. Phys.*, **34**, 69 (1998).

[111] D. V. Kupriyanov and O. S. Vasyutinskii, *Chem. Phys.*, **171**, 25 (1993).

[112] D. V. Kupriyanov, B. N. Sevastianov, and O. S. Vasyutinskii, *Z. Phys. D.*, **15**, 105 (1990).

[113] A. J. Alexander, *Phys. Chem. Chem. Phys.*, **7**, 3693 (2005).

[114] P. M. Regan, D. Ascenzi, A. Brown, G. G. Balint-Kurti, and A. J. Orr-Ewing, *J. Chem. Phys.*, **112**, 10259 (2000).

[115] A. Brown and G. G. Balint-Kurti, *J. Chem. Phys.*, **113**, 1870 (2000).

[116] C. C. Marston and G. G. Balint-Kurti, *J. Chem. Phys.*, **91**, 3571 (1989).

[117] D. Kosloff and R. Kosloff, *J. Comput. Phys.*, **52**, 35 (1983).

[118] A. Vibok and G. G. Balint-Kurti, *J. Phys. Chem.*, **96**, 8712 (1992).

[119] G. G. Balint-Kurti, R. N. Dixon, and C. C. Marston, *Int. Rev. Phys. Chem.*, **11**, 317 (1992).

[120] R. Kosloff, *J. Phys. Chem.*, **92**, 2087 (1998).

[121] E. J. Heller, *J. Chem. Phys.*, **68**, 2066 (1978).

[122] E. J. Heller, *J. Chem. Phys.*, **68**, 3891 (1978).

[123] E. J. Heller, *Acc. Chem. Res.*, **14**, 368 (1981).

[124] J. M. Teule, G. C. Groenenboom, D. W. Neyer, D. W. Chandler, and M. H. M. Janssen, *Chem. Phys. Lett.*, **320**, 177 (2000).

[125] M. Brouard, A. P. Clark, C. Vallance, and O. S. Vasyutinskii, *J. Chem. Phys.*, **119**, 771 (2003).

[126] M. Brouard, R. Cireasa, A. P. Clark, T. J. Preston, and C. Vallance, *J. Chem. Phys.*, **124**, 064309 (2006).

[127] A. M. Coroiu, D. H. Parker, G. C. Groenenboom, J. Barr, I. T. Novalbos, and B. J. Whitaker, *Eur. Phys. J. D.*, **38**, 151 (2006).

[128] A. J. H. M. Meijer, G. C. Groenenboom, and A. van der Avoird, *J. Chem. Phys.*, **101**, 7603 (1994).

[129] B.-Y. Chang, R. C. Hoetzlein, J. A. Mueller, J. D. Geiser, and P. L Houston, *Rev. Sci. Instr*, **69**, 1665 (1998).

[130] J. Luque, Lifbase (ver. 2.0) `http://www.sri.com/psd/lifbase/`, 2011.

[131] A. C. Kummel, G. O. Sitz, and R. N. Zare, *J. Chem. Phys.*, **85**, 6874 (1986).

[132] A. C. Kummel, G. O. Sitz, and R. N. Zare, *J. Chem. Phys.*, **88**, 6707 (1988).

[133] Y. Mo and T. Suzuki, *J. Chem. Phys.*, **109**, 4691 (1998).

[134] K. Takahashi, O. Yamamoto, and T. Inomata, *Proc. Combust. Inst.*, **29**, 2447 (2002).

[135] W. H. Press, S. A. Teukolski, W. T. Vetterling, and B. P. Flannery, *Numerical Recipies in FORTRAN 77: The Art of Scientific Computing*, Cambridge University Press, 2nd ed., 1992.

[136] Y. Asano and S. Yabushita, *Chem. Phys. Lett.*, **372**, 348 (2003).

[137] IUPAC Subcommittee on Gas Kinetic Data Evaluation `http://www.iupac-kinetic.ch.cam.ac.uk/`, 2011.

[138] R. S. Mulliken, *Phys. Rev.*, **36**, 1440 (1930).

[139] Y. Matsumi, K. Tonokura, and M. Kawasaki, *J. Chem. Phys.*, **97**, 1065 (1992).

[140] L. Li, R. J. Lipert, J. Lobue, W. A. Chupka, and S. D. Colson, *Chem. Phys. Lett.*, **151**, 335 (1988).

[141] A. Bracker, *An Investigation of Polarized Atomic Photofragments using the Ion Imaging Technique* PhD thesis, Berkeley, (1997).

[142] A. J. Alexander, Z. H. Kim, S. A. Kandel, R. N. Zare, T. P. Rakitzis, Y. Asano, and S. Yabushita, *J. Chem. Phys.*, **113**, 9022 (2000).

[143] R. W. Diesen, J. C. Wahr, and S. E. Adler, *J. Chem. Phys.*, **50**, 3635 (1969).

[144] Y. Matsumi, M. Kawasaki, T. Sato, T. Kinugawa, and T. Arikawa, *Chem. Phys. Lett.*, **155**, 486 (1989).

[145] P. C. Samartzis, I. Sakellariou, T. Gougousi, and T. N. Kitsopoulos, *J. Chem. Phys.*, **107**, 43 (1997).

[146] Y. Wang, H.-P. Loock, J. Cao, and C. X. W. Qian, *J. Chem. Phys.*, **102**, 808 (1995).

[147] Y. B. Band, K. F. Freed, and D. J. Kouri, *Chem. Phys. Lett.*, **79**, 233 (1981).

[148] P. C. Samartzis, B. L. G. Bakker, T. P. Rakitzis, D. H. Parker, and T. N. Kitsopoulos, *J. Chem. Phys.*, **110**, 5201 (1999).

[149] Z. H. Kim, A. J. Alexander, S. A. Kandel, T. P. Rakitzis, and R. N. Zare, *Faraday Discuss.*, **113**, 27 (1999).

[150] S. D. Peyerimhoff and R. J. Buenker, *Chem. Phys.*, **57**, 279 (1981).

[151] Y. Asano and S. Yabushita, *J. Phys. Chem. A*, **105**, 9873 (2001).

[152] D. B. Kokh, A. B. Alekseyev, and R. J. Buenker, *J. Chem. Phys.*, **115**, 9298 (2001).

[153] L. G. M. de Macedo and W. A. de Jong, *J. Chem. Phys.*, **128**, 041101 (2008).

[154] T. P. Rakitzis, S. A. Kandel, A. J. Alexander, Z. H. Kim, and R. N. Zare, *Science*, **281**, 1346 (1998).

[155] T. P. Rakitzis and R. N. Zare, *J. Chem. Phys.*, **110**, 3341 (1999).

[156] T. R. Sharples, *REMPI-TOF Studies of Photofragment Polarization* DPhil thesis, Oxford University, (2010).

[157] K. W. Kolasinski, *Surface science. Foundations of Catalysis and Nanoscience*, John Wiley & Sons, 2nd ed., 2008.

[158] R. J. Hemley, D. G. Leopold, J. L. Roebber, and V.Vaida, *J. Chem. Phys.*, **79**, 5219 (1983).

[159] A. E. Douglas and I. Zanon, *Can. J. Phys.*, **42**, 627 (1964).

[160] W. C. Price and D. M. Simpson, *Proc. R. Soc. London. Ser. A*, **165**, 272 (1938).

[161] C. Ramasastry and K. R. Rao, *Indian J. Phys.*, **21**, 313 (1947).

[162] A. D. Walsh, *J. Chem. Soc.*, page 2266 (1953).

[163] S. P. McGlynn, J. W. Rabalais, J. M. McDonald, and V. M. Scherr, *Chem. Rev.*, **71**, 73 (1971).

[164] F. R. Greening and G. W. King, *J. Mol. Spec.*, **59**, 312 (1976).

[165] J. L. Roebber and V. Vaida, *J. Chem. Phys.*, **83**, 2748 (1985).

[166] C. Cossart-Magos, M. Horani, M. Jungen, and F. Launay, *J. Chem. Phys.*, **104**, 7412 (1996).

[167] M. F. Arendt and L. J. Butler, *J. Chem. Phys.*, **109**, 7835 (1998).

[168] H. Xu and J. A. Joens, *Geophys. Res. Lett.*, **20**, 1035 (1993).

[169] G. Herzberg, *Molecular Spectra and Molecular Structure III. Electronic Spectra and Electronic Structure of Polyatomic Molecules*, D. Van Nostrand Company, Ltd., 1976.

[170] C. Starrs, M. N. Jego, A. Mank, and J. W. Hepburn, *J. Phys. Chem.*, **96**, 6526 (1992).

[171] A. Mank, C. Starrs, M. N. Jego, and J. W. Hepburn, *J. Chem. Phys.*, **104**, 3609 (1996).

[172] I. M. Waller and J. W. Hepburn, *J. Chem. Phys.*, **87**, 3261 (1987).

[173] C. Z. Bisgaard, O. J. Clarkin, G. Wu, A. M. D. Lee, O. Geβner, C. C. Hayden, and A. Stolow, *Science*, **323**, 1464 (2009).

[174] D. Townsend, H. Satzger, T. Ejdrup, A. M. D. Lee, H. Stapelfeldt, and A. Stolow, *J. Chem. Phys.*, **125**, 234302 (2006).

[175] H. T. Liou, P. Dan, T. Y. Hsu, H. Yang, and H. M. Lin, *Chem. Phys. Lett.*, **192**, 560 (1992).

[176] H. T. Liou, K. L. Huang, and M. C. Chen, *Chem. Phys. Lett.*, **266**, 591 (1997).

[177] J. Chen. Y. Guo, X. Zhou, Y. Shi, S. Liu, and X. Ma, *J. Phys. Chem. A.*, **111**, 5382 (2007).

[178] Z. Hu, W-B. Lee, X.-P. Zhang, P-Y. Wei, and K-C. Lin, *Chem. Phys. Chem.*, **9**, 422 (2008).

[179] K. Hara and D. Phillips, *J. Chem. Soc. Faraday Trans. 2*, **74**, 1441 (1978).

[180] A. P. Baronavski and J. C. Owrutsky, *Chem. Phys. Lett.*, **221**, 419 (1994).

[181] S. C. Yang, A. Freedman, M. Kawasaki, and R. Bersohn, *J. Chem. Phys.*, **72**, 4058 (1980).

[182] V. R. McCrary, R. Lu, D. Zakheim, J. A. Russell, J. B. Halpern, and W. M. Jackson, *J. Chem. Phys.*, **83**, 3481 (1985).

[183] H. Kanamori and E. Hirota, *J. Chem. Phys.*, **86**, 3901 (1987).

[184] M. C. Addison, R. J. Donovan, and C. Fotakis, *Chem. Phys. Lett.*, **74**, 58 (1980).

[185] G. Black and L. E. Jusinski, *Chem. Phys. Lett.*, **124**, 90 (1986).

[186] T. N. Kitsopoulos, C. R. Gebhardt, and T. P. Rakitzis, *J. Chem. Phys.*, **115**, 9727 (2001).

[187] D. Xu, J. Huang, and W. M. Jackson, *J. Chem. Phys.*, **120**, 3051 (2004).

[188] W. S. McGivern, O. Sorkhabi, A. H. Rizvi, A. G. Suits, and S. W. North, *J. Chem. Phys.*, **112**, 5301 (2000).

[189] W.-B. Tzeng, H.-M. Yin, W.-Y. Leung, J.-Y. Luo, S. Nourbakhsh, G. D. Flesch, and C. Y. Ng., *J. Chem. Phys.*, **88**, 1658 (1988).

[190] J. G. Frey and P. Felder, *Chem. Phys.*, **202**, 397 (1996).

[191] P. Farmanara, V. Stert, and W. Radloff, *J. Chem. Phys.*, **111**, 5338 (1999).

[192] J. E. Butler, W. S. Drozdoski, and J. R. McDonald, *Chem. Phys.*, **50**, 413 (1980).

[193] M. D. Barry, N. P. Johnson, and P. A. Gorry, *J. Phys. E: Sci. Instrum.*, **19**, 815 (1986).

[194] M. Brouard, A. V. Green, F. Quadrini, and C. Vallance, *J. Chem. Phys.*, **127**, 084304 (2007).

[195] Y. Sato, Y. Matsumi, M. Kawasaki, K. Tsukiyama, and R. Bersohn, *J. Phys. Chem.*, **99**, 16307 (1995).

[196] W.-H. Yuen, DPhil thesis, Oxford University, (2012).

[197] V. V. Kuznetsov and O. S. Vasyutinskii, *J. Chem. Phys.*, **123**, 034307 (2005).

[198] V. V. Kuznetsov and O. S. Vasyutinskii, *J. Chem. Phys.*, **127**, 044308 (2007).

[199] M. Brouard, A. Goman, S. J. Horrocks, A. J. Johnsen, F. Quadrini, and W.-H. Yuen, *J. Chem. Phys.*, **127**, 144304 (2007).

[200] G. Winnewisser and R. L. Cook, *J. Mol. Spec.*, **28**, 266 (1968).

[201] G. Maroulis, C. Makris, D. Xenides, and P. Karamanis, *Mol. Phys.*, **98**, 481 (2000).

[202] K. Anderson and A. J. Sadlej, *Phys. Rev. A.*, **46**, 2356 (1992).

[203] R. R. Reddy, Y. N. Ahammed, K. R. Gopal, and D. B. Basha, *Astrophys. and Space Science*, **286**, 419 (2003).

[204] A. S. Beatty, R. C. Shiell, D. Chang, and J. W. Hepburn, *J. Chem. Phys.*, **110**, 8476 (1999).

[205] G. A. Garcia, L. Nahon, and I. Powis, *Rev. Sci. Instrum.*, **75**, 4989 (2004).

[206] C. X. W. Qian, A. Ogai, L. Iwata, and H. Reisler, *J. Chem. Phys.*, **92**, 4296 (1990).

[207] C. X. W. Qian, A. Ogai, J. Brandon, Y. Y. Bai, and H. Reisler, *J. Phys. Chem.*, **95**, 6763 (1991).

[208] R. N. Zare, *Ber. Bunsenges. Phys. Chem.*, **86**, 422 (1982).

[209] R. Liyanage and R. J. Gordon, *J. Chem. Phys.*, **107**, 7209 (1997).

[210] D. W. Neyer, A. J. R. Heck, and D. W. Chandler, *J. Chem. Phys.*, **110**, 3411 (1999).

[211] D. W. Neyer, A. J. R. Heck, and D. W. Chandler, *J. Phys. Chem. A.*, **103**, 10388 (1999).

[212] H. Kawamata, H. Kohguchi, T. Nishide, and T. Suzuki, *J. Chem. Phys.*, **125**, 133312 (2006).

[213] M. Brouard, F. Quadrini, and C. Vallance, *J. Chem. Phys.*, **127**, 084305 (2007).